1-1-2010

The Fourier Spectrum Element Method For Vibration And Power Flow Analysis Of Complex Dynamic Systems

Hongan Xu
Wayne State University,

Recommended Citation

Xu, Hongan, "The Fourier Spectrum Element Method For Vibration And Power Flow Analysis Of Complex Dynamic Systems" (2010). *Wayne State University Dissertations.* Paper 225.

THE FOURIER SPECTRAL ELEMENT METHOD FOR VIBRATION AND POWER FLOW ANALYSIS OF COMPLEX DYNAMIC SYSTEMS

by

HONGAN XU

DISSERTATION

Submitted to the Graduate School

of Wayne State University,

Detroit, Michigan

in partial fulfillment of the requirements

for the degree of

DOCTOR OF PHILOSOPHY

2011

MAJOR: MECHANICAL ENGINEERING

Advisor Date

ACKNOWLEDGEMENTS

First of all, the utmost gratitude goes to my advisor, Prof. Wen Li. I would like to thank him for his initial encouragement and patient guidance during my Ph.D study. He has always been a wonderful mentor to me and I have learned a great deal from him throughout the past five years.

I am also grateful to Dr. Carl Howard who provided testing facilities for my collaborative research at the University of Adelaide in Australia.

I would also like to thank my committee members, Prof. Sean Wu, Prof. Chin An Tan and Prof. Gongkang Fu. Particularly, I express my appreciation to Prof. Sean Wu for his assistance in my research.

I am also thankful to Logesh Kumar Natarajan and Dr. Jian Wang for their helps on the experimental testing. I am also grateful to my research partner Xuefeng Zhang and Dr. Jingtao Du for their valuable discussions.

Special thanks are given to my wife, Yanxia, for her love, patience, sacrifice and supports. My sincere appreciation is also extended to my parents for encouraging me and taking care of my lovely daughter Xiaoxiao.

Finally, I would like to give my appreciations to all those who helped me but not mentioned here.

TABLE OF CONTENTS

APPENDIX

LIST OF TABLES

LIST OF FIGURES

CHAPTER I

INTRODUCTION

1.1 Background

Noise and vibration are one of the primary design concerns for automotive, aircraft, appliance, equipment, and other machinery manufacturers. Identifying dominant noise and vibration sources and understanding their effects on dynamic systems are of vital importance to improving product quality and solving practical noise and vibration problems.

A dynamic system typically exhibits distinctively different response characteristics in different frequency ranges. At low frequencies, Finite Element Analysis (FEA) is the most commonly used tool for the dynamic analysis of complex structures. It is widely believed that the low frequency limit of FEA methods is only limited by computing resources. However, there are actually some other intrinsic reasons that make FEA methods ineffective, even useless, at high frequencies, regardless of computer resource considerations (Rabbiolo *et al*., 2004). While the idea of dividing a structure into a large number of elements is theoretically necessary to represent its geometry, it is clearly not suitable for high frequency applications because the presence of inevitable manufacturing errors or variations tends to make deterministic FEA results erratic and unreliable.

At high frequencies, a response spectrum tends to become smooth without strong modal showings; thus, deterministic methods are usually no longer useful. Instead, the Statistical Energy Analysis (SEA) method has emerged as a major technique for the analyses of complex dynamic systems at high frequencies (Lyon, 1975). In an SEA model, the original dynamic system is divided into a number of subsystems (or mode groups) on which the solution variables are usually the frequency- and space-averaged energy levels. The coupling between any two subsystems is described by the so-called Coupling Loss Factor (CLF) that basically regulates the energy flows through the junction. Theoretically, the CLFs are typically calculated based on wave formulations for the interaction of two semi-infinite subsystems. Consequently, the modal details of the individual sub-systems are simply ignored, which often results in a smoothened estimate of the model variables such as the wave transmission coefficients or coupling loss factors. The flaw of this process may be seen by the fact that the CLFs are usually assumed to be independent of the modal overlap, which is shown not to be the case for small modal overlap factors (Mace & Rosenberg, 1999; Wester & Mace 1996; Yap & Woodhouse, 1996). The issues and concerns related to the irregularities and varieties of the SEA solutions have also been investigated by other researchers (Craik et al., 1991; Fahy, 1997; Fahy & Mohamed, 1992).

Between the low-frequency and the high-frequency ranges, there is a widely recongnized mid-frequency range that is critical to the engineering design of dynamic systems because the dominant excitation bands often fall in this region in real-world dynamic problems. However, the mid-frequency range is not clearly defined in practice. In fact, the medium frequency region for a “uniform” structure implies where the structure shows a highly volatile and uncertain behavior in response to an excitation or minor changes. Medium-frequency problems are also referred to as a dynamic system that exhibits mixed coherent global and incoherent local motions (Langley & Bremner, 1999; Shorter & Langley, 2005) or consists of subsystems with distinctively different modal densities (Zhao & Vlahopoulos, 2004). In some sense, it is accepted that the mid-frequency range is where the conventional deterministic methods such as FEA are not appropriate, but the SEA assumptions are not yet fulfilled. Many analytical methods have been developed to address mid-frequency problems.

Dynamic Stiffness Methods (DSM) are often used to calculate the power flows between beams/plates or in frameworks (Park & Hong, 2001; Bercin & Langley, 1996; Langley, 1990). In the dynamic stiffness methods, the displacements at both ends of a beam are determined in terms of the complex amplitudes for each wave component from which one can derive the relationship between the general force and displacement vectors.

Spectral Element Method (SEM) is another powerful technique for the vibration and energy flow analysis of simple or complex beam systems (Doyle, 1989; Ahmida & Arruda, 2001; Igawa *et al*., 2004). In SEM each uniform beam or rod can be considered as a super-element on which the flexural, longitudinal and torsional waves will be expressed in terms of exact beam solutions. As a result, the coupling of various waves at a junction can be easily dealt with by following a FE-like assembling procedure.

Analytical techniques based on the theory of receptance have also been used to study the energy flows between structures like rods, beams and plates (Keane & Price, 1991; Keane, 1992; Beshara & Keane, 1997, 1998). In receptance methods, the relationship between the coupling forces and the displacements at the ends of a beam is derived by making use of Green's functions for the uncoupled beam under boundary conditions compatible with the entire system. Green's function can be expressed either in a closed form or as the expansion of the modes for the beam with appropriate boundary conditions. It has also been employed to model more complicated junctions involving a number of connecting beams and the interactions of the flexural, longitudinal, and torsional wave (Shankar & Keane, 1995; Farag & Pan, 1997).

The advantage of these methods is that each beam is considered as a fundamental element and a FEA-like assembling process can be followed to allow it to be used for composite structures. However, they all have some inherent technical and practical limits or difficulties. For instance, the applications of SEM, DSM, and receptance methods are primarily limited to beam frameworks because an analytical solution is generally not available for other types of structural components such as plates or shells. Other well-recognized problems or concerns include the following: solutions become increasingly difficult for large values of coupling stiffness; the numerical break-down of the standard beam functions approximately after the first dozen modes and the slow convergence of the modal expansions when the boundary/coupling conditions cannot be assumed correctly (Shankar & Keane, 1995).

The Differential Quadrature (DQ) method, which was first proposed in the early 1970s (Bellman, 1971; & Bellman etc., 1972), has been successfully applied to plate and beam-plate coupling problems (Laura & Gutierrez, 1994; Shu & Wang, 1999; Zeng & Bert，2001). This method provides a numerical scheme for finding a discrete form of a solution, where the derivatives of a function at a given point are expressed in terms of the values of the functions at a number of discrete points which are properly distributed over the entire solution domain. Despite its certain degree of success in various physical and engineering applications, the DQ method has some inherent limitations in choosing the basis functions, grid points and weighting coefficients. For instance, the Delta-grids commonly used in approximating the second order derivatives can potentially lead to an ill-conditioned weighting coefficient matrix (Laura & Gutierrez, 1994).

The Trefftz method, which is classified into indirect and direct ones, is also employed for analyzing plate problems (Cheung *et al*., 1993; Jin *et al*., 1990; Hochard & Proslier, 1992; Kita & Kamiya, 1995). While the indirect Trefftz method is to approximate the solution by superposing a complete set of functions (T-functions) that exactly satisfy the governing equations, the direct one is based on the boundary integral equation derived from the weighted residual expressions of the governing equation. The Trefftz method is advantageous in terms of the reduction of computation load compared to the element base methods. In order to secure the convergence, this method requires a complete set of shape functions representing any possible field variable distributions in a continuum domain. Whereas such type of shape functions are not always available, their practical convergence is not always guaranteed due to the poor condition of the involved model matrices (Desmet, 2002).

Another method, often referred to as the Energy Finite Element Method (EFEM or EFEA), has also received considerable attention (Nefske & Sung, 1989; Bouthier & Bernhard, 1992; Cho & Bernhard, 1998; Zhao & Vlahopoulos, 2004). The primary variable in the EFEM is the time-averaged energy density, and the governing equation for the energy density is derived in the form of heat conduction equation. As a result, the power flow field can be solved using a standard finite element code by modifying the model input parameters accordingly. The EFEM was originally considered a promising technique for mid-frequency analysis probably because it allows for modeling the spatial variation of the energy density in a subsystem. However, if the elements are equivalently viewed as the subsystems in an SEA model, then it is not difficult to understand that they will be more likely to violate the premises or conditions that have failed the SEA methods to mid frequency problems. Actually, the relationship between the power flow and energy density for coupled beams, which leads to the heat conduction analogy, was shown to be valid only for beams in terms of the local space-averaged powers (Wohlever & Bernhard, 1992). It is also observed that the EFEA results, even after spatially averaged, tend to have larger errors at or near the boundary and junction lines (Klos, 2004). In addition, due to the discontinuity of energy density at the junctions of different structural members, the power transfer coefficients need to be calculated for each of the different joints, which usually require considerable efforts.

In addition, many hybrid techniques have been developed to address the mixed behaviors at mid-frequencies; for example, they include the following: FEM+SEA (Zhao & Vlahopoulos, 2004; Langley & Bremner, 1999; Shorter & Langley, 2005), Fuzzy methods (Soize, 1993, 1995, 1998), FEM+Integral description (Fischer et al., 1995), SEA+Analytical solution (Li & Lavrich, 1996), FEA+Smooth Integral Formulation (Pratellesi *et al*. 2009).

Because of the aforementioned problems and concerns, the development of a robust and more sophisticated method that is capable of tackling mid-frequency problems, simplifying solution algorithms/procedures, universally dealing with various coupling and boundary conditions, and eliminating approximations or assumptions that may be questionable or violated under the real system condition is of great interest to both researchers and application engineers.

1.2 General description of research approach

It is generally accepted that trigonometric functions are probably the most desired set for expanding a function or an analytical solution because of their completeness and orthogonality, as well as for their excellent stability in numerical calculations. The research approach employed in this dissertation is based on a modified Fourier series method proposed by Li (2000, 2002). For completeness, this Fourier series method will be briefly illustrated here.

A continuous function defined over a domain can be expanded into a Fourier series inside the domain excluding boundary points. Take a beam problem for example. The displacement solution $w(x)$ on a beam of length L is required to have up to the fourth derivatives, that is, $w(x) \in C^3$. Mathematically, the displacement function $w(x)$ can be viewed as a part of an *even function* defined over [-L, L], as shown in Fig. 1.1(a), and the Fourier expansion of this even function then only contains the cosine terms. The Fourier cosine series is able to correctly converge to $w(x)$ at *any* point over [0, L]. However, its derivative $w'(x)$ is an odd function over [-L, L] leading to a jump at end locations. Thus, its Fourier series expansion (sine series) will accordingly have a convergence problem due to the discontinuity at end points.

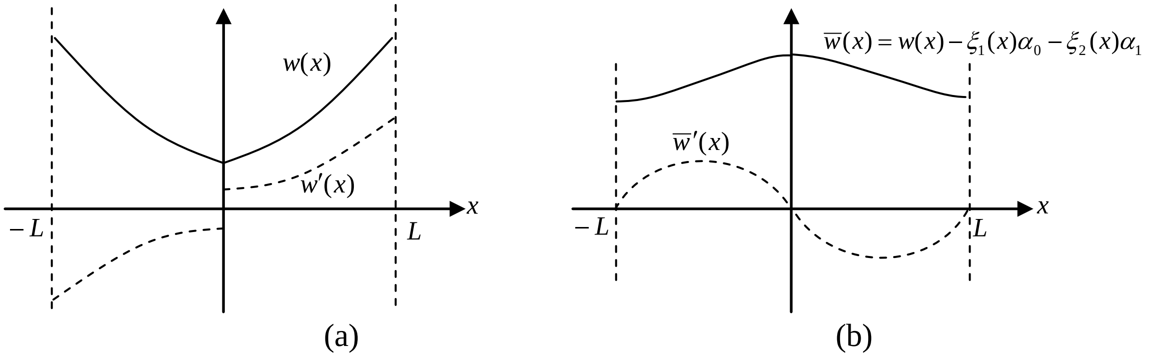

Figure 1.1 An illustration of the possible discontinuities of the displacement at the end points, and how they can be equivalently removed mathematically.

To overcome this problem, we alternatively consider a new function

$$\overline{w}(x) = w(x) - \xi_1(x)\alpha_0 - \xi_2(x)\alpha_1 \tag{1.1}$$

where $\alpha_0 = w'(x)\big|_{x=0}$, $\alpha_1 = w'(x)\big|_{x=L}$ and $\xi_1(x)$ ($\xi_2(x)$) denotes a sufficiently smooth function in an arbitrary closed form whose derivative is set equal to 1 and 0 (0 and 1) at x=0 and L, respectively (Li, 2000). Essentially, $\overline{w}(x)$ represents a residual beam function which is continuous over [0, L] and has zero-slopes at the both ends, as shown in Fig. 1.1(b). Apparently, the cosine series representation of $\overline{w}(x)$ is able to converge correctly to the function itself and its first derivative at every point on the beam. Analogously, discontinuities potentially associated with the third-order derivative can be removed by adding two more similar terms in Eq. (1.1) expressed as (Li, 2000)

$$\overline{w}(x) = w(x) - \xi_1(x)\alpha_0 - \xi_2(x)\alpha_1 - \xi_3(x)\beta_0 - \xi_4(x)\beta_1 \qquad (\lambda_m = m\pi / L) \tag{1.2}$$

where $\overline{w}(x)=\sum_{m=0}^{\infty}a_m\cos\lambda_m x$, $\beta_0=w'''(x)\big|_{x=0}$, $\beta_1=w'''(x)\big|_{x=L}$, and $\xi_3(x)$ ($\xi_4(x)$) has the same meaning as $\xi_1(x)$ ($\xi_2(x)$). The "physical impact" of this mathematical manipulation is to construct a desired residual displacement function $\overline{w}(\xi)$ that is ensured to have at least three continuous derivatives over the entire definition domain (including the boundary points).

The displacement can also be expanded into a sine series. In that case, the supplementary terms are used to remove the discontinuities potentially associated with the displacement and its second-order derivative at the ends. A detailed comparison between the sine and cosine series in terms of the convergence speed has been discussed in Ref. (Li, 2002).

For two-dimension problems, taking a plate of length a and width b as an example, its displacement function in the $x-$ and $y-$ direction can be expressed accordingly as

$$\overline{w}(x,y)=w(x,y)-\sum_{i=1}^{4}\left[\xi_b^i(y)\alpha_i(x)+\xi_a^i(x)\beta_i(y)\right] \tag{1.3}$$

where $\overline{w}(x,y)=\sum_{m}^{\infty}\sum_{n=0}^{\infty}A_{mn}\cos\lambda_m x\cos\lambda_n y$ with $\lambda_m=m\pi/a$, $\lambda_n=n\pi/b$,

$$\alpha_0(x)=w'(x,y)\big|_{y=0}\ ,\ \alpha_1(x)=w'(x,y)\big|_{y=b}\ ,\ \alpha_3(x)=w'''(x,y)\big|_{y=0}\ ,\ \alpha_4(x)=w'''(x,y)\big|_{y=b}\ ,$$

$$\beta_0(y)=w'(x,y)\big|_{x=0}\ ,\ \beta_1(y)=w'(x,y)\big|_{x=a}\ ,\ \beta_3(y)=w'''(x,y)\big|_{x=0}\ ,\ \beta_4(y)=w'''(x,y)\big|_{x=a}\ .$$

and $\xi_a^i(x)$ (or $\xi_b^i(y)$) represent a set of closed-form sufficiently smooth functions defined over [0, a] (or [0, b]). The term ''sufficiently smooth'' implies that third-order derivatives of these functions exist and are continuous at any point on the plate.

The form of complementary functions in Eqs. (1.1-3) have not been explicitly specified. Actually, any function sufficiently smooth such as polynomials and trigonometric functions can be used. Thus, this idea essentially opens an avenue for systematically defining a complete set of admissible or trial functions that can be used in the Rayleigh-Ritz methods and universally applied to different boundary conditions for various structural components. The excellent accuracy and convergence of the Fourier series solutions have been repeatedly demonstrated for beams (Li, 2000, 2002; Li & Xu, 2009; and Xu & Li, 2008) and plates (Li, 2004; Li & Daniels, 2002; Du *et al.*, 2007; Li *et al*., 2009; and Zhang & Li, 2009) under various boundary conditions.

1.3 Objective and outline

The primary objective of this research is to generalize the Fourier Spectral Element Method (FSEM) to form a universal solution for the vibration and energy flow analyses of complex built-up structures, which are considered as an assembly of interconnected basic structural components such as beams and plates. Another purpose is to employ FSEM to investigate the statistical dynamic responses of and vibratory energy flows in built-up structures in the presence of model uncertainties resulting from engineering and manufacturing errors and variances. The remaining of this dissertation is structured as below.

Chapter 2 presents an exact series solution for the vibration analysis of dynamic systems consisting of any number of collinearly- and elastically-coupled beams. This model is then used to study the dynamic behavior of multi-span bridges under moving loads.

Chapter 3 proposes a closed-form solution for vibrations of 2-D and 3-D Euler-Bernoulli beams. Combined with Rayleigh-Ritz procedure, this solution is subsequently used to develop a general modeling method which can be broadly applied to the complex (2-D and 3-D) frame structures. The dynamic responses of and vibratory energy flows in some exemplary beam frames are analytically and experimentally investigated.

Chapter 4 aims to derive a general solution for vibrations of the built-up plate assemblies.

The plate assembly considered is assumed to have general boundary conditions and consist of any number of arbitrarily oriented rectangular plates. The modal characteristics of the considered plate assemblies under various boundary conditions are studied. The accuracy and versatility of the present solution are also validated by experimental predictions.

Chapter 5 develops an analytical solution for the beam-plate system. This solution is first utilized to study the effects on the modal properties for a beam-reinforced plate of various (plate and beam) support conditions, general coupling conditions, and reinforcing arrangements with respect to the number, orientations, and lengths of attached beams. In addition, a set of modal tests are also conducted for validating the presented solution. Furthermore, the characteristics of power flows and kinetic energy distributions for a stiffened plate are explored when the model is subjected to various support conditions, coupling configurations, and irregular spaced stiffeners.

In Chapter 6, the validity of the assumption in SEA that the coupling loss factors calculated in isolation remain the same under the actual system environment is firstly revisited. Secondly, the FSEM combined with the Monte Carlo Simulation (MCS) is used for estimating the dynamic behavior of built-up structures in the presence of uncertain model properties with focusing on the mid-frequency vibration characteristics.

Chapter 7 generalizes the conclusions of this research and provides some suggestions for the future work.

CHAPTER II

AN EXACT SOLUTION FOR THE VIBRATION OF MULTI-SPAN BEAM SYSTEMS

2.1 Introduction

The vibrations of multi-span beams are of considerable interest to many engineering areas such as bridge dynamics (Lee, 1996; Henchi & Fafard, 1997; Dugush & Eisenberger, 2002), vibration localizations and vibro-acoustic responses of periodic structures (Ungar, 1966; Mead, 1996; Hodges & Woodhouse, 1983), system parameter identifications and structural health monitoring (Zhu & Law, 1999), and others (Wu & Thompson, 2000). Beams with various structural attachments or complicating factors have been extensively studied for many years. While modern numerical methods such as the Finite Element Method (Hino *et al*., 1984; Olsson, 1985) can be generally used for the dynamic analyses of multi-span beams, some insightful information or details may easily be lost in the numerical processes. In addition, a grid-based solution method tends to become cumbersome in certain applications involving, such as, moving loads. Thus, analytical solutions are often desired in studying the dynamics of distributed systems.

A number of solution methods have been developed for solving various beam problems. The assumed mode method (Lee, 1994; Zheng *et al.*, 1998; Cha, 2005; Ichikawa & Miyakawa, 2000) is perhaps the most popular and straightforward analytical method for solving a single- or multi-span beam problem. In this method, an intermediate support is often viewed as the lumped element which is added to the main beam. The assumed modes are typically the beam functions that are usually extracted under the unloaded or unconstrained conditions. Ichikawa and Miyakawa (2000) gave a solution for a uniform continuous beam under a concentrated load moving at variable velocity. The solution was based on the mode superposition method and the final system equations in the case of variable velocity were solved numerically using the central difference method. The vibration of a multi-span non-uniform beam was studied by Zheng and Cheung (1998) using the modified beam vibration functions as the assumed modes. Other commonly used methods include Laplace transformations (Hamada, 1981; Chang, 2001), the methods of Lagrange multipliers (Dowell, 1979), the Green's function methods (Abu-Hilal, 2002; Foda & Abduljabbar, 1998), and dynamic stiffness methods (Leung & Zeng, 1994) to name a few.

Many of the aforementioned methods will require a varying level of modifications or adaptations to account for the variations in boundary conditions, intermediate supports, and/or the number of spans. For instance, when the unconstrained beam functions are used as the assumed mode shapes, one typically needs to first determine the eigenfunctions for the given boundary conditions. This problem itself may become a sizeable task if the beam is elastically restrained at either or both ends. In addition, the beam eigenfunctions tend to become numerically unstable for large modal indexes, which demands special treatments in numerical calculations. In most investigations, the term "multi-span beams" usually refers to a continuous beam with a number of intermediate supports. Although the beams may be allowed to have different physical or geometrical properties for each span, the beam displacement and its first derivatives are usually required to be continuous over the entire beam length. This condition can be easily violated when the translational or rotational coupling between any two adjacent spans is not sufficiently strong to ensure a smooth transition of the displacement or its derivative at the junction. Many modern structures such as railroad tracks, pipeline and bridges are assembled from some fundamental building blocks through joints. Thus, it is important to extend the definition of a multi-span beam to a dynamic system consisting of a number of beams coupled together through various joints. Accordingly, the continuity requirement on the displacement function needs to be replaced with the dynamic equilibrium conditions.

A modified Fourier series method was previously developed for determining the vibration of a single beam with arbitrary boundary supports (Li, 2000) and the vibrational energy flows between two beams coupled together via a set of joints (Li, 2007; Li *et al.*, 2005). It has been shown that not only does this method universally apply to any boundary conditions, but also the solution shows an excellent numerical behavior regarding its accuracy and speed of convergence. In this chapter, this method is extended to multi-span beam systems. The term multi-span beam system is used to indicate that the beam displacement or rotation is not necessarily continuous at a junction or an intermediate support. Here a beam refers to a section between any two points such as two adjacent intermediate supports which are modeled as a combination of translational and rotational springs. The couplings between beams are also described by two springs of arbitrary stiffnesses. This method offers an accurate and unified solution to this class of beam systems in that any boundary and coupling conditions can be directly simulated by simply varying the stiffness values accordingly.

2.2 Vibration of multiple coupled beams with arbitrary boundary conditions

2.2.1 An exact Fourier series

Fig. 2.1 shows a dynamic system consisting of multiple beams coupled together via a set of joints which are modeled by linear and rotational springs. The use of the coupling springs between two adjacent beams allows accounting for the effects of some non-rigid or resilient connectors. The conventional rigid connectors can be considered as a special case when the stiffnesses of these springs become substantially large with reference to the bending rigidities of the involved beams. Each of beams may also be independently supported on a set of elastic restraints at both ends. All the traditional intermediate supports and homogeneous boundary conditions (*i.e.*, the combinations of the simply supported, free, guided and clamped end conditions) can be readily obtained from these general boundary conditions by accordingly setting the stiffness constants of the restraining springs to be equal to zero or infinity.

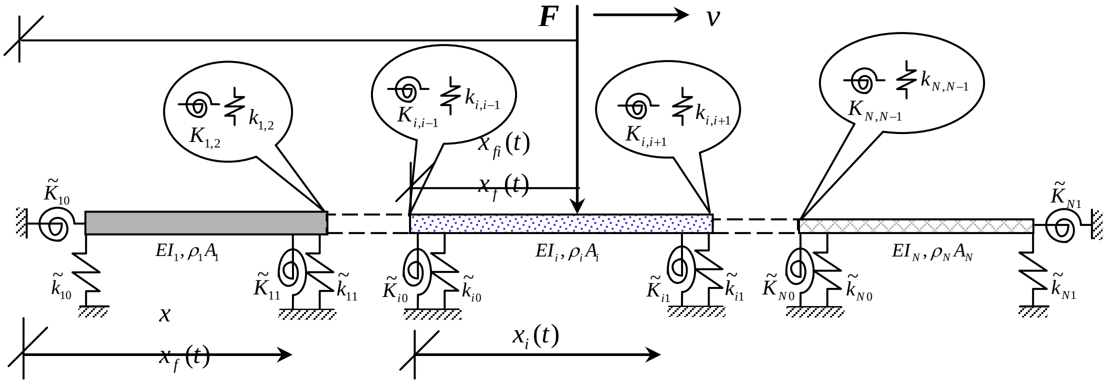

Figure 2.1 An illustration of a multi-span beam system

The differential equation for the vibration of the *i*-th beam is well known as

$$D_i \, d^4 w_i(x) / d x^4 - \rho_i S_i \omega^2 w_i(x) = f_i(x) \qquad (i = 1, 2, ..., N) \tag{2.2.1}$$

where w_i, D_i, ρ_i, and S_i are respectively the flexural displacement, the bending rigidity, the mass density and the cross-sectional area of beam *i*, and ω is angular frequency. The boundary and compatibility conditions can be expressed as

at $x_i = 0$,

$$k_{i,i-1}(w_i - w_{i-1}) + \tilde{k}_{i0} w_i = -D_i w_i''' \tag{2.2.2}$$

$$K_{i,i-1}(w_i' - w'_{i-1}) + \tilde{K}_{i0} w_i' = D_i w_i'' \tag{2.2.3}$$

at $x_i = L_i$,

$$k_{i,i+1}(w_i - w_{i+1}) + \tilde{k}_{i1} w_i = D_i w_i''' \tag{2.2.4}$$

$$K_{i,i+1}(w_i' - w'_{i+1}) + \tilde{K}_{i1} w_i' = -D_i w_i'' \tag{2.2.5}$$

at the left end (of the first beam),

$$\tilde{k}_{10} w_1 = -D_1 w_1''', \qquad \tilde{K}_{10} w_1' = D_1 w_1'' \tag{2.2.6-7}$$

at the right end (of the *N*-th beam),

$$\tilde{k}_{N1} w_N = D_N w_N''', \qquad \tilde{K}_{N1} w_N' = -D_N w_N'' \tag{2.2.8-9}$$

where $k_{i,j}$ and $K_{i,j}$ denote the stiffnesses of the linear and rotational springs at the function of beam *i* and *j*, respectively; $\tilde{k}_{i,0}$, $\tilde{k}_{i,1}$ are the stiffnesses of linear springs, and $\tilde{K}_{i,0}$, $\tilde{K}_{i,1}$ are the stiffnesses of the rotational springs at the left and right ends of beam *i*, respectively.

All the conventional homogeneous beam boundary conditions can be considered as the special cases of Eqs. (2.2.6-9). For example, the simply supported boundary condition can be easily obtained by letting the stiffnesses of the translational and rotational springs be infinity and zero, respectively. On the *i*-th beam, the displacement will be sought in the form of

$$w_i(x) = \sum_{m=0}^{\infty} A_{i,m} \cos \lambda_{i,m} x + p_i(x) \ , \ 0 \le x \le L_i, \qquad (\lambda_{i,m} = m\pi / L_i) \tag{2.2.10}$$

where L_i is the length of beam *i*.

In Eq. (2.2.10), an auxiliary function $p_i(x)$ is introduced to improve the convergence of the series expansion at end points, x_i =0, L_i. It is specifically required to satisfy the following conditions:

$$p_i'''(0) = w_i'''(0) = \alpha_{i0} \ , \ p_i'''(L_i) = w_i'''(L_i) = \alpha_{i1} \tag{2.2.11-12}$$

$$p_i'(0) = w_i'(0) = \beta_{i0} \ , \ p_i'(L_i) = w_i'(L_i) = \beta_{i1} \tag{2.2.13-14}$$

The benefits of using such an auxiliary function have been discussed in reference (Li, 2000). Theoretically, the auxiliary function $p_i(x)$ may be any sufficiently smooth function explicitly defined over [0, L_i], and thus there is an infinite number of possible choices. Here the auxiliary function is simply chosen to be a polynomial, that is,

$$p_i = \boldsymbol{\zeta}_i(x)^T \boldsymbol{\alpha}_i \tag{2.2.15}$$

where $\boldsymbol{\alpha}_i = \{\alpha_{i0}, \alpha_{i1}, \beta_{i0}, \beta_{i1}\}^T$ (2.2.16)

and
$$\boldsymbol{\zeta}_i(x)^T = \begin{Bmatrix} -(15x^4 - 60L_i x^3 + 60L_i^{\,2}x^2 - 8L_i^{\,4})/360L_i \\ (15x^4 - 30L_i^{\,2}x^2 + 7L_i^{\,4})/360L_i \\ (6L_i x - 2L_i^{\,2} - 3x^2)/6L_i \\ (3x^2 - L_i^{\,2})/6L_i \end{Bmatrix} \tag{2.2.17}$$

It should be noted that although the same symbol is used, the *x*-coordinate in Eq. (2.2.17) actually represents a local coordinate system with its origin at the left end of each beam. However, the use of different local coordinate systems is simply for the sake of mathematical convenience. Thus far, the auxiliary function has been fully defined within 4 unknown boundary constants, $\boldsymbol{\alpha}_i = \{\alpha_{i0}, \alpha_{i1}, \beta_{i0}, \beta_{i1}\}^T$. In what follows, it will be shown that these unknowns can be explicitly expressed as the functions of Fourier coefficients. Substituting Eqs. (2.2.10-17) into Eqs. (2.2.2-9) leads to

$$\begin{aligned} k_{i,i-1}&\left(\sum_{m=0}^{\infty}(-1)^m A_{i-1,m} - \frac{7L_{i-1}^{\,3}\alpha_{i-1,0}}{360} - \frac{8L_{i-1}^{\,3}\alpha_{i-1,1}}{360} + \frac{\beta_{i-1,0}L_{i-1}}{6} + \frac{\beta_{i-1,1}L_{i-1}}{3}\right) \\ &= D_i\alpha_{i,0} + (k_{i,i-1} + \tilde{k}_{i0})\left(\sum_{m=0}^{\infty} A_{i,m} + \frac{8L_i^{\,3}\alpha_{i,0}}{360} + \frac{7L_i^{\,3}\alpha_{i,1}}{360} - \frac{\beta_{i,0}L_i}{3} - \frac{\beta_{i,1}L_i}{6}\right) \end{aligned} \tag{2.2.18}$$

$$(K_{i,i-1} + \tilde{K}_{i0})\beta_{i,0} = K_{i,i-1}\beta_{i-1,1} + D_i\left(-\sum_{m=1}^{\infty}\lambda_{i,m}^2 A_{i,m} - \frac{\alpha_{i,0}L_i}{3} - \frac{\alpha_{i,1}L_i}{6} + \frac{\beta_{i,1}}{L_i} - \frac{\beta_{i,0}}{L_i}\right) \tag{2.2.19}$$

$$\begin{aligned} &(k_{i,i+1} + \tilde{k}_{i1})\left(\sum_{m=0}^{\infty}(-1)^m A_{i,m} - \frac{7L_i^{\,3}\alpha_{i,0}}{360} - \frac{8L_i^{\,3}\alpha_{i,1}}{360} + \frac{\beta_{i,0}L_i}{6} + \frac{\beta_{i,1}L_i}{3}\right) = \\ &\quad D_i\alpha_{i,1} + k_{i,i+1}\left(\sum_{m=0}^{\infty} A_{i+1,m} + \frac{8L_{i+1}^{\,3}\alpha_{i+1,0}}{360} + \frac{7L_{i+1}^{\,3}\alpha_{i+1,1}}{360} - \frac{\beta_{i+1,0}L_{i+1}}{3} - \frac{\beta_{i+1,1}L_{i+1}}{6}\right) \end{aligned} \tag{2.2.20}$$

$$(K_{i,i+1}+\tilde{K}_{i1})\beta_{i,1}=K_{i,i+1}\beta_{i+1,0}-D_i\left(\sum_{m=1}^{\infty}(-1)^{m+1}\lambda_{i,m}^2A_{i,m}+\frac{\alpha_{i,0}L_i}{6}+\frac{\alpha_{i,1}L_i}{3}+\frac{\beta_{i,1}}{L_i}-\frac{\beta_{i,0}}{L_i}\right) \quad (2.2.21)$$

The above equations can be rewritten in a matrix form as

$$\mathbf{H}_{i,i-1}\boldsymbol{\alpha}_{i-1}+\mathbf{H}_{i,i}\boldsymbol{\alpha}_i+\mathbf{H}_{i,i+1}\boldsymbol{\alpha}_{i+1}=\sum_{m=0}^{\infty}\left(\mathbf{Q}_{i,i-1}^m\mathbf{A}_{i-1,m}+\mathbf{Q}_{i,i}^m\mathbf{A}_{i,m}+\mathbf{Q}_{i,i+1}^m\mathbf{A}_{i+1,m}\right) \quad (2.2.22)$$

where

$$\mathbf{H}_{i,i}=\begin{bmatrix} \frac{8(k_{i,i-1}+\tilde{k}_{i0})L_i^{\ 3}}{360}+D_i & \frac{7(k_{i,i-1}+\tilde{k}_{i0})L_i^{\ 3}}{360} & \frac{-(k_{i,i-1}+\tilde{k}_{i0})L_i}{3} & \frac{-(k_{i,i-1}+\tilde{k}_{i0})L_i}{6} \\ \frac{7(k_{i,i+1}+\tilde{k}_{i1})L_i^{\ 3}}{360} & \frac{8(k_{i,i+1}+\tilde{k}_{i1})L_i^{\ 3}}{360}+D_i & \frac{-(k_{i,i+1}+\tilde{k}_{i1})L_i}{6} & \frac{-(k_{i,i+1}+\tilde{k}_{i1})L_i}{3} \\ \frac{L_iD_i}{3} & \frac{L_iD_i}{6} & (K_{i,i-1}+\tilde{K}_{i0})+\frac{D_i}{L_i} & \frac{-D_i}{L_i} \\ \frac{L_iD_i}{6} & \frac{L_iD_i}{3} & \frac{-D_i}{L_i} & (K_{i,i+1}+\tilde{K}_{i1})+\frac{D_i}{L_i} \end{bmatrix} \quad (2.2.23)$$

$$\mathbf{H}_{i,i+1}=\begin{bmatrix} 0 & 0 & 0 & 0 \\ \frac{8k_{i,i+1}L_{i+1}^{\ 3}}{360} & \frac{7k_{i,i+1}L_{i+1}^{\ 3}}{360} & \frac{-k_{i,i+1}L_{i+1}}{3} & \frac{-k_{i,i+1}L_{i+1}}{6} \\ 0 & 0 & 0 & 0 \\ 0 & 0 & -K_{i,i+1} & 0 \end{bmatrix} \quad (2.2.24)$$

$$\mathbf{H}_{i,i\text{-}1}=\begin{bmatrix} \frac{7k_{i,i\text{-}1}L_{i-1}^{\ 3}}{360} & \frac{8k_{i,i\text{-}1}L_{i-1}^{\ 3}}{360} & \frac{-k_{i,i\text{-}1}L_{i-1}}{6} & \frac{-k_{i,i\text{-}1}L_{i-1}}{3} \\ 0 & 0 & 0 & 0 \\ 0 & 0 & 0 & -K_{i,i\text{-}1} \\ 0 & 0 & 0 & 0 \end{bmatrix} \quad (2.2.25)$$

$$\mathbf{Q}_{i,i}^m=\left\{-(k_{i,i-1}+\tilde{k}_{i0}) \quad (-1)^m(k_{i,i+1}+\tilde{k}_{i1}) \quad -D_i\lambda_{i,m}^2 \quad (-1)^mD_i\lambda_{i,m}^2\right\}^{\mathrm{T}} \quad (2.2.26)$$

$$\mathbf{Q}_{i,i-1}^m=\left\{(-1)^mk_{i,i-1} \quad 0 \quad 0 \quad 0\right\}^{\mathrm{T}} \text{ and } \mathbf{Q}_{i,i+1}^m=\left\{0 \quad -k_{i,i+1} \quad 0 \quad 0\right\}^{\mathrm{T}} \quad (2.2.27\text{-}28)$$

Eq. (2.2.22) consists of 4 linear algebraic equations that essentially relate the 12 boundary constants to the Fourier expansion coefficients. To fully determine the boundary constants, one has to apply Eq. (2.2.22) in turn to each beam, resulting in a total of 4*N* equations which can be expressed as

$$\overline{\mathbf{H}}\overline{\boldsymbol{\alpha}} = \sum_{m=0}^{\infty} \overline{\mathbf{Q}}^{m} \mathbf{A}_{m} \tag{2.2.29}$$

where $\overline{\boldsymbol{\alpha}} = \{\boldsymbol{\alpha}_1, \boldsymbol{\alpha}_2, ..., \boldsymbol{\alpha}_N\}^T$ and $\overline{\mathbf{A}}_m = \{\mathbf{A}_{1,m}, \mathbf{A}_{2,m}, ..., \mathbf{A}_{N,m}\}^T$ (2.2.30-31)

$$\overline{\mathbf{H}} = \begin{bmatrix} \mathbf{H}_{1,1} & \mathbf{H}_{1,2} & \mathbf{0} & \cdots & \mathbf{0} & \mathbf{0} & \mathbf{0} & \cdots & \mathbf{0} & \mathbf{0} \\ \mathbf{H}_{2,1} & \mathbf{H}_{2,2} & \mathbf{H}_{2,3} & \cdots & \mathbf{0} & \mathbf{0} & \mathbf{0} & \cdots & \mathbf{0} & \mathbf{0} \\ \vdots & \vdots & \vdots & \cdots & \vdots & \vdots & \vdots & \cdots & \vdots & \vdots \\ \mathbf{0} & \mathbf{0} & \mathbf{0} & \cdots & \mathbf{H}_{i,i-1} & \mathbf{H}_{i,i-1} & \mathbf{H}_{i,i-1} & \cdots & \mathbf{0} & \mathbf{0} \\ \vdots & \vdots & \vdots & \cdots & \vdots & \vdots & \vdots & \cdots & \vdots & \vdots \\ \mathbf{0} & \mathbf{0} & \mathbf{0} & \cdots & \mathbf{0} & \mathbf{0} & \mathbf{0} & \cdots & \mathbf{H}_{N,N-1} & \mathbf{H}_{N,N} \end{bmatrix} \tag{2.2.32}$$

and

$$\overline{\mathbf{Q}}^{m} = \begin{bmatrix} \mathbf{Q}^m_{1,1} & \mathbf{Q}^m_{1,2} & \mathbf{0} & \cdots & \mathbf{0} & \mathbf{0} & \mathbf{0} & \cdots & \mathbf{0} & \mathbf{0} \\ \mathbf{Q}^m_{2,1} & \mathbf{Q}^m_{2,2} & \mathbf{Q}^m_{2,3} & \cdots & \mathbf{0} & \mathbf{0} & \mathbf{0} & \cdots & \mathbf{0} & \mathbf{0} \\ \vdots & \vdots & \vdots & \cdots & \vdots & \vdots & \vdots & \cdots & \vdots & \vdots \\ \mathbf{0} & \mathbf{0} & \mathbf{0} & \cdots & \mathbf{Q}^m_{i,i-1} & \mathbf{Q}^m_{i,i} & \mathbf{Q}^m_{i,i+1} & \cdots & \mathbf{0} & \mathbf{0} \\ \vdots & \vdots & \vdots & \cdots & \vdots & \vdots & \vdots & \cdots & \vdots & \vdots \\ \mathbf{0} & \mathbf{0} & \mathbf{0} & \cdots & \mathbf{0} & \mathbf{0} & \mathbf{0} & \cdots & \mathbf{Q}^m_{N,N-1} & \mathbf{Q}^m_{N,N} \end{bmatrix} \tag{2.2.33}$$

The unknown constants can now be solved from Eq. (2.2.29) as

$$\overline{\boldsymbol{\alpha}} = \sum_{m=0}^{\infty} \widetilde{\mathbf{H}}\overline{\mathbf{Q}}^{m} \mathbf{A}_{m} \tag{2.2.34}$$

where

$$\widetilde{\mathbf{H}} = \begin{Bmatrix} \widetilde{\mathbf{H}}_1 \\ \vdots \\ \widetilde{\mathbf{H}}_i \\ \vdots \\ \widetilde{\mathbf{H}}_N \end{Bmatrix} = \overline{\mathbf{H}}^{-1} \quad \text{and} \quad \overline{\mathbf{Q}}^{m} = \begin{Bmatrix} \overline{\mathbf{Q}}^m_1 \\ \overline{\mathbf{Q}}^m_2 \\ \vdots \\ \overline{\mathbf{Q}}^m_i \\ \vdots \\ \overline{\mathbf{Q}}^m_N \end{Bmatrix} \tag{2.2.35-36}$$

with $$\overline{\mathbf{Q}}_1^m = \begin{Bmatrix} \mathbf{Q}_{1,1}^m \\ \mathbf{Q}_{2,1}^m \\ \mathbf{0} \\ \mathbf{0} \\ \mathbf{0} \end{Bmatrix}, \qquad \overline{\mathbf{Q}}_i^m = \begin{Bmatrix} \mathbf{0} \\ \mathbf{Q}_{i-1,i}^m \\ \mathbf{Q}_{i,i}^m \\ \mathbf{Q}_{i+1,i}^m \\ \mathbf{0} \end{Bmatrix}, \qquad \text{and} \qquad \overline{\mathbf{Q}}_N^m = \begin{Bmatrix} \mathbf{0} \\ \mathbf{0} \\ \mathbf{0} \\ \mathbf{Q}_{N-1,N}^m \\ \mathbf{Q}_{N,N}^m \end{Bmatrix} \tag{2.2.37-39}$$

In light of Eq. (2.2.35), the boundary constants for beam *i* can be expressed as

$$\boldsymbol{\alpha}_i = \sum_{m=0}^{\infty} \tilde{\mathbf{H}}_i \overline{\mathbf{Q}}^m \mathbf{A}_{i,m} \tag{2.2.40}$$

Making use of Eqs. (2.2.15) and (2.2.40), Eq. (2.2.10) becomes

$$w_i(x) = \sum_{m=0}^{\infty} A_{i,m}(\cos\lambda_{i,m}x + \boldsymbol{\zeta}_i(x)^T \tilde{\mathbf{H}}_i \overline{\mathbf{Q}}_i^m) + \sum_{\substack{j=1,N \\ j\neq i}} \sum_{m=0}^{\infty} A_{j,m} \boldsymbol{\zeta}_j(x)^T \tilde{\mathbf{H}}_i \overline{\mathbf{Q}}_j^m \tag{2.2.41}$$

It should be mentioned that the boundary and coupling conditions, Eqs. (2.2.2-9), have been explicitly used in establishing the relations between the boundary constants in the polynomials and the Fourier expansion coefficients. Thus, the Fourier coefficients are now only required to satisfy the governing differential equations. By substituting Eq. (2.2.41) into Eq. (2.2.1), multiplying both sides with $\cos\lambda_{im}x + \boldsymbol{\zeta}_i(x)^T \tilde{\mathbf{H}}_i \overline{\mathbf{Q}}_i^m$, and integrating the result from 0 to L_i, one is able to obtain

for m = 1,2,3… ,

$$\sum_{m'=1}^{\infty}(\delta_{mm'} + S_{i,m'm}^{ii})\lambda_{i,m'}^4 A_{i,m'} - \bar{\rho}_i\omega^2\Big[\big(S_{i,m0}^{ii} + Z_{i,m0}^{ii}\big)A_{i,0} +$$

$$\sum_{m'=1}^{\infty}\big(\delta_{mm'} + S_{i,mm'}^{ii} + S_{i,m'm}^{ii} + Z_{i,mm'}^{ii}\big)A_{i,m'} + \sum_{\substack{j=1 \\ j\neq i}} \sum_{m'=0}^{\infty}\big(S_{i,mm'}^{ij} + Z_{i,mm'}^{ij}\big)A_{j,m'}\Big] = f_{i,m} \tag{2.2.42}$$

for m = 0,

$$S^{ii}_{i,00}A_{i,0}+\sum_{m'=1}^{\infty}\left(S^{ii}_{i,0m'}+\lambda^{4}_{i,m'}S^{ii}_{i,m'0}\right)A_{i,m'}+\sum_{\substack{j=1\\ j\neq i}}\sum_{m'=0}^{\infty}S^{ij}_{i,0m'}A_{j,m'}-$$

$$\bar{\rho}_i\omega^2\left((2+Z^{ii}_{i,00})A_{i,0}+\sum_{m'=1}^{\infty}\left(S^{ii}_{i,m'0}+Z^{ii}_{i,0m'}\right)A_{i,m'}+\sum_{\substack{j=1\\ j\neq i}}\sum_{m'=0}^{\infty}Z^{ij}_{i,0m'}A_{j,m'}\right)=f_{0,m} \quad (2.2.43)$$

where $S^{pq}_{r,mm'}=\mathbf{P}^{m}_{p}\tilde{\mathbf{H}}_r\bar{\mathbf{Q}}^{m'}_{q}$ (p, q, r = i-1, i, i+1), $Z^{pq}_{r,mm'}=(\bar{\mathbf{Q}}^{m}_{p})^{T}\tilde{\mathbf{H}}^{T}_{r}\mathbf{\Xi}_{p}\tilde{\mathbf{H}}_{r}\bar{\mathbf{Q}}^{m'}_{q}$ (2.2.44-45)

$$\mathbf{P}_{pm}=\begin{cases}\dfrac{2}{L_p}\left\{1/\lambda_{p,m}{}^{4}\quad(-1)^{m+1}/\lambda_{p,m}{}^{4}\quad -1/\lambda_{p,m}{}^{2}\quad(-1)^{m}/\lambda_{p,m}{}^{2}\right\}, & m\neq 0\\ \dfrac{2}{L_p}\left\{-1\ 1\ 0\ 0\right\}\qquad , & m=0\end{cases} \quad (2.2.46)$$

and

$$\mathbf{\Xi}_p=2/L_p\int_0^{L_p}\boldsymbol{\zeta}_p(x)^{T}\boldsymbol{\zeta}_p(x)dx=\begin{bmatrix}\dfrac{2L_p{}^{6}}{4725} & & & \\ \dfrac{127L_p{}^{6}}{302400} & \dfrac{2L_p{}^{6}}{4725} & sym. & \\ -\dfrac{4L_p{}^{4}}{945} & -\dfrac{31L_p{}^{4}}{7560} & \dfrac{2L_p{}^{2}}{45} & \\ -\dfrac{31L_p{}^{4}}{7560} & -\dfrac{4L_p{}^{4}}{945} & \dfrac{7L_p{}^{2}}{180} & \dfrac{2L_p{}^{2}}{45}\end{bmatrix} \quad (2.2.47)$$

In addition, it is not difficult to verify that

$$S^{ii}_{i,m'm}\lambda^{4}_{i,m'}=S^{ii}_{i,mm'}\lambda^{4}_{i,m}\,,\quad Z^{ii}_{i,m'm}=Z^{ii}_{i,mm'} \quad (2.2.48\text{-}49)$$

and

$$S^{ii}_{i,0m'}+\lambda^{4}_{i,m'}S^{ii}_{i,m'0}\equiv 0 \quad (2.2.50)$$

Making use of Eq. (2.2.50), Eq. (2.2.43) simplifies to

$$S^{ii}_{i,00}A_{i,0}+\sum_{\substack{j=1\\ j\neq i}}\sum_{m'=0}^{\infty}S^{ij}_{i,0m'}A_{j,m'}-$$

$$\bar{\rho}_i\omega^2\left((2+Z^{ii}_{i,00})A_{i,0}+\sum_{m'=1}^{\infty}\left(S^{ii}_{i,m'0}+Z^{ii}_{i,0m'}\right)A_{i,m'}+\sum_{\substack{j=1\\ j\neq i}}\sum_{m'=0}^{\infty}Z^{ij}_{i,0m'}A_{j,m'}\right) \quad (2.2.51)$$

The final system can be written in a matrix form as

$$\left(\overline{\mathbf{K}} - \omega^2 \overline{\mathbf{M}}\right)\overline{\mathbf{A}} = \overline{\mathbf{F}} \tag{2.2.52}$$

where

$$\overline{\mathbf{K}} = \begin{bmatrix} \mathbf{K}_{11} & \mathbf{K}_{12} & \cdots & \mathbf{K}_{1,i-1} & \mathbf{K}_{1,i} & \mathbf{K}_{1,i+1} & \cdots & \mathbf{K}_{1,N-1} & \mathbf{K}_{1,N} \\ \mathbf{K}_{21} & \mathbf{K}_{22} & \cdots & \mathbf{K}_{2,i-1} & \mathbf{K}_{2,i} & \mathbf{K}_{2,i+1} & \cdots & \mathbf{K}_{2,N-1} & \mathbf{K}_{2,N} \\ \vdots & \vdots & \vdots & \vdots & \vdots & \vdots & \vdots & \vdots & \vdots \\ \mathbf{K}_{i,1} & \mathbf{K}_{i,2} & \cdots & \mathbf{K}_{i,i-1} & \mathbf{K}_{i,i} & \mathbf{K}_{i,i+1} & \cdots & \mathbf{K}_{i,N-1} & \mathbf{K}_{i,N} \\ \vdots & \vdots & \vdots & \vdots & \vdots & \vdots & \vdots & \vdots & \vdots \\ \mathbf{K}_{N,1} & \mathbf{K}_{N,2} & \cdots & \mathbf{K}_{N,i-1} & \mathbf{K}_{N,i} & \mathbf{K}_{N,i+1} & \cdots & \mathbf{K}_{N,N-1} & \mathbf{K}_{N,N} \end{bmatrix} \tag{2.2.53}$$

$$\overline{\mathbf{M}} = \begin{bmatrix} \mathbf{M}_{11} & \mathbf{M}_{12} & \cdots & \mathbf{M}_{1,i-1} & \mathbf{M}_{1,i} & \mathbf{M}_{1,i+1} & \cdots & \mathbf{M}_{1,N-1} & \mathbf{M}_{1,N} \\ \mathbf{M}_{21} & \mathbf{M}_{22} & \cdots & \mathbf{M}_{2,i-1} & \mathbf{M}_{2,i} & \mathbf{M}_{2,i+1} & \cdots & \mathbf{M}_{2,N-1} & \mathbf{M}_{2,N} \\ \vdots & \vdots & \vdots & \vdots & \vdots & \vdots & \vdots & \vdots & \vdots \\ \mathbf{M}_{i,1} & \mathbf{M}_{i,2} & \cdots & \mathbf{M}_{i,i-1} & \mathbf{M}_{i,i} & \mathbf{M}_{i,i+1} & \cdots & \mathbf{M}_{i,N-1} & \mathbf{M}_{i,N} \\ \vdots & \vdots & \vdots & \vdots & \vdots & \vdots & \vdots & \vdots & \vdots \\ \mathbf{M}_{N,1} & \mathbf{M}_{N,2} & \cdots & \mathbf{M}_{N,i-1} & \mathbf{M}_{N,i} & \mathbf{M}_{N,i+1} & \cdots & \mathbf{M}_{N,N-1} & \mathbf{M}_{N,N} \end{bmatrix} \tag{2.2.54}$$

$$\overline{\mathbf{F}} = \left\{\mathbf{F}_1 \quad \mathbf{F}_2 \quad \cdots \quad \mathbf{F}_i \quad \cdots \quad \mathbf{F}_N\right\} \text{ and } \overline{\mathbf{A}} = \left\{\mathbf{A}_1 \quad \mathbf{A}_2 \quad \cdots \quad \mathbf{A}_i \quad \cdots \quad \mathbf{A}_N\right\} \tag{2.2.55-56}$$

with the notations $\mathbf{F}_i = \{f_{i,0}, f_{i,1}, f_{i,2}, ...\}^T$ and $\mathbf{A}_i = \{A_{i,0}, A_{i,1}, A_{i,2}, ...\}^T$

The elements of the stiffness and mass matrices are defined as follows

for $m, m' = 0, 1, 2, 3, \ldots,$

$$K_{pq,mm'} = \delta_{pq}(1-\delta_{0m})(1-\delta_{0m'})(\delta_{mm'} + S^{pq}_{p,m'm})\lambda^4_{pm'}$$

$$+\delta_{pq}\delta_{0m'}\delta_{m0}S^{pq}_{p,00} + (1-\delta_{pq})\delta_{m0}S^{pq}_{p,0m'} \tag{2.2.57}$$

$$M_{pq,mm'} = \delta_{pq}(1-\delta_{0m})(1-\delta_{0m'})(\delta_{mm'} + S^{pq}_{p,mm'} + S^{pq}_{p,m'm} + Z^{pq}_{p,mm'}) +$$

$$\delta_{pq}\delta_{0m'}\delta_{m0}(2+Z^{pq}_{p,00}) + \delta_{pq}\delta_{0m'}(S^{pq}_{p,m0} + Z^{pq}_{p,m0}) + \delta_{pq}\delta_{m0}(S^{pq}_{p,m'0} + Z^{pq}_{p,m'0})(-1)^{\delta_{m0}+\delta_{m'0}-1} +$$

$$(1-\delta_{pq})(1-\delta_{0m})(S^{pq}_{p,mm'} + Z^{pq}_{p,mm'}) + (1-\delta_{pq})\delta_{m0}Z^{pq}_{p,0m'} \tag{2.2.58}$$

and $$f_{p,m} = 2/L_p \int_0^{L_p} \left(\cos \lambda_{pm} x + \boldsymbol{\zeta}_p(x)^T \tilde{\mathbf{H}}_p \overline{\mathbf{Q}}_p^m \right) f_p(x) dx \qquad (2.2.59)$$

Eq. (2.2.52) represents a set of linear algebraic equations from which the unknown Fourier coefficients can be readily determined for a given loading condition. This equation will reduce to a standard matrix characteristic equation if the right-side force vector is set to be zero. All the eigenvalues and eigenvectors are readily obtained from the characteristic equation. Each of the eigenvectors actually contains the Fourier coefficients for the corresponding modes; the physical mode shapes can be simply calculated using Eq. (2.2.41).

2.2.2 Results and discussions

The first example involves a uniform cantilever beam of 2.5m long. The related geometrical and material parameters are given in the second column of Table 2.1. In the context of the current formulation for multi-span beams, this single beam can be equivalently viewed as a system consisting of a number of identical beams rigidly coupled together; for instance, it is here broken into two beams of 1m and 1.5m long, respectively. The clamped support at the left end (also the rigid coupling condition between these two beams) can be easily simulated by setting the stiffnesses of the corresponding springs to be infinitely large which is actually represented by a very large number, 10^{10}, in the numerical calculations.

Table 2.1 A list of beam parameters and material properties

Variables	Beam 1	Beam2	Beam3
L (m)	1.0	1.5	2.0
S (m^2)	5×10^{-5}	1.5×10^{-5}	5×10^{-5}
I (m^4)	10^{-10}	5×10^{-11}	10^{-10}
E (GPa)	207	207	207
ρ (kg/m^3)	7800	7800	7800

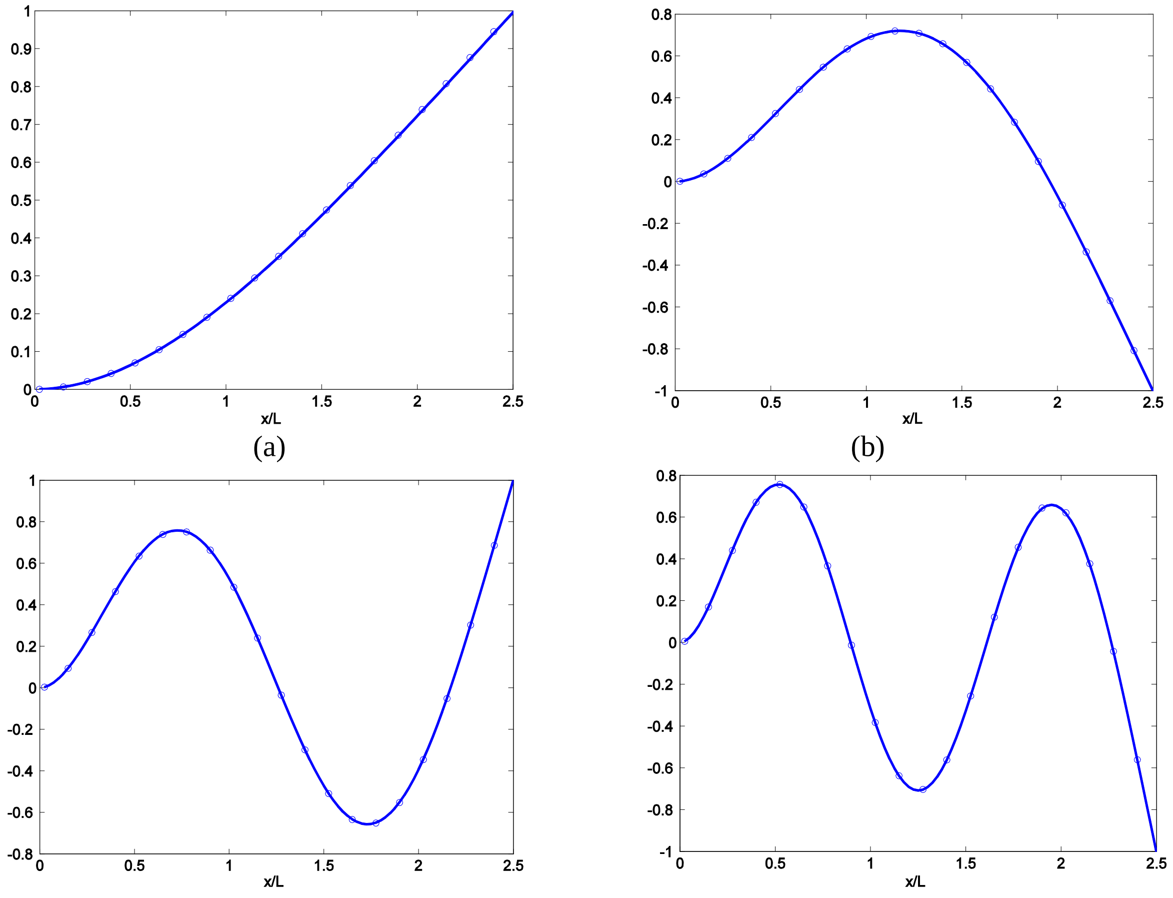

(a) (b) (c) (d)

Figure 2.2 The mode shapes for the first four modes of a cantilever beam: (a) 1st mode; (b) 2nd mode; (c) 3rd mode; (d) 4th mode. —, current method; ○, classical

Obviously, the free condition at the right end can be represented by simply setting both stiffnesses for the corresponding springs to zero. Since the modal properties for such a beam can be determined analytically from the classical beam theory, this example provides an opportunity of checking the numerical behaviors of the current solution proposed for a multi-beam system.

Table 2.2 The ten lowest natural frequencies for a cantilever beam

1	2	3	4	5	6	7	8	9	10
1.4586[a]	9.1401	25.595	50.154	82.909	123.86	172.98	230.30	295.86	369.51
1.4588[b]	9.1404	25.589	50.155	82.909	123.85	172.98	230.30	295.81	369.51

[a] Current method,
[b] Exact

In Table 2.2, the calculated first ten natural frequencies are compared with the theoretical ones for a cantilever beam; an excellent agreement is seen between these two sets of results. It should be pointed out that in the current calculation the series expansion on each beam has been truncated to M = 12. The mode shapes for the first four modes are plotted in Fig. 2.2. As expected, the two sets of modes are essentially identical.

Table 2.3 Natural Frequencies calculated using different truncation numbers

Mode	Current Method					Exact
	M = 6	M = 8	M = 10	M = 12	M = 15	
1	1.4586	1.4586	1.4586	1.4586	1.4586	1.4584
2	9.1409	9.1407	9.1407	9.1407	9.1407	9.1404
3	25.597	25.595	25.595	25.595	25.594	25.589
4	50.174	50.161	50.157	50.154	50.154	50.155
5	82.933	82.915	82.911	82.909	82.909	82.909
6	123.99	123.89	123.87	123.86	123.85	123.85
7	173.24	173.05	173.00	172.98	172.98	172.98
8	231.46	230.55	230.37	230.30	230.30	230.30
9	297.39	296.20	295.94	295.86	295.82	295.81
10	371.07	369.76	369.57	369.51	369.50	369.51

To understand the convergence characteristic of the current series solution, Table 2.3 shows the natural frequencies determined by using different truncation numbers. Based on these results, it can be said that the current solution behaves nicely with respect to its numerical accuracy and convergence. In the literature, the displacement function for each beam/span is often sought as an expansion of the beam (characteristic) functions determined under a set of boundary conditions presumably compatible with the actual system environment. Such solution techniques may be broadly categorized as the component mode synthesis method. It is known that the solution based on the free-interface modes tends to have a problem of slow-convergence (Shankar & Keane, 1995; Tan, 2001). An improved accuracy may result from the use of the fixed-interface modes plus several constraint modes (Kobayashi & Sugiyama, 2001). However, although the beam functions constitute a complete set, the convergence and derivability (for calculating other physical variables such as moments and forces) of the resulting series expansion cannot be easily estimated mathematically.

In comparison, the convergence characteristics have been well understood for the Fourier series expansions (Li, 2000). The excellent numerical stability is another attractive feature of the Fourier series solution. In comparison, the standard beam functions suffer a well-know numerical break-down approximately after the first dozen of modes, which demands special treatments in numerical calculations.

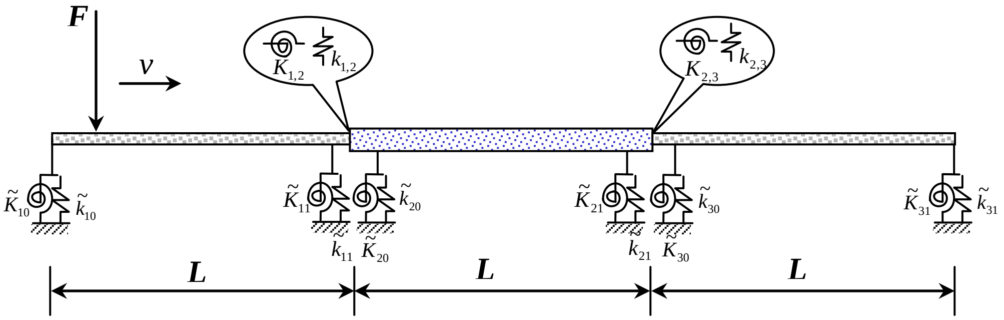

Figure 2.3 Three elastically coupled beams with arbitrary boundary supports

Now, we consider a general case involving three beams elastically coupled together, as illustrated in Fig. 2.3. The related beam parameters are summarized in Table 2.1. The left end of the system is clamped and the right end is simply supported. In addition, each beam is independently supported at both ends in the form of elastic constraints. The details of the supporting and coupling conditions are described in Table 2.4 in terms of the spring constants. For example, the simply supported condition at the right end is accomplished through setting $\tilde{k}_{3,1} = 10^{10}$ N/m and $\tilde{K}_{3,1}$ = 0 (refer to Fig. 2.3 for the notations). A moderate stiffness value indicates the possibility of a confined relative motion between the two coupling points (one of them may represent the ground).

Listed in Table 2.5 are the ten lowest natural frequencies for this three-beam system. The FEA results obtained using an ANSYS model are also presented there as a reference. In the FEA model the element size is chosen as 0.01*m*, which is considered small enough to accurately capture the spatial variation of these modes. In the current calculation, the series expansion for each beam is truncated to include only the first 10 terms (M = 10).

Table 2.4 Stiffness values for the boundary and coupling springs of a three-beam system

Stiffness for beam1	Stiffness for beam2	Stiffness for beam3	Stiffness for joints
$\tilde{k}_{1,0} = 10^{10}$ N/m	$\tilde{k}_{2,0}$ = 4000 N/m	$\tilde{k}_{3,0}$ = 5000 N/m	$k_{1,2}$ = 1000 N/m
$\tilde{k}_{1,1}$ = 5000 N/m	$\tilde{k}_{2,1}$ = 4000 N/m	$\tilde{k}_{3,1} = \infty$	$k_{2,3}$ = 1000 N/m
$\tilde{K}_{1,0} = \infty$	$\tilde{K}_{2,0}$ = 1000 Nm/rad	$\tilde{K}_{3,0}$ = 2000 Nm/rad	$K_{1,2}$ = 200 Nm/rad
$\tilde{K}_{1,1}$ = 2000 Nm/rad	$\tilde{K}_{2,1}$ = 1000 Nm/rad	$\tilde{K}_{3,1}$ = 0	$K_{2,3}$ = 200 Nm/rad

Table 2.5 Ten lowest natural frequencies for a three-beam system

1	2	3	4	5	6	7	8	9	10
4.3675[a]	13.646	13.842	21.689	26.697	34.322	42.115	46.902	58.147	62.465
4.3675[b]	13.646	13.848	21.689	26.697	34.325	42.116	46.903	58.149	62.467

[a] Current method,

[b] FEA

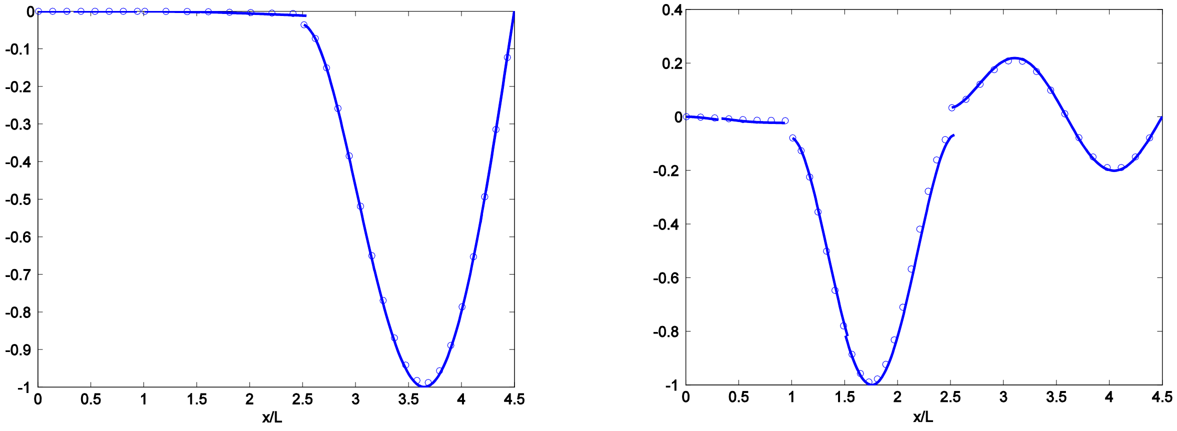

(a) (b)

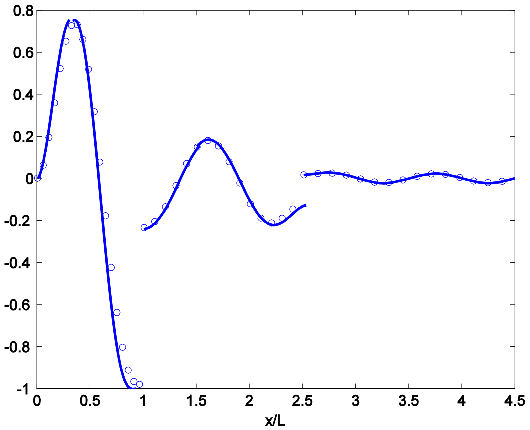

(c)

Figure 2.4 Selected plots of the mode shapes for the three elastically coupled beams: (a) 1st mode; (b) 3rd mode; (c) 8th mode. —, current method; ○, FEA

The mode shapes for a few "randomly" selected modes are plotted in Fig. 2.4 together with the FEA results. Because of the elastic couplings, the displacements on the beams are no longer continuous across the junctions. It is seen (and also predictable) that the displacement jumps at the junctions tend to increase with the modal order. These plots also show the presence of mode or vibration localization. Traditionally, the vibration localization is associated with a slight dislocation of an immediate support of otherwise perfectly periodic multi-span beam. It should become clear that the coupling conditions add another dimension to this phenomenon, and potentially play an important role in influencing or controlling the vibration localization.

2.3 Dynamic behavior of multi-span bridges under moving loads

The vibration of a multi-span bridge subjected to a moving load has been investigated in a generic manner. Unlike in most previous multi-span bridge models, the displacement and its derivatives are not here required to be continuous at the intermediate supports or any other locations. In other words, the joints between spans can be considered as the design variables and optimized to achieve desired performance. In essence, the current model is a more general representation of multi-span bridges in that each span can be independently supported and arbitrarily coupled to its neighbors via a set of joints of any stiffness values.

Since the traditional beam and material parameters have been extensively studied and well understood regarding their effect on the bridge vibration, this investigation is specifically focused on a set of rarely attempted model variables: the coupling conditions between spans.

2.3.1 Description of the analysis method

For a multi-span bridge under moving loads, as shown in Fig. 2.1, the differential equation for the vibration of the *i*-th beam is well known as

$$D_i\, d^4 w_i(x,t) \big/ d\,x^4 + \rho_i A_i\, d^2 w_i(x,t) \big/ d\,t^2 = \sum_{j=1}^{J} F_j \delta(x - x_{j,i}^f(t)) \quad (i = 1, 2, ..., N) \qquad (2.3.1)$$

where $w_i(x,t)$, D_i, ρ_i, and S_i are respectively the flexural displacement, the bending rigidity, the mass density and the cross-sectional area of *i*-th beam; ω is angular frequency and x represents the local co-ordinate measured from the left end of the *i*-th span; and *j* is the number of loads acting on the *i*-th beam at moment *t*, F_j is the magnitude of the *j*-th load, δ is the Dirac delta function, and $x_{fi}(t)$ is the load position measured from the left end of the *i*-th beam. Sometimes, unit step functions are used in Eq. (2.3.1) to explicitly specify whether a moving load is present or past. For simplicity, they are here dropped from Eq. (2.3.1) since the load position described in terms of delta function has already contained this information, *i.e.*, the *j*-th load is not present to the *i*-th beam if $x_{j,i}^f(t)$ >L_i or <0.

When a single load travels along a beam, the dynamic response can be treated as having two parts: the forced vibration caused by the load directly acting on the beam, and the residual free vibration caused by the load that has passed the beam. As a consequence, phenomena of resonance and cancellation may occur when a bridge is under the action of multiple loads. Therefore, the loading conditions (*e.g.*, the number of loads and their traveling speeds) are of critical importance to a bridge design. From mathematical point of view, however, Eq. (2.3.1) simply represents a linear system whose response to multiple loads can be actually considered as the superposition of its responses to each individual load. Thus, only one moving force will be explicitly considered in this study since our primary objective is to examine if and how the coupling conditions between spans can affect the bridge vibration. The load profile is defined by $\ddot{x}_f(t) = a = \text{const.}$, $\dot{x}_f(t) = v = v_0 + at$ and $x_f(t) = v_0 t + at^2/2$, where $x_f(t)$ is the load position measured from the left end of the first beam, a is the acceleration of the moving load, $v = v(t)$ is its velocity, and v_0 is the initial velocity at time $t = 0$ when the load is just about to enter the first beam.

The boundary and coupling conditions for the *i*-th beam can be expressed as

at $x = 0$,

$$k_{i,i-1}(w_i(x,t) - w_{i-1}(x,t)) + \tilde{k}_{i0} w_i(x,t) = -D_i w_i'''(x,t) \tag{2.3.2}$$

$$K_{i,i-1}(w_i'(x,t) - w'_{i-1}(x,t)) + \tilde{K}_{i0} w_i'(x,t) = D_i w_i''(x,t) \tag{2.3.3}$$

at $x = L_i$,

$$k_{i,i+1}(w_i(x,t) - w_{i+1}(x,t)) + \tilde{k}_{i1} w_i(x,t) = D_i w_i'''(x,t) \tag{2.3.4}$$

$$K_{i,i+1}(w_i'(x,t) - w'_{i+1}(x,t)) + \tilde{K}_{i1} w_i'(x,t) = -D_i w_i''(x,t) \tag{2.3.5}$$

at the left end (of the first beam),

$$\tilde{k}_{10} w_1(x,t) = -D_1 w_1'''(x,t), \qquad \tilde{K}_{10} w_1'(x,t) = D_1 w_1''(x,t) \tag{2.3.6-7}$$

at the right end(of the *N*-th beam),

$$\tilde{k}_{N1} w_N(x,t) = D_N w_N'''(x,t), \qquad \tilde{K}_{N1} w_N'(x,t) = -D_N w_N''(x,t) \tag{2.3.8-9}$$

where, refer to Fig. 2.1, $k_{i,j}$ and $K_{i,j}$ denote the stiffnesses of the linear and rotational springs at the junction of beams *i* and *j*, respectively; $\tilde{k}_{i,0}$, $\tilde{k}_{i,1}$ are the stiffnesses of linear springs, and $\tilde{K}_{i,0}$, $\tilde{K}_{i,1}$ the stiffnesses of the rotational springs at the left and right ends of beam *i*, respectively.

As mentioned in section 2.2, all the conventional homogeneous beam boundary conditions can be considered as the special cases of Eqs. (2.3.6-9). For each beam, the displacement will be sought in the form of

$$w_i(x,t) = \sum_{m=0}^{\infty} A_{i,m}(t)\cos\lambda_{i,m}x + p_i(x,t) \ , \quad 0 \le x \le L_i \ , \ (\lambda_{i,m} = \frac{m\pi}{L_i}) \ , \tag{2.3.10}$$

where L_i is the length of *i*-th beam.

In Eq. (2.3.10), an auxiliary function $p_i(x, t)$ was introduced to improve the accuracy and convergence of the series expansion at the end points, x =0 and L_i. It is specifically required to satisfy the following conditions:

$$p_i'''(0,t) = w_i'''(0,t) = \alpha_{i0} \ \text{ and } \ p_i'''(L_i,t) = w_i'''(L_i,t) = \alpha_{i1} \tag{2.3.11-12}$$

$$p_i'(0,t) = w_i'(0,t) = \beta_{i0} \ \text{ and } \ p_i'(L_i,t) = w_i'(L_i,t) = \beta_{i1} \tag{2.3.13-14}$$

The expression of such an auxiliary function was given by Eqs. (2.2.15-2.2.17).

Substituting Eqs. (2.3.10-14) and Eqs. (2.2.15-17) into (2.3.2-9) leads to

$$k_{i,i-1}\left(\sum_{m=0}^{\infty}(-1)^m A_{i-1,m}(t) - \frac{7L_{i-1}{}^3\alpha_{i-1,0}}{360} - \frac{8L_{i-1}{}^3\alpha_{i-1,1}}{360} + \frac{\beta_{i-1,0}L_{i-1}}{6} + \frac{\beta_{i-1,1}L_{i-1}}{3}\right)$$

$$= D_i\alpha_{i,0} + (k_{i,i-1} + \tilde{k}_{i0})\left(\sum_{m=0}^{\infty} A_{i,m}(t) + \frac{8L_i{}^3\alpha_{i,0}}{360} + \frac{7L_i{}^3\alpha_{i,1}}{360} - \frac{\beta_{i,0}L_i}{3} - \frac{\beta_{i,1}L_i}{6}\right) \tag{2.3.15}$$

$$(K_{i,i-1}+\tilde{K}_{i0})\beta_{i,0} = K_{i,i-1}\beta_{i-1,1} + D_i\left(-\sum_{m=1}^{\infty}\lambda_{i,m}^2 A_{i,m}(t) - \frac{\alpha_{i,0}L_i}{3} - \frac{\alpha_{i,1}L_i}{6} + \frac{\beta_{i,1}}{L_i} - \frac{\beta_{i,0}}{L_i}\right) \qquad (2.3.16)$$

$$(k_{i,i+1}+\tilde{k}_{i1})\left(\sum_{m=0}^{\infty}(-1)^m A_{i,m}(t) - \frac{7L_i^{3}\alpha_{i,0}}{360} - \frac{8L_i^{3}\alpha_{i,1}}{360} + \frac{\beta_{i,0}L_i}{6} + \frac{\beta_{i,1}L_i}{3}\right) =$$

$$D_i\alpha_{i,1} + k_{i,i+1}\left(\sum_{m=0}^{\infty}A_{i+1,m}(t) + \frac{8L_{i+1}^{3}\alpha_{i+1,0}}{360} + \frac{7L_{i+1}^{3}\alpha_{i+1,1}}{360} - \frac{\beta_{i+1,0}L_{i+1}}{3} - \frac{\beta_{i+1,1}L_{i+1}}{6}\right) \qquad (2.3.17)$$

$$(K_{i,i+1}+\tilde{K}_{i1})\beta_{i,1} = K_{i,i+1}\beta_{i+1,0} - D_i\left(\sum_{m=1}^{\infty}(-1)^{m+1}\lambda_{i,m}^2 A_{i,m}(t) + \frac{\alpha_{i,0}L_i}{6} + \frac{\alpha_{i,1}L_i}{3} + \frac{\beta_{i,1}}{L_i} - \frac{\beta_{i,0}}{L_i}\right) \qquad (2.3.18)$$

In matrix form, the above equations reduce to

$$\mathbf{H}_{i,i-1}\boldsymbol{\alpha}_{i-1} + \mathbf{H}_{i,i}\boldsymbol{\alpha}_i + \mathbf{H}_{i,i+1}\boldsymbol{\alpha}_{i+1} = \sum_{m=0}^{\infty}\left(\mathbf{Q}_{i,i-1}^m\mathbf{A}_{i-1,m}(t) + \mathbf{Q}_{i,i}^m\mathbf{A}_{i,m}(t) + \mathbf{Q}_{i,i+1}^m\mathbf{A}_{i+1,m}(t)\right) \qquad (2.3.19)$$

The definition of matrices $\mathbf{H}_{i,i-1}, \mathbf{H}_{i,i}, \mathbf{H}_{i,i+1}$ and vectors $\mathbf{Q}_{i,i-1}^m, \mathbf{Q}_{i,i}^m, \mathbf{Q}_{i,i+1}^m$ are given in Eqs. (2.2.23-28). Following the procedure described in section 2.2, one can obtain total of 4*N* equations as

$$\boldsymbol{\alpha}_i = \sum_{m=0}^{\infty}\tilde{\mathbf{H}}_i\overline{\mathbf{Q}}_i^m\mathbf{A}_{i,m}(t) \qquad (2.3.20)$$

Making use of Eqs. (2.2.15) and (2.3.20), Eq. (2.3.10) can be expressed as

$$w_i(x,t) = \sum_{m=0}^{\infty}A_{i,m}(t)(\cos\lambda_{i,m}x + \boldsymbol{\zeta}_i(x)^T\tilde{\mathbf{H}}_i\overline{\mathbf{Q}}_i^m) + \sum_{\substack{j=1,N\\ j\neq i}}\sum_{m=0}^{\infty}A_{j,m}(t)\boldsymbol{\zeta}_j(x)^T\tilde{\mathbf{H}}_i\overline{\mathbf{Q}}_j^m \qquad (2.3.21)$$

Substituting Eq. (2.3.21) into (2.3.1) and following the standard Galerkin procedure, one is able to obtain (Xu & Li, 2008)

$$[\mathbf{K}_{pq}]\{\mathbf{A}_q\} + [\mathbf{M}_{pq}]\{\ddot{\mathbf{A}}_q\} = \{\mathbf{F}_p\} \qquad (p, q = 1, 2, 3, ..., N) \qquad (2.3.22)$$

where $K_{pq,mm'}$ and $M_{pq,mm'}$ are defined by Eqs. (2.2.57-58), and

$$f_{p,m} = 2\big/L_p \int_0^{L_p} \left(\cos\lambda_{pm} x + \boldsymbol{\zeta}_p(x)^T \tilde{\mathbf{H}}_p \overline{\mathbf{Q}}_p^m\right) f_p(x - x_{fi}(t))dx \qquad (2.3.23)$$

for $m, m' = 0, 1, 2, 3, \ldots$ and $p, q = 1, 2, 3, \ldots, N$. Eq. (2.3.22) represents a set of coupled second-order differential equations with respect to time which can be solved by the direct numerical integration. The Newmark-β algorithm is used to perform the numerical integration.

2.3.2 Results and discussions

In order to validate the current model and analysis code, we will first consider a multi-span beam problem that was previously studied by Henchi and Fafard (1997). As illustrated in Fig. 2.3, this example involves a three-span stepped beam subjected to a single concentrated moving load. The relevant beam and material parameters are listed in Table 2.6.

Table 2.6 Beam and material properties

L (m)	ρ (Kg/m^3)	ρA (Kg/m)	E (N/m^2)	EI (Nm^2)	F (N)
20	7800	1000	10.48×10^{10}	1.96×10^{9}	9.48×10^{3}

Under the current framework, this stepped continuous beam can be viewed as a collection of three separate beams that are rigidly coupled together. The continuous beam is assumed to be simply supported at its ends and the two joint locations. The simply supported condition can be readily modeled by simply setting the stiffnesses of the (linear and rotational) coupling springs equal to infinity and zero, respectively.

Table 2.7 Comparison of natural frequencies

1	2	3	4	5	6
6.204[a]	7.579	11.795	24.095	26.365	37.561
6.204[b]	7.581	11.974	24.207	26.439	37.282

[a] Current method,
[b] [Henchi & Fafard, 1997]

The calculated natural frequencies for the first six modes are compared in Table 2.7 with those given by Henchi and Fafard (1997). Now, assume the beam is subjected to a point load, $F = 9.48 \times 10^3$ N, moving at a constant speeds v =35.57m/s. Plotted in Fig. 2.5 are the corresponding deflections at the midpoint locations of all three spans. The results obtained by Henchi and Fafard (1997) are also shown there for comparison. An excellent agreement is observed between these two sets of solutions. This problem was also studied by Dugush and Eisenberger for different beam parameters and load profiles. It is here sufficient to say that the current results also match closely with those given by Dugush and Eisenberger (2002).

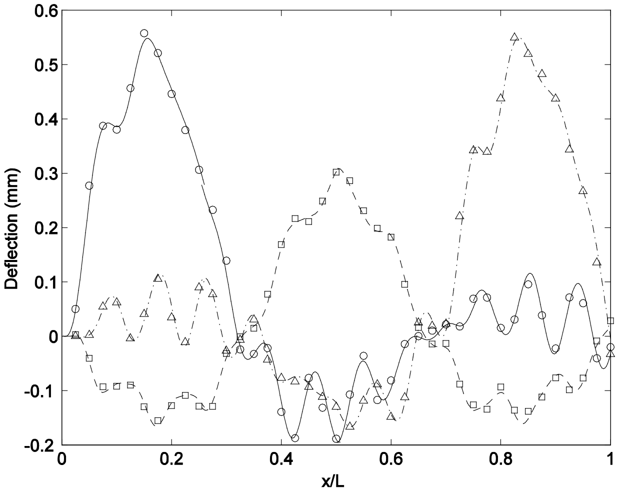

Figure 2.5 Flexural deflection at the midpoint of each span for v =35.57m/s: span 1: —, current, ○, [Henchi & Fafard, 1997]; span 2: - - -, current, □, [Henchi & Fafard, 1997]; and span 3: -·-, current, Δ, [Henchi & Fafard, 1997]

Before proceeding to examination of the elastic couplings between spans, we will first consider a modified version of the above problem which involves a single uniform beam elastically supported at its ends. This kind of problems was previously investigated by Yang *et al.*, (2004). For convenience, all the related parameters will remain the same except that the bending stiffness for the mid-span is reduced to *EI*, same as the other spans to achieve the uniformity required for a single-span beam. It should be mentioned that the two intermediate supports are also removed. Thus, we now deal with a uniform beam of length 3*L* elastically supported, at each end, by a linear spring of stiffness, say, $k = 10^{10}$ N/m. The deflections at the center of the beam are plotted in Fig. 2.6 for two different load speeds. The results obtained using the solution given by Yang *et al*., (2004) are also presented there. A good comparison is observed between these two sets of results.

In a traditional multi-span beam problem, the beam displacement and its first derivative are both required to be continuous over the entire beam length. In many real-world applications, regardless of whether purposely or not, the joints between different spans may not always be modeled as being infinitely rigid. Thus, joint stiffnesses, or coupling conditions between spans, will actually constitute an additional set of model parameters, and may meaningfully affect the bridge vibration. While the roles of beam parameters and/or loading conditions have been extensively studied, the effect of the between-span coupling conditions on the dynamic behavior of a bridge was barely attempted before. Thus, the subsequent discussions will be primarily focused on the effect of the coupling conditions.

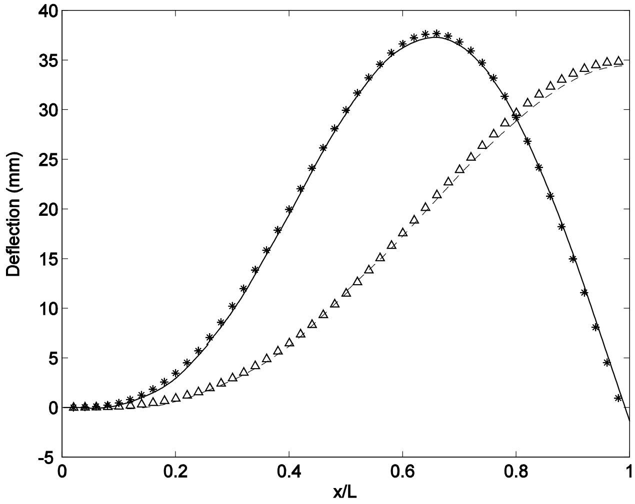

Figure 2.6 Flexural deflection at the midpoint of a continuous elastically supported beam under a load with two different velocities: v=35.57m/s m/s: —, current method, *, [Yang *et al*., 2004]; and v=71.25m/s: - - -, current method, Δ, [Yang *et al*., 2004].

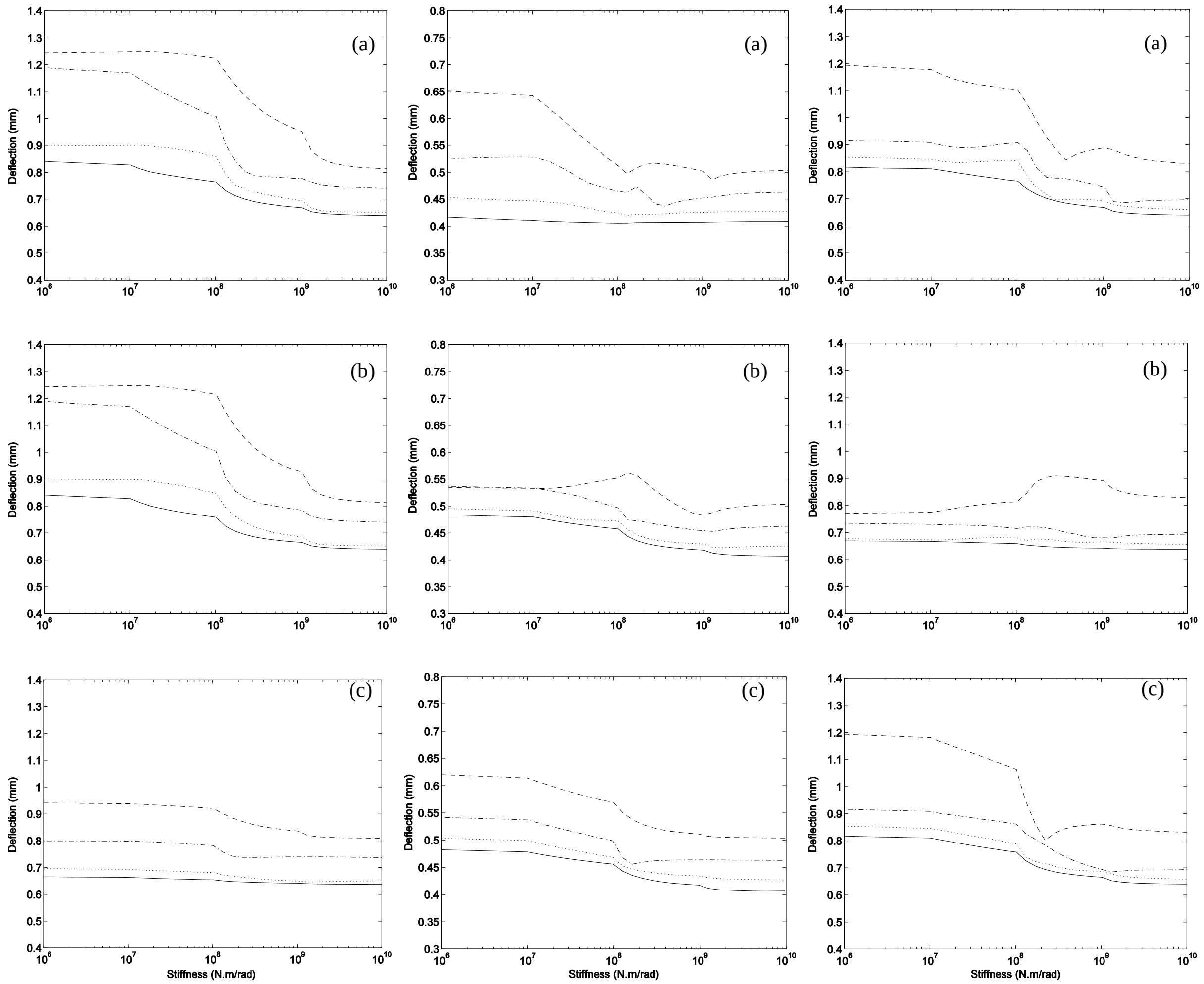

(I) (II) (III)

Figure 2.7 Peak-peak deflection at the midpoint of each span for a few load profiles defined by a constant acceleration a = 2m/s^2 and different initial velocities: (I) 1st span; (II) 2nd span; (III) 3rd span. (a) elastic-elastic; (b) elastic-rigid; and (c) rigid-elastic. —, v=5m/s; ·····, v=17.87m/s; -·-, v=35.57m/s; ---, v=71.25 m/s

As illustrated in Fig. 2.3, there are up to eight independent springs associated with each span in a general support/coupling configuration. Theoretically, each of these springs can be considered as an independent design variable, which makes it a formidable task to study a general case involving an arbitrary combination of these variables. For simplicity, we will again consider the three-span beam problem with only one modification: the continuity requirement for the first derivative is relaxed at junctions of the spans. That is, two rotational springs, $K_{1,2}$ and

$K_{2,3}$, of equal stiffness are now placed between the spans while the displacement is still assumed to be continuous over the entire length.

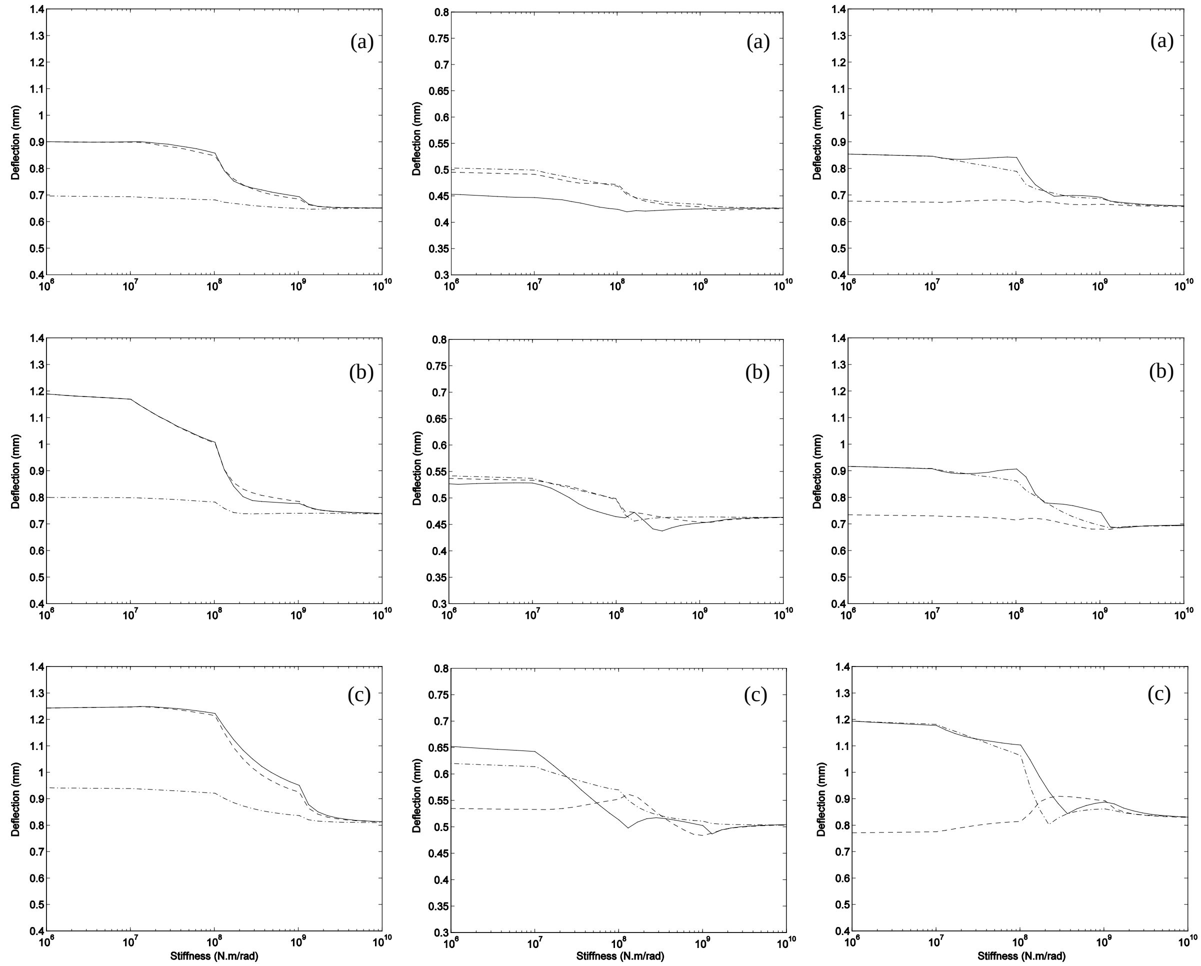

(I) (II) (III)

Figure 2.8 Peak-peak deflection at the midpoint of each span for a constant acceleration a = 2 m/s^2 and different initial velocities: (I) 1st span; (II) 2nd span; (III) 3rd span. (a) v =17.87 m/s; (b) v =35.57 m/s; (c) v =71.25 m/s. —, elastic-elastic; -·-, rigid-elastic; ---, elastic-rigid

Three different arrangements are considered: (1) spans 1 and 2 are elastically connected via a rotational spring while spans 2 and 3 are rigidly coupled together (ER); (2) spans 2 and 3 are elastically connected while spans 1 and 2 are rigidly coupled together (RE); and (3) all three spans are elastically coupled together (EE). In all these cases, the rotational stiffness will vary from 10^6 and 10^{10} Nm/rad. The peak – peak value (the algebraic difference between the extremes of the deflection) at the midpoint of each span is utilized to evaluate the dynamic behavior of the beam system. Fig. 2.7 shows the peak – peak values vs. the stiffness of the coupling springs for a few different load profiles. It is seen that as the stiffness increases, the deflection at the midpoint of each span typically decreases until $K \cong 10^8$ (or $KL/EI \cong 1$). The dynamic responses tend to exhibit a strong dependence on the coupling stiffness near this "critical" value. The peak – peak values typically increases with the traveling speed of the load for a given coupling stiffness and configuration.

To better understand the effect of coupling conditions, the results in Fig. 2.7 are re-plotted in Fig. 2.8 based on the coupling configurations. It is observed that the deflections on span 1 are almost the same for the EE and ER configurations. A possible explanation is that the peak deflections occur when the load is still located on the first span. Since the time elapsed to reach this stage is relatively short, the wave front may not yet have arrived at or bounced back from the junction (between spans 2 and 3) which differentiates the EE and ER configurations. As a consequence, the initial response of span 1 is primarily dictated by the local end conditions which are essentially the same in both configurations. A similar comparison can be made between the EE and RE configurations regarding the deflections on span 3 for $K \leq 10^7$. As the spring stiffness becomes sufficiently large, all the three configurations will essentially degenerate into a continuous multi-span beam, and the responses tend to become the same as repeatedly shown in Fig. 2.8.

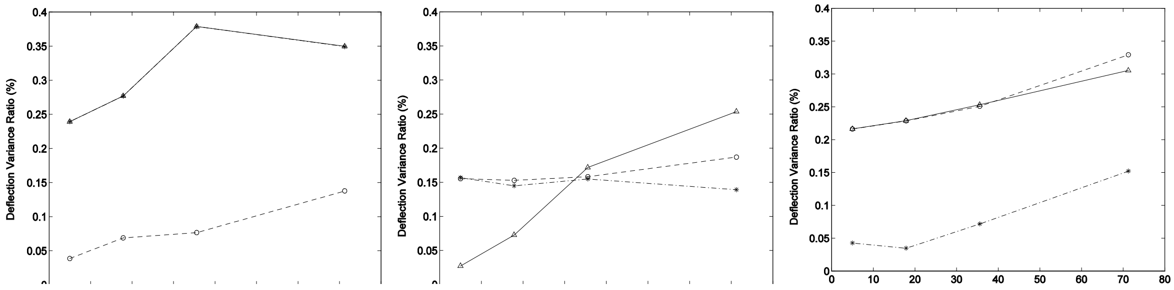

(a) (b) (c)

Figure 2.9 Variation ratio for the peak-peak deflection at the midpoint of each span for a constant acceleration *a* = 2 m/s^2: (a) span 1; (b) span 2; (c) span 3. —Δ, elastic-elastic; ---○, rigid-elastic; -·-*, elastic-rigid

The above results have consistently indicated that the dynamic behavior of a multi-span bridge may become strongly dependent upon the coupling conditions between spans. Since in practice the stiffness values can vary easily by several orders of magnitude, their impact on the dynamic behavior will be better assessed in terms of the variance ratio, as plotted in Fig. 2.9.

The variance ratio is defined as the difference between the maximum and minimum peak-peak deflections (normalized by the maximum) for all the given stiffness values. A larger variance ratio indicates a more significant influence of the coupling conditions on the dynamic behavior of the bridge. It is evident from Fig. 2.9 that the deflections or the dynamic behavior of a bridge can be substantially influenced by the coupling conditions.

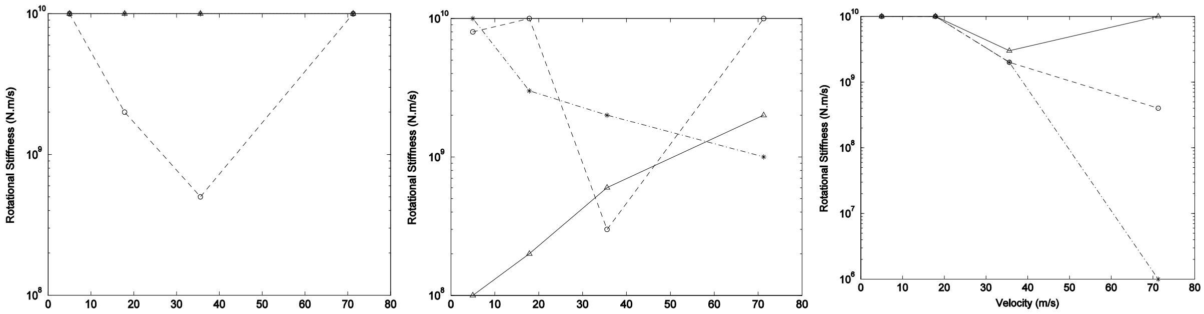

(a) (b) (c)

Figure 2.10 The rotational coupling stiffness that corresponds to the smallest peak-peak deflection at the midpoint of each span for a constant acceleration *a* = 2 m/s^2: (a) span 1; (b) span 2; (c) span 3. —Δ elastic-elastic; ---○ rigid-elastic; -·-* elastic-rigid

In terms of bridge design, a large variance ratio implies certain room for improving bridge performance through varying or optimizing the coupling conditions between spans. For example, a set of preferred joint stiffnesses (corresponding to the minimum peak-peak deflection) are shown in Fig. 2.10 for the specified load speeds. It is clear that the rigid coupling does not always result in the smallest deflection, as one may intuitively believe.

It should be pointed out that these optimal stiffness values were actually determined based on the local vibration data and vary from span to span. In practice, one may have to first define a global objective or cost function so that a unique set of optimal joint parameters can be found accordingly. Since the coupling conditions, unlike many other structural parameters, can be modified in a more drastic and cost-effective manner, they have potential to become an important design option for a significant improvement of bridge performance.

2.4 Conclusions

An exact series solution has been presented for determining the dynamic characteristics of a multi-span beam system with arbitrary boundary conditions. The coupling between any two neighboring beams is generically described by two (linear and rotational) springs, which allows a more realistic account of many rigid and non-rigid joints encountered in practical applications. Since each beam is elastically restrained independently (in addition to the elastic couplings), the current method can be readily and universally applied to any boundary conditions with no need of modifying the basis functions or adapting solution procedures as often required in other methods.

It has been shown through numerical examples that the modal properties can be accurately calculated for a multi-beam system under general boundary and coupling conditions.

Unlike in most multi-span beam models, the displacement and its derivatives are here not required to be continuous at a junction, which is of interest to certain engineering applications such as vehicle-bridge interaction.

As a typical application of the proposed model in practice, the vibration of a multi-span bridge subjected to a moving load has been investigated in a generic manner. It has been demonstrated through numerical examples that the coupling conditions will generally have a direct and meaningful impact on the vibration on each span. In particular, the peak－peak deflection on a span is strongly dependent upon the coupling conditions local to that span, and less sensitive to the coupling conditions at distant junctions. For a given coupling arrangement, the peak－peak deflection on each span typically increases with the traveling speed of a load. In comparison with many other design variables, a coupling stiffness can be practically varied easily by several orders of magnitude. It is found, however, that the dynamic behavior becomes particularly sensitive to the coupling conditions near the critical stiffness value defined by $KL/EI \cong 1$. Thus, the large design space may be practically compressed into a much smaller one. Finally, a large variance ratio for the deflection on each span shall be understood as a good potential for improving bridge design through optimizing the coupling conditions between spans.

CHAPTER III

VIBRATION AND POWER FLOW ANALYSES OF FRAME STRUCTURES

3.1 Introduction

Although the SEM, DSM, and receptance methods provide an analytical solution for beam frameworks, they are only restricted to the beams that have to present certain degree of uniformity regarding the material and geometrical properties; otherwise, beam functions are not generally available. In dealing with a beam structure, the system solution is often expressed in terms of the modal properties for each individual beam by assuming the coupling end(s) is free. The modal properties thus obtained may also be alternatively used to determine the transfer functions, Green functions or receptance functions between the responses and the reaction forces (including moments) at the junctions in the actual system environment. While this solution procedure may be reasonably good for calculating the modal properties or the vibrational response of the composite structure to an external load, the basic fact still cannot be changed; that is, the modal properties for each beam are actually determined by freeing the “coupling” end(s). As a consequence, the displacement functions constructed using these component modes will not be able to accurately represent the reaction forces/moments (which depend upon the second and third derivatives of the displacement functions) at the coupling ends. This problem is expected to become more remarked in a power flow analysis because the reaction forces and moments will have to be calculated explicitly at the junctions. Although for an elastic joint the coupling forces and moments can be respectively calculated from the relative translational and rotational displacements, the calculations will understandably break down when the coupling stiffnesses become very high. As a matter of fact, the use of free-free beam functions was found particularly difficult for the intermediate coupling strength (Keane, 1992).

In this chapter, a closed-form series solution is proposed for vibrations of 2-D and 3-D Euler-Bernoulli beams. This solution is subsequently generalized into a modeling method which can be broadly applied to the built-up (2-D and 3-D) frame structures. In this general modeling method, the interactions between the beams are described in a weak form of the Rayleigh-Ritz principle, which allows the current method to fully take advantages of the powerful FEA formulations and flexible implementation schemes.

3.2 Analytical solution for vibrations of built-up frame structures

3.2.1 Description of the analytical solution

Fig. 3.1 shows two built-up 2-D and 3-D frame structures. They simply represent a collection of beams. In order to be able to account for the varieties of the possible coupling configurations, a junction is considered as a combination of a number of joints with each of them being uniquely used to connect a pair of beams. For example, if three beams meet at a junction, then three independent joints will be specified there (between beam 1 and 2, beam 1 and 3, and beam 2 and 3). In structural analysis, each joint will be represented by three springs corresponding respectively to the axial, flexural and rotational displacements. When the beams are rigidly connected together, one needs to simply set the spring constants to be infinitely large. The use of the coupling springs will allow accounting for the flexibility of the joints, which may be more important at higher frequencies.

For generality, we will discuss vibrations in 3-D space of a built-up frame. That is, the vibrations on each beam are fully described by displacements in the longitudinal, torsional and two transverse directions based on the Euler-Bernoulli beam theory. Obviously, the transverse, torsional and longitudinal displacements are directly coupled together at a joint. The analytical procedure for the 2-D frame is essentially identical to the 3-D case but the beam displacements are described in the in-plane transverse and longitudinal directions.

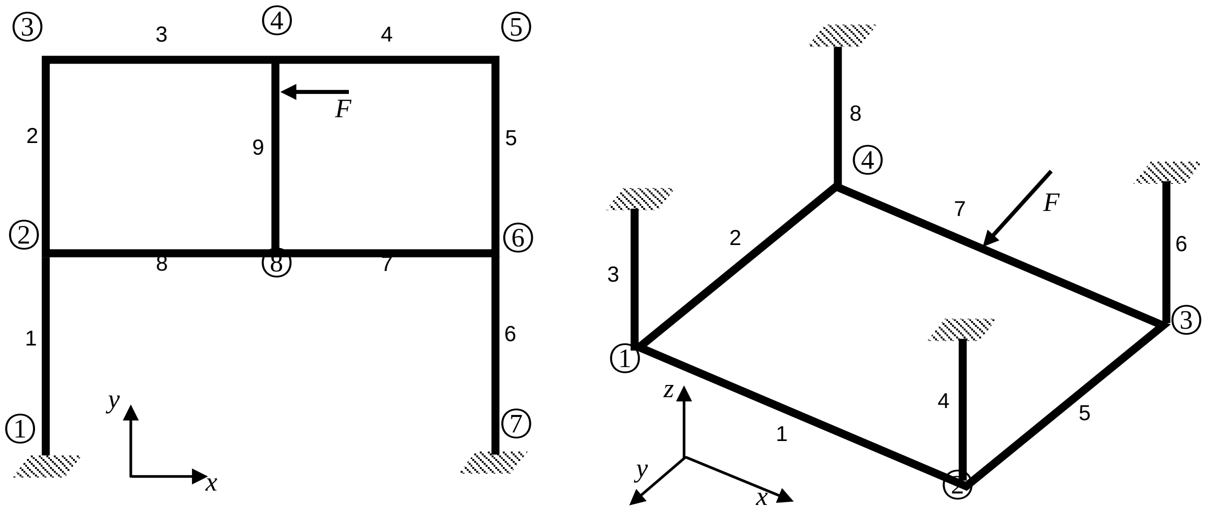

(a) (b)

Figure 3.1 Exemplary built-up frames: (a) a 2-D frame; (b) a 3-D frame

In the current solution, the harmonic displacements of the free vibration of each beam, *e.g.* the *i*-th beam, can be expressed as

$$W_{i,r}(x,t)=w_{i,r}(x)e^{j\omega t}\,,\; U_i(x,t)=u_i(x)e^{j\omega t}\,,\; \Theta_i(x,t)=\theta_i(x)e^{j\omega t} \tag{3.1-3}$$

where ω denotes the radian natural frequency of vibration and *t* is time, $j=\sqrt{-1}$.

The amplitudes of the displacements will be sought in a closed form as

$$w_{i,r}(x)=\sum_{m}^{M}A^{w}_{ir,m}\cos\lambda_m x+\sum_{n}^{4}B^{w}_{ir,n}\sin\lambda_n x \tag{3.4}$$

$$u_i(x)=\sum_{m}^{M}A^{u}_{i,m}\cos\lambda_m x+\sum_{n}^{2}B^{u}_{i,n}\sin\lambda_n x \tag{3.5}$$

$$\theta_i(x)=\sum_{m=0}^{M}A^{\theta}_{i,m}\cos\lambda_m x+\sum_{n=1}^{2}B^{\theta}_{i,n}\sin\lambda_n x \tag{3.6}$$

where $\lambda_m = m\pi / L_i$, L_i is the length of the *i*-th beam, the subscript r (= z or y) denote the bending displacement about z or y axis; A_i^q and B_i^q (q = w, u or θ) are the expansion coefficients to be determined.

In Eq. (3.4) the cosine series is supplemented by four sine terms. The inclusion of these additional terms actually plays a vitally important role in taking care of the possible discontinuities (or jumps), at the end points, with the first and third derivatives of the displacement function when it is periodically extended (with a period $2L_i$) onto the entire x-axis. Specifically, these auxiliary terms are chosen in such a way that they will, regardless of boundary/coupling conditions, be equal to the values of the first and third derivatives of the displacement function at both end points. Mathematically, this requirement can be readily satisfied by any four properly scaled closed-form functions which are linearly independent and sufficiently smooth over $[0, L_i]$. In the previous studies (Li, 2000; Xu & Li, 2008; Li & Xu, 2009), the auxiliary functions are simply selected as polynomials. The reason for using sine functions here is because they exhibit some desired characteristics such as being orthogonal to many of the cosine functions. Because for the longitudinal and torsional displacements only the first derivative are of concern at the end points, only two auxiliary terms are needed in Eqs. (3.4-5).

The elastic deformations $\left(w_{i,r}, u_i, v_i\right)$ of each beam are defined with respect to a local coordinate system $\left(x_i, y_i, z_i\right)$ which leads to various coupling scenarios between each adjoining pair of beams. Similarly, the coupling between beams is treated as an elasticity described by a set of six simple linear and rotational springs. Each elasticity has its own principal axes indicated by (p, q, r). In order to ease the computation, a global coordinate system $\left(x, y, z\right)$ is used for defining the whole frame and coupling/restraint springs, as shown in Fig. 3.2.

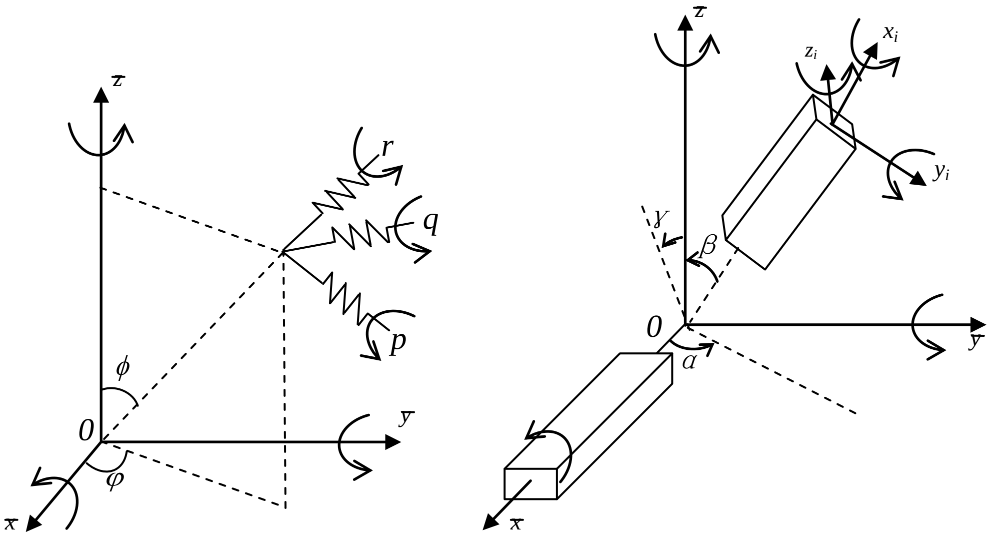

(a) (b)

Figure 3.2 The coordinate transformation scheme: (a) for a beam; (b) for the spring

The coordinate transformation (between local and global) of displacements of the *i*-th beam on the coupling joint is realized by a matrix

$$\mathbf{R}_i = \begin{bmatrix} \hat{\mathbf{R}}_i & \mathbf{0} \\ \mathbf{0} & \hat{\mathbf{R}}_i \end{bmatrix} \tag{3.7}$$

with

$$\hat{\mathbf{R}}_i = \begin{bmatrix} \cos\alpha_i \cos\beta_i & (\sin\alpha_i \cos\beta_i \sin\gamma_i - \cos\gamma_i \sin\beta_i) & (\sin\alpha_i \cos\beta_i \cos\gamma_i + \sin\beta_i \sin\gamma_i) \\ \cos\alpha_i \sin\beta_i & (\sin\alpha_i \sin\beta_i \sin\gamma_i + \cos\gamma_i \cos\beta_i) & (\sin\alpha_i \sin\beta_i \cos\gamma_i - \sin\gamma_i \cos\beta_i) \\ -\sin\gamma_i & \cos\alpha_i \sin\gamma_i & \cos\alpha_i \cos\gamma_i \end{bmatrix} \tag{3.8}$$

The displacement of the *i*-th beam on the coupling joint has the form

$$\overline{\mathbf{U}}_i = \mathbf{R}_i \mathbf{U}_i \tag{3.9}$$

where $\mathbf{U}_i$ is the displacement vector defined in the local coordinates, written as

$$\mathbf{U}_i = \begin{bmatrix} u_i & w_{i,y} & w_{i,z} & \dfrac{\partial \theta_i}{\partial x} & \dfrac{\partial w_{i,z}}{\partial x} & \dfrac{\partial w_{i,y}}{\partial x} \end{bmatrix}^T e^{j\omega t} \tag{3.10}$$

Analogously, the coupling between beams and the boundary restraints of each beam are specified in the global coordinate in terms of the stiffness transformation matrix $\mathbf{R}_s$

$$\overline{\mathbf{K}}_s = \mathbf{R}_s diag\begin{bmatrix} k_p & k_q & k_r & K_p & K_q & K_r \end{bmatrix}\mathbf{R}_s^T \tag{3.11}$$

where $diag(.)$ denotes the diagonal matrix formed from the listed elements, k_j and K_j ($j = x, y,$ or z), are, respectively, the linear stiffness in and the rotational stiffness about the *j*-direction, and

$$\mathbf{R}_s = \begin{bmatrix} \hat{\mathbf{R}}_s & \mathbf{0} \\ \mathbf{0} & \hat{\mathbf{R}}_s \end{bmatrix} \tag{3.12}$$

with $$\hat{\mathbf{R}}_s = \begin{bmatrix} \cos\varphi_s \cos\phi_s & \cos\varphi_s \sin\phi_s & -\sin\varphi_s \\ -\sin\phi_s & \cos\phi_s & 0 \\ \sin\varphi_s \cos\phi_s & \sin\varphi_s \sin\phi_s & \cos\varphi_s \end{bmatrix} \tag{3.13}$$

being the transformation matrix whose elements are simply the direction cosines of the axes of the springs.

Previously, the Fourier coefficients are solved by directly using the boundary conditions and the governing equations (Xu & Li, 2008). Following this process, the coefficients for the sine terms will be considered as some intermediate variables, and first solved from the boundary/coupling conditions in terms of the Fourier coefficients for the cosine functions. Subsequently, all the coefficients for the cosine terms will become fully independent and can be determined directly from the governing equations by following the standard Fourier solution procedures. Although this solution scheme may represent the most natural choice mathematically, it will lead to fully-populated coefficient matrices for the final system equations. As an alternative solution process which may actually be preferred in practice, all the expansion coefficients (for the sine and cosine terms) are now treated as independent variables, and are solved, in an approximate manner, by using the powerful Rayleigh-Ritz method. In this way, only the neighboring beams will be directly coupled together in final system equations, as manifested in the highly sparse stiffness and mass matrices. However, the most important outcome is that this solution process will allow us to develop a new class of numerical methods for complex structures by taking advantages of the progresses in the finite element methods. Two important distinctions will have to be drawn between the current and FE methods: first, the elements here represent a more meaningful structural component; and second, the element unknowns are now the Fourier expansion coefficients instead of the nodal variables. The corresponding pros and cons are case-dependent, and will become obvious in many applications.

The expressions for the total potential and kinetic energies of the frame, respectively, are given in a global sense

$$\mathbf{V} = \sum_{i}^{N_b} \left(\mathbf{V}_i + \mathbf{V}_i^{B.C} \right) + \sum_{i=1}^{N_b} \sum_{j=i}^{N_b} \left(1 - \delta_{ij} \right) \mathbf{V}_{ij}^{c} \tag{3.14}$$

$$\mathbf{T} = \sum_{i}^{N_b} \mathbf{T}_i \tag{3.15}$$

where N_b is the total number of beam elements; $\mathbf{V}_i$ represents the strain energies due to the elastic deformations of the *i*-th beam; $\mathbf{V}_i^{B.C}$ designates the potential energies stored in the boundary springs of the *i*-th beam; $\mathbf{V}_{ij}^{c}$ accounts for the potential energies associated with coupling springs between the *i*-th and the *j*-th beams; and $\mathbf{T}_i$ is the kinetic energies corresponding to the vibrations of the *i*-th beam.

Specifically, the potential and kinetic energies of the individual beam in terms of the assumed displacements can be written as

$$\mathbf{V}_i = \frac{1}{2}\int_0^{L_i}\left[E_i\left(I_{i,z}\left(\frac{\partial^2 W_{i,y}}{\partial x^2}\right)^2 + I_{i,y}\left(\frac{\partial^2 W_{i,z}}{\partial x^2}\right)^2 + S_i\left(\frac{\partial U_i}{\partial x}\right)^2\right) + G_i J_i\left(\frac{\partial \Theta_i}{\partial x}\right)^2\right]dx \tag{3.16}$$

$$\mathbf{V}_i^{B.C} = \left(\overline{\mathbf{U}}_i{}^T \overline{\mathbf{K}}_{B.C}^0 \overline{\mathbf{U}}_i\right)_{x=0} + \left(\overline{\mathbf{U}}_i{}^T \overline{\mathbf{K}}_{B.C}^{L_i} \overline{\mathbf{U}}_i\right)_{x=L_i} \tag{3.17}$$

$$\mathbf{T}_i = \frac{1}{2}\int_0^{L_i}\left[\rho_i\left(S_i \dot{W}_{i,y}^2 + S_i \dot{W}_{i,z}^2 + S_i \dot{U}_i^2 + J_i \dot{\Theta}_i^2\right)\right]dx \tag{3.18}$$

where $I_{i,y}$, $I_{i,z}$ E_i, J_i, G_i, ρ_i, and S_i, are respectively the moment inertia about *y* and *z* axes, Young’s modulus, torsional rigidity, shear modulus, mass density, and the cross-sectional area of the *i*-th beam.

The definitions for the boundary spring stiffness matrices $\overline{\mathbf{K}}_{B.C}^0$ and $\overline{\mathbf{K}}_{B.C}^{L_i}$ follow the transformation form given in Eqs. (3.11-13). The potential energy stored in the coupling springs with respect to global coordinates can be written as

$$\mathbf{V}_{ij}^c = \left(\overline{\mathbf{U}}_i - \overline{\mathbf{U}}_j\right)^T \overline{\mathbf{K}}_s \left(\overline{\mathbf{U}}_i - \overline{\mathbf{U}}_j\right) \tag{3.19}$$

By substituting Eqs. (3.9 and 3.11) into Eq. (3.19), one obtain

$$\mathbf{V}_{ij}^c = \mathbf{U}_i^T \mathbf{H}_i \mathbf{U}_i + \mathbf{U}_j^T \mathbf{H}_j \mathbf{U}_j - \mathbf{U}_i^T \mathbf{H}_{ij} \mathbf{U}_j - \mathbf{U}_j^T \mathbf{H}_{ij}^T \mathbf{U}_i \tag{3.20}$$

The new terms introduced in Eq. (3.20) are defined as follows

$$\mathbf{H}_i = \mathbf{R}_i^T \mathbf{R}_s diag\begin{bmatrix} k_p & k_q & k_r & K_p & K_q & K_r \end{bmatrix} \mathbf{R}_s^T \mathbf{R}_i \tag{3.21}$$

$$\mathbf{H}_j = \mathbf{R}_j^T \mathbf{R}_s diag\begin{bmatrix} k_p & k_q & k_r & K_p & K_q & K_r \end{bmatrix} \mathbf{R}_s^T \mathbf{R}_j \tag{3.22}$$

$$\mathbf{H}_{ij} = \mathbf{R}_i^T \mathbf{R}_s diag\begin{bmatrix} k_p & k_q & k_r & K_p & K_q & K_r \end{bmatrix} \mathbf{R}_s^T \mathbf{R}_j \tag{3.23}$$

The classical Hamilton’s principle is now applied

$$\int_{t_1}^{t_2} \delta(\mathbf{V} - \mathbf{T})dt = 0 \tag{3.24}$$

Substituting Eqs. (3.14-23) into Eq. (3.24) and minimizing the Rayleigh quotient with respect to the Fourier coefficients $A_m^w, A_m^u, \cdots, B_n^u$, and B_n^θ yields the free vibration eigenproblem.

$$\left\{\mathbf{K} - \omega^2 \mathbf{M}\right\}\mathbf{\Phi} = \mathbf{0} \tag{3.25}$$

here $\mathbf{K}$ is the system stiffness matrix, and has the form

$$\mathbf{K} = \left[\begin{array}{cccccc} \mathbf{K}_{11} & \cdots & \mathbf{K}_{1i} & \cdots & \mathbf{K}_{1j} & \cdots \\ & \ddots & \vdots & \vdots & \vdots & \cdots \\ & & \mathbf{K}_{ii} & \vdots & \mathbf{K}_{ij} & \cdots \\ & & & \ddots & \vdots & \cdots \\ & \mathit{Symmetric} & & & \mathbf{K}_{jj} & \cdots \\ & & & & & \ddots \end{array}\right] \tag{3.26}$$

where $\mathbf{K}_{ii}$ and $\mathbf{K}_{jj}$ stand for the total stiffness matrix of the *i*-th and the *j*-th beams respectively; and $\mathbf{K}_{ij}$ represents the cross coupling stiffness matrix between the *i*-th and the *j*-th beams; particularly, $\mathbf{K}_{ii}$ can be written as a summation

$$\mathbf{K}_{ii} = \mathbf{K}_{ii}^0 + \mathbf{K}_{ii}^c \tag{3.27}$$

where $\mathbf{K}_{ii}^0$ and $\mathbf{K}_{ii}^c$ denote contributions due to the beam itself and the coupling between beams respectively.

The system mass matrix $\mathbf{M}$ is written in the form

$$\mathbf{M} = diag\left[\mathbf{M}_1 \quad \cdots \quad \mathbf{M}_i \quad \cdots\right] \tag{3.28}$$

where $\mathbf{M}_i$ is the mass matrix of the *i*-th beam.

The coefficient vector $\mathbf{\Phi}$ in Eq. (3.25) is defined as

$$\mathbf{\Phi} = \left\{\mathbf{\Phi}_1^u \quad \mathbf{\Phi}_{1,y}^w \quad \mathbf{\Phi}_{1,z}^w \quad \mathbf{\Phi}_1^\theta \quad \cdots \quad \mathbf{\Phi}_i^u \quad \mathbf{\Phi}_{i,y}^w \quad \mathbf{\Phi}_{i,z}^w \quad \mathbf{\Phi}_i^\theta \quad \cdots\right\} \tag{3.29}$$

where subscripts $w_{i,y}$, $w_{i,z}$, u_i and θ_i indicate a quantity related to the displacement type of the *i*-th beam, respectively. The component vectors in Eq. (3.29) are given by

$$\mathbf{\Phi}_{i,y}^{w} = \left\{A_{iy,0}^{w} \quad \cdots \quad A_{iy,M}^{w}, \quad B_{iy,1}^{w} \quad B_{iy,2}^{w} \quad B_{iy,3}^{w} \quad B_{iy,4}^{w}\right\}_{1\times(M+5)}^{T} \tag{3.30}$$

$$\mathbf{\Phi}_{i,z}^{w} = \left\{A_{iz,0}^{w} \quad \cdots \quad A_{iz,M}^{w}, \quad B_{iz,1}^{w} \quad B_{iz,2}^{w} \quad B_{iz,3}^{w} \quad B_{iz,4}^{w}\right\}_{1\times(M+5)}^{T} \tag{3.31}$$

$$\mathbf{\Phi}_{i}^{u} = \left\{A_{i,0}^{u} \quad \cdots \quad A_{i,M}^{u}, \quad B_{i,1}^{u} \quad B_{i,2}^{u}\right\}_{1\times(M+3)}^{T} \tag{3.32}$$

$$\mathbf{\Phi}_{i}^{\theta} = \left\{A_{i,0}^{\theta} \quad \cdots \quad A_{i,M}^{\theta}, \quad B_{i,1}^{\theta} \quad B_{i,2}^{\theta}\right\}_{1\times(M+3)}^{T} \tag{3.33}$$

Although the expressions of the stiffness and mass matrices are very lengthy, they can be easily derived by following the standard Rayleigh-Ritz procedures, and are given in Appendix A. Once the stiffness and mass matrices are calculated, the modal properties can be readily obtained from Eq. (3.25) by solving a simple matrix eigenvalue problem. The modal frequencies for the structure are directly related to the eigenvalues. The actual modes, however, will have to be determined by substituting the eigenvectors into Eqs. (3.4-6) because each of the eigenvectors contains all the Fourier coefficients for the corresponding mode.

3.2.2 Results and discussions

Let's first look at a planer frame shown in Fig. 3.1(a). Based on its physical compositions, it will be respectively divided into 9 beams, as labeled in the figure. For simplicity, it is assumed that all these beams are made of steel: Young's modulus $E = 2.07\times10^{11}$ N/m^2, Poisson ratio $\mu = 0.29$, mass density $\rho = 7800$ kg/m^3; and have the same length L = 1m, cross-sectional area $S = 10^{-5}$ m^2, and moment inertia $I = 10^{-10}$ m^4. The two legs of the structure are rigidly fixed to the ground, and all the joints are assumed to be infinitely rigid.

The first 15 calculated natural frequencies are given in Table 3.1. The FEM results obtained from an ANSYS model are also presented as comparison. The series expansions are truncated to $M = 7$ in the calculation. An excellent agreement is observed between these two sets of solutions, which indicates that the current solution converges adequately fast with a small truncation number. The mode shapes for the first 4 modes are plotted in Fig. 3.3.

Table 3.1 Calculated natural frequencies for a planar frame

Mode	Current (Hz)	FEA (Hz)	Error (%)
1	3.1950	3.1961	0.034
2	9.4588	9.4586	-0.002
3	11.397	11.396	-0.009
4	27.145	27.144	-0.004
5	34.107	34.105	-0.006
6	37.887	37.885	-0.005
7	46.280	46.275	-0.011
8	50.898	50.893	-0.010
9	57.967	57.962	-0.009
10	57.994	57.989	-0.009
11	62.724	62.729	0.008
12	63.034	63.041	0.011
13	107.42	107.43	0.009
14	122.70	122.73	0.024
15	126.20	126.23	0.024

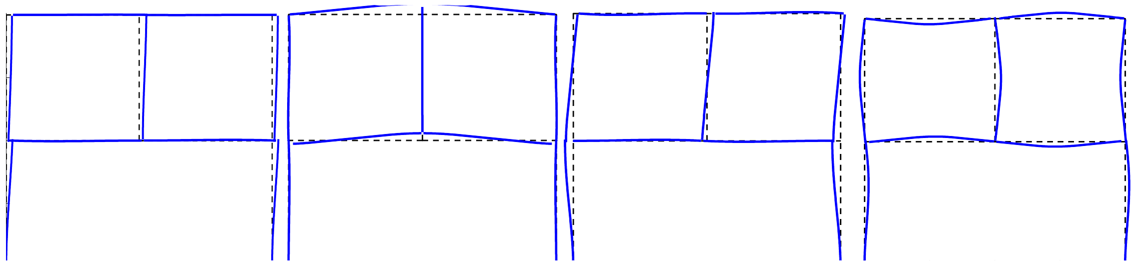

(a) (b) (c) (d)

Figure 3.3 Mode shapes of a planar frame: (a) 1st mode; (b) 2nd mode; (c) 3rd mode; (d) 4th mode

The next example is about a 3-D frame shown in Fig. 3.1(b). It is divided into 8 beams rigidly coupling together at 4 joints, as labeled in the figure. While the material and physical properties in this case are identical to those of the planar frame, the length for beams 1, 2, 5 and 7 is 2m, and for 3, 4, 6, and 8 is 1m. Other related model parameters such as cross section area S, moment inertias I_y and I_z are all identical to those in the 2-D case. The four legs of the structure are rigidly attached to the ground. The truncation number $M = 7$ is still used in this case for the series expansions.

Table 3.2 Calculated natural frequencies for a 3-D frame

Mode	Current (Hz)	FEA (Hz)	Error (%)
1	4.338	4.335	0.0692
2	4.338	4.335	0.0692
3	5.647	5.642	0.088
4	6.257	6.255	0.0312
5	7.488	7.487	0.0134
6	10.686	10.678	0.0745
7	10.688	10.679	0.0841
8	11.131	11.123	0.0719
9	11.131	11.123	0.0719
10	13.231	13.224	0.0529
11	13.231	13.224	0.0529
12	14.513	14.500	0.0896
13	28.668	28.665	0.0104
14	29.905	29.885	0.0669
15	29.905	29.885	0.0669

The first 15 calculated modal frequencies are listed in Table 3.2 for the 3-D frame structure. The results obtained using FEA models (ANSYS) are also presented there for comparison. An excellent agreement is seen between these two solution methods. To better understand the modal characteristics, the first six modes are plotted in Fig. 3.4.

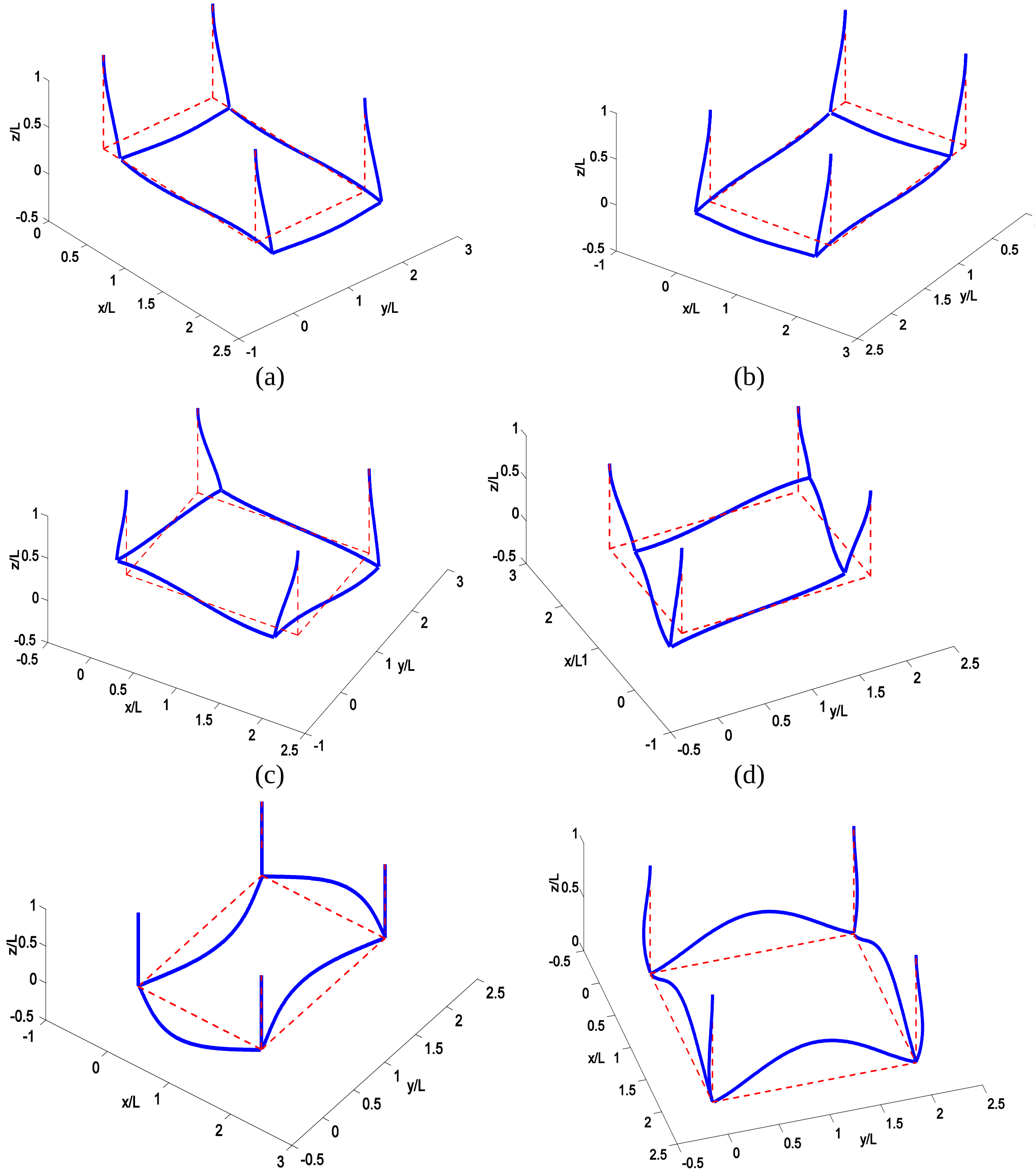

(a)

(b)

(c)

(d)

(e)

(f)

Figure 3.4 Mode shapes of a 3-D frame: (a) 1st mode; (b) 2nd mode; (c) 3rd mode; (d) 4th mode; (e) 5th mode; (d) 6th mode

3.3 Experimental study

In order to testify the proposed method, in this section, we will conduct a series of experiments on three types of coupled beam structures: a planar frame, a 3-D frame and a combo beam assembly, as shown in Figs. 3.5(a), 3.6(a) and 3.7(a) respectively. These test structures consist of a bunch of square cross-sectional steel beams with common properties listed in Table 3.3. For the ladder and table shaped frames, beams are connected together through 2-D or 3-D welding spots as illustrated by Figs. 3.5(b) and 3.6(b) respectively. These welding spots essentially represent the rigid coupling conditions among beams. For the combo frame shown in Fig. 3.7(a), it is obtained by simply assembling the ladder and table frames via screws depicted in Fig. 3.7(b).

(a) (b)

Figure 3.5 A ladder shaped frame for testing: (a) the whole shape; (b) a typical 2-D joint

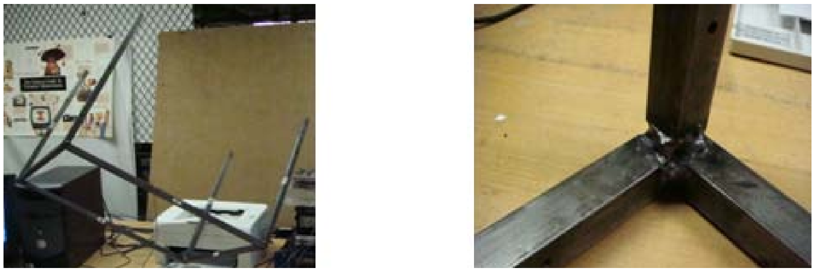

(a) (b)

Figure 3.6 A table shaped 3-D frame for testing: (a) the whole shape; (b) a typical 3-D joint

(a) (b)

Figure 3.7 A combo beam assembly for testing: (a) the whole shape; (b) a screw joint

Table 3.3 Material and physical properties of beam frames for testing

Description	Symbol	Unit	Value
Young's modulus	E	N/m^2	2.05×10^{11}
Shear modulus	G	N/m^2	0.8×10^{11}
Mass density	ρ	Kg/m^3	7800
Poisson ratio	μ	-----	0.29
Structural damping	η	-----	0.002

The experiment arrangement is to simulate a free boundary condition by hanging the structures through a soft rubber band from the ceiling. The frames were transversely excited by an impact hammer (PCB086C01) and the response was measured by a uni-axial accelerometer (B&K4508). The Data Acquisition (DAQ) hardware used in the experiment is NI USB-9234, and the software for analyzing the vibration signals is Toolbox "Sound and Vibration 6.0" of LabView 2009.

3.3.1 Modal testing of a 2D frame

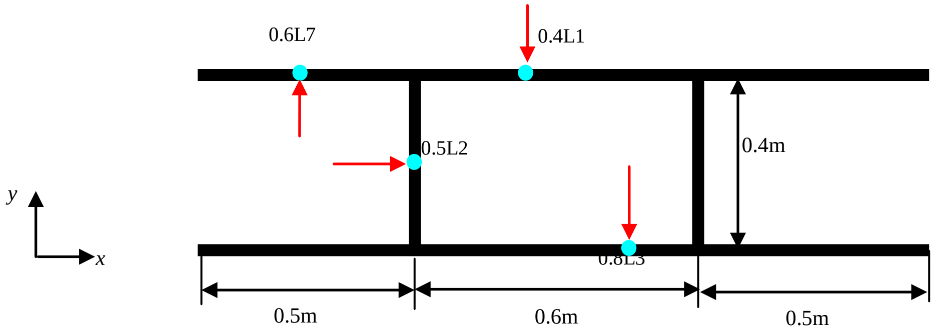

Figure 3.8 A ladder frame dimensions, and excitation and response locations

The test planer frame composed of 8 beams is made of steel (AISI A1018 cold drawn), and has the parameters as following: Young's modulus E = 205 GPa, mass density ρ=7870 kg/m^3, Poisson ratio $\mu = 0.29$, cross-sectional area S = 3.61×10^{-4} m^2, moment inertias $I_y = I_z$ = 0.11×10^{-7} m^4, and tosional rigidity J = 0.22×10^{-7}m^4 . The overall dimensions of the structure as well as the excitation and response locations are presented in Fig. 3.8.

As illustrated in the figure, a force is executed on beam 1 along the *y* direction, and the response points are located, respectively, on beam 1 along *y* axis, beam 2 along *x* axis, beam 3 along *y* axis, and beam 7 along *y* axis. The measured and predicted frequency response functions (FRF) are plotted in Figs. 3.9-12 respectively for the four response locations. An overall good agreement can be seen between the theoretical predications and experimental results in all cases. Nevertheless, a frequency shift exists between 200Hz and 1000Hz, and becomes larger with increasing the frequency in these figures.

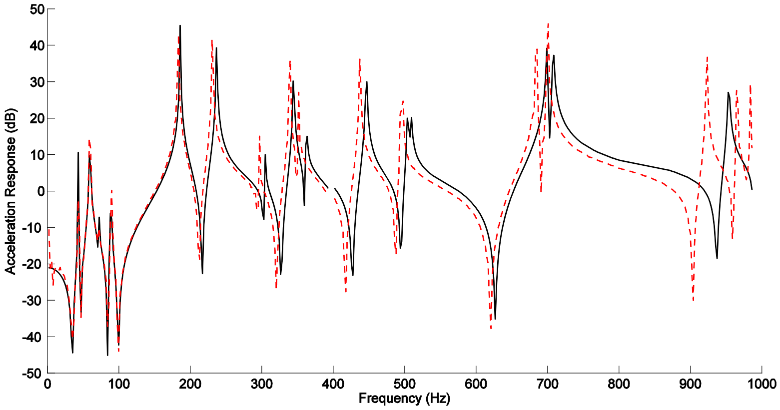

Figure 3.9 FRF of a ladder frame at point 1 in *y*- axis: — prediction; --- test

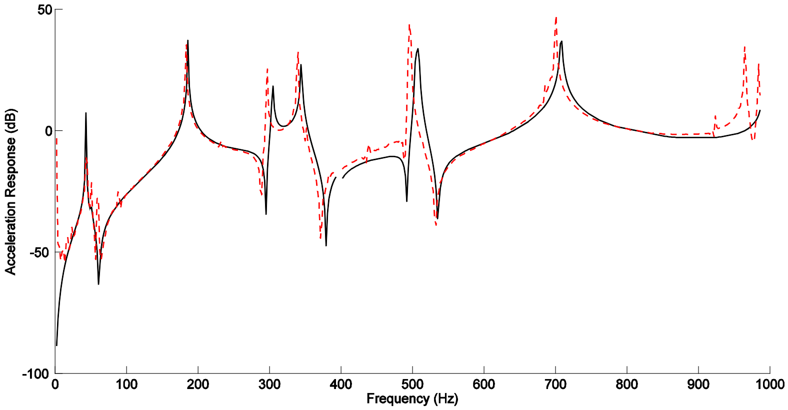

Figure 3.10 FRF of a ladder frame at point 2 in *x*- axis: — prediction; --- test

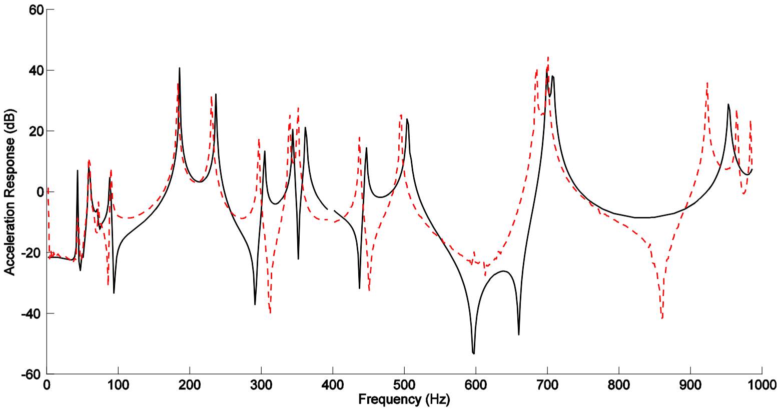

Figure 3.11 FRF of a ladder frame at point 3 in the *y*- axis: — prediction; --- test

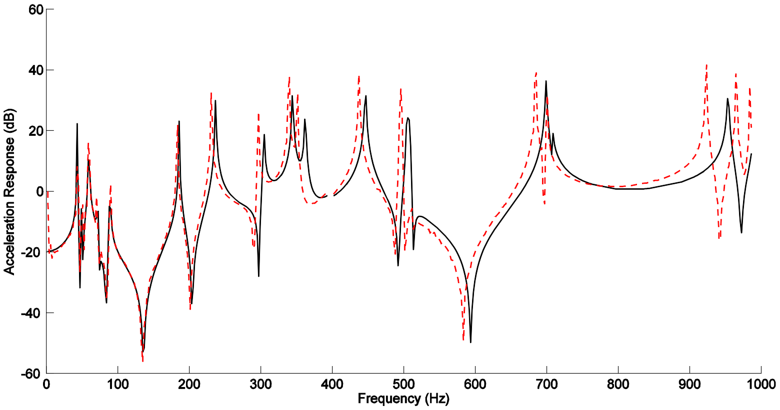

Figure 3.12 FRF of a ladder frame at point 7 in the *y*- axis: — prediction; --- test

Moreover, Fig. 3.11 indicates a slight difference of curve shapes between the theoretical and experimental predictions. The possible explanations for the discrepancies between the theoretical predictions and experimental estimations lie in: 1) the theoretical model does not account for the uncertainties of the actual coupling configurations at the joints; 2) the cross-coupling between the in-plane and out-plane modes may be induced by the out-plane component of the exciting force. At approximately 100Hz, 230Hz, 450Hz and 920Hz in Fig. 3.10, small peaks exist in the experimental estimations which do not appear in the theoretical predictions. This is because the response point (accelerometer) was not exactly located at the center of beam 2, so it breaks the symmetric response characters of the structure, thus introduce the extra resonances as a result.

3.3.2 Modal testing of a 3D frame

The next experiment is to validate the proposed solution for the 3-D frame. The considered structure shown in Fig. 3.6(a) consists of 8 identical beams, and is made of the same material as the one used for the 2-D frame in Section 3.3.1. The geometrical parameters of the constituent beams are: cross-sectional area S = 2.25×10^{-4} m^2, tosional rigidity J = 0.84×10^{-8}m^4, and moment inertias I_z = I_z = 0.42×10^{-8} m^4. Two positions for the exciting force were considered in this case as presented in Fig. 3.13 along with response locations.

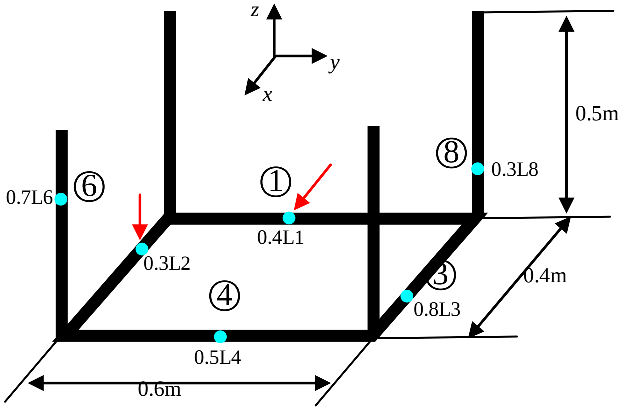

Figure 3.13 A table frame dimensions, and excitation and response locations

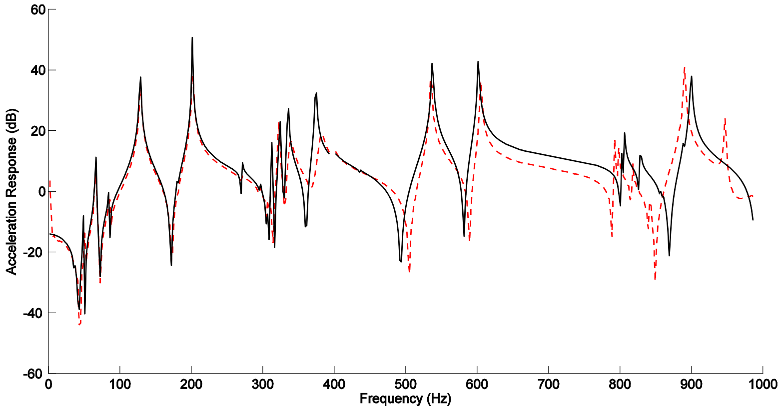

Figure 3.14 FRF of a table frame at the driving point 1 in x-axis: — prediction; --- test

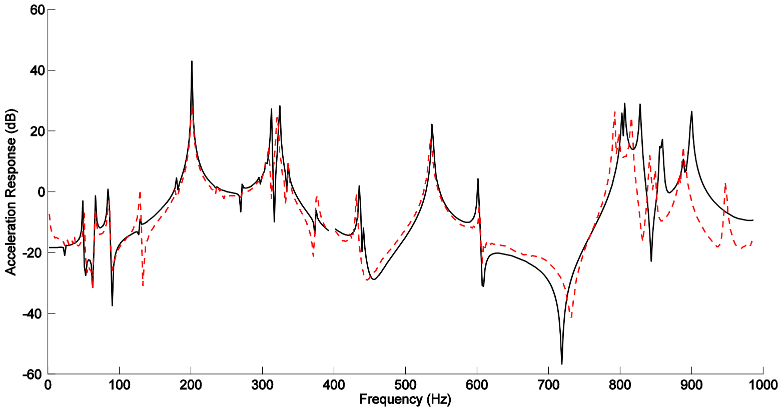

Figure 3.15 FRF of a table frame at point 8 in *x*- axis with respect to the force at point 1 in *x*-axis: — prediction; --- test

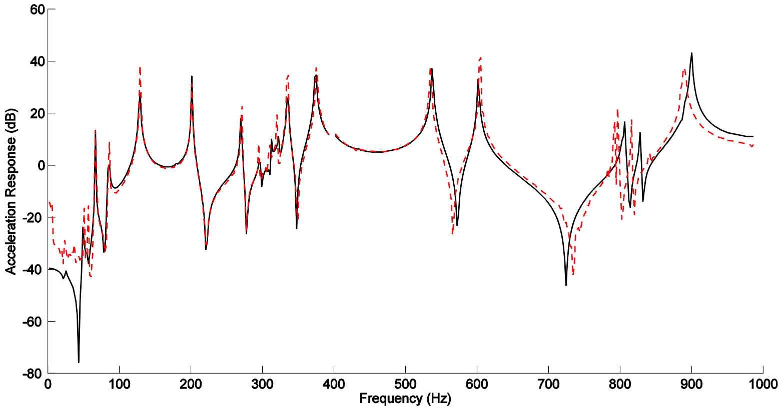

Figure 3.16 FRF of a table frame at point 3 in *y*-axis with respect to the force at point 1 in *x*-axis: — prediction; --- test

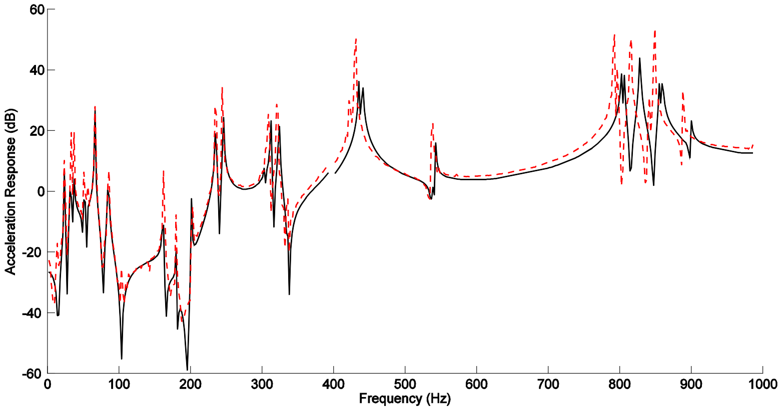

Figure 3.17 FRF of a table frame at point 6 in *x*- axis with respect to the force at point 2 in *z*-axis: — prediction; --- test

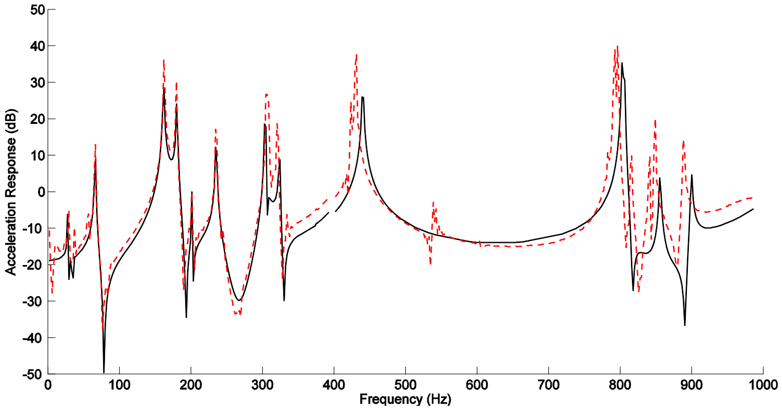

Figure 3.18 FRF of a table frame at point 4 in *x*- axis with respect to the force at point 2 in *z*-axis: — prediction; --- test

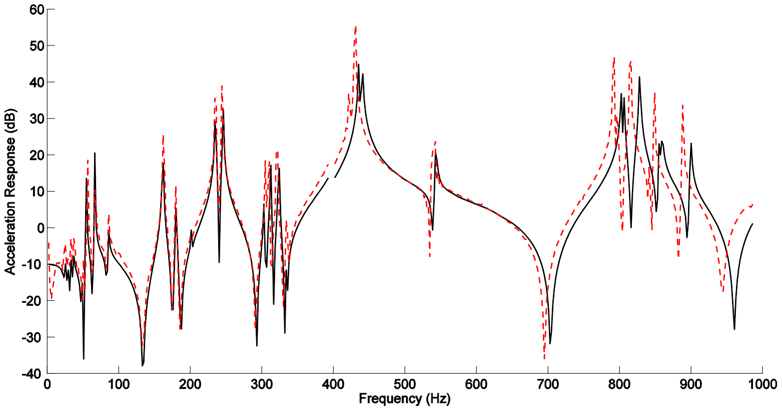

Figure 3.19 FRF of a table frame at the driving point 2 in *z*-axis: — prediction; --- test

Figs. 3.14-19 compare the FRFs obtained by the proposed solution and experiments. It can be seen that the agreement between the two sets of results is quite good except that a small frequency shift occurs at the range above 700Hz for Figs. 3.14-16, and above 400Hz for Figs. 3.17-19, respectively. The root causes for the frequency-shift could also be attributed to those inferred in the planar frame case.

3.3.3 Modal testing of a combo frame

A combo beam frame, shown in Fig. 3.7(a), is considered as the test structure. The excitation and response locations on this frame are illustrated in Fig. 3.20.

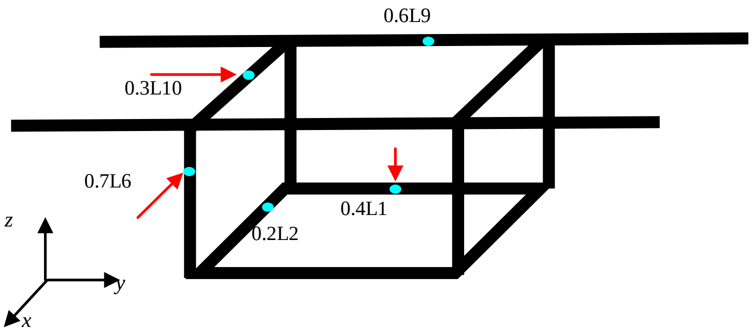

Figure 3.20 The excitation and response locations on a combo beam assembly

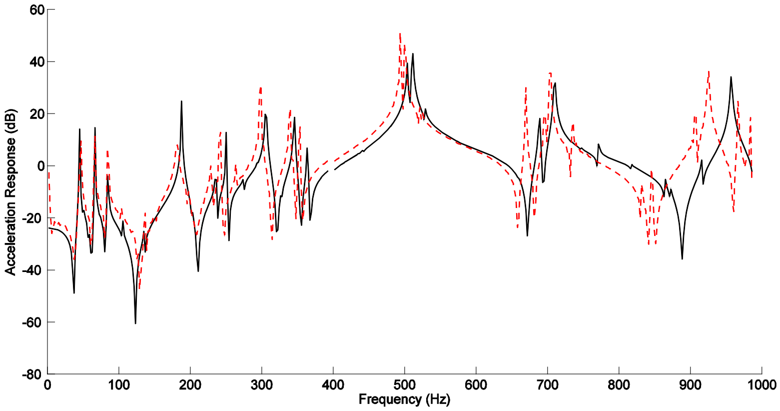

Figure 3.21 FRF of a combo frame at the driving point 10 in *y*-axis: — prediction; --- test

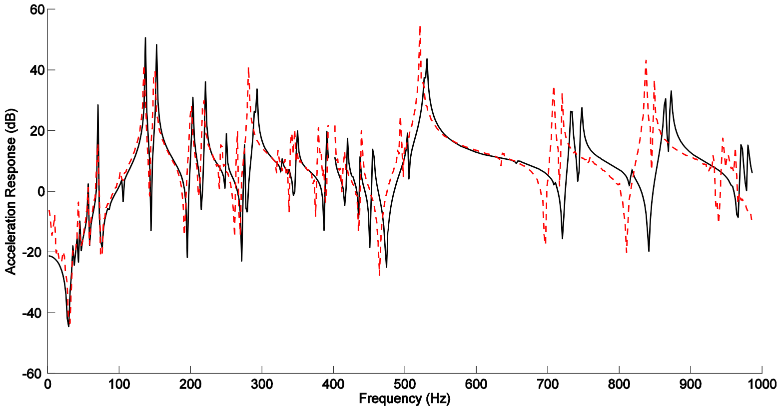

Figure 3.22 FRF of a combo frame at the driving point 1 in *z*- axis: — prediction; --- test

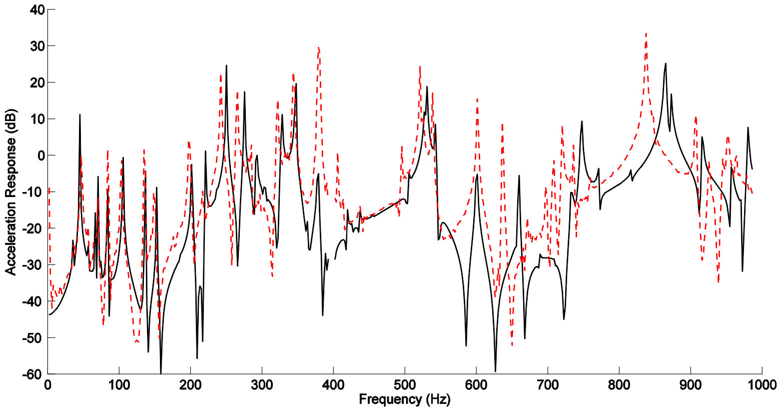

Figure 3.23 FRF of a combo frame at point 2 in *y*- axis with respect to the force at point 1 in *z*-axis: — prediction; --- test

Comparisons between the measured and predicted FRFs are illustrated in Figs. 3.21-25 for five response locations. Two sets of results match fairly good overall in all cases, and the general characters of the spectra are correctly predicted. It can be noted that the frequency shift appears to occur in a lower frequency range compared to the 2-D and 3-D frames. In particular, the frequency shift is more noticeable in Fig. 3.25 where both the exciting and response points are located at point 6.

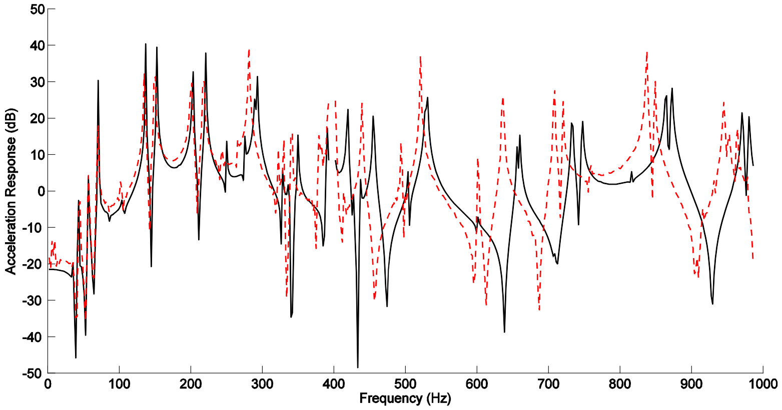

Figure 3.24 FRF of a combo frame at point 9 in *z*-axis with respect to the force at point 1 in *z*-axis: — prediction; --- test

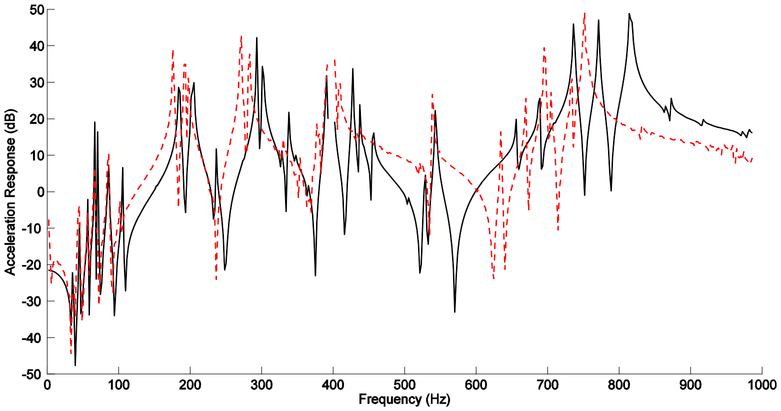

Figure 3.25 FRF of a combo frame at the driving point 6 in *x*- axis: — prediction; --- test

One possible cause for the large frequency shift in Fig. 3.25 is resulted from the restraining imperfections presented in a joint connecting the two frames. As shown in Fig. 3.7b, a screw only linearly restrains the movements in *x*-, *y*- and *z*- directions without rotation restrictions in the *x*-*y* plane, which indicates that the joint is not as perfect rigid as assumed in the theoretical models. Therefore, when the response/driving point is close to the joint and the considered FRF is located in the *x*-*y* plane, the restraining imperfections of the joint tends to exert more impacts on the measured FRF consequently.

3.4 Power flow analysis

When a load applies to the structure, a force vector will appear on the right-hand-side of Eq. (3.25). For instance, if a concentrated harmonic force $f_i^{w_r}$ is applied to the *i*-th beam at position $x = x_{ifw}$, the elements of the force vector are written as

$$f_{i,m}^{w_r} = f_i^{w_r} \cos\frac{m\pi}{L_i} x_{i,w_r}, \qquad m = 0,1,\ldots,M \tag{3.4.1}$$

$$f_{i,n}^{w_r} = f_i^{w_r} \sin\frac{n\pi}{L_i} x_{i,w_r}, \qquad n = 1,2,3,4 \tag{3.4.2}$$

where the subscript *r* (= *z* or *y*) denote the bending displacement about *z* or *y* axis.

Once the Fourier coefficients, and hence the displacements, are determined over beam *i*; power flows through its ends can be readily calculated from

$$P_{\zeta,i} = P_{\zeta,i}^{w_r} + P_{\zeta,i}^{u} + P_{\zeta,i}^{\theta}, \quad \zeta = 0, L_i \tag{3.4.3}$$

where

$$P_{\zeta,i}^{w_r} = \frac{1}{2}\Re\left[j\omega E_i I_i \left(\frac{\partial^3 w_{i,r}(\zeta)}{\partial x^3} conj(w_{i,r}(\zeta)) + \frac{\partial^2 w_{i,r}(\zeta)}{\partial x^2} conj(\frac{\partial\ w_{i,r}(\zeta)}{\partial x}) \right) \right] \tag{3.4.4}$$

$$P_{\zeta,i}^{u} = \frac{1}{2}\Re\left[j\omega E_i S_i \frac{\partial u_i(\zeta)}{\partial x} conj(u_i(\zeta)) \right] \tag{3.4.5}$$

$$P_{\zeta,i}^{\theta} = \frac{1}{2}\Re\left[j\omega G_i J_i \frac{\partial \theta_i(\zeta)}{\partial x} conj(\theta_i(\zeta)) \right] \tag{3.4.6}$$

with $P_{\zeta,i}^{w_r}$, $P_{\zeta,i}^{u}$, and $P_{\zeta,i}^{\theta}$ being the powers transmitted through the flexural, axial, and rotational displacements, respectively.

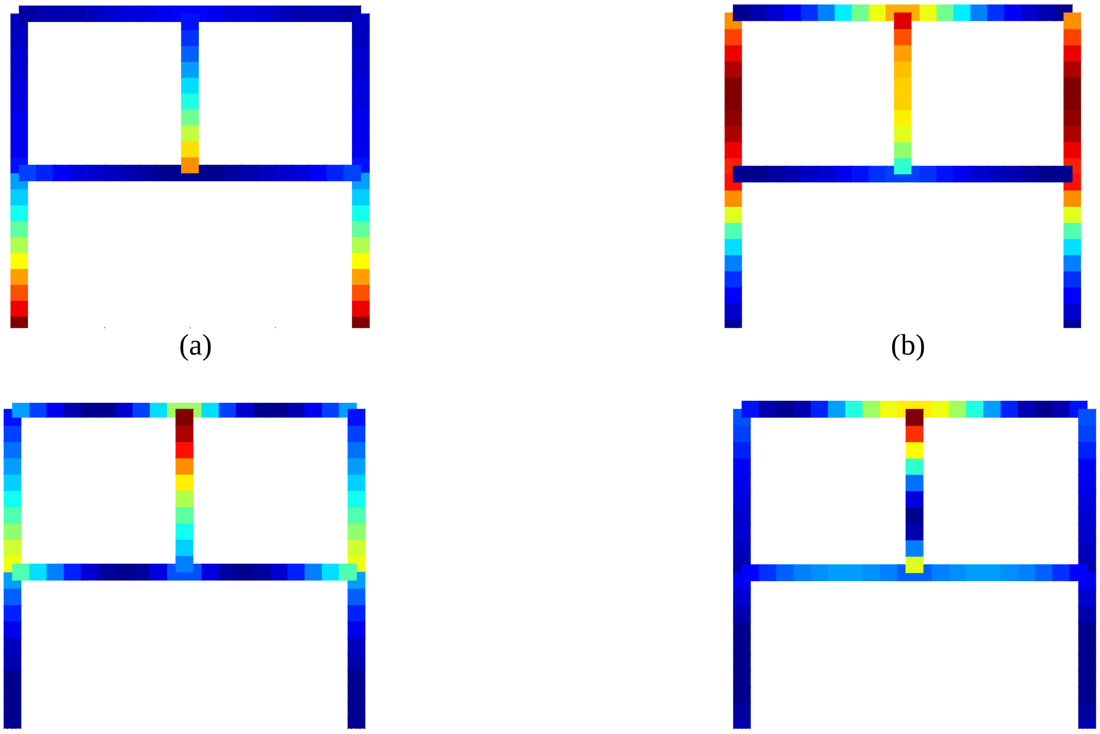

(a) (b) (c) (d)

Figure 3.26 Strain energy for a planar beam: (a) 4Hz; (b) 20Hz; (c) 40Hz; and (d) 100Hz

For the planar frame shown in Fig. 3.1(a), a unit force is applied on beam 9 in the transverse direction at a distance of $0.1\,L_9$ away from joint 4. A uniform structural damping of 1% is assumed for the whole structure. No extra damping is applied to the joints although the damping coefficients can be separately specified for each joint. The contour plots of the strain energy density are given in Fig. 3.26 for three different frequencies.

Instead of the frequency response functions, the strain energy densities are given simply to illustrate the easiness of post-processing the results here. Actually, in the mid- to high-frequency range, the strain energy (density) may be a more meaningful variable than the displacement in assessing the severity of a vibration problem or the effectiveness of vibration control measure.

While the strain energy density can also be obtained from other numerical models through post-processing the discretized displacement data, some quantities (such as, the power flows though a junction) may not be so easily calculated because it is often difficult to ensure the accuracy of differential operations performed numerically. In this method, however, most variables of interest can be easily derived through appropriate mathematical manipulations including differentiations.

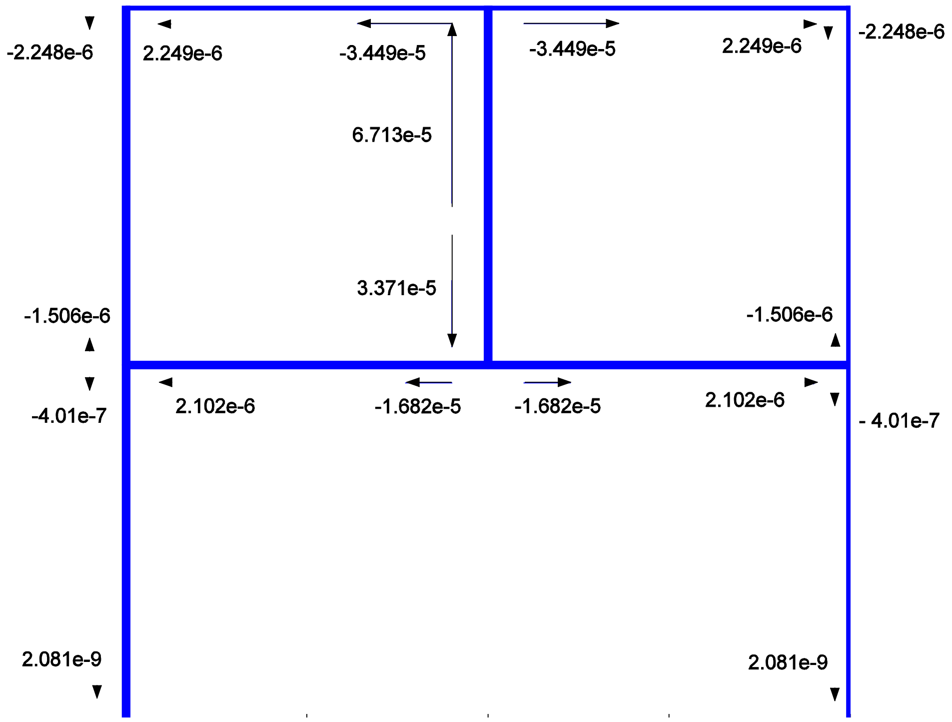

Figure 3.27 Power flows in a planar frame at 100Hz

The power flows in the frame at 100 Hz is shown in Fig. 3.27. In the plot, the arrows are used to indicate the flow directions of the net powers at the beam ends, and the lengths indicate the amounts of associated power flows. The net power transferred from one beam to another is the sum of power flows separately associated with the flexural, rational and axial displacements. For non-dissipative joints, the total powers flowing into a junction will have to be equal to zero. This power balance condition is evident in the plot.

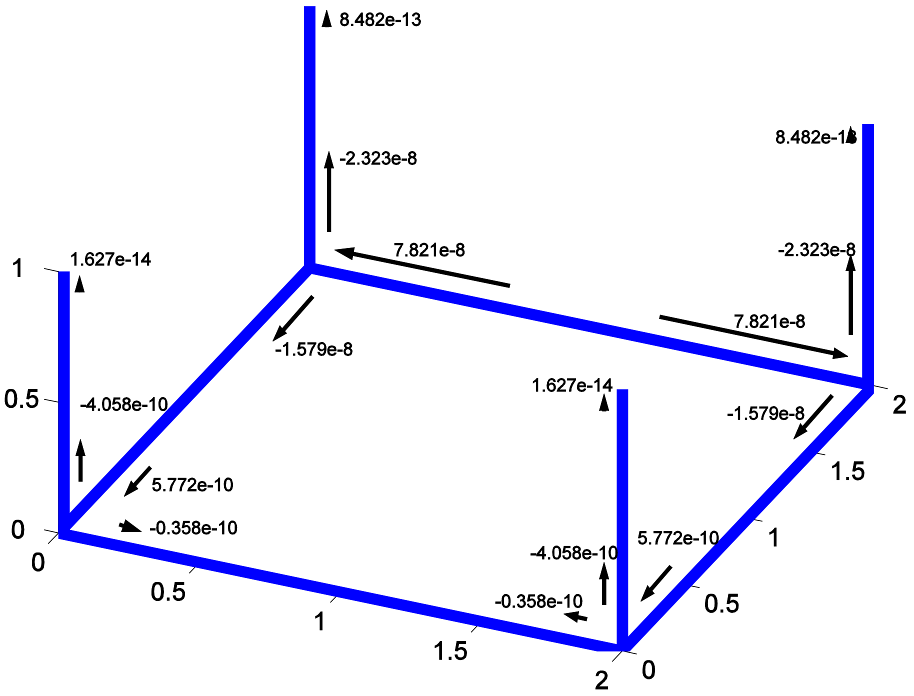

Figure 3.28 Power flows in a 3-D frame at 700Hz

In comparison with vibration or strain energy levels, power flows usually provide more reliable information on where the vibration sources are located.

3.3 Conclusions

A closed-form solution for vibrations of 2-D and 3-D Euler-Bernoulli beams is proposed in this chapter. The displacements over each beam are expressed as a modified Fourier series where the auxiliary functions are simply selected as 4-term sine functions for flexural deflections, and 2-term sine functions for longitudinal and torsional displacements. Regardless of boundary/coupling conditions, the auxiliary functions are equal to the values of the first and third derivatives of the displacement function at both end points. With the help of the auxiliary functions, the displacement functions and their derivatives (up to 3rd) are guaranteed to be continuous on the boundaries when the displacement function is periodically extended (with a period $2L$) onto the entire x-axis.

Based on this solution, a general method for modeling vibrations of and power flows in built-up (2-D and 3-D) frame structures is subsequently developed. In this general solution, the frame is divided into a number of beam elements and the displacements of each beam are defined in its local coordinate. The powerful Rayleigh-Ritz procedure is used to determine the expansion coefficients in an approximate manner. As a result, only the neighboring beams will be directly coupled together in the final system, which significantly simplifies the calculations.

The proposed method is also validated numerically and experimentally. The calculated modal properties have shown an excellent agreement with those obtained from FEA models. An overall good agreement is found between the theoretical predictions and the experimental results. However, a frequency shift exists between the predicted and measured natural frequencies, which may result from the uncertainties of the actual coupling configurations at the joints and the cross-coupling between the in-plane and out-plane modes.

CHAPTER IV

A GENERAL SOLUTION FOR VIBRATIONS OF BUILT-UP PLATE ASSEMBLIES

4.1 Introduction

The plate assemblies consisting of a number of thin rectangular plates joined at edges are extensively used in various engineering structures, such as car bodies, ship hulls, aerospace structures and building structures. Determining the vibration of such structures is of interest to both researchers and engineers. In addition to the well-known numerical methods such as statistical energy analysis (Langley & Contoni, 2004) and the finite element method (Popplewell, 1971 & 1975), several analytical approaches have been developed to study the vibration of and power flow in coupled plate structures. In solving for plate assembly problems, the displacement field is usually written in terms of admissible functions that satisfy the geometrical boundary conditions for each plate and compatibility conditions on the interfaces between adjoining plates. Dickinson and Warburton (1967) investigated the flexural vibrations of a box-like structure using a sine series where the beam functions are used as the shape functions. The solution to the free vibrations of the plate is divided into two parts, each corresponding to a plate having at least two parallel edges simply supported. The box vibration modes are classified into symmetrical or anti-symmetrical modes by assuming all the common edges to be simply supported. This treatment yields a simplified relationship of bending moments on the joints and deflections on the free edges. Finally, they derived an analytical solution from a series of equations simultaneously satisfying the boundary conditions and the coupling relationships. Instead of the beam functions, the orthogonal polynomials are employed as admissible functions by Kim and Dickinson (1987) and Yuan and Dickinson (1992 & 1993) to analyze the line supported plate system and coupled plates, respectively. However, one can encounter a numerical difficulty when using a higher order polynomial due to its numerical instability resulting from computer round-off errors. The wave propagation method is also widely used by researchers (Langley, 1991; Rebillard & Guyader, 1995; Park & Hong, 2001; Fulford & Peterson, 2000) for dynamic analysis of plate structures. Langley (1991) studied both periodic and non-periodic stiffened panels using wave transmission and reflection coefficients at the structural discontinuities. Rebillard and Guyader (1995) developed an analytical formulation to study the vibration behavior of plates connected at any angle. In their study, the equations of bending and in-plane motions are expressed in terms of a wave formulation and then solved by using a semi-modal decomposition. However, in a particular part of the excited plate where both wave solutions are summed, overflow problems may occur due to the difference between two large and similar values in the exponential functions. Park and Hong (2001) applied energy equations to examine the propagation of longitudinal waves and in-plane shear waves in two-plate structure coupled at a certain angle. The wave formulation was also exploited by Fulford and Peterson (2000) to study the vibration energy flow in the built-up plate systems with a point-like connection between adjacent elements. The dynamic stiffness matrix method developed by Langley (1989) was applied to study the integrated aircraft panels, aerospace box-type structures (Khumbah & Langley, 1998) and built-up plate assemblies (Bercin & Langley, 1996; Bercin, 1997) by involving the in-plane vibrations. The receptance technique originally proposed by Azimi *et al.* (1984) has also received more attention recently for investigating the power flows in plate systems. Beshara and Keane (1998) adopted the receptance approach to study the power flows across the compliant and dissipative couplings where the response of each structure is described in terms of Green functions. Kim *et al.* (1994) extended the method to the interactions of any number of plates at a common junction. Cuschieri (1990) proposed a mobility approach to study the energy transfer through an L-shaped junction. Grice and Pinnington (2000 & 2002) performed analyses on both flexural and in-plane vibrations of a thin-plate box using a “hybrid” method that combines finite element analysis and analytical impedances.

All of the preceding analytical methods are based on a common assumption that plates are simply supported along, at least, a pair of opposite edges perpendicular to the coupling edges. There is no investigation available in the literature that can deal with the vibration of a general plate assembly *with arbitrary boundary conditions and coupling configurations*. The objective of this chapter is to develop a general solution for elastically bounded plate assemblies composed of any number of rectangular plates coupled at arbitrary angles. In the following analytical procedure, the plate assembly is divided into a number of constituent plates naturally according to its physical composition as in an SEA model, and its dynamic characteristics and responses are actually determined in a way similar to that of FEA methods. The final system equations are established by using the Rayleigh-Ritz procedure, and the unknown Fourier expansion coefficients are determined from the standard eigen-solutions. The present solution is demonstrated to work well by comparing the simulation results with those obtained from other techniques including finite element and experimental testing.

4.2 Theoretical formulations

4.2.1 Description of the general built-up plate assembly

The general plate assembly considered in this study consists of any number of arbitrarily oriented rectangular plates of various material and physical properties, as shown in Fig. 4.1. All the plates are assumed to have general boundary conditions and are elastically connected via a set of springs.

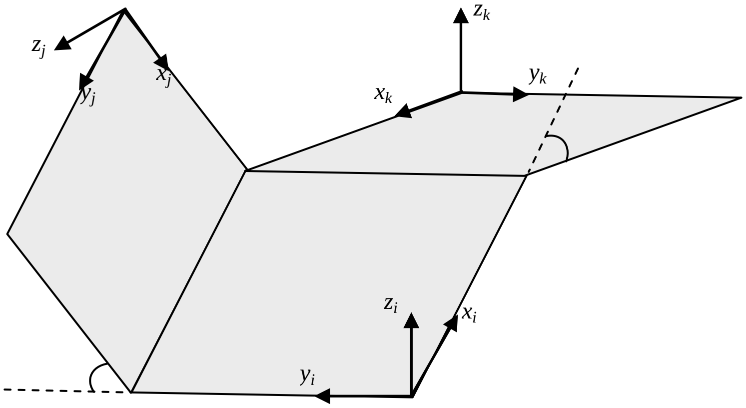

Figure 4.1 Schematic of a plate assembly with arbitrarily oriented components

Consider an individual plate of length *a*, width *b* and thickness *h* and take coordinate *x* in the length direction and *y* in the width direction, the displacements of out-of-plane and in-plane vibrations can be expressed as

$$W_i(x,y,t) = w_i(x,y)e^{j\omega t} \tag{4.1}$$

$$U_i(x,y,t) = u_i(x,y)e^{j\omega t} \tag{4.2}$$

$$V_i(x,y,t) = v_i(x,y)e^{j\omega t} \tag{4.3}$$

where ω denotes the radian natural frequency of vibration and *t* is time, $j = \sqrt{-1}$.

As previously done for a single plate, the amplitudes of the transverse displacement (Li & Zhang, 2009) will be expressed as

$$w_i(x,y) = \sum_{m=0}^{\infty}\sum_{n=0}^{\infty} A^w_{i,mn}\cos\lambda_{am}x\cos\lambda_{bn}y + \sum_{l=1}^{4}\left(\zeta_b^l(y)\sum_{m=0}^{\infty} a^l_{i,m}\cos\lambda_{am}x + \zeta_a^l(x)\sum_{n=0}^{\infty} b^l_{i,n}\cos\lambda_{bn}y\right) \tag{4.4}$$

and the in-plane displacements (Du & Li, 2007) as

$$u_i(x,y) = \sum_{m=0}^{\infty}\sum_{n=0}^{\infty} A^u_{i,mn}\cos\lambda_{am}x\cos\lambda_{bn}y + \sum_{l=1}^{2}\left(\xi_b^l(y)\sum_{m=0}^{\infty} c^l_{i,m}\cos\lambda_{am}x + \xi_a^l(x)\sum_{n=0}^{\infty} d^l_{i,n}\cos\lambda_{bn}y\right) \tag{4.5}$$

$$v_i(x,y)=\sum_{m=0}^{\infty}\sum_{n=0}^{\infty}A^{v}_{i,mn}\cos\lambda_{am}x\cos\lambda_{bn}y+\sum_{l=1}^{2}\left(\xi^{l}_{b}(y)\sum_{m=0}^{\infty}e^{l}_{i,m}\cos\lambda_{am}x+\xi^{l}_{a}(x)\sum_{n=0}^{\infty}f^{l}_{i,n}\cos\lambda_{bn}y\right) \tag{4.6}$$

where $\lambda_{am}=m\pi/a_i$, $\lambda_{bn}=n\pi/b_i$, and $A^{w}_{mn},A^{u}_{mn},A^{v}_{mn},\cdots,e^{l}_{m}$, and f^{l}_{n} represent the Fourier coefficients of Fourier series expansions. The supplementary functions, $\zeta^{l}_{b}(y)$, $\zeta^{l}_{a}(x)$, $\xi^{l}_{b}(y)$ and $\xi^{l}_{a}(x)$, are defined in Appendix B. These supplementary functions are used to deal with the possible discontinuities (at the edges) potentially exhibited by a displacement function and its derivatives when they are periodically extended onto the entire *x-y* plane as directly implied by a Fourier expansion.

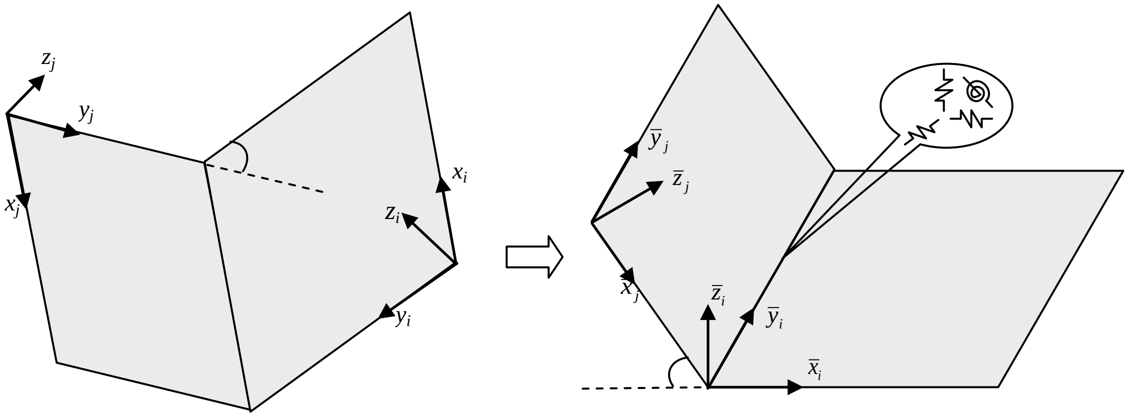

Figure 4.2 The co-ordinate transformation scheme of two coupled plates

The elastic deformations (w_i,u_i,v_i) of each plate are defined with respect to a local coordinate system (x_i,y_i,z_i), which leads to various coupling scenarios between each adjoining pair of plates. In order to ease the computation, a second local coordinate system $(\bar{x}_i,\bar{y}_i,\bar{z}_i)$ is actually used for every plate, as shown in Fig. 4.2. It is a simple matter to transform the displacement vector from one coordinate system to another.

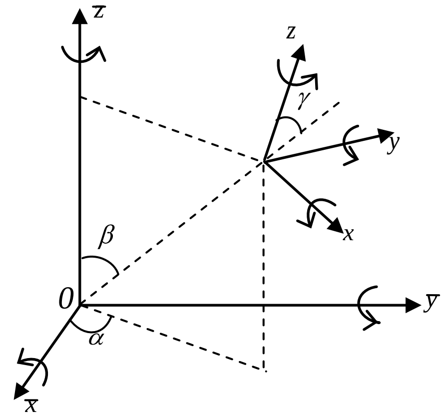

Figure 4.3 The coordinate of springs

Assume that the local coordinate system (x_i, y_i, z_i) can be obtained by rotating the $(\bar{x}_i, \bar{y}_i, \bar{z}_i)$ system about $\bar{z}_i$ axis by an angle α, about $\bar{y}_i$ axis by an angle β, and about $\bar{x}_i$ axis by an angle γ_i, respectively. The coordinate transformation between the two sets of local systems is accomplished by a matrix

$$\mathbf{P} = \begin{bmatrix} \hat{\mathbf{P}} & 0 \\ 0 & \hat{\mathbf{P}} \end{bmatrix} \tag{4.7}$$

with

$$\hat{\mathbf{P}} = \begin{bmatrix} \cos\alpha\cos\beta & (\sin\alpha\cos\beta\sin\gamma - \cos\gamma\sin\beta) & (\sin\alpha\cos\beta\cos\gamma + \sin\beta\sin\gamma) \\ \cos\alpha\sin\beta & (\sin\alpha\sin\beta\sin\gamma + \cos\gamma\cos\beta) & (\sin\alpha\sin\beta\cos\gamma - \sin\gamma\cos\beta) \\ -\sin\gamma & \cos\alpha\sin\gamma & \cos\alpha\cos\gamma \end{bmatrix} \tag{4.8}$$

For the displacements on the junction line of a plate, one may write

$$\overline{\mathbf{Y}}_i = \mathbf{P}_i \mathbf{Y}_i \tag{4.9}$$

where $\mathbf{Y}_i$ is the displacement vector defined in the local coordinates, written as

$$\mathbf{Y}_i = \left\{ w_i \quad u_i \quad v_i \quad \frac{\partial w_i}{\partial r_i} \quad \frac{\partial u_i}{\partial r_i} \quad \frac{\partial v_i}{\partial r_i} \right\}^T e^{j\omega t} \tag{4.10}$$

where r_i $(= x_i$ or y_i) denotes the axis of the plate local coordinate.

It should be noted that the rotation displacements ($\frac{\partial u_i}{\partial r_i}$ and $\frac{\partial v_i}{\partial r_i}$) on the edges caused by in-plane deformations are not considered when modeling the boundary restraints and coupling conditions (Du & Li, 2007). Therefore, $\frac{\partial u_i}{\partial r_i}$ and $\frac{\partial v_i}{\partial r_i}$ will be simply set to zero in the following calculations. Similarly, the coupling between plates is treated as an elastic line connection described by a set of six simple linear and rotational springs. Assuming that *x*, *y* and *z* are the principal axes of these springs locally defined on the junction line between the *i*-th and the *j*-th plates, then its stiffness matrix in global coordinates can be expressed as

$$\overline{\mathbf{K}}_s = \mathbf{Q}_{ij}\mathbf{K}_s\mathbf{Q}_{ij}^T \tag{4.11}$$

with

$$\mathbf{K}_s = diag\begin{bmatrix} k_x & k_y & k_z & K_x & K_y & K_z \end{bmatrix} \tag{4.12}$$

where $diag(.)$ denotes the diagonal matrix formed from the listed elements, k_j and K_j ($j = x, y,$ or z), are, respectively, the linear stiffness in and the rotational stiffness about the *j*-direction.

4.2.2 Solution for the coupled plate structure

The expressions for the total potential and kinetic energies of the plate assembly, respectively, are given by

$$\mathbf{V} = \sum_{i}^{N_p}\left(\mathbf{V}_i + \mathbf{V}_i^{B.C}\right) + \sum_{i=1}^{N_p}\sum_{j=i}^{N_p}\left(1-\delta_{ij}\right)\mathbf{V}_{ij}^c \tag{4.13}$$

$$\mathbf{T} = \sum_{i=1}^{N_p}\mathbf{T}_i \tag{4.14}$$

where N_p is the total number of plate components; $\mathbf{V}_i$ represents the strain energies due to the bending and in-plane motions of the *i*-th plate; $\mathbf{V}_i^{B.C}$ designates the potential energies stored in the boundary springs of the *i*-th plate; $\mathbf{V}_{ij}^{c}$ accounts for the potential energies associated with coupling springs between the *i*-th and the *j*-th plate; and $\mathbf{T}_i$ is the kinetic energies corresponding to the vibrations of the *i*-th plate.

Specifically, the potential and kinetic energies of the individual plate in terms of the assumed displacements can be written as

$$\mathbf{V}_i = \frac{D_i}{2}\int_0^{a_i}\int_0^{b_i}\left[\frac{\partial^2 W_i}{\partial x^2}+\frac{\partial^2 W_i}{\partial y^2}+2\mu\frac{\partial^2 W_i}{\partial x^2}\frac{\partial^2 W_i}{\partial y^2}+2(1-\mu)\left(\frac{\partial^2 W_i}{\partial x\partial y}\right)^2\right]dxdy\ +$$

$$\frac{G_i}{2}\int_0^{a_i}\int_0^{b_i}\left[\left(\frac{\partial U_i}{\partial x}+\frac{\partial V_i}{\partial y}\right)^2-2(1-\mu)\frac{\partial U_i}{\partial x}\frac{\partial V_i}{\partial y}+\frac{(1-\mu)}{2}\left(\frac{\partial U_i}{\partial x}+\frac{\partial V_i}{\partial x}\right)^2\right]dxdy \qquad (4.15)$$

$$\mathbf{V}_i^{B.C} = \frac{1}{2}\left[\left(\mathbf{Y}_i^T\overline{\mathbf{K}}_{B.C}^{x,0}\mathbf{Y}_i\right)_{x=0}+\left(\mathbf{Y}_i^T\overline{\mathbf{K}}_{B.C}^{x,a}\mathbf{Y}_i\right)_{x=a_i}+\left(\mathbf{Y}_i^T\overline{\mathbf{K}}_{B.C}^{y,0}\mathbf{Y}_i\right)_{y=0}+\left(\mathbf{Y}_i^T\overline{\mathbf{K}}_{B.C}^{y,b}\mathbf{Y}_i\right)_{y=b_i}\right] \qquad (4.16)$$

and

$$\mathbf{T}_i = \frac{1}{2}\int_0^{a_i}\int_0^{b_i}\rho_i h_i\left[\dot{W}_i^2+\dot{U}_i^2+\dot{V}_i^2\right]dxdy \qquad (4.17)$$

where $D_i = E_i h_i^3/12(1-\mu_i^2)$ is the flexible rigidity of the *i*-th plate; E_i, G_i, μ_i, ρ_i and h_i are Young's modulus, the extensional rigidity, Poisson's ratio, the mass density and thickness of the *i*-th plate, respectively. The definitions for the boundary spring matrices $\overline{\mathbf{K}}_{B.C}^{x,0}$, $\overline{\mathbf{K}}_{B.C}^{x,a}$, $\overline{\mathbf{K}}_{B.C}^{y,0}$ and $\overline{\mathbf{K}}_{B.C}^{y,b}$ follow the rules of orthogonal transformation of the stiffness matrix given by Eqs. (4.11) and (4.12).

The potential energy stored in the coupling springs with respect to global coordinates can be written as

$$\mathbf{V}_{ij}^{c}=\frac{1}{2}\left[\left(\overline{\mathbf{Y}}_{i}-\overline{\mathbf{Y}}_{j}\right)^{T}\overline{\mathbf{K}}_{s}\left(\overline{\mathbf{Y}}_{i}-\overline{\mathbf{Y}}_{j}\right)\right] \tag{4.18}$$

By substituting Eqs. (4.9) and (4.11) into Eq. (4.18), one obtains

$$\mathbf{V}_{ij}^{c}=\frac{1}{2}\left[\,\mathbf{Y}_{i}^{T}\mathbf{H}_{i}\mathbf{Y}_{i}+\mathbf{Y}_{j}^{T}\mathbf{H}_{j}\mathbf{Y}_{j}-\mathbf{Y}_{i}^{T}\mathbf{H}_{ij}\mathbf{Y}_{j}-\mathbf{Y}_{j}^{T}\mathbf{H}_{ij}^{T}\mathbf{Y}_{i}\,\right] \tag{4.19}$$

The new terms introduced in Eq. (4.19) are defined as follows

$$\mathbf{H}_{i}=\mathbf{P}_{i}^{T}\mathbf{Q}_{ij}\mathbf{K}_{s}\mathbf{Q}_{ij}^{T}\mathbf{P}_{i}\ ,\ \mathbf{H}_{j}=\mathbf{P}_{j}^{T}\mathbf{Q}_{ij}\mathbf{K}_{s}\mathbf{Q}_{ij}^{T}\mathbf{P}_{j}\ ,\ \mathbf{H}_{ij}=\mathbf{P}_{i}^{T}\mathbf{Q}_{ij}\mathbf{K}_{s}\mathbf{Q}_{ij}^{T}\mathbf{P}_{j} \tag{4.20-22}$$

The classical Hamilton's principle is now used

$$\int_{t_1}^{t_2}\delta\left(\mathbf{V}-\mathbf{T}\right)dt=0 \tag{4.23}$$

Substituting Eqs. (4.13-22) into Eq. (4.23) and minimizing the Hamilton's function with respect to the Fourier coefficients $A_{mn}^{w}, A_{mn}^{u}, A_{mn}^{v}, \cdots, e_{m}^{l}$, and f_{n}^{l} yield the characteristic equations

$$\left\{\mathbf{K}-\omega^{2}\mathbf{M}\right\}\mathbf{\Phi}=\mathbf{0} \tag{4.24}$$

where $\mathbf{K}$ is the system stiffness matrix having the form

$$\mathbf{K}=\begin{bmatrix}\mathbf{K}_{11} & \cdots & \mathbf{K}_{1i} & \cdots & \mathbf{K}_{1j} & \cdots \\ & \ddots & \vdots & \vdots & \vdots & \cdots \\ & & \mathbf{K}_{ii} & \vdots & \mathbf{K}_{ij} & \cdots \\ & & & \ddots & \vdots & \cdots \\ & \mathit{Symm} & & & \mathbf{K}_{jj} & \cdots \\ & & & & & \ddots \end{bmatrix} \tag{4.25}$$

where $\mathbf{K}_{ii}$ and $\mathbf{K}_{jj}$ stand for the stiffness matrix of the *i*-th and the *j*-th plates, respectively; and $\mathbf{K}_{ij}$ represents the cross coupling stiffness matrix between the *i*-th and the *j*-th plates. In particular, $\mathbf{K}_{ii}$ can be written as a summation

$$\mathbf{K}_{ii}=\mathbf{K}_{ii}^{0}+\mathbf{K}_{ii}^{c} \tag{4.26}$$

where $\mathbf{K}_{ii}^{0}$ and $\mathbf{K}_{ii}^{c}$ denote contributions from the plate itself and the coupling between plates, respectively.

The system mass matrix $\mathbf{M}$ is written in the form

$$\mathbf{M} = diag\begin{bmatrix}\mathbf{M}_1 & \cdots & \mathbf{M}_i & \cdots\end{bmatrix} \tag{4.27}$$

where $\mathbf{M}_i$ is the mass matrix of the *i*-th plate.

The stiffness and mass matrices $\mathbf{K}_{ii}^{0}$ and $\mathbf{M}_i$ of the individual plate can be found in paper (Du *et al.*, 2010). Therefore, a detailed description is not presented here. The expressions for other matrices are given in Appendix C.

The coefficient vector $\mathbf{\Phi}$ in Eq. (4.24) is defined as

$$\mathbf{\Phi} = \begin{Bmatrix}\mathbf{\Phi}_{w_1} & \mathbf{\Phi}_{u_1} & \mathbf{\Phi}_{v_1} & \cdots & \mathbf{\Phi}_{w_i} & \mathbf{\Phi}_{u_i} & \mathbf{\Phi}_{v_i} & \cdots\end{Bmatrix} \tag{4.28}$$

where subscripts w_i , u_i and v_i indicate a quantity related to the displacement types of the *i*-th plate, respectively. The component vectors in Eq. (4.28) are defined as

$$\begin{aligned}\mathbf{\Phi}_{w_i} = \{& A_{i,00}^{w}, A_{i,01}^{w}, \cdots, A_{i,m0}^{w}, A_{i,m1}^{w}, \cdots, A_{i,m'n'}^{w}, \cdots, A_{i,MN}^{w}, a_{i,0}^{1} \cdots, a_{i,M}^{1}, a_{i,0}^{2} \cdots, a_{i,M}^{2}, \\ & a_{i,0}^{3} \cdots, a_{i,M}^{3}, a_{i,0}^{4} \cdots, a_{i,M}^{4}, b_{i,0}^{1} \cdots, b_{i,N}^{1}, b_{i,0}^{2} \cdots, b_{i,N}^{2}, b_{i,0}^{3}, \cdots, b_{i,N}^{3}, b_{i,0}^{4}, \cdots, b_{i,N}^{4} \}\end{aligned} \tag{4.29}$$

$$\begin{aligned}\mathbf{\Phi}_{u_i} = \{& A_{i,00}^{u}, A_{i,01}^{u}, \cdots, A_{i,m0}^{u}, A_{i,m1}^{u}, \cdots, A_{i,m'n'}^{u}, \cdots, A_{i,MN}^{u}, e_{i,0}^{1} \cdots, e_{i,M}^{1}, e_{i,0}^{2} \cdots, e_{i,M}^{2}, \\ & f_{i,0}^{1} \cdots, f_{i,M}^{1}, f_{i,0}^{2} \cdots, f_{i,M}^{2} \}\end{aligned} \tag{4.30}$$

$$\begin{aligned}\mathbf{\Phi}_{v_i} = \{& A_{i,00}^{v}, A_{i,01}^{v}, \cdots, A_{i,m0}^{v}, A_{i,m1}^{v}, \cdots, A_{i,m'n'}^{v}, \cdots, A_{i,MN}^{v}, g_{i,0}^{1} \cdots, g_{i,M}^{1}, g_{i,0}^{2} \cdots, g_{i,M}^{2}, \\ & h_{i,0}^{1} \cdots, h_{i,M}^{1}, h_{i,0}^{2} \cdots, h_{i,M}^{2} \}\end{aligned} \tag{4.31}$$

The solution of the characteristic Eq. (4.24) will yield the natural frequencies and the eigenvectors. For a given natural frequency, the corresponding eigenvector actually contains all the Fourier coefficients that can be subsequently used to construct the mode shape according to Eqs. (4.4-6). Although this study is only focused on the free vibration of a built-up plate structure, the response of the system to an applied load can be easily considered by simply including the work done by this load in the Lagrangian, which eventually leads to a force term on the right side of Eq. (4.23). Once the displacements are determined for each plate, other quantities of interest can be calculated directly through the appropriate mathematical operations on the analytical form of solutions.

4.3. Results and discussions

4.3.1. Numerical calculation

The free vibration of open and closed boxes, which were previously studied by Dickinson and Warburton (1967), will be used as examples here. The physical and material properties of the box-type structure adopted in the numerical simulations are taken from Dickinson's paper. The overall dimensions of the box are $9.6 \times 12.0 \times 14.4$ in. The open box is essentially the same as the closed one but with the 14.4×9.6 in face removed. All the plates constituting the box have the same thickness $h = 0.125$ in and are made of the same material: $E = 30 \times 10^6$ lbf/in^2, ρ = 0.284 lbf/in^3, and $\mu = 0.3$.

The box-type structure is divided into individual plates, and each plate has its own local coordinate, as illustrated in Fig. 4.4. In the numerical simulations, all coupling joints between plates are assumed to be rigid by setting the stiffness for coupling springs to a very large number. Several different boundary conditions will be considered by adjusting the values of the boundary spring stiffness accordingly. While the stiffness matrix of each constituent plate is calculated under its local coordinate, cross coupling terms between each set of plates are calculated in a global coordinate. Finally, the system stiffness matrix is achieved by assembling these stiffness matrices in a way analogous to that of the FEA. After the convergence and accuracy of the solution are verified numerically, the series expansions will be simply truncated to $M=N=7$ in all the subsequent calculations.

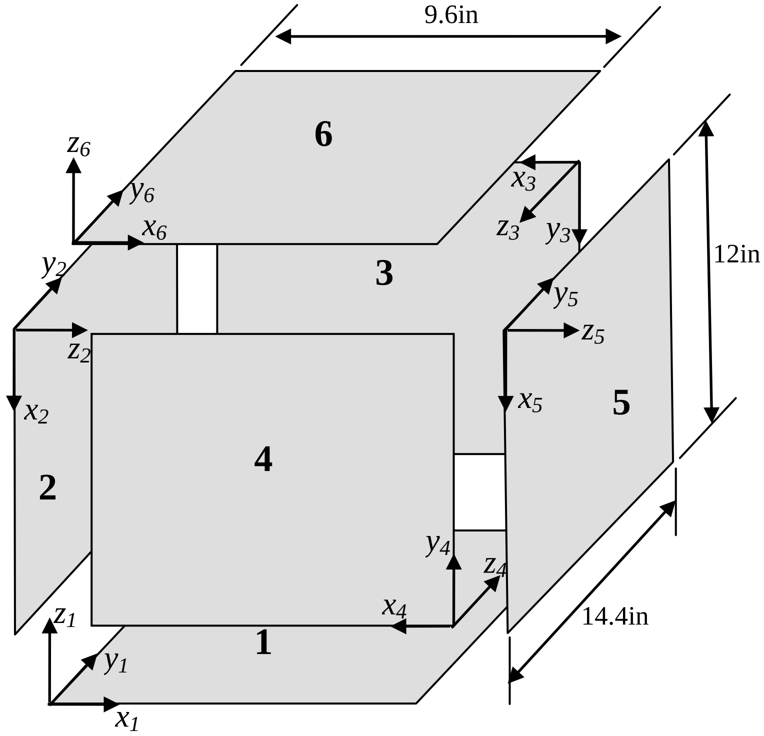

Figure 4.4 Schematic of a box-type structure

4.3.2 Experimental testing

In order to verify the proposed solution, a 5-plate open box was built with the same specs as that used in the numerical simulations, as shown in Fig. 4.5. Due to the unavailability of the original material used in Dickinson's paper, a similar flat mild steel plate (AISI 1018 cold rolled) of 0.125in thickness was chosen for the test structure. This type of material has Young's modulus $E = 29.7 \times 10^6$ lbf/in^2, mass density $\rho = 0.284$ lbf/in^3 and Poisson ratio $\mu = 0.29$, which are slightly different from those specified used by Dickinson (1967). The plates were seamlessly welded together. The box was transversely excited by an impact hammer (PCB086C01), and the flexural vibration was measured using a uni-axial accelerometer (B&K4508). The excitation location was slightly moved away from the center of plate 5, and the accelerometer was placed at various locations on the box surfaces. The natural frequencies were identified as the distinct sharp peaks of the frequency response functions (FRF). Mode shape measurements were carried out by manually roving the accelerometer over uniformly spaced grids of over uniformly-spaced grids of 11×11 on plates 2 and 5, and 7×11 on plates 1, 3 and 4, for a total 473 points. A free boundary condition was used in the testing by suspending the box with soft rubber bands.

Figure 4.5 Experimental setup for the modal testing of a box-type structure

4.3.3 A 5-plate open box structure

In order to examine the accuracy of the present solution, we will first consider an open box with all common edges simply supported along the flexural direction, for which an analytical solution is available (Dickinson & Warburton, 1967). Table 4.1 shows the first 17 natural frequencies, and it can be seen that the present results agree very well with those predicted by Dickinson (1967). A close agreement (a maximum relative error within 5%) was also observed between the theoretical and experimental results given by Dickinson (1967).

The first eight modes are shown in Fig. 4.6.

Table 4.1 Natural frequencies (Hz) of an open box with common edges simply supported

Mode	Natural frequencies (Hz)			Difference (%)	
1	94.15 [a]	94 [b]	99[c]	-0.16 [f]	4.90 [g]
2	113.39	113	115	-0.35	1.40
3	190.04	190	194	-0.02	2.04
4	219.19	219	222	-0.09	1.27
5	235.69	234	239	-0.72	1.38
6	246.55	246	246	-0.22	-0.22
7	286.72	287	285	0.10	-0.60
8	297.82	298	289	0.06	-3.05
9	341.83	341	337	-0.24	-1.43
10	349.29	348	346	-0.37	-0.95
11	371.42	370	372	-0.38	0.16
12	432.98	433	434	0.00	0.24
13	451.39	451	454	-0.09	0.57
14	505.85	504	497	-0.37	-1.78
15	521.71	522	527	0.06	1.00
16	536.13	537	560	0.16	4.26
17	551.79	----	----	----	----

[a] Results from present approach,

[b] Results from theoretical predictions of Ref. [Dickinson,1967],

[c] Results from experiment in Ref. [Dickinson,1967],

[d] Results from current experiment,

[e] Results from ANSYS,

[f] Results between present approach and the theoretical prediction in Ref. [Dickinson,1967],

[g] Results between present approach and experiment in Ref. [Dickinson,1967],

[h] Results between present approach and experiment,

[i] Results between present approach and ANSYS,

The percentage difference in the table is defined as:
Difference = (reference value – present value) / reference value × 100%

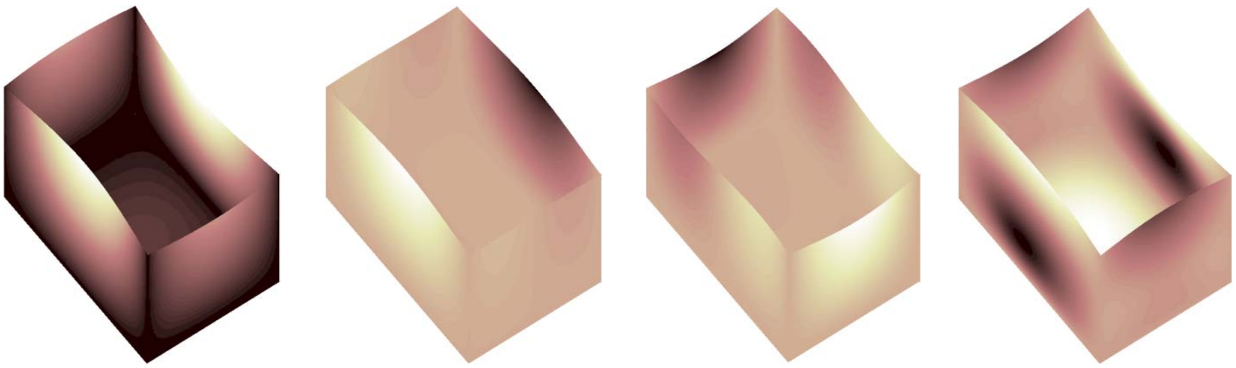

(a) (b) (c) (d)

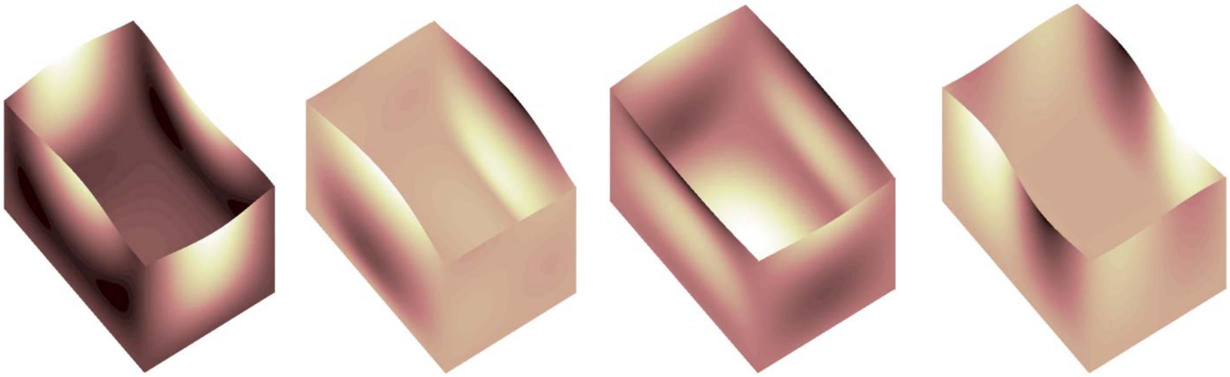

(e) (f) (g) (h)

Figure 4.6 Mode shapes for an open box with common edges simply supported: (a) 1st mode; (b) 2nd mode; (c) 3rd mode; (d) 4th mode; (e) 5th mode; (f) 6th mode; (g) 7th mode; (h) 8th mode

The second example concerns a free open box. Table 4.2 shows a comparison of the results obtained from various means. The FEA results are calculated using an ANSYS model with 40×40 SHELL63 elements for each plate. This type of element has four nodes each having six degrees of freedom.

Table 4.2 Natural frequencies (Hz) of a free open box

Mode	Natural frequencies (Hz)				Difference (%)		
1	55.46[a]	59[c]	66[d]	55.51[e]	6.00[g]	15.97[h]	0.09[i]
2	93.840	99	95	94.09	5.21	1.22	0.27
3	140.23	146	147	140.64	3.95	4.61	0.29
4	207.51	217	203	208.19	4.37	-2.22	0.33
5	221.68	228	210	222.03	2.77	-5.56	0.16
6	234.61	240	235	235.52	2.25	0.17	0.39
7	258.16	261	249	258.52	1.09	-3.68	0.14
8	295.50	306	273	295.91	3.43	-8.24	0.14
9	326.11	337	330	327.52	3.23	1.18	0.43
10	346.49	352	344	348.18	1.57	-0.72	0.49
11	358.38	360	353	360.05	0.45	-1.52	0.46
12	369.50	375	400	371.10	1.47	7.63	0.43
13	437.58	448	448	438.85	2.33	2.33	0.29
14	452.07	459	----	453.73	1.51	----	0.37
15	504.43	504	485	506.05	-0.09	-4.01	0.32
16	529.00	545	527	529.35	2.94	-0.38	0.07
17	544.80	565	545	547.41	3.58	0.04	0.48

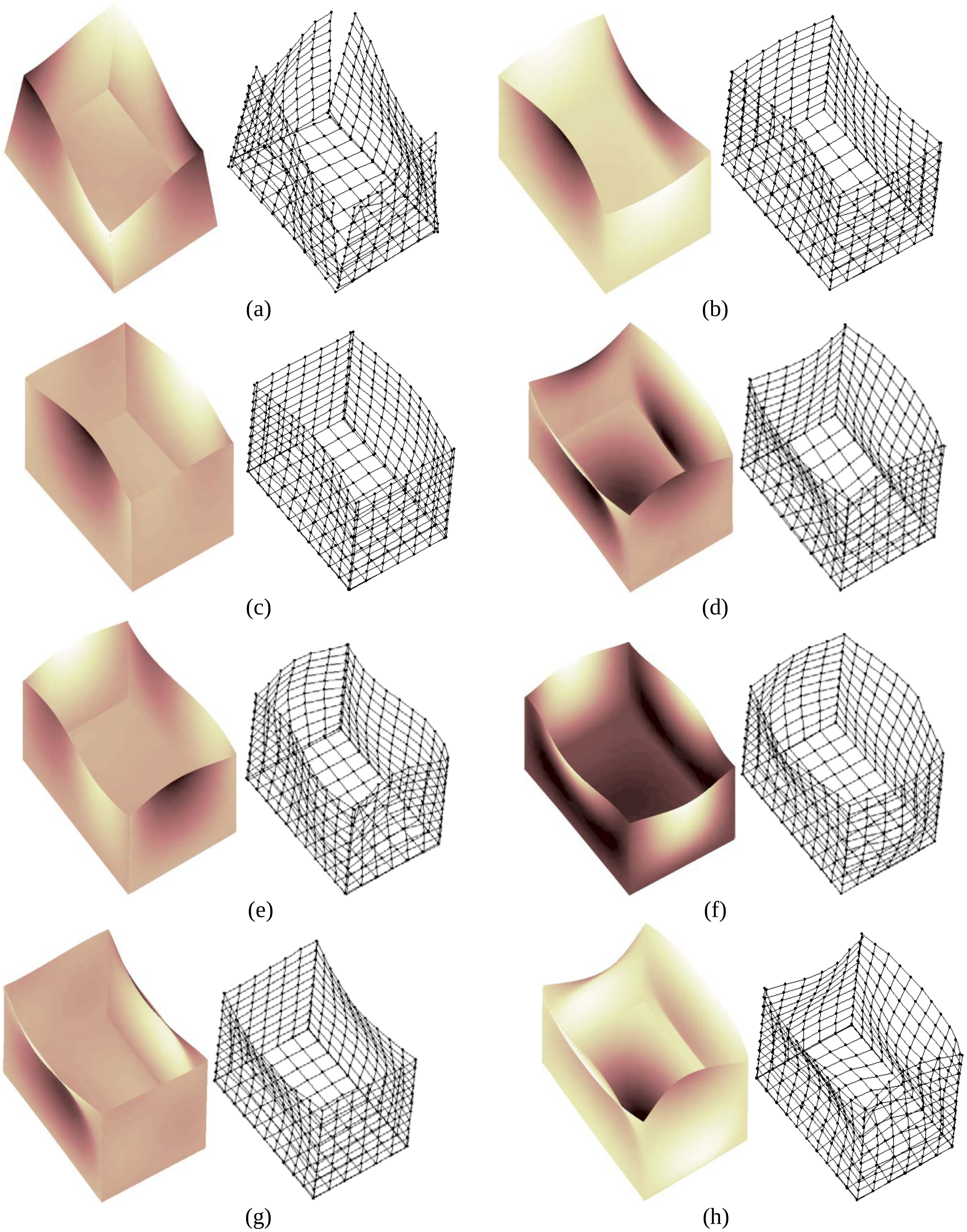

(a) (b) (c) (d) (e) (f) (g) (h)

Figure 4.7 Mode shapes for a free open box: (a) 1st mode; (b) 2nd mode; (c) 3rd mode; (d) 4th mode; (e) 5th mode; (f) 6th mode; (g) 7th mode; (h) 8th mode

The results given in Table 4.2 show a good comparison (a maximum relative difference within 0.5%) between the present and FEA models. A decent agreement is also observed between the current analytical and experimental results.

Table 4.3 Natural frequencies (Hz) of an open box with different boundary conditions

	Natural frequencies (Hz)				Difference (%)	
Mode	CCCC		CSFF		CCCC	CSFF
1	199.46[a]	199.23[e]	111.50[a]	110.44[e]	-0.12[i]	-0.96[i]
2	218.25	218.68	204.22	203.27	0.20	-0.47
3	271.01	271.04	221.50	218.89	0.01	-1.19
4	293.52	293.98	239.17	237.73	0.16	-0.61
5	332.16	332.24	265.93	264.83	0.02	-0.42
6	391.19	391.56	300.64	298.40	0.09	-0.75
7	406.63	406.98	328.50	327.34	0.09	-0.35
8	469.31	469.65	364.39	360.64	0.07	-1.04
9	494.74	497.99	400.03	400.06	0.65	0.01
10	529.23	528.52	432.87	436.56	-0.13	0.85
11	600.17	601.89	473.16	478.86	0.29	1.19
12	601.50	602.77	482.89	484.62	0.21	0.36
13	622.80	626.02	531.38	529.86	0.51	-0.29
14	679.03	678.37	543.13	553.11	-0.10	1.80
15	704.94	705.59	558.53	562.23	0.09	0.66
16	715.63	717.64	601.92	603.32	0.28	0.23
17	721.04	720.06	629.27	639.58	-0.14	1.61

It is evident from Table 4.2 that Dickinson's experiment tends to give a higher estimate of the natural frequencies. This is probably caused by some subtle differences in the boundary conditions and material properties of the test structure. In Dickinson's experiment, he placed the box on foam plastic pads to simulate an effectively "free" boundary condition. Nowadays, a free boundary condition was typically simulated by suspending the box with soft rubber bands. As mentioned earlier, both Young's modulus and the Poisson ratio of the material used in the present experiment are slightly smaller than those of the material used by Dickinson. The first eight flexible natural modes are plotted in Fig. 4.7 and their experimental counterparts are also

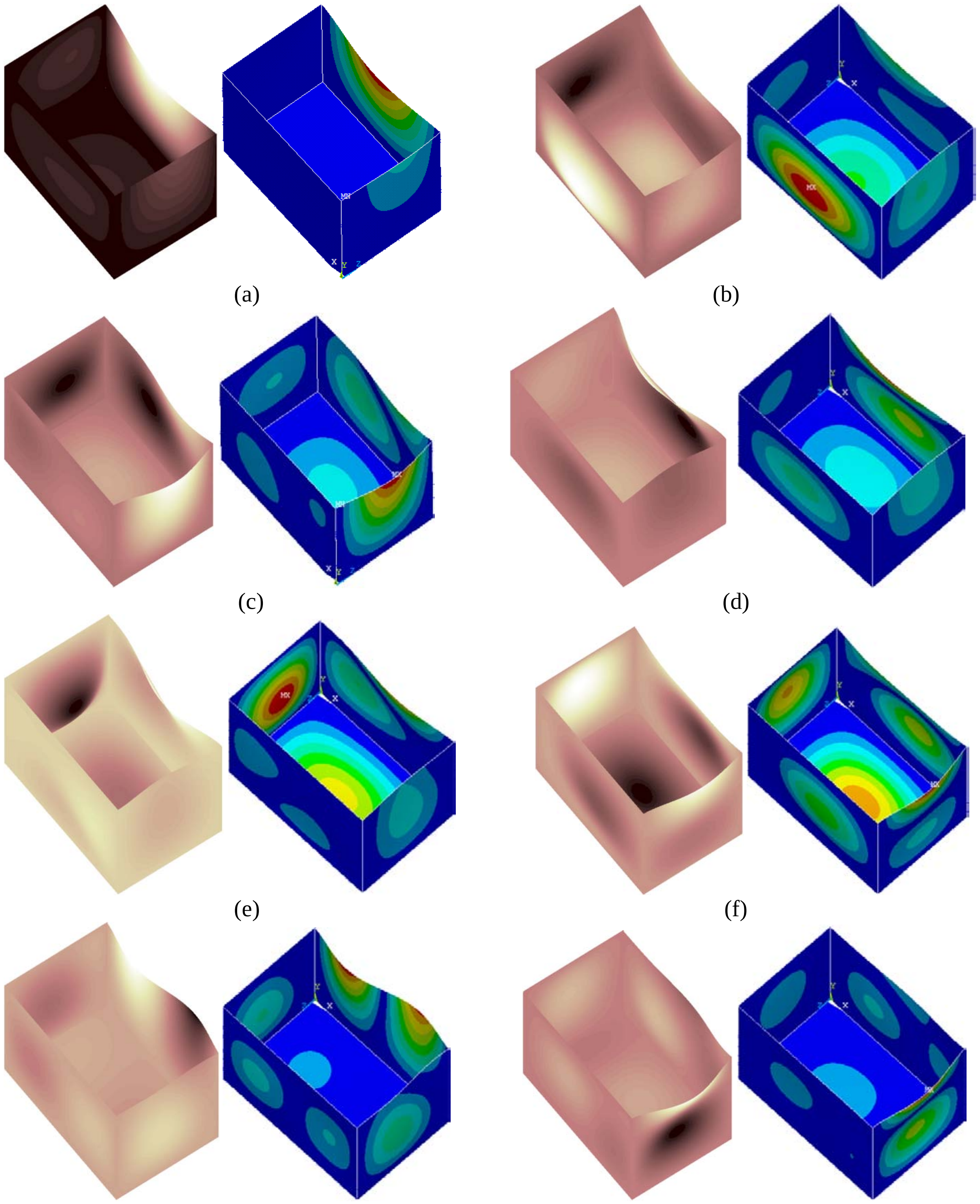

(a) (b)

(c) (d)

(e) (f)

(g) (h)

Figure 4.8 The mode shapes for a CSFF open box: (a) 1st mode; (b) 2nd mode; (c) 3rd mode; (d) 4th mode; (e) 5th mode; (f) 6th mode; (g) 7th mode; (h) 8th mode

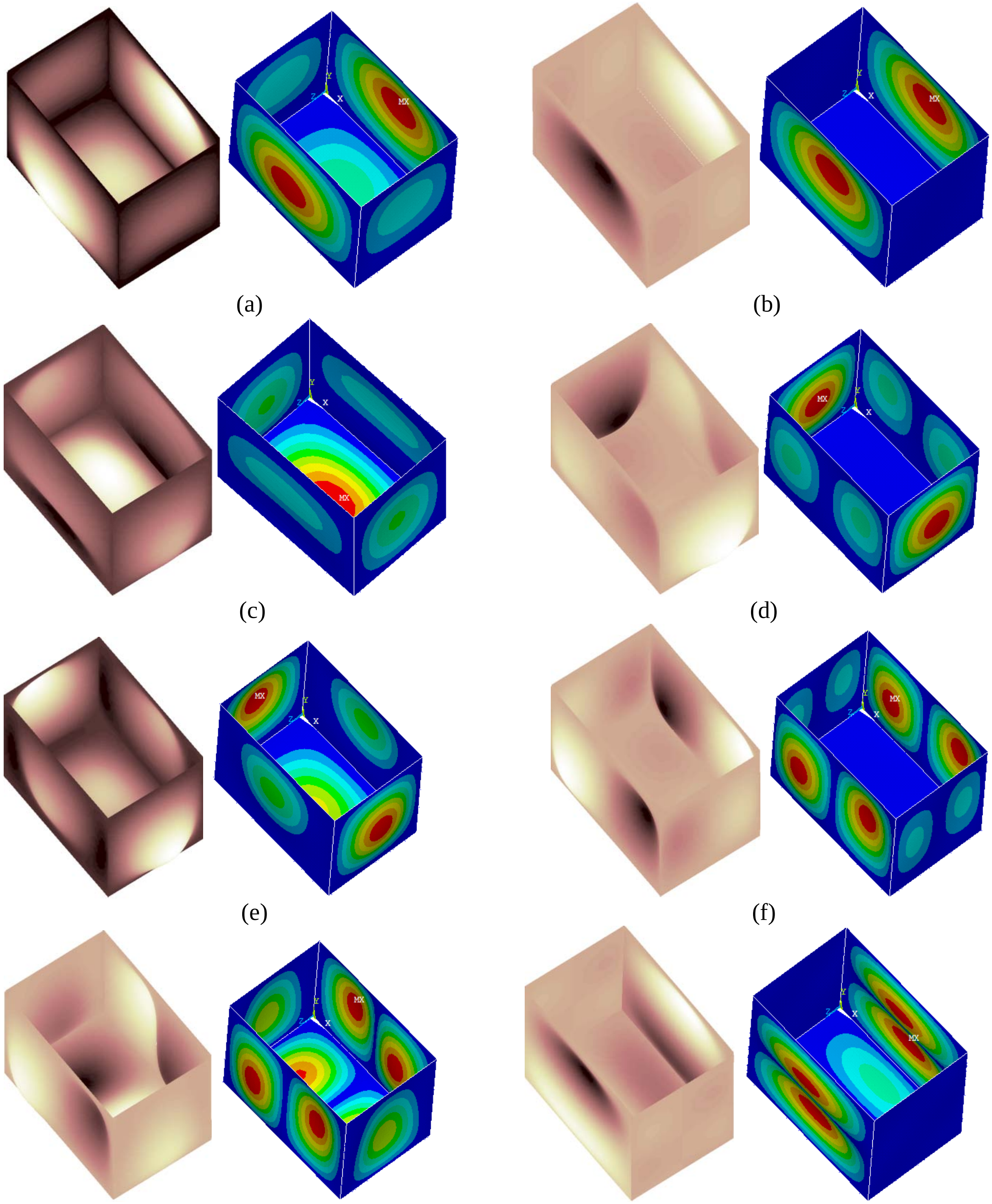

(a) (b)

(c) (d)

(e) (f)

(g) (h)

Figure 4.9 The mode shapes for a CCCC open box: (a) 1st mode; (b) 2nd mode; (c) 3rd mode; (d) 4th mode; (e) 5th mode; (f) 6th mode; (g) 7th mode; (h) 8th mode shown there as a comparison. There is a good match between the theoretical and experimental plots.

In the next example, we study the effect of restraining the free edges of the open box. The boundary conditions for the free edges are defined with respect to the local coordinates and described by four capital letters; for instance, CSFF represents the box clamped at $x_5 = 0,$ simply supported at $y_3 = 0$, free at $x_2 = 0$ and at $y_4 = b_4$ (refer to Fig. 4.4). The simply supported boundary condition is only applied on the flexural vibration rather than the in-plane vibration. Nevertheless, the clamped boundary condition refers to a configuration in which the clamped condition is applied to the flexural vibration and simply supported condition the in-plane vibrations (Du *et al*., 2007). The calculated results are listed in Table 4.3 for two boundary conditions, CCCC and CSFF. Since these configurations were never studied before, only FEA results are included there for comparison. An excellent agreement is observed between these two sets of results. It should be pointed out that unlike the other analytical techniques the current method does not involve any modifications to the solution procedures or formulations in dealing with different boundary conditions; modifying boundary conditions is as simple as changing the material or geometrical parameters. The mode shapes corresponding to two boundary conditions are depicted in Figs. 4.8 and 4.9, respectively.

4.3.4 A 6-plate closed box structure

The first scenario of the boundary conditions of a closed box is identical to those specified by Dickinson (1967), for which it is assumed that the base is effectively simply supported and the remaining edges of the box are free to rotate but not move in translation. This type of boundary conditions was simulated by using socket head screws to fix the box at each corner in Dickinson’s study (1967). The natural frequencies calculated using the current method are presented in Table 4.4 together with those theoretically and experimentally obtained by Dickinson. These three sets of results match satisfactorily with each other.

Table 4.4 Natural frequencies (Hz) of a closed box with common edges simply supported

Mode	Natural frequencies (Hz)			Difference (%)	
1	179.03 [a]	179 [b]	177 [c]	-0.02 [f]	-1.15 [g]
2	202.51	203	194	0.24	-4.39
3	257.09	258	247	0.35	-4.09
4	271.74	272	269	0.09	-1.02
5	282.88	283	----	0.04	----
6	332.42	333	329	0.17	-1.04
7	383.03	384	----	0.25	----
8	396.16	397	390	0.21	-1.58
9	435.76	437	425	0.28	-2.53
10	453.56	455	476	0.32	4.71
11	485.08	486	488	0.19	0.60
12	497.55	499	499	0.29	0.29
13	568.77	570	563	0.22	-1.02
14	575.20	577	580	0.31	0.83
15	622.53	624	----	0.24	----
16	646.92	648	643	0.17	-0.61
17	672.34	----	----	----	----

The last example concerns a free closed box. Table 4.5 shows the results obtained from the current method, Dickinson’s measurement and a FEA model. Again, a good comparison is seen among the three sets of data. The first eight mode shapes are plotted in Fig. 4.10. Although the mode shapes for the first scenario are not shown here to save space, it suffices to say that a similar level of agreement was also achieved.

By comparing Tables 4.4 and 4.5, one may find that the natural frequencies of a free closed box tend to be higher than those of a closed box for the boundary conditions defined by Dickinson (1967). This phenomenon indicates that for a closed box, imposing additional constraints on its edges does not necessarily produce higher natural frequencies. When the box is simply supported along each edge of the constituent plates, the in-plane motion of the plate is effectively eliminated leading to a “decoupling” between the transverse and in-plane displacements.

Table 4.5 Natural frequencies (Hz) of a free closed box

Mode	Natural frequencies (Hz)			Difference (%)	
1	178.74[a]	178[c]	178.59[e]	-0.42 [g]	-0.08[i]
2	230.60	228	230.32	-1.14	-0.12
3	269.50	264	270.92	-2.08	0.52
4	281.07	282	281.98	0.33	0.32
5	302.78	297	302.29	-1.95	-0.16
6	330.97	328	331.58	-0.91	0.18
7	398.67	395	398.25	-0.93	-0.11
8	400.34	399	399.58	-0.34	-0.19
9	452.26	451	450.95	-0.28	-0.29
10	475.54	479	473.97	0.72	-0.33
11	485.59	495	486.08	1.90	0.10
12	499.18	497	499.04	-0.44	-0.03
13	567.78	571	566.46	0.56	-0.23
14	577.72	580	576.83	0.39	-0.15
15	625.82	634	625.86	1.29	0.01
16	645.30	643	642.44	-0.36	-0.45
17	659.75	----	672.21	----	1.85

On the other hand, the out- and in-plane motions become fully coupled via the common edge between each pair of adjacent plates for a free box, which induces higher order in-plane modes interacting with lower flexural modes. As a result, the corresponding natural frequencies are raised slightly for a free box.

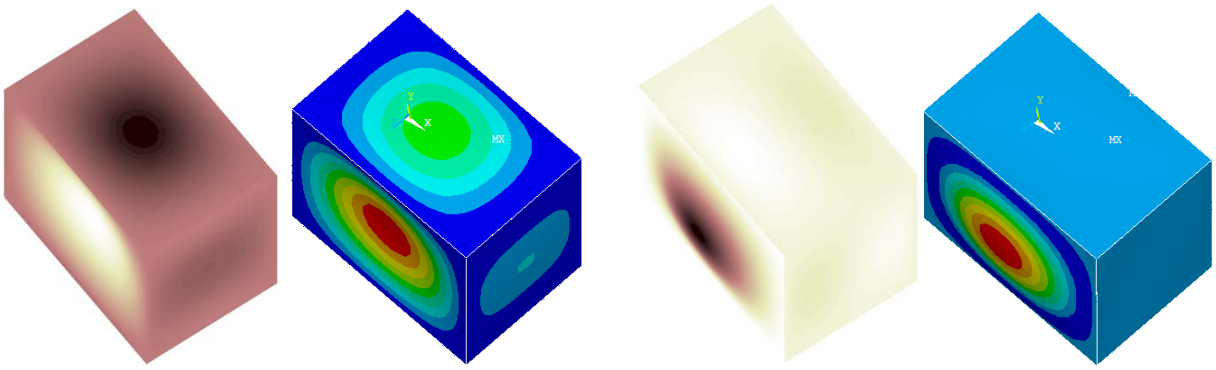

(a)

(b)

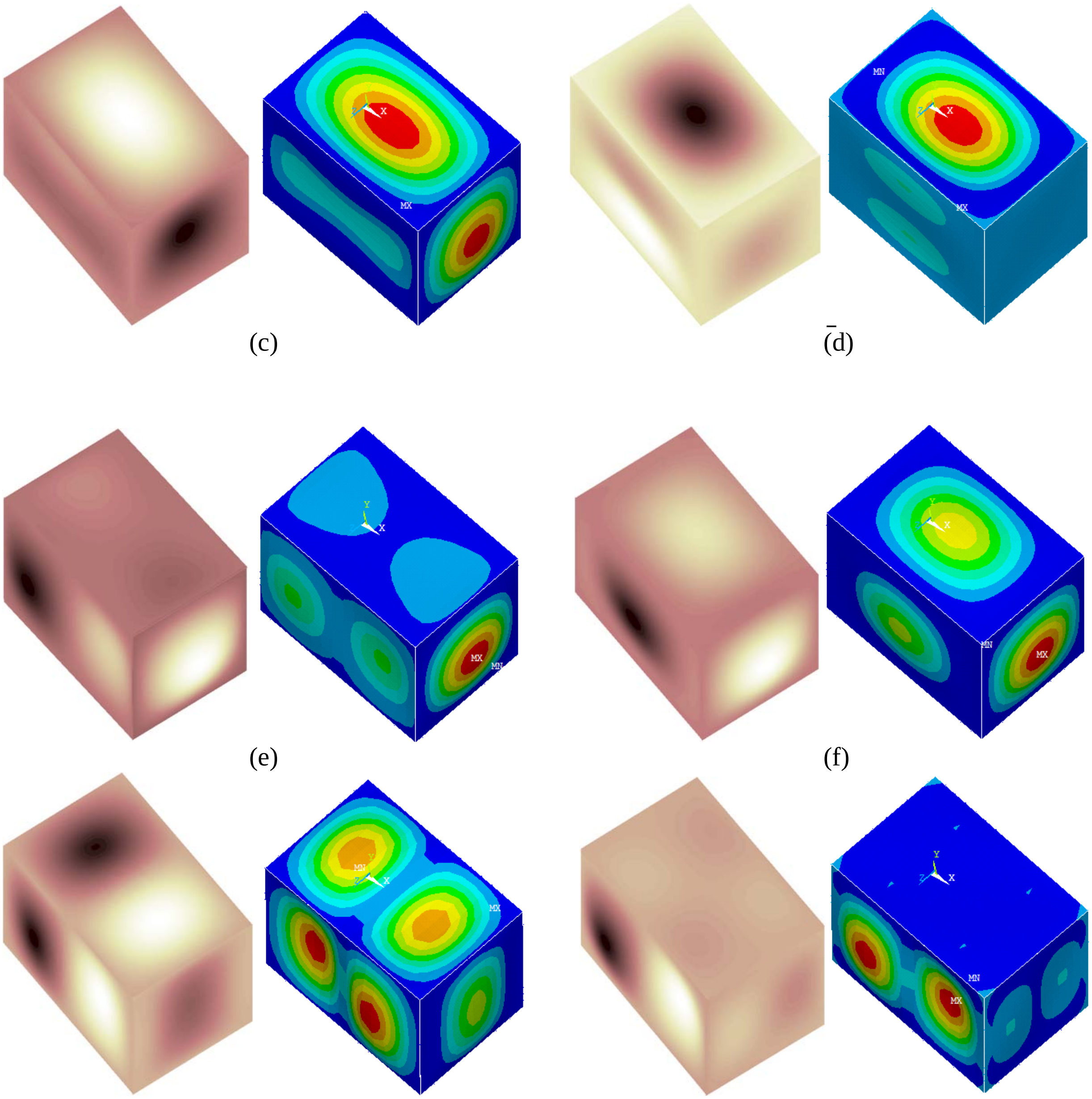

(c) (d)

(e) (f)

(g) (h)

Figure 4.10 The mode shapes for a free closed box: (a) 1st mode; (b) 2nd mode; (c) 3rd mode; (d) 4th mode; (e) 5th mode; (f) 6th mode; (g) 7th mode; (h) 8th mode

4.4 Energy distributions of a closed box structure

The strain energy of any area on the *i*-th plate can be obtained by rewriting Eq. (4.15)

$$\mathbf{V}_{i,S} = \frac{D_i}{2}\int_S \left[\frac{\partial^2 W_i}{\partial x^2} + \frac{\partial^2 W_i}{\partial y^2} + 2\mu \frac{\partial^2 W_i}{\partial x^2}\frac{\partial^2 W_i}{\partial y^2} + 2(1-\mu)\left(\frac{\partial^2 W_i}{\partial x \partial y} \right)^2 \right] dS$$

$$+ \frac{G_i}{2}\int_S \left[\left(\frac{\partial U_i}{\partial x} + \frac{\partial V_i}{\partial y} \right)^2 - 2(1-\mu)\frac{\partial U_i}{\partial x}\frac{\partial V_i}{\partial y} + \frac{(1-\mu)}{2}\left(\frac{\partial U_i}{\partial x} + \frac{\partial V_i}{\partial x} \right)^2 \right] dS \qquad (4.32)$$

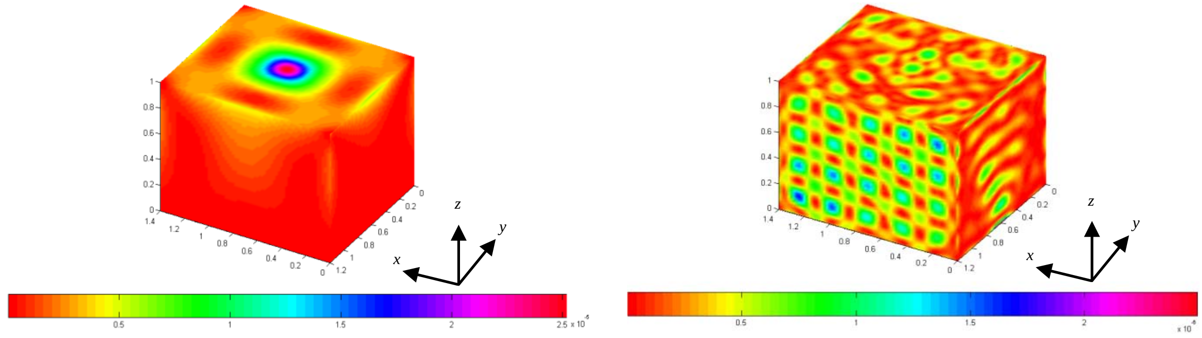

(a) (b)

Figure 4.11 The strain energy distribution for a free closed box subjected to a unit force on the top surface at (0.5a, 0.5b): (a) 15Hz; (b) 300Hz

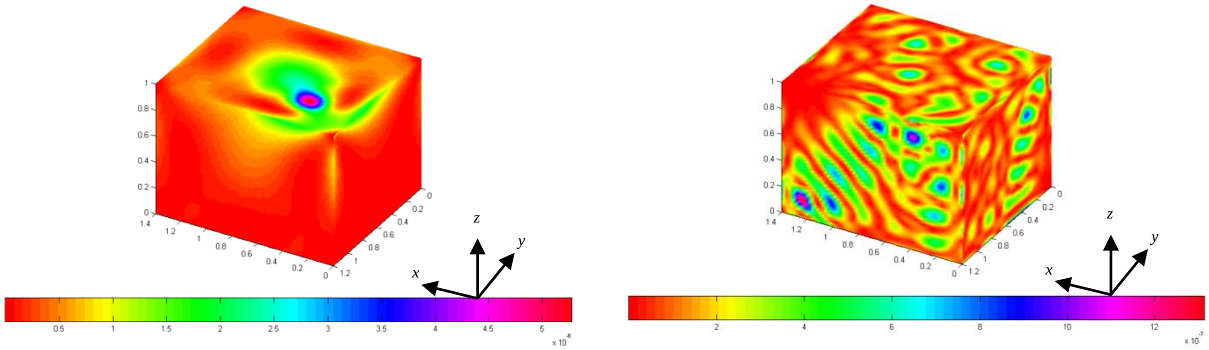

(a) (b)

Figure 4.12 The strain energy distribution for a free closed box subjected to a unit force on the top surface at (0.25a, 0.25b): (a) 15Hz; (b) 300Hz

As an example, consider a box with dimensions 1.4×1.2×1.0 m. It is made of steel with material properties: E = 207GPa, $\rho = 7800\text{kg/m}^3$ and $\mu = 0.29$. The thickness for all constituent plates is h = 0.008m. Suppose a unit force is applied on the top side of the box at two different locations (0.5*a*, 0.5*b*) and (0.25*a*, 0.25*b*), Figs. 4.11 and 4.12 plot the strain energy distributions for the two exciting locations, respectively. The strain energy distribution is shown to be strongly dependent on the frequency among other factors.

4.5 Conclusions

A general solution using FSEM is developed for vibrations of the built-up plate assemblies. In this solution, a plate assembly is divided into a number of individual plates. The Rayleigh-Ritz method is used to derive the final system stiffness matrix and solve for the responses of the plate system. Particularly, the boundary conditions and compatibility conditions are all faithfully enforced as in the actual system environment, rather than somehow approximated or assumed like in many, if not all, other techniques.

Numerical examples involving open and closed box structures are presented for several different boundary conditions. Excellent agreements are repeatedly shown between the current solution and other techniques including FEA and experimental testing. By removing the restriction that at least two opposite edges are simply-supported for each plate in a plate structure, the current method can be effectively applied to many real-world structures under various boundary and coupling conditions.

CHAPTER V

VIBRATION AND POWER FLOW ANALYSIS OF BEAM–PLATE SYSTEMS

5.1 Free vibration of stiffened plates

5.1.1 Introduction

Plates reinforced by beams or ribs represent a class of structural components which are widely used in many applications such as hull decks, bridges, land and space vehicles, and buildings. Reinforcement schemes are often of direct interest in structural designs. The vibrations of stiffened plates have been extensively studied using various analytical and numerical techniques, as comprehensively reviewed in refs. (Mukherjee & Mukhopadhyay, 1986; Mukhopadhyay & Mukherjee, 1989; Liew *et al*., 1995).

Orthotropic plate and grillage approximations are two common models used in the early literature (Mukhopadhyay & Mukherjee, 1989). While the former treats the stiffened plate as an equivalent orthotropic plate by smearing the stiffeners into the plate, the latter approximates the stiffeners as a grid attached to the plate. Other approaches, such as, wave propagation approaches (Cremer & Heckl, 1972; Heckl, 1961; Maidanik, 1962; Langley & Heron; Zalizniak *et al*., 1991), transfer matrix methods (McDaniel & Henderson, 1974), Rayleigh-Ritz methods (Liew, *et al*., 1994), and the finite difference methods (Asku & Ali, 1976; Cox & Bernfield, 1959), have also been developed to investigate various aspects of vibrations of stiffened plates.

Although the FEM is capable of predicting the vibrations of complex structures with fairly good accuracy, its deficiencies also become evident which include, for example, a requirement of the perfect match between the 2-D mesh for a plate and a number of 1-D meshes for beams. These problems have prompted researchers to seek alternative approaches for the vibration analysis of stiffened plates. Dozio and Ricciardi (2009) proposed a combined analytical-numerical method to predict the eigenpairs of rib-stiffened plates. In their study, the assumed modes method is used to derive the equations of motions of the plate and the rib separately, leading to the sparse stiffness and mass matrices. The differential quadrature method was utilized by Zeng and Bert (2001) for studying the free vibration of eccentrically stiffened plates. In order to avoid the FEM difficulties encountered in the meshing process, Peng *et al.* (2006) employed a mesh-free Galerkin method for the free vibration and stability analysis of stiffened plates. Because there is no mesh used in this method, the stiffeners can be placed anywhere on the plate. A hybrid formulation from combing the conventional FEA with Energy FEA (EFEA) was presented by Hong *et al.* (2006) in studying flexible vibrations of plates with spot-welded stiffening beams. The flexible plate and stiffening beams are modeled by the EFEA and conventional FEA, respectively.

In recent studies, a plate and its stiffeners are often treated as separate elements, and the interaction forces in the governing equations are determined from the compatibility conditions on the interfaces. The connections between the plate and stiffeners are typically viewed as rigid coupling to easily satisfy the continuity conditions (Liew, *et al*., 1994; Chiba & Yoshida, 1996; Cox & Bernfield, 1959; Dozio & Ricciardi, 2009; Zeng & Bert, 2001; Peng *et al*., 2006). However, this simple treatment is not always appropriate in real-world applications. In practice, the stiffeners are often spot-welded or fixed to a plate through screws, rivets, and so on. Therefore, the coupling conditions between the plate and stiffeners are not known exactly. This uncertainty may be one of the causes for scattering of vibrational responses. To better model the coupling conditions, Zalizniak *et al.* (1991) and Arruda *et al*. (2007) treated the plate-beam connections as elastic joints in their studies of the wave transmissions between plate and beams.

Various aspects of the reinforcing arrangements have been studied by many researchers (Nair & Rao, 1984; Xu *et al.*, 2005; Ouisse & Guyader, 2003; Shastry & Venkateswara, 1977) in terms of their impacts on the dynamic characteristics of the resulting plate-beam systems. For example, Liew *et al.* (1994), and Wu and Liu (1988) investigated how the natural frequencies of the combined structure will be affected by the aspect ratio of the plate and the properties of the stiffeners. The torsional vibrations of the stiffeners were taken into account in ref. (Liew *et al.*, 1994). Bhat (1982) studied the effects of non-uniform stiffener spacing. Using FEM models, Nair and Rao (1984) examined the impact on the natural frequencies of the length of a stiffener. Although reinforcing beams are typically placed evenly in a parallel or orthogonal pattern in most cases, the orientations of stiffeners are found to play an important role in affecting the response of and power flows in the composite system (Xu *et al.*, 2005). Ouisse and Guyader (2003) investigated the influence of beam placement angle on the dynamic behavior of the coupled systems. Using the finite element method, Shastry and Venkateswara (1977) examined the fundamental frequencies of rectangular plates for several different orientation arrangements of stiffeners. Other approaches were also used to investigate the structural characteristics of stiffened plates (Sheikh & Mukhopadhyay, 1993; Barik & Mukhopadhyay, 1999; Marcelin, 2006; Ojeda *et al.*, 2005).

Although the vibrations of stiffened plates have been extensively studied for decades, most of the reported investigations are based on the condition that plates are simply supported along, at least, a pair of opposite edges. In comparison, there is little attention paid to the vibrations of stiffened plates under other boundary conditions and/or non-rigid coupling conditions between a plate and beams. The investigation in this chapter aims at filling these analytical gaps and understanding the effects on the modal properties of various (plate and beam) support conditions, general coupling conditions, and reinforcing arrangements with respect to the number, orientations, and lengths of attached beams.

5.1.2 Theoretical formulations

Fig. 5.1 shows a rectangular plate reinforced by a number of stiffeners (or beams) with arbitrary placement angles (only one stiffener is shown in Fig. 5.1 for clarity). The vibrations of both the plate and stiffeners are generally considered as three-dimensional: the plate has three independent (one transverse and two in-plane) displacements, and each of the stiffeners has four independent (one axial, one rotational and two transverse) displacements. The plate with length a, width b and thickness h is assumed to lie in the x-y plane. The boundary conditions for the plate are generally specified, along each edge, as elastic restraints which are described in terms of 4 sets of uniformly distributed springs of arbitrary stiffnesses (refer to Fig. 5.1).

Suppose a beam with length L_b, width w and thickness t is attached to the plate with an arbitrary angle φ. For convenience, vibrations of the beam are described in a local coordinate system (x', y', z'), as shown in Fig. 5.1. Unlike in many studies the beam, which starts from (L_{xb}, L_{yb}) and ends at (L_{xe}, L_{ye}), is not necessarily placed flush with the edges of the plate. The plate-beam connection is here treated as a line joint described by a set of six springs. At this junction, the beam bending about z' axis (or torsion about x' axis) is directly coupled with the in-plane (or transverse) vibrations of the plate. In many cases, it is possible to divide the plate and beam displacements into two independent groups and solve them separately based on the premise that the in-plane and longitudinal modes tend to have much higher natural frequencies. However since this assertion is not readily verified *a priori*, and the in- and out-of-plane vibrations are no longer decoupled for two plates connected at an angle, all the displacements for the plate and beams will be here considered as being coupled together, and determined simultaneously from solving the final combined system.

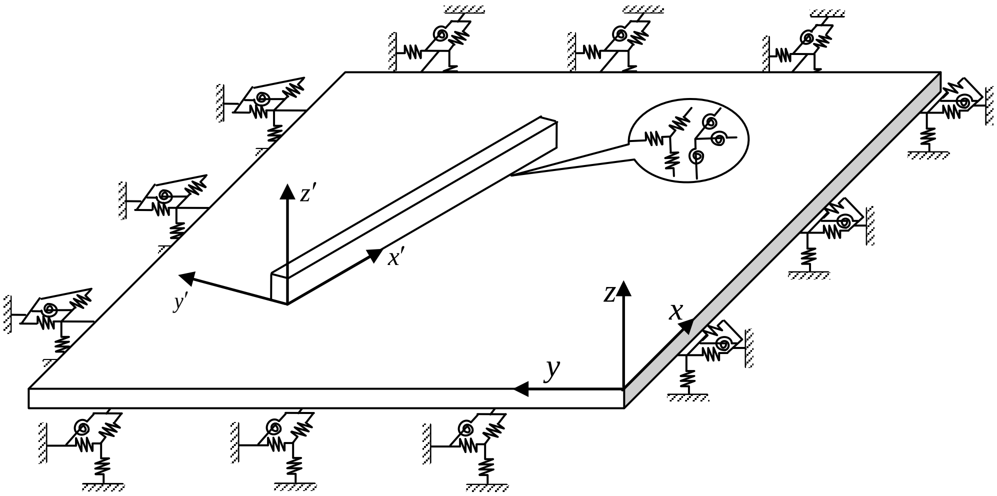

Figure 5.1 An elastically restrained rectangular plate reinforced by arbitrarily orientated beams

In order to be able to account for the general coupling conditions between the plate and beams, a set of six types of distributed elastic springs is specified along the line junction. The orientations of the springs are individually defined with reference to the local coordinate system attached to each beam. The familiar rigid coupling condition in a direction can be easily created by setting the stiffness for the corresponding spring to be equal to infinity. For simplicity, it is assumed here that the coupling and restraining springs have a uniform stiffness distribution along a line.

The series representations of the displacement functions for the plate and the beam in 3-D space are given, respectively, by Eqs. (3.1-6) in chapter 3 and Eqs. (4.1-6) in chapter 4. The Rayleigh-Ritz method is still employed to determine the unknown series coefficients.

The Lagrangian L for the beam-plate coupling system can be generally expressed as

$$L = V - T \tag{5.1}$$

where V and T respectively denote the total potential and kinetic energies which are defined as

$$V = V_{p\_out} + V_{p\_in} + V_{B.C}^{p} + \sum_{i}^{N} \left(V_{b,i} + V_{coup}^{pb_i} \right) \tag{5.2}$$

and

$$T = T_p + \sum_{i}^{N} T_{b,i} \tag{5.3}$$

where N is the total number of stiffeners; V_{p_out} and V_{p_in} represent the strain energies due to the bending and in-plane motions, respectively; $V_{B.C}^{p}$ designates the potential energy stored in the boundary springs of the plate; $V_{b,i}$ denotes the strain energy of the *i*-th beam; $V_{coup}^{pb_i}$ accounts for the potential energies associated with coupling springs between the *i*-th beam and the plate; and $T_{b,i}$ and T_p are the kinetic energies corresponding to the vibrations of the *i*-th beam and the plate, respectively.

Specifically, the potential and kinetic energies of the plate can be written as

$$V_{p\_out} = \frac{D_p}{2} \int_0^a \int_0^b \left[w_{p,xx}^2 + w_{p,yy}^2 + 2\mu w_{p,xx} w_{p,yy} + 2(1-\mu) w_{p,xy}^2 \right] dxdy \tag{5.4}$$

$$V_{p\_in} = \frac{G_p}{2} \int_0^a \int_0^b \left[\left(u_{p,x} + v_{p,y} \right)^2 - 2(1-\mu) u_{p,x} v_{p,y} + \frac{(1-\mu)}{2} \left(u_{p,y} + v_{p,x} \right)^2 \right] dxdy \tag{5.5}$$

$$\begin{aligned} V_{B.C}^{p} = {} & \frac{1}{2} \int_0^b \left[\left(k_{fx0}^{p} w_p^2 + K_{x0}^{p} w_{p,x}^2 + k_{lx0}^{p} u_p^2 + k_{sx0}^{p} v_p^2 \right)_{x=0} + \left(k_{fx1}^{p} w_p^2 + K_{x1}^{p} w_{p,x}^2 + k_{lx1}^{p} u_p^2 + k_{sx1}^{p} v_p^2 \right)_{x=a} \right] dy + \\ & \frac{1}{2} \int_0^a \left[\left(k_{fy0}^{p} w_p^2 + K_{y0}^{p} w_{p,y}^2 + k_{lx0}^{p} u_p^2 + k_{sy0}^{p} v_p^2 \right)_{y=0} + \left(k_{fy1}^{p} w_p^2 + K_{y1}^{p} w_{p,y}^2 + k_{ly1}^{p} u_p^2 + k_{sy1}^{p} v_p^2 \right)_{y=b} \right] dx \end{aligned} \tag{5.6}$$

and

$$T_p = \frac{1}{2} \int_0^a \int_0^b \rho_p h \left[\dot{w}_p{}^2 + \dot{u}_p{}^2 + \dot{v}_p{}^2 \right] dxdy \tag{5.7}$$

where $D_p = E_p h^3 / 12(1-\mu^2)$ is the flexible rigidity of the plate; E_p, G_p, μ, ρ_p and h are Young's modulus, the extensional rigidity, Poisson's ratio, mass density and the thickness of the plate, respectively.

The potential and kinetic energies of the *i*-th beam can be expressed as

$$V_{b,i}=\frac{1}{2}\int_0^{L_i}\left[D_{by',i}w_{bz',x'x'}^2dx'+D_{bz',i}w_{by',x'x'}^2dx'+E_{b,i}S_iu_{b,x'}^2+G_{b,i}J_i\theta^2\right]dx' \tag{5.8}$$

$$T_{b,i}=\frac{1}{2}\int_0^{L_i}\rho_b\left[S_i\dot{w}_{bz'}^2+S_i\dot{w}_{by'}^2+S_iu_b^2+J_i\dot{\theta}^2\right]dx' \tag{5.9}$$

where $D_{by',i}$, $D_{bz',i}$, J_i, $E_{b,i}$, $G_{b,i}$, $\rho_{b,i}$, S_i, and L_i are respectively the bending rigidities in the $x'-z'$ and $x'-y'$ planes, torsional rigidity, Young's modulus, shear modulus, mass density, the cross-sectional area, and the length of the *i*-th beam.

The coupling between the plate and a stiffener is treated as an elastic line connection along the beam which is described by a set of six distributed springs. The potential energies stored in the coupling springs can be written as

$$V_c^{pb_i}=\frac{1}{2}\int_0^{L_i}\left[k_{z'}^{pb_i}\left(w_p-w_{bz'}\right)^2+k_{y'}^{pb_i}\left(v_p\cos\varphi-u_p\sin\varphi-w_{by'}\right)^2+k_{x'}^{pb_i}\left(v_p\sin\varphi+u_p\cos\varphi-u_b\right)^2\right]dx'+$$

$$\frac{1}{2}\int_0^{L_i}\left[K_{y'}^{pb_i}\left(w_{p,x'}-w_{bz',x'}\right)^2+K_{z'}^{pb_i}\left(\frac{1}{2}\left(v_{p,x}-u_{p,y}\right)-w_{by',x'}\right)^2+K_{x'}^{pb_i}\left(w_{p,y'}-\theta\right)^2\right]dx' \tag{5.10}$$

where $K_{y'}^{pb_i}, K_{z'}^{pb_i}, K_{x'}^{pb_i}, k_{z'}^{pb_i}, k_{y'}^{pb_i}$, and $k_{x'}^{pb_i}$ respectively denote the stiffnesses of the coupling springs, and φ is the orientation angle of the beam with respect to the plate. In Eq. (5.10), the potential energy associated with the beam-plate couplings is expressed in terms of the local (beam) co-ordinates (x',y',z') which are such defined that the x'-axis always lies on the beam and $z'=z$, as shown in Fig. 5.2. The derivatives with respect to the local co-ordinates can be determined from

$$w_{p,x'}=\frac{\partial w_p}{\partial x}l_x+\frac{\partial w_p}{\partial y}l_y,\ w_{p,y'}=-\frac{\partial w_p}{\partial x}l_y+\frac{\partial w_p}{\partial y}l_x \tag{5.11-12}$$

where $l_x = \sin\varphi$ and $l_y = \cos\varphi$ are the direction cosines of the beam axis.

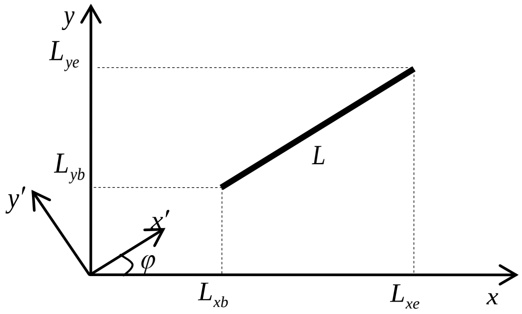

Figure 5.2 Schematic of an arbitrarily placed beam and its local coordinate system

By substituting Eqs. (5.2-10) into (5.1) and minimizing Lagrangian against all the unknown Fourier coefficients, one will obtain a system of linear equations in a matrix form as

$$\left\{\begin{bmatrix}\mathbf{K}_p & \mathbf{K}_{pb}\\ \mathbf{K}_{pb}^T & \mathbf{K}_b\end{bmatrix} - \omega^2\begin{bmatrix}\mathbf{M}_p & 0\\ 0 & \mathbf{M}_b\end{bmatrix}\right\}\mathbf{A} = 0 \tag{5.13}$$

where $\mathbf{K_p}$, $\mathbf{K_b}$, and $\mathbf{K_{pb}}$ are the stiffness matrices respectively corresponding to the plate, the beams and the coupling between them; $\mathbf{M_p}$ and $\mathbf{M_b}$ denote the mass matrices for the plate and the beams, respectively. The detailed expressions for these matrices are given in Appendix E.

The coefficient vector **A** in Eq. (5.13) is defined as

$$\mathbf{A} = \begin{bmatrix}\mathbf{W}_p & \mathbf{U}_p & \mathbf{V}_p & \cdots\cdots & \mathbf{W}_{b,z'}^i & \mathbf{W}_{b,y'}^i & \mathbf{U}_b^i & \Theta_b^i & \cdots\cdots\end{bmatrix} \tag{5.14}$$

where subscripts p and b respectively indicate an quantity related to the plate and beam, and superscript i to the i-th beam. Component vectors in Eq. (5.14) are given by

$$\begin{aligned}\mathbf{W}_p = \{&A_{00}^p, A_{01}^p, \cdots, A_{m0}^p, A_{m1}^p, \cdots, A_{m'n'}^p, \cdots, A_{MN}^p, a_{i,0}^1 \cdots, a_{i,M}^1, a_{i,0}^2 \cdots, a_{i,M}^2,\\ &a_{i,0}^3 \cdots, a_{i,M}^3, a_{i,0}^4 \cdots, a_{i,M}^4, b_{i,0}^1 \cdots, b_{i,N}^1, b_{i,0}^2 \cdots, b_{i,N}^2, b_{i,0}^3, \cdots, b_{i,N}^3, b_{i,0}^4, \cdots, b_{i,N}^4\}\end{aligned} \tag{5.15}$$

$$\begin{aligned}\mathbf{U}_p = \{&B_{00}^p, B_{01}^p, \cdots, B_{m0}^p, B_{m1}^p, \cdots, B_{m'n'}^p, \cdots, B_{MN}^{pu}, e_{i,0}^1 \cdots, e_{i,M}^1, e_{i,0}^2 \cdots, e_{i,M}^2,\\ &f_{i,0}^1, \cdots, f_{i,M}^1, f_{i,0}^2 \cdots, f_{i,M}^2\}\end{aligned} \tag{5.16}$$

$$\mathbf{V}_p = \Big\{C_{00}^p, C_{01}^p, \cdots, C_{m0}^p, C_{m1}^p, \cdots, C_{m'n'}^p, \cdots, C_{MN}^p, g_{i,0}^1 \cdots, g_{i,M}^1, g_{i,0}^2 \cdots, g_{i,M}^2,$$

$$h_{i,0}^1, \cdots, h_{i,M}^1, h_{i,0}^2 \cdots, h_{i,M}^2\Big\} \tag{5.17}$$

$$\mathbf{W}_{b,z'}^i = \Big\{A_{iz',0}^b \quad \cdots \quad A_{iz',M}^b, \quad B_{iz',1}^b \quad B_{iz',2}^b \quad B_{iz',3}^b \quad B_{iz',4}^b\Big\}^T \tag{5.18}$$

$$\mathbf{W}_{b,y'}^i = \Big\{A_{iy',0}^b \quad \cdots \quad A_{iy',M}^b, \quad B_{iy',1}^b \quad B_{iy',2}^b \quad B_{iy',3}^b \quad B_{iy',4}^b\Big\}^T \tag{5.19}$$

$$\mathbf{U}_b^i = \Big\{A_{iu,0}^b \quad \cdots \quad A_{iu,M}^b, \quad B_{iu,1}^b \quad B_{iu,2}^b\Big\}^T \tag{5.20}$$

$$\Theta_b^i = \Big\{A_{i\theta,0}^b \quad \cdots \quad A_{i\theta,M}^b, \quad B_{i\theta,1}^b \quad B_{i\theta,2}^b\Big\}^T \tag{5.21}$$

It is clear from Eq. (5.13) that the natural frequencies and eigenvectors for the stiffened plate can now be directly obtained by solving a standard matrix eigenvalue problem. The response of the system to an applied load can be readily considered by simply including the work done by this load in the Lagrangian, which will eventually lead to a force term on the right side of Eq. (5.13). Once the displacements are determined for the plate and beams, other quantities of interest such as reaction forces and power flows can be calculated directly from the appropriate mathematical operations on the analytical form of the displacement solutions, which can only be done when the solutions are constructed as sufficiently smooth as required in the strong formulations, and the series expansions are uniformly convergent to the highest involved derives, the third derivatives in shear force expressions.

5.1.3 Results and discussions

A number of numerical examples will be given in this section. Fig. 5.3 shows a rectangular plate orthogonally stiffened by a number of beams. In the following calculations, it is assumed that the plate and its stiffeners are made of the same material: $E_p = 207$GPa, $\rho_p =$

7800kg/m^3, $\mu = 0.3$, $G_b = E_p / 2(1+\mu)$ for the stiffeners, and $G_p = E_p h/(1-\mu^2)$ for the plate. The geometric properties of the stiffeners with a rectangular cross-section are taken as those previously used in ref. (Liew, 1994) for the purpose of comparison. The boundary conditions of the plate are described by four capital letters; for instance, SCFC means that the plate is simply supported at x = 0, clamped at y = b, free at x = a, and clamped at y = 0.

Table 5.1 Frequency parameters, $\Omega = \left(\omega b^2 / \pi^2\right)\sqrt{\rho_p h / D_p}$, for a CCCC square plate with one x-wise stiffening beam placed at b/2

	$\Omega = \left(\omega b^2 / \pi^2\right)\sqrt{\rho_p h / D_p}$					
M=N	1	2	3	4	5	6
7	3.7802	7.4433	7.8140	10.9811	13.2505	14.3334
9	3.7781	7.4430	7.8088	10.9803	13.2486	14.3327
12	3.7732	7.4428	7.8073	10.9801	13.2481	14.3310
13	3.7721	7.4428	7.8060	10.9800	13.2478	14.3298
14	3.7720	7.4428	7.8060	10.9790	13.2473	14.3298
	3.8136[a]	7.4276	8.0853	11.0444	13.3380	14.6492
	3.7947[b]	7.4771	7.9970	10.9490	13.2376	14.4261
	3.7859[c]	7.4426	7.8193	10.9663	13.2496	14.3384

[a] Results from Ref. (Dozio & Ricciardi, 2009)
[b] Results from Ref. (Liew *et al.*, 1994)
[c] Results from ANSYS with 200 × 200 elements

To check the correctness and accuracy of the present solution, we will first consider a configuration previously studied in refs. (Liew *et al.*, 1994; Dozio & Ricciardi, 2009). A plate has only one stiffener lying parallel to x-axis at y=b/2 with following parameters: the aspect ratio a/b=1, the ratio of thickness to width h/b=0.01, the width ratio w/b=0.01, and the height ratio t/h=1. The calculated first six frequency parameters, $\Omega = \left(\omega b^2 / \pi^2\right)\sqrt{\rho_p h / D_p}$, are shown in Table 5.1 together with three sets of reference data for a CCCC plate with the stiffener rigidly attached to it. A clamped edge is a special case of the elastic supports when the stiffnesses for the restraining springs all become infinitely large (which is represented by a very large number, 1.0 $\times 10^{11}$, in the actual calculations). The rigid coupling between the beam and plate is treated in the same way. A good comparison is observed between the current and other reference results. The results in Table 5.1 also show a great convergence characteristic when different truncation numbers are used in the series expansions. Since the solution converges adequately fast, the series expansions will be simply truncated to $M=N=9$ in all the subsequent calculations.

Table 5.2 Frequency parameters, $\Omega = \left(\omega b^2/\pi^2\right)\sqrt{\rho_p h / D_p}$, for a rectangular plate stiffened by one *x*-wise stiffening beam at *b*/2 with different boundary conditions and stiffener height ratios

B.C.	*t/h*	$\Omega = \left(\omega b^2/\pi^2\right)\sqrt{\rho_p h / D_p}$					
		1	2	3	4	5	6
SSSS	1	1.2401	2.0373	3.3898	4.2500	5.0124	5.3027
		1.2435[a]	2.0379	3.3941	4.2512	5.0045	5.3040
		1.2411[b]	2.0146	3.3768	4.2517	5.0072	5.2766
	1.5	1.2447	2.1089	3.5984	4.2553	5.0251	5.6653
		1.2457[a]	2.1066	3.6067	4.2524	5.0093	5.7115
		1.2456[b]	2.1060	3.6040	4.2555	5.0228	5.7029
SCSC	1	2.3869	2.9465	4.0854	5.8468	6.4378	7.0273
		2.3873 [a]	2.9513	4.1096	5.9104	6.4386	7.0320
		2.3722[b]	2.9281	4.0643	5.8265	6.4370	7.0301
	1.5	2.3777	2.9949	4.2800	6.2276	6.4392	7.0332
		2.3781[a]	3.0022	4.3262	6.3773	6.4396	7.0373
		2.3776[b]	2.9954	4.2960	6.2969	6.4400	7.0471
FFFF	1	0.5726	0.6707	1.4822	1.5962	2.2270	2.5734
		0.5737[b]	0.6750	1.4853	1.5852	2.2204	2.5771
	1.5	0.6152	0.6748	1.4892	1.6840	2.2193	2.5787
		0.6153[b]	0.6786	1.4929	1.6851	2.2183	2.5877

[a] Results from Ref. (Dozio & Ricciardi, 2009)
[b] Results from ANSYS with 200×200 elements

In the next example, by changing the aspect ratio to *a/b* = 2, the frequency parameters are calculated for two different height ratios, *t/h*=1 and 1.5. The results are shown in Table 5.2 for three different boundary conditions: SSSS, SCSC, and FFFF. To understand the impact of the stiffener height ratio, the frequency parameters corresponding to the first mode in the FFFF case are highlighted in Table 5.3. The current results match well with those obtained using other techniques in all these cases. However, it should be pointed out that unlike the other techniques the current method does not require any modification to the formulations or solution procedures in dealing with different boundary conditions; modifying a boundary condition is as simple as changing a material or geometrical parameter such as Young's modulus or mass density.

Table 5.3 The first frequency parameter, $\Omega=\left(\omega b^2/\pi^2\right)\sqrt{\rho_p h/D_p}$, for a FFFF rectangular plate with significantly different stiffener height ratios

$t/h=1$	$t/h=2$	$t/h=4$	$t/h=6$	$t/h=8$	$t/h=10$
0.5726	0.6744	0.7148	0.7851	0.8550	0.9067
0.5737[a]	0.6774	0.7206	0.7926	0.8635	0.9179

[a] Results from ANSYS with 200×200 elements

Table 5.4 Frequency parameters, $\Omega=\left(\omega b^2/\pi^2\right)\sqrt{\rho_p h/D_p}$, for an SSSS square plate with one central x- wise beam and one central y-wise beam

$\Omega=\left(\omega b^2/\pi^2\right)\sqrt{\rho_p h/D_p}$					
1	2	3	4	5	6
2.2093	5.6924	5.7006	8.0514	11.1823	11.5398
2.2027[a]	5.7195	5.7195	8.0469	11.2071	11.6966
2.2017[b]	5.7167	5.7167	8.0552	11.1909	11.6785
2.1996[c]	5.6933	5.6933	8.0511	11.1824	11.6492

[a] Results from Ref. (Dozio & Ricciardi, 2009)
[b] Results from Ref. (Liew *et al.*, 1994)
[c] Results from ANSYS with 200×200 elements

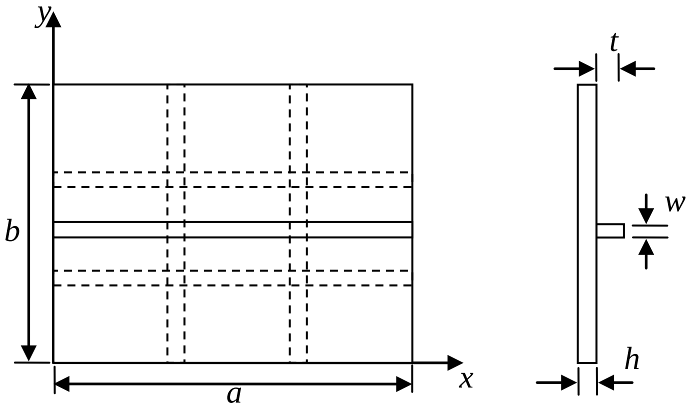

Figure 5.3 An illustration of plate and beam positions and reinforcement plans

Table 5.5 Frequency parameters, $\Omega = \left(\omega b^2/\pi^2\right)\sqrt{\rho_p h/D_p}$, for a rectangular plate stiffened by two *x*-wise and two *y*-wise evenly distributed beams with different boundary conditions and stiffener height ratios

B.C.	t/h	$\Omega = \left(\omega b^2/\pi^2\right)\sqrt{\rho_p h/D_p}$					
		1	2	3	4	5	6
SSSS	1	1.2874	2.0784	3.4670	4.4583	5.0993	5.4345
		1.2992[a]	2.0845	3.4689	4.4657	5.1837	5.4341
		1.2990[b]	2.0840	3.4677	4.4627	5.1801	5.4291
	1.5	1.3808	2.2000	3.7674	4.7877	5.3029	5.9622
		1.3852[a]	2.2291	3.7852	4.7950	5.4760	6.0493
		1.3855[b]	2.2296	3.7863	4.7935	5.4764	6.0444
SCSC	1	2.5213	2.9772	4.1325	5.9331	6.6582	7.1526
		2.5411[a]	3.0777	4.1455	6.0176	6.7364	7.2821
		2.5387[b]	3.0713	4.1283	5.9881	6.7250	7.2693
	1.5	2.7298	3.2712	4.3987	6.6347	7.0756	7.6353
		2.7426[a]	3.3015	4.4135	6.6563	7.1881	7.6484
		2.7404[b]	3.2969	4.4024	6.6374	7.1780	7.6403
CCCC	1	2.6155	3.4339	4.8172	6.7269	6.9395	7.5273
		2.6347[a]	3.4660	4.8544	6.8068	7.0342	7.6675
		2.6315[b]	3.4474	4.8306	6.7908	7.0014	7.5801
	1.5	2.8309	3.7683	5.2257	7.1831	7.7656	8.0681
		2.8522[a]	3.8090	5.2872	7.2543	7.8368	8.2815
		2.8528[b]	3.7893	5.2683	7.2651	7.8194	8.1636

[a] Results from Ref. (Dozio & Ricciardi, 2009)
[b] Results from Ref. (Liew *et al.*, 1994)

Other reinforcement configurations involving more stiffeners are also considered here. Table 5.4 shows the frequency parameters for an SSSS square plate with a pair of perpendicular stiffeners symmetrically placed with respect to the plate center. Given in Table 5.5 are the results for a plate stiffened by two evenly distributed beams in the *x*-direction, and two in the *y*-direction (as illustrated by the dash lines in Fig. 5.3). Next example involves a non-symmetric reinforcement configuration in which two beams are placed along two edges at $y = 0$ and $x = 0$. The related model parameters are chosen as follows: a=0.6m, b=0.4m, h = 0.008m, w/b = 0.01, and t/h = 1. Listed in Table 5.6 are the frequency parameters for the plate with six different boundary conditions: FCSF, FFCF, FSSF, FCCF, SFFC, and SFFS. Since these cases were not studied previously, the current results are only compared with the FEM data. Even though the conventional Rayleigh-Ritz solutions based on the "corresponding" beam functions are not presented, it can be speculated that they are most likely to become less accurate for this kind of problems because the stiffeners located along one or more plate edges tends to have some meaningful effects on the actual boundary conditions for the plate.

Table 5.6 Frequency parameters, $\Omega = \left(\omega b^2 / \pi^2\right)\sqrt{\rho_p h / D_p}$, for a rectangular plate stiffened by one *x*-wise beam at *y*=0 and one *y*-wise beam at *x*=0 with various boundary conditions

B.C.	$\Omega = \left(\omega b^2 / \pi^2\right)\sqrt{\rho_p h / D_p}$					
	1	2	3	4	5	6
FCSF	0.4575	1.1730	2.4084	2.8168	3.3847	5.1699
	0.4599[a]	1.1776	2.4154	2.8182	3.3822	5.1625
FFCF	0.1607	0.5297	1.0016	1.8239	2.5373	2.8387
	0.1613[a]	0.5303	1.0046	1.8299	2.5387	2.8432
FSSF	0.2300	1.0353	1.7754	2.7122	2.8521	4.7314
	0.2269[a]	1.0303	1.7722	2.7046	2.8280	4.6932
FCCF	0.5186	1.4243	2.4457	3.2962	3.5552	5.5365
	0.5255[a]	1.4371	2.4561	3.3119	3.5673	5.5482
SFFC	0.4511	1.1131	2.3258	2.6060	3.3046	4.9401
	0.4501[a]	1.1109	2.3245	2.6006	3.2946	4.9181
SFFS	0.2320	0.9830	1.7014	2.5096	2.7780	4.5401
	0.2302[a]	0.9765	1.6970	2.5006	2.7544	4.4983

All the boundary conditions thus far considered still fall into the category of the "classical" ones for which the beam functions have been well established. In many real applications, one may have to consider a more complicated class (or, the mixed type) of boundary conditions which are specified in terms of elastic restraints at an edge. As an example, we consider a plate having one *x*-direction stiffener at *y*=2*b*/3. Each of its four edges is now elastically restrained by the transverse and rotational springs with stiffness 10^5 N/m and 10^4 N.m/rad, respectively. In addition, a pair of in-plane springs with the same stiffness, 10^9 N/m, is applied to edge y=0.

Table 5.7 Frequency parameters, $\Omega=\left(\omega b^2/\pi^2\right)\sqrt{\rho_p h/D_p}$, for a rectangular elastically restrained plate stiffened by one x-wise beam at y=2b/3

$\Omega=\left(\omega b^2/\pi^2\right)\sqrt{\rho_p h/D_p}$							
1	2	3	4	5	6	7	8
0.1484	0.2558	0.3741	0.9861	1.1383	2.1625	2.4032	2.8245
0.1498[a]	0.2587	0.3776	0.9892	1.1424	2.1667	2.4073	2.828

[a] Results from ANSYS with 200×200 elements

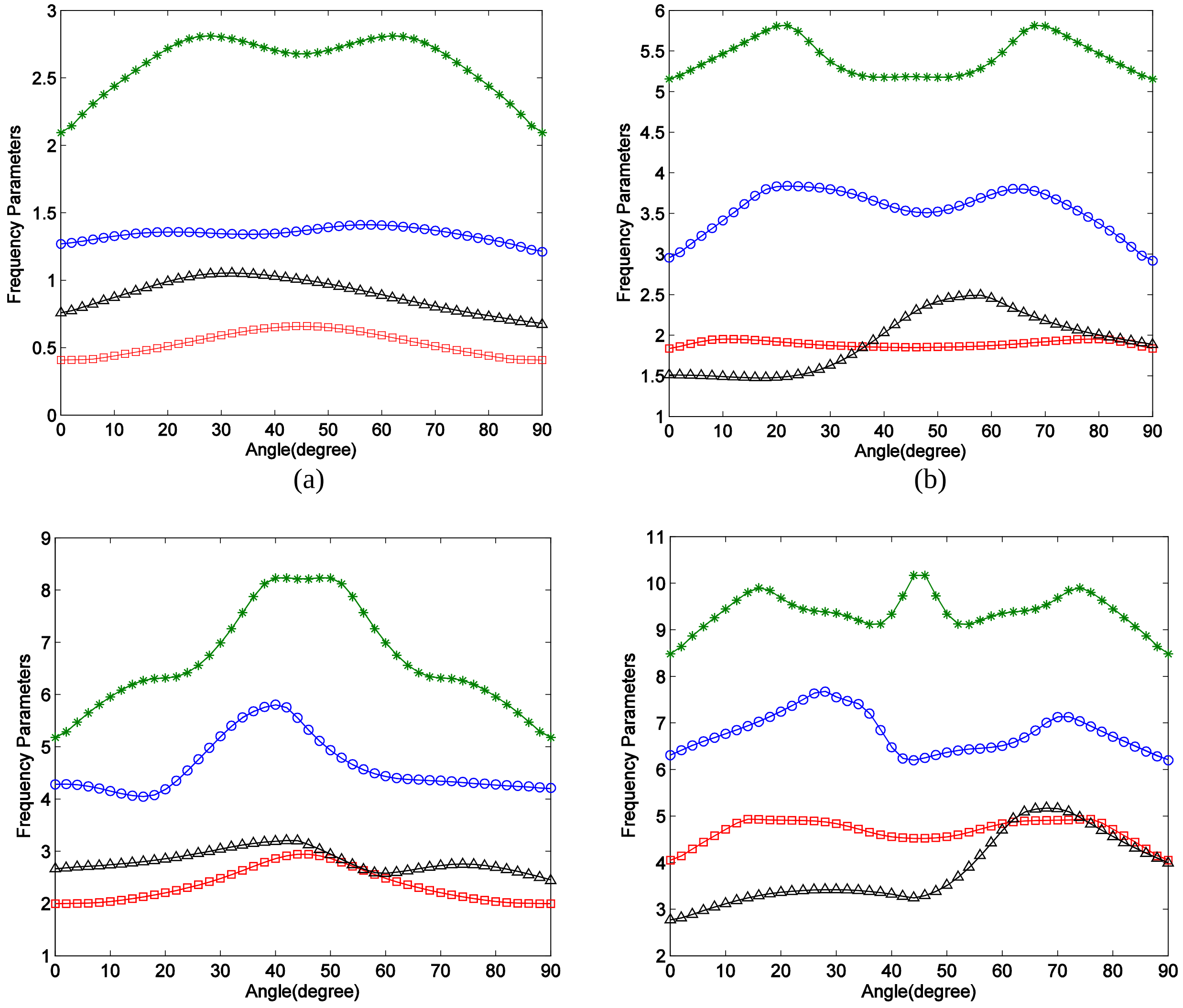

(a) (b)

(c) (d)

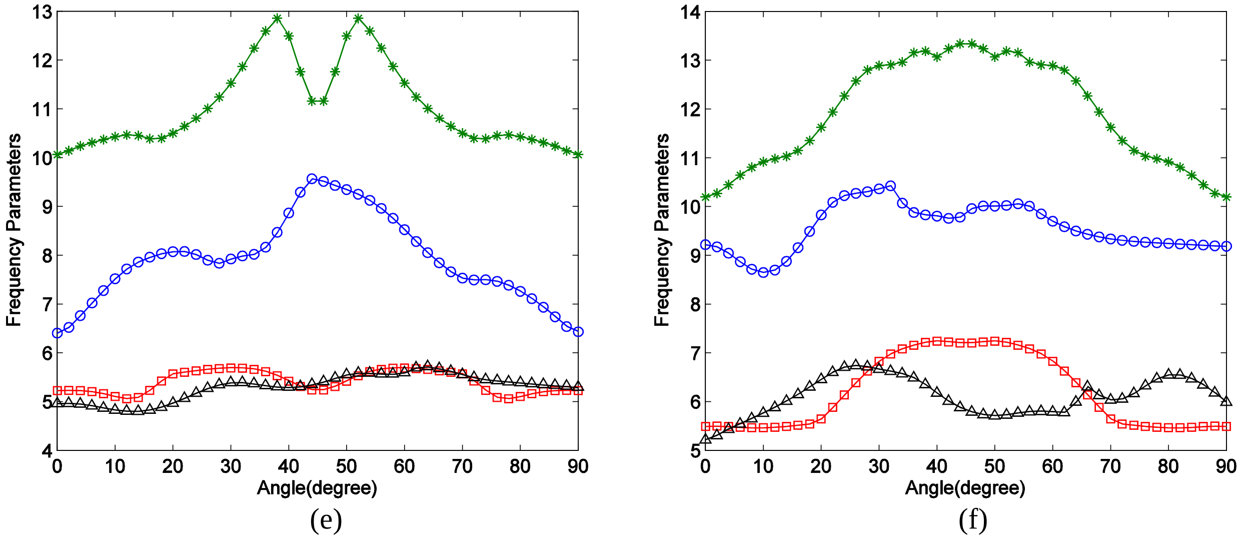

Figure 5.4 The first six frequency parameters versus orientation angle of the stiffening beam: (a) 1st mode; (b) 2nd mode; (c) 3th mode; (d) 4th mode; (e) 5th mode; (f) 6th mode. △ FFFS; □ SFFS; ○ SSFS; * SSSS

All other parameters are kept the same as in the previous example. The calculated frequency parameters are given in Table 5.7 together with the FEM results. While the unifying nature of the current method has been adequately demonstrated through varying the boundary conditions, its capability cannot be fully recognized without examining some nonconventional reinforcement configurations. In most investigations, the coupling between the plate and its stiffeners are simply considered as completely rigid, which is typically enforced in terms of the compatibility conditions between the displacements for the plate and stiffeners. In many modern structures, stiffeners are often glued, bolted or spot-welded to plates, thus allowing separations between plates and stiffeners at the interfaces. In other cases, even though the coupling is substantially strong between some degrees of freedom (*e.g.*, between flexural displacements), the bonding may actually be quite weak between others (*e.g.*, between rotational displacements). Thus, it is of practical interest to understand the effects of the coupling conditions on the modal characteristics of a stiffened plate. Take a FSSS plate with one *y*-direction beam at *x*=0 for example. The geometric parameters are specified as: a/b=1, h/b=0.02, w/b=0.02, and t/h=1. The calculated frequency parameters are listed in Table 5.8 for a wide range of coupling stiffnesses from k_x=k_y=k_z =10^3 N/m to 10^9 N/m. For simplicity, the couplings through rotational springs are ignored here, that is, K_x=K_y=K_z=0. The results clearly show that the coupling conditions can significantly affect the dynamic characteristics of the combined system.

Table 5.8 Frequency parameters, $\Omega = \left(\omega b^2/\pi^2\right)\sqrt{\rho_p h/D_p}$, for a FSSS square plate stiffened by one y-wise beam at x=0 with various coupling spring stiffness

kx,ky,kz	$\Omega = \left(\omega b^2/\pi^2\right)\sqrt{\rho_p h/D_p}$							
	1	2	3	4	5	6	7	8
10^3	0.2326	0.2327	0.2327	0.2331	0.2372	1.1874	2.1750	2.8258
	0.2305 [a]	0.2307	0.2327	0.2346	0.2347	1.1846	2.1745	2.8126
10^4	0.7297	0.7359	0.7359	0.7360	0.7370	1.1965	2.2843	2.8292
	0.7253 [a]	0.7295	0.7359	0.7392	0.7423	1.1937	2.2839	2.8161
10^5	1.1797	2.2893	2.3113	2.3271	2.3272	2.3272	2.9120	3.1768
	1.1768 [a]	2.2760	2.3061	2.3197	2.3271	2.3464	2.9011	3.1776
10^6	1.2340	2.8102	4.1895	5.9011	6.0351	7.3583	7.3589	7.3591
	1.2310 [a]	2.7962	4.1846	5.8756	6.0165	7.2673	7.3584	7.3982
10^7	1.2831	2.8427	4.4088	6.1903	6.1964	9.4004	9.6477	11.2829
	1.2799 [a]	2.8283	4.4035	6.1639	6.1766	9.3917	9.5995	11.2412
10^8	1.2948	2.8499	4.5311	6.2040	6.3591	9.6736	9.7737	11.5443
	1.2916 [a]	2.8355	4.5256	6.1839	6.3330	9.6645	9.7249	11.5201
10^9	1.2968	2.8517	4.5551	6.2060	6.3974	9.7377	9.8015	11.5502
	1.2938 [a]	2.8369	4.5501	6.1848	6.3738	9.7286	9.7543	11.5201

[a] Results from ANSYS with 200×200 elements

Table 5.9 Frequency parameters for the first mode, $\Omega = \left(\omega b^2/\pi^2\right)\sqrt{\rho_p h/D_p}$, of a square plate with a stiffener placed in different angles

	$\Omega = \left(\omega b^2/\pi^2\right)\sqrt{\rho_p h/D_p}$						
B.C.	0^o	15^o	30^o	45^o	60^o	75^o	90^o
FFFS	0.7582	0.9212	1.0502	1.0081	0.8877	0.7709	0.6711
SFFS	0.4078	0.4816	0.5912	0.6596	0.5912	0.4816	0.4078
SSFS	1.2684	1.3455	1.3461	1.3614	1.4079	1.3414	1.2110
SSSS	2.0941	2.5562	2.8022	2.6768	2.8022	2.6130	2.0941

As mentioned earlier, it is required in a FEA model that a 2-D mesh for the plate has to match seamlessly with 1-D meshes for beams. The cumbersome of this requirement will become more evident from this final example which is used to examine the effects of the orientation of a stiffening beam.

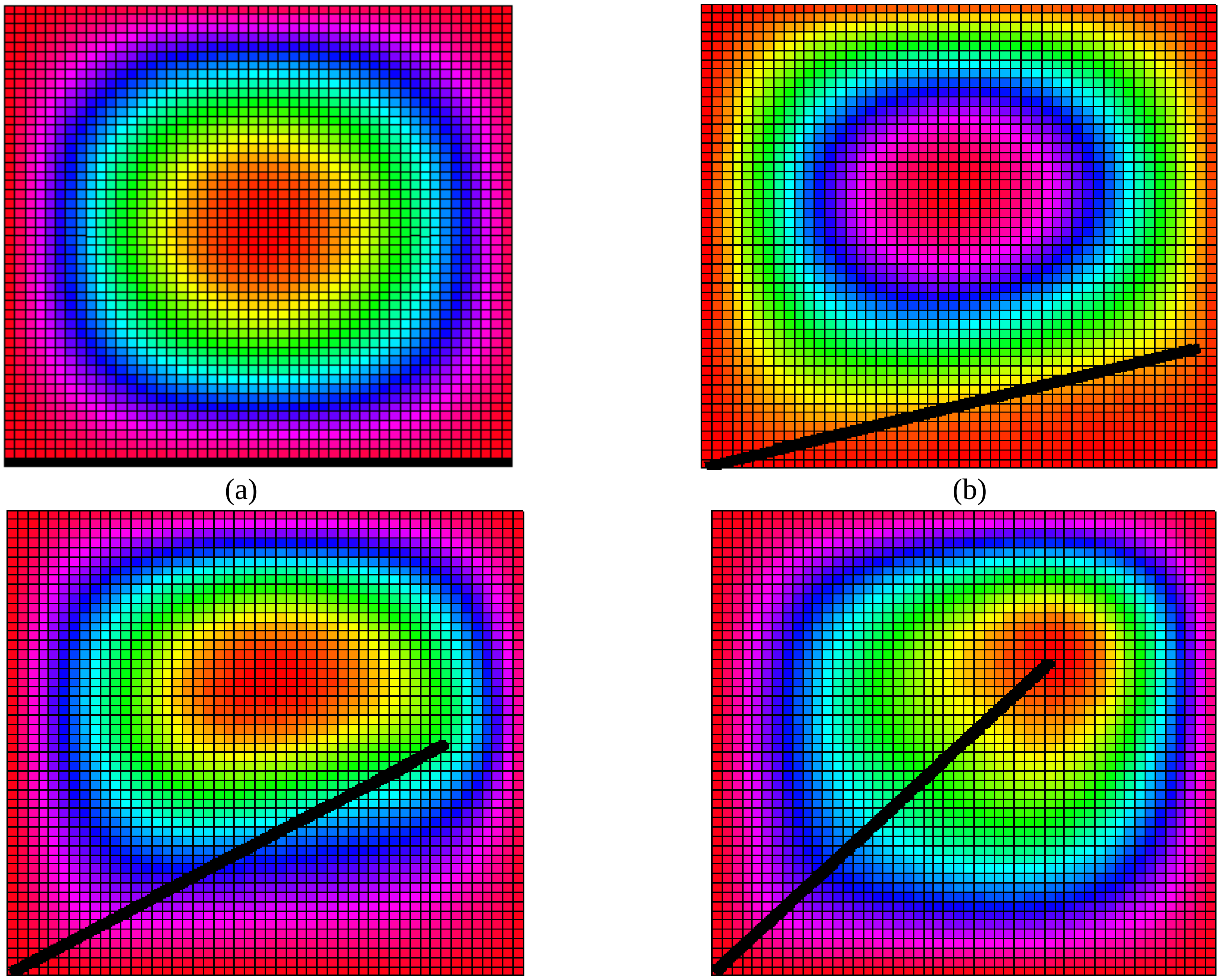
(a) (b) (c) (d)

Figure 5.5 The first mode shape for an SSSS plate stiffened by one beam with various orientations: (a) $\phi=0^{\circ}$; (b) $\phi=15^{\circ}$; (c) $\phi=30^{\circ}$; (d) $\phi=45^{\circ}$

Assume a square plate with the following geometric parameters: $h/b=0.01$, $w/b=0.01$ and $t/h=10$. Only a single beam of length b is rigidly attached to it for a number of configurations: while one end is fixed to (0,0), the other end is placed at various angles from 0 to 90°, as illustrated in Fig. 5.4. Four different boundary conditions are considered for the plate: FFFS, SFFS, SSFS, and SSSS. Table 5.9 shows the calculated frequency parameters of the first mode versus the orientation angle of the stiffening beam. The first six frequency parameters are plotted in Fig. 5.4 as the functions of the orientation angle of the stiffening beam. It can be seen that the frequency parameters vary significantly with the orientation angle, and the shapes of these curves strongly depend upon the boundary conditions. As illustrated in Fig. 5.4, the curves are symmetric about 45 ° for the two symmetric boundary conditions, SFFS and SSSS. In comparison, the curves exhibit an "irregular" shape toward the other two boundary conditions, FFFS and SSFS. The first mode for the SSSS plate is shown in Fig. 5.5 for four different stiffener orientation angles. When the stiffener lies in the *x*-axis ($\varphi = 0^{\circ}$), its presence is only manifested in the restraining effect against the rotation along edge *y*=0. The first frequency parameter, 2.09, is thus slight higher than that, 2.0, for a simply supported plate, and lower than 2.18 when a uniform rotational restraint of *Ka*/*D*=1 is added to each edge of the simply supported plate (Li & Zhang, 2009). The increase of the frequency parameter for other orientation angles, which peaks near 28° (see Fig. 5.4(a)), can be understood as the outcome of reducing the effective sizes of the plate due to the reinforcement. These results clearly show that the dynamic behaviors of a stiffened plate can be meaningfully manipulated through modifying reinforcement configurations.

The frequency parameters can be quite sensitive to the minor change of the beam placement angle. High sensitivity zones are dependent upon the frequency parameters and the boundary conditions. Take the simply supported case for example. The high sensitivity zones are approximately located at 0°-20°, 20°-30°, 25°-35°, 40°-45°, 30°-45°, and 25°-35° for these six frequencies, respectively. While these characterizations are specifically related to the selected set of model parameters and boundary conditions, similar behaviors are expected to be also observable on other systems. Such information can be of practical importance to structural design and noise and vibration control; in the high sensitivity zones, even a slight deviation of the stiffener orientation can result in significant modifications to the modal characteristics of a system.

5.2 Experimental validation

(a) (b)

Figure 5.6 A test beam-plate structure: (a) the whole shape; (b) a typical plate-beam junction

The test structure shown in Fig. 5.6(a) consists of a thin rectangular plate and a table frame discussed in chapter 3.3.2. The plate is made of steel (ASTM A 1008 CS Type B): E = 200 GPa, ρ =7872 kg/m^3, $\mu = 0.29$, and thickness $h = 0.0019$ m. As shown in Fig. 5.6(b), all edges of the plate are screwed to the frame to approximate a rigid line connection between the plate and beams.

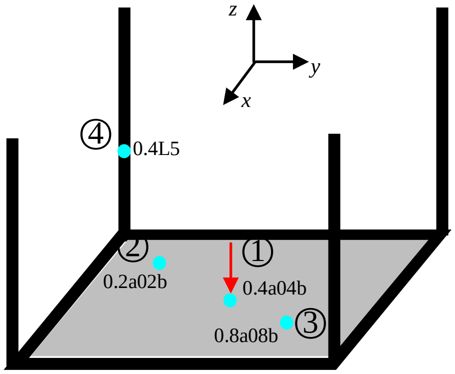

Figure 5.7 The excitation and response locations for a test beam-plate structure

An impact force is applied on the plate at point 1, and the responses are measured at point 1, 2, 3 and 4, respectively, as shown in Fig. 5.7. A structural damping 0.002 was assumed in the model. The boundary condition for the structure is set as being free in the testing, which is simulated by hanging it with rubber bands. The mode shapes were measured by manually roving the accelerometer over a uniformly-spaced grid of 11 × 6 on the plate, and 6 points on each vertical beam.

Several flexural modes are plotted in Fig. 5.8. In the experiment, accelerometers were used for measuring the responses in the *x*- and *y*- directions. It is noted that there are some distortions in the experimental beam shapes, which may be caused by the slight “displacements” of the accelerometers.

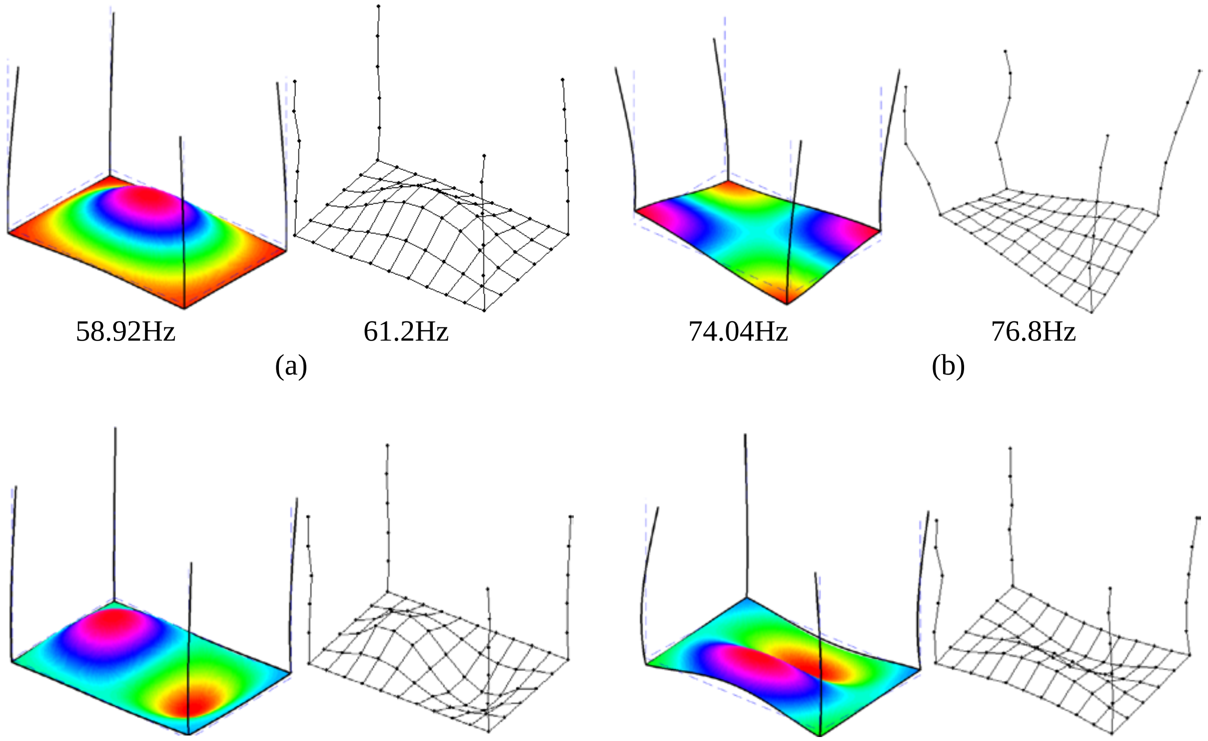

58.92Hz 61.2Hz

(a)

74.04Hz 76.8Hz

(b)

117.15Hz 115.5Hz

(c)

137.15Hz 158.5Hz

(d)

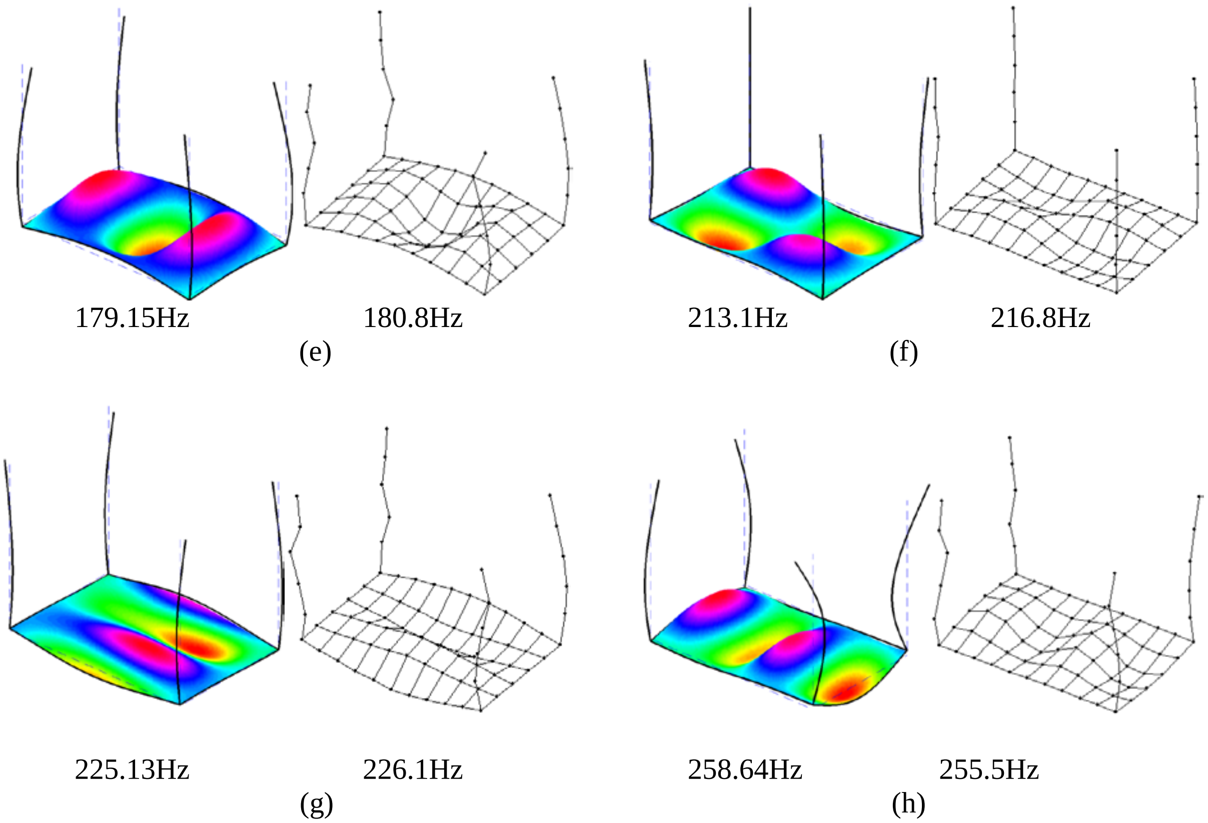

179.15Hz 180.8Hz
(e)

213.1Hz 216.8Hz
(f)

225.13Hz 226.1Hz
(g)

258.64Hz 255.5Hz
(h)

Figure 5.8 Mode shapes for a beam-plate structure: (a) 8th mode; (b) 10th mode; (c) 11th mode; (d) 12th mode; (e) 14th mode; (f) 16th mode; (g) 17th mode; (h) 19th mode

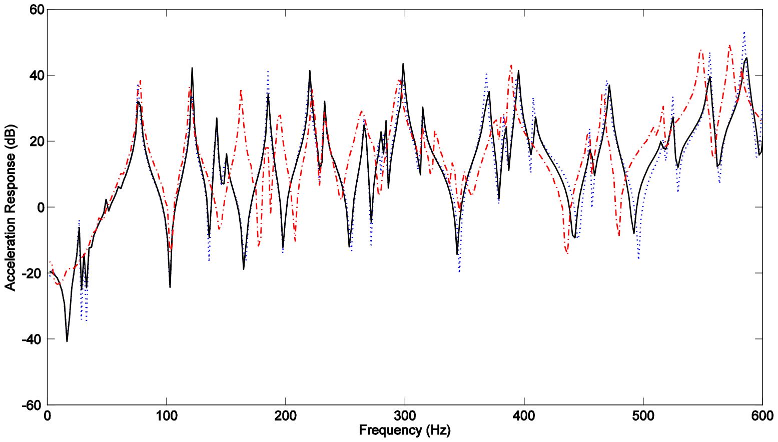

Figure 5.9 FRF of a beam-plate structure at the driving point (point 1) in *z*- axis: — Prediction; ---- FEA; -·-·- Test

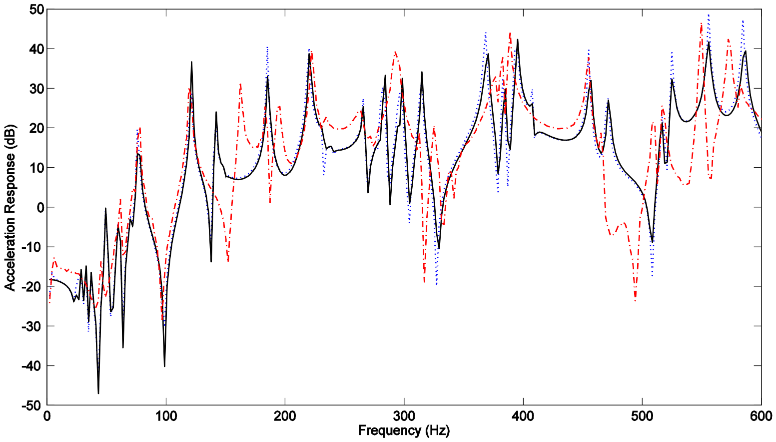

Figure 5.10 FRF of a beam-plate structure at point 2 in *z*- axis with respect to the force at point 1 in *z*- axis: — Prediction; ---- FEA; -·-·- Test

The predicted FRF’s (by using a FEA and the current models) are compared with the measured in Figs. 5.9-5.13 for a few selected locations. Although the two prediction models have produced the same results, the agreement between the analytical and experimental results is not as good as that for the beam structures (refer to chapter 3). This is believed to be caused by the complications (regarding the coupling conditions) present in the actual structure tested. This shall not diminish the significance of the present method since its results are adequately validated by the FEA model.

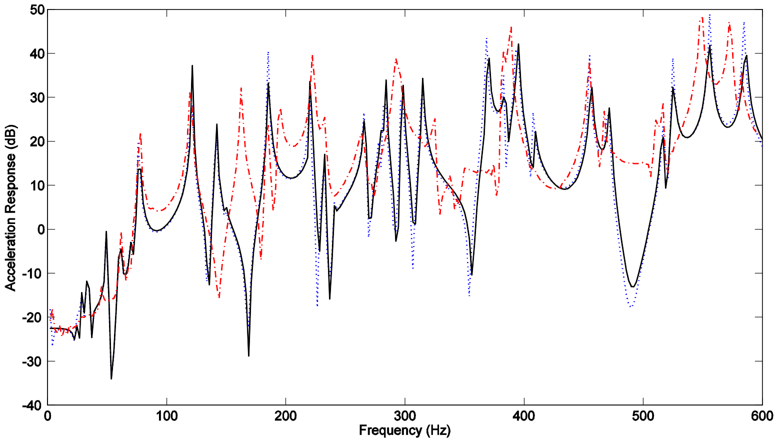

Figure 5.11 FRF of a beam-plate structure at point 3 in *z*- axis with respect to the force at point 1 in *z*- axis: — Prediction; ---- FEA; -·-·- Test

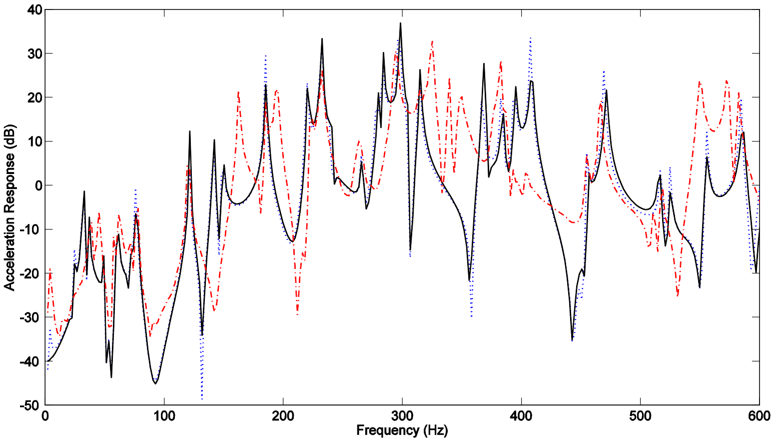

Figure 5.12 FRF of a beam-plate structure at point 4 in *x*- axis with respect to the force at point 1 in *x*- axis: — Prediction; ---- FEA; -·-·- Test

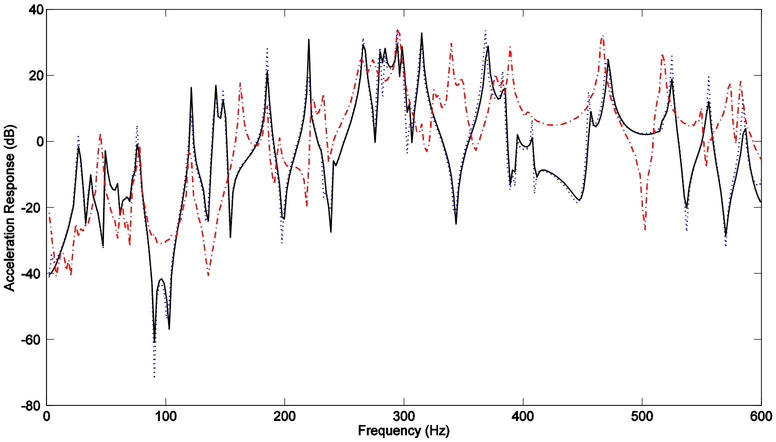

Figure 5.13 FRF of a beam-plate structure at point 4 in *y*-axis with respect to the force at point 1 in *y*- axis: — Prediction; ---- FEA; -·-·- Test

5.3 Power flow in a stiffened plate

5.3.1 Introduction

The determination of energy distributions of and power flows through stiffened plates is of significant importance in the study of vibration transmission and structure-borne sound propagation in built-up structures. Many researchers have studied the vibration power flows in structures using various analytical and numerical methods.

The wave propagation approach has been developed primarily to study power flows through connections of semi-infinite or infinite plates and beams. Goyder and White (1980) examined the near and far field power flow of an infinite plate with a single line stiffener under a force or moment excitation. When torsional waves are excited in the beam, it was found that the beam plays a dominant role at high frequencies and the plate becomes more important at low frequencies regarding the vibration power transmission. Combining the Bloch theorem associated with the wave propagation approach, Mead (1986) used phased array receptance functions to obtain an analytical solution for a plate stiffened by an infinite number of beams. He also studied the relationship between the wave propagation constants and the “pass/stop bands” of an infinite periodic ribbed plate. Mead’s work has been extended by many researchers to address the vibrations and power flows of periodic structures from various aspects (Roy & Plunkett, 1986; Hodges & Woodhouse, 1983; Langley, 1994; Mead, 1996).

Statistical Energy Analysis (SEA) has been used to predict power flows between coupled beams and plates at high frequencies or for high modal density (Lyon & Dejong, 1995; Tso & Hansen, 1998). Limited by its basic assumptions (Hodges & Woodhouse, 1986) which include, for example, weak coupling, reverberant wave fields, and the “rain on the roof” excitations, SEA can only provide global space- and frequency- averaged information of field variables at high can only provide global space- and frequency- averaged information of field variables at high frequencies without indicating local distributions of the variables (Carcaterra & Sestieri, 1995).

Power flow paths are often identified with the help of structural intensity that indicates both the magnitude and the direction of energy flows at any point on a structure. Finite Element Analysis (FEA) has been extensively adopted to investigate power flows and structural intensities of connected systems (Hambric, 1990; Xu *et al.*, 2004 & 2005; Grice & Pinnington, 2000; Gavric & Pavic, 1993). Hambric (1990) considered a dissipative cantilever plate with stiffeners. The intensity field was calculated at the nodes as a product of forces and velocities. It was found that power flows are discontinuous across the element boundaries. Xu *et al.* (2004 & 2005) investigated the power transmission paths in stiffened plates and the relationships between the structural intensity and structural mode shapes as well. They found that the total amount of injected or transmitted power flows were dependent upon natural frequencies of the whole structure and the relative percentage of the power flows through the cross section of the plate or stiffeners depended on the ratio of their relative flexural rigidity. FEA is capable of identifying spatial variations of the power flow field in substructures with fair accuracy only in low frequencies. This is because at higher frequencies, wavelengths become shorter, so finer meshes are required leading to an increased difficulty with modeling and analysis.

Although a combined use of the FEA and SEA can satisfactorily cover the low and high ends of the frequency range of practical interest, the existence of the gap in between has prompted researchers to seek different approaches to predict power flows in the mid-frequency range. Nefske and Sung (1989) proposed a differential equation, analogous to the heat conduction equation, to describe the spatial dependence of the spectral-averaged energy density. The power flow field can be solved using a standard finite element code by modifying the model input parameters accordingly. Wohlever and Bernhard (1992) used the time- and space-averaged energy density to derive an analogous thermal energy density equation. Based on the steady state heat flow model, a power flow analysis (PFA) was developed by Seo and Hong (2003) to study the power flow of reinforced beam-plate coupled structures. In that method, the primary response variable is the vibration energy density of the structure, and the secondary response variable is the vibration intensity vector which is proportional to the gradient of the energy density. Although some satisfactory results were obtained using the heat conduction model-based methods as described in refs. (Nefske and Sung, 1989; Wohlever & Bernhard, 1992; Seo and

Hong, 2003; Han *et al.*1997), Carcaterra and Sestieri (1995) noted that thermal analogy is usually not valid in describing time-averaged energy density, especially for complex structures due to the inadequacy of the energy to represent the mechanical power balance.

Many other analytical methods have been developed for predicting vibratory power flows between some basic structural members with various coupling fashions. Among them, the structural mobility approach is often used to calculate the power flow in beams, plates, and beam-plate coupled systems (Cuschieri, 1990 & 1998; Rook & Singh, 1998). The power flows into the source substructure and across the substructures are expressed in terms of the input and transfer structural mobility functions, respectively. When the structural mobility functions are used to represent the coupling between the substructures, the power flow analysis does not require frequency or spatial averaging.

The modal expansion method is another analytical technique for the vibration and power flow analysis of coupled or stiffened plate systems (Guyader *et al.*, 1982; Wang *et al.*, 2002; Rook & Singh, 1996; Lin, 2008). Wang *et al.* (2002) examined the power flow characteristics of L-shaped plates by complementing normal dynamic equations with geometric compatibility equations. In their technique, both out- and in-plane displacements are expressed as the superposition of principle mode shapes. As a result, a power flow density vector is derived to illustrate the power flows in the plate by combining the force balance and geometric compatibility conditions at the coupling edge. Rook and Singh (1996) discussed the modal truncation issues in synthesis procedures for the vibratory power flow and dissipation. They pointed out that the truncation of the component modes in synthesis techniques may cause significant errors in the calculations of localized harmonic vibration responses and power flows. As a remedy, they used different linearly independent basis functions such as eigenvectors and

Lanczos vectors to describe motions in different components with constrained boundary conditions at their interfaces. Accordingly, the completeness and convergence of the modal superposition have been greatly improved. A simple analytical solution was developed by Lin (2008) to predict the vibration response of finite periodic irregular ribbed plates by employing the modal expansion technique. While closed form solutions are obtained in terms of the input mobility and kinetic energies of a ribbed plate, contributions of the modal coupling force and moment at each rib location to the ribbed plate response are explicitly considered in the solution. He identified two groups of wave propagation zones according to the two coupling mechanisms at the beam/plate interfaces: shear force couplings and moment couplings.

Analytical methods based on the use of receptance theory have been developed by Keane (1992) for coupled beams and by Farag and Pan (1998) for coupled rectangular plates. Other techniques, such as the transfer matrix method (Xie, 1998) and the Rayleigh-Ritz method (Bhat, 1982; Langley, 1989), have also been adopted to investigate the vibration and power flows in stiffened plate systems.

Various aspects of stiffened plate vibrations have been explored by many researchers. Goyder and White (1980) studied impacts of the force and torque (moment) excitations on the power flows in beam-stiffened plates. Using a numerical integration for structural intensities, Xu *et al.* (2004 & 2005) investigated the effects on power flow paths of the stiffeners with different geometrical parameters and reinforced directions. The influence of irregular spacing or misplaced stiffeners on vibratory response and energy transmissions of a periodic stiffened plate was studied by Hodges and Woodhouse (1983), Lin (2008), Xie (1998), and Bhat (1982).

Although vibrations of stiffened plates have been extensively studied for decades, most of the reported investigations are based on the condition that plates are simply supported along at least a pair of opposite edges. There is a lack of studies on whether the vibration of a stiffened plate will behave meaningfully different under other boundary conditions or how it can be affected by the non-rigid coupling conditions between a plate and the reinforcing beams. This section is to extend the work of section 5.1 to the power flow analysis of periodically reinforced plates. The power flows and kinetic energy distributions are studied against certain factors such as boundary conditions for beams/plate, beam-plate coupling configurations. When a plate has multiple periodically placed beam stiffeners, it typically displays the "pass" and "stop" bands over which the wave propagations can and cannot occur, respectively (Langley, 1994). However, if dislocation exists due to a slight misplacement of a stiffener or deviations of its property from the standard value, it can blur the "propagation" and "non-propagation" zones leading to vibration localizations. The effect of the misplacement of stiffeners on the "pass" and "stop" bands will also be discussed in this section.

5.3.2 Calculating power flows and kinetic energies of the beam-plate system

Once vibrations are known for the plate and beams in section 5.1.2, other variables of interest such as the power flows through the junction or in the plate can be calculated easily, especially in view of the current analytical form of solutions.

The time-averaged power input into the stiffened plate can be calculated from

$$\langle P_{in} \rangle = \frac{1}{2}\Re\left\{ f v^{*} \right\} \tag{5.22}$$

where f is the complex amplitude of the excitation force, the asterisk denotes the complex conjugate, and v is the velocity at the driving location.

The expression for the structural intensity along the *x*-axis, which corresponds to the power flow per unit width of the plate including both flexural and in-plane components, is given by

$$I_x(x,y) = -\frac{1}{2}\Re\left\{Q_x \dot{w}_p{}^* - M_{xx}\left(\frac{\partial \dot{w}_p}{\partial x}\right)^* - M_{xy}\left(\frac{\partial \dot{w}_p}{\partial y}\right)^* + N_{xx}\dot{u}^* + N_{xy}\dot{v}^*\right\} \tag{5.23}$$

where Q_x, M_{xx}, M_{xy}, N_{xx}, and N_{xy} respectively denote shear force, bending moment, torsional moment, in-plane normal and shear forces, and defined by

$$Q_x = -D_p\left(\frac{\partial^3 w_p}{\partial x^3} + \frac{\partial^3 w_p}{\partial x \partial y^2}\right) \tag{5.24}$$

$$M_x = -D_p\left(\frac{\partial^2 w_p}{\partial x^2} + \mu\frac{\partial^2 w_p}{\partial y^2}\right) \tag{5.25}$$

$$M_{xy} = -D_p(1-\mu)\frac{\partial^2 w_p}{\partial x \partial y} \tag{5.26}$$

$$N_{xx} = \frac{E_p h}{1-\mu^2}\left(\frac{\partial u_p}{\partial x} + \mu\frac{\partial v_p}{\partial y}\right) \tag{5.27}$$

$$N_{xy} = \frac{E_p h}{2(1+\mu)}\left(\frac{\partial u_p}{\partial y} + \frac{\partial v_p}{\partial x}\right) \tag{5.28}$$

The expression of the structural intensity along the *y*-axis can be derived similarly and will not be given here for conciseness. The power flow across any cross section of the plate can be obtained by integrating the structural intensity over its entire length. For instance, the time averaged total power flow across the line $x = x_0$ is thus expressed as

$$\left\langle P_{x=x_0}\right\rangle = \int_0^b I_x(x_0, y)dy \tag{5.29}$$

Since the kinetic energy is directly associated with the velocity response of a structure, it is a convenient and useful quantity to describe structural dynamic behaviors (Carcaterra & Sestieri, 1995; Lin, 2008). The time averaged and steady state kinetic energy of any given area on the plate can be obtained by rewriting Eq. (5.7)

$$\langle T_S \rangle = \frac{1}{2}\int_S \rho_p h\left[\dot{w}_P{}^2 + \dot{u}_P{}^2 + \dot{v}_P{}^2\right]dS \tag{5.30}$$

The time averaged and steady state kinetic energy of a beam including flexural, axial, and torsional vibrations can be similarly calculated from Eq. (5.9).

5.3.3 Results and discussions

A rectangular plate with four beam stiffeners evenly distributed in the *x*-axis direction will be employed as an exemplary structure throughout the chapter, as shown in Fig. 5.14. The plate has a uniform thickness $h = 0.01\,\mathrm{m}$, length $a = 2\,\mathrm{m}$, and width $b = 1\,\mathrm{m}$. Each of the beam stiffeners has a rectangular cross section $S = 0.1 \times 0.01\,\mathrm{m}^2$. The material properties for the plate and beams are given as: $E_p = 207\mathrm{GPa}$, $\rho_p = 7800\mathrm{kg/m}^3$, $\mu = 0.3$, and $G_b = E_b / [2(1+\mu)]$ for beams and $G_p = E_p h / [(1-\mu^2)]$ for the plate, respectively. A structural damping $\eta = 0.01$ is assumed for both the plate and stiffening beams. The boundary conditions of the plate are described by four capital letters; for instance, SCFF indicates that the plate is simply supported at *x* = 0, clamped at *y* = *b*, free at *x* = *a* and *y* = 0.

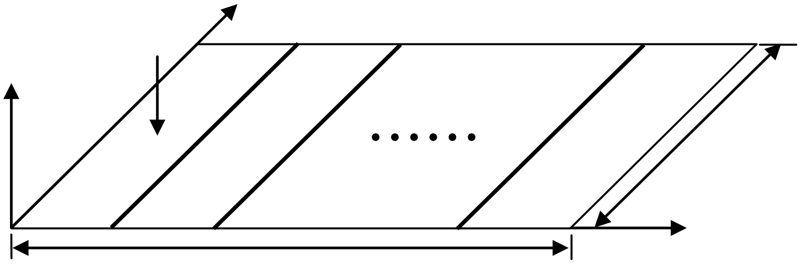

Figure 5.14 Schematic of a periodically stiffened plate

Table 5.10 lists the first six non-dimensional frequency $\Omega=\left(\omega L_b^2/\pi^2\right)\sqrt{\rho_p h/D_p}$ for the stiffened plate simply supported along each edge. FEA results obtained using an ANSYS model are also given there for comparison. In the FEA model, the plate and beam elements are selected as SHELL63 and BEAM4, respectively. A good agreement is observed between these two sets of results. The first four mode shapes are plotted in Fig. 5.15.

Table 5.10 Non-dimensional frequency, $\Omega=\left(\omega L_b^2/\pi^2\right)\sqrt{\rho_p h/D_p}$, for a SSSS rectangular plate stiffened by four equally spaced *y*-wise beams

$\Omega=\left(\omega L_b^2/\pi^2\right)\sqrt{\rho_p h/D_p}$					
1	2	3	4	5	6
11.6716[a]	11.6781	11.9630	12.2888	12.3135	17.1861
11.7051[b]	11.7062	11.9772	12.3931	12.4013	17.3042

[a] Results of current method

[b] Results from ANSYS with 100×50 elements

The existing vibration analysis of periodically reinforced plate have been mostly restricted to the cases in which a plate is simply supported at least along two edges perpendicular to the reinforcements. In comparison, the current method is able to handle any boundary conditions, as illustrated in the following examples.

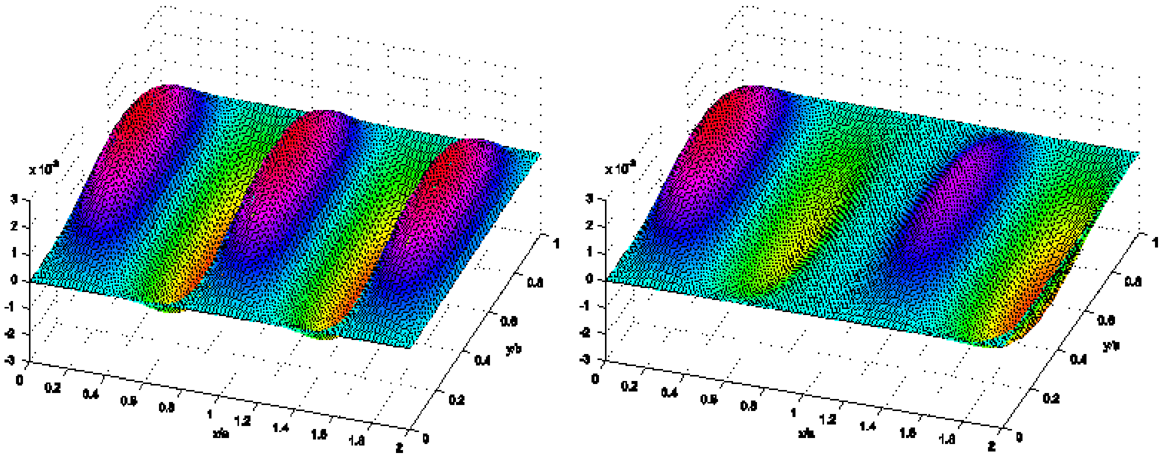

(a) (b)

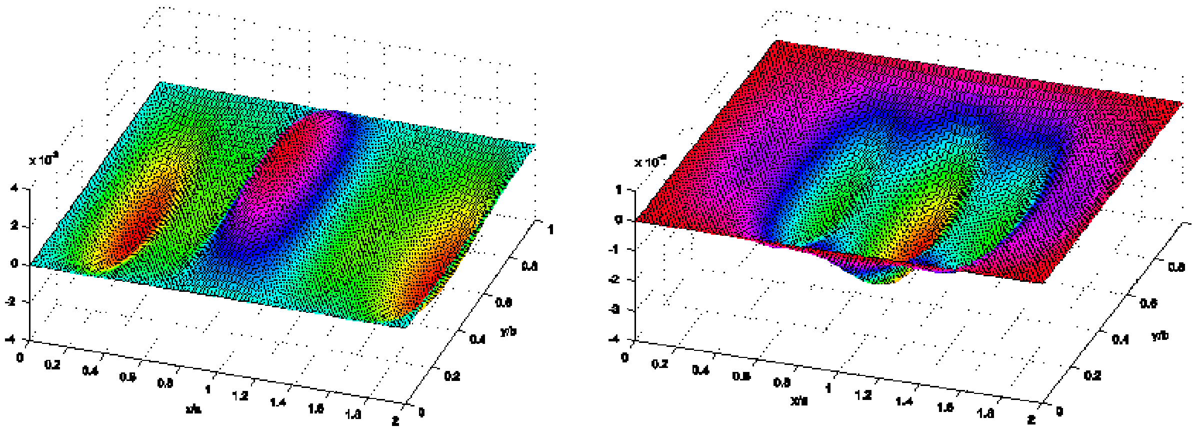

(c) (d)

Figure 5.15 Mode shapes for a SSSS rectangular plate stiffened by four evenly distributed *y*-wise beam. (a) 1st mode; (b) 2nd mode; (c) 3 rd mode; (d) 4th mode

The stiffened plate concerned here is simply supported at a pair of edges along the *y*-axis, and elastically restrained at the other pair of edges along the *x*-axis. While the stiffnesses for the bending and in-plane springs are set to zero and infinity ($ka^3/D_p = 10^6$), respectively, the flexural restraining spring stiffness is considered as a series of different levels with ka^3/D_p varying from 0 to 10^6. A normal harmonic unit force is applied at a position (0.2m, 0.7m) on the plate. The power flow in the stiffened plate is studied by the ratio of the power transmitted through the center line of each section to the input power.

Plotted in Fig. 5.16 is the power transmitted through the center line of the third section normalized by the input power for a range of restraining stiffnesses. The power transfer ratios of other bays were also calculated but not shown here because of the similarity found in results. It is seen that for weaker restraint $ka^3/D_p < 4000$, the (input) power travels almost freely downward in the *x*-direction in the frequency range below $\Omega = 40$. As the spring stiffness increases, some pass and stop bands start to develop although their widths vary considerably. It should be noted that the pass/stop bands in this case are not as remarked as they are for an infinite or semi-infinite ribbed plate. This is because when the plate has finite dimensions, the waves reflected from the boundaries tend to blur the pass/stop bands, indicating the incapability of the classical periodic theory in predicting the rich vibration characteristics of finite periodically stiffened plates (Wu & White, 1995; Lin, 2008). The power transfer ratios for other sections were also calculated, and they exhibited the similar characteristics.

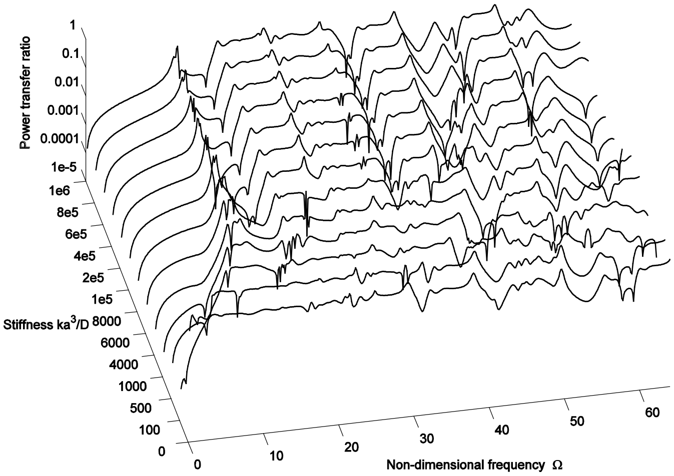

Figure 5.16 The ratio of the power transmitted through the 3rd bay to the input power against the stiffness of elastic springs along the edges $y = 0$ and $y = b$

Kinetic energy distribution can be used as a measure of energy dissipation, and hence another means of illustrating the structural power flows. For the stiffened plate considered in this case, the vibration energy of each stiffening beam contributes to only a small fraction of the total vibration energy of the stiffened plate. Thus, beam kinetic energies are not included in the kinetic energy distribution calculations in the subsequent analysis (Lin, 2008).

Fig. 5.17 shows the ratios of the kinetic energy for each section to the total kinetic energy for four different elastic stiffness values: ka^3/D_p=0, 10^3, 10^5, 10^6. Consider the weak elastic restraints as in Figs. 5.17a and 5.17b. The kinetic energies in each bay are basically comparable in the frequency range up to Ω=40. In other words, kinetic energies are evenly distributed and input power uniformly dissipated in each bay. The corresponding frequency range is often

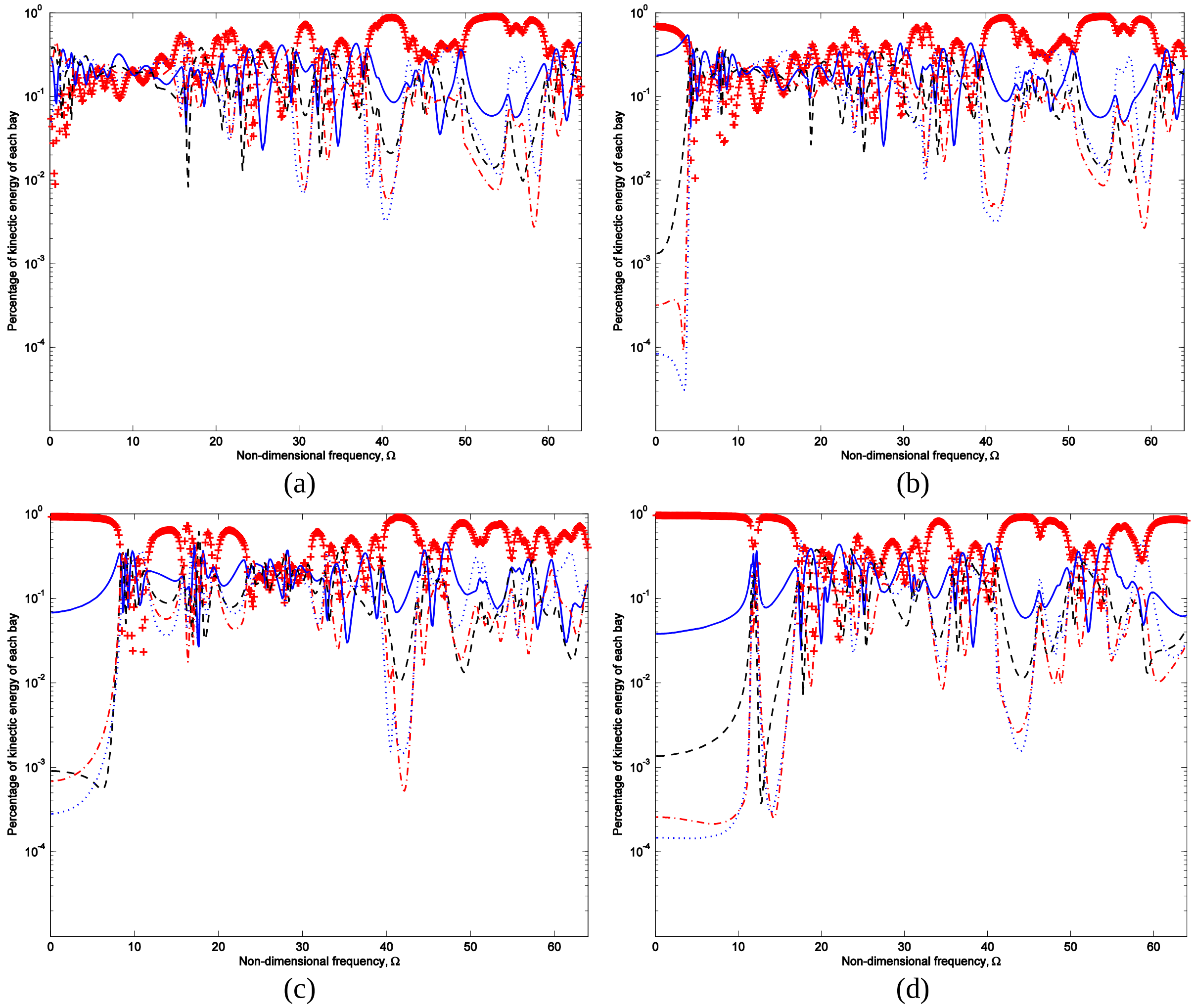

Figure 5.17 The ratio of the kinetic energy of each bay to the total kinetic energy of the plate for different stiffnesses for the elastic restraints at $y = 0$ and $y = b$, + : 1st bay, ― : 2nd bay, --- : 3rd bay, ―·― : 4th bay, ···· : 5th bay, (a) SFSF; (b) $ka^3/D_p = 1000$; (c) $ka^3/D_p = 10^5$; (d) $ka^3/D_p = 10^6$

referred to as a pass band in which the vibration energy can be transmitted easily from one section to another. On the other hand, as evident from Figs. 5(a) and 5(b), the source bay can completely dominate the total kinetic energy in a frequency range, for example, from Ω=0 to 10. In such a frequency range, the so-called stop band, the input power is basically trapped locally without traveling out to the rest of the structure.

As the spring stiffness increases, as shown in Figs. 5.17c and 5.17d, the stop/pass bands tend to occur more frequently and become narrower. It is interesting to note that the first stop band covers the lowest frequencies, and its width increases with the spring stiffness. This phenomenon may be explained as follows. When the restraining stiffness is small, the stiffened plate behaves like a one-piece structure. As a result, a load applied to one location is easily felt at another point via the global motion of the plate, and the reinforcing beams manifest themselves primarily in "slightly" modifying the plate response in the form of added structural features. However, when the restraining stiffness become sufficiently large, the (simply supported–like) boundary conditions for the plate are also directly applicable the beams. Thus, each of the sections divided by beams essentially represents an isolated structure until the beams become actively involved at adequately high frequencies. The extreme scenario is that when the beams and the elastic restraints are infinitely rigid, the five sections of the plate will then become totally uncoupled with each having the clamped boundary condition along the beam(s). This should explain the appearance of the first stop bands in Figs. 5.17(b-d) and the increase of their widths with the restraining stiffness.

A careful comparison of Figs. 5.16 and 5.17 will confirm the close correlation between the power flow and kinetic energy distributions. The Impact of plate boundary conditions on the structural power flows in a stiffened plate can also be effectively understood by studying the structural intensity filed. The structural intensity at any point is readily calculated using Eq. (5.23) since the related derivatives can be analytically obtained by directly differentiating Eqs. (4.4-4.6). Plot of structural intensity allows a direct visualization of vibrational power flows. Take the previous problem for example. Figures 5.18a and 5.18b show typical structural intensity fields for a frequency, *e.g.*, $\Omega = 13$, in a pass band. When the elastic restraint becomes stronger, frequency $\Omega = 13$ moves into the stop bands. The corresponding structural intensity fields are

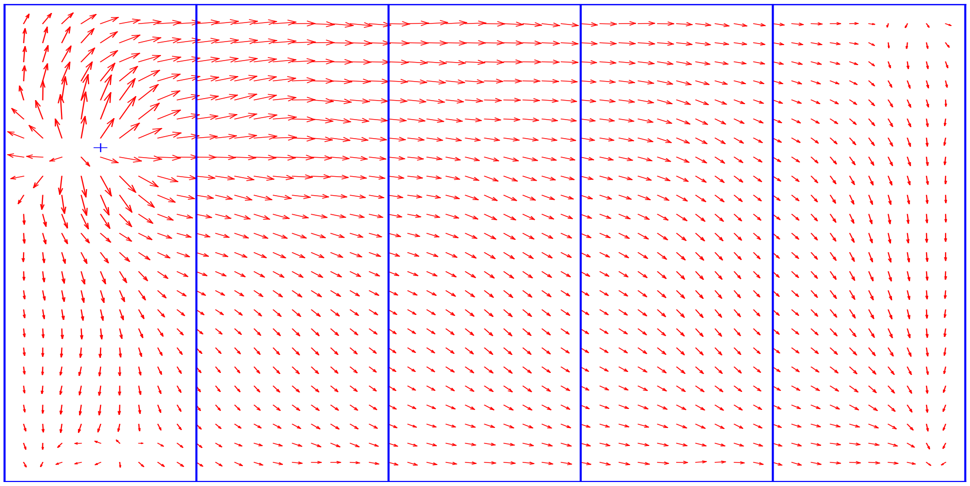

(a)

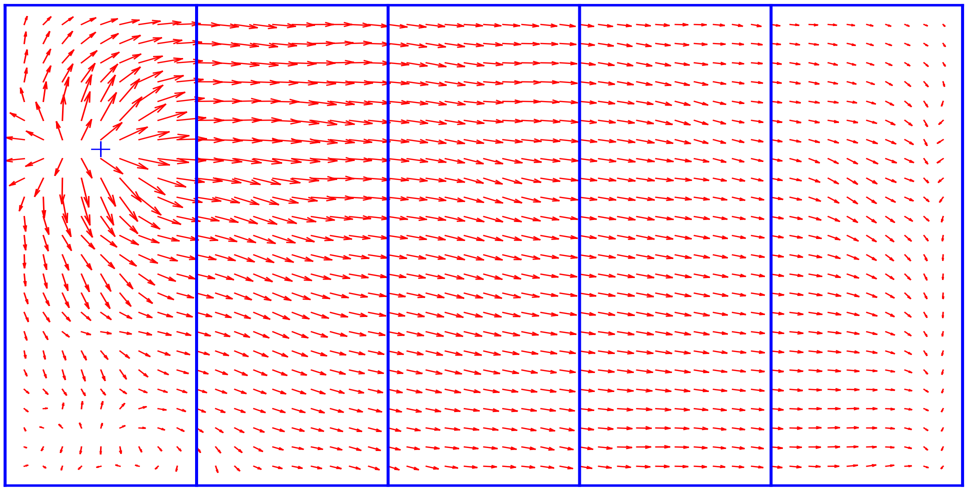

(b)

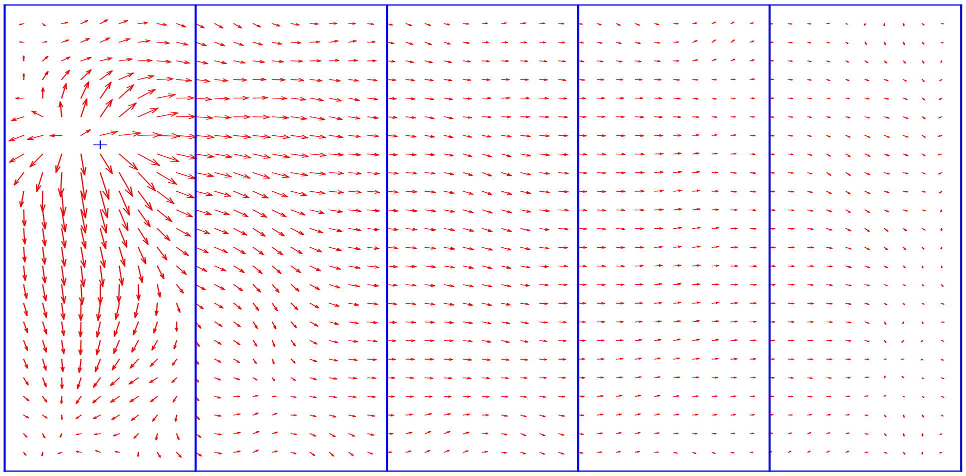

(c)

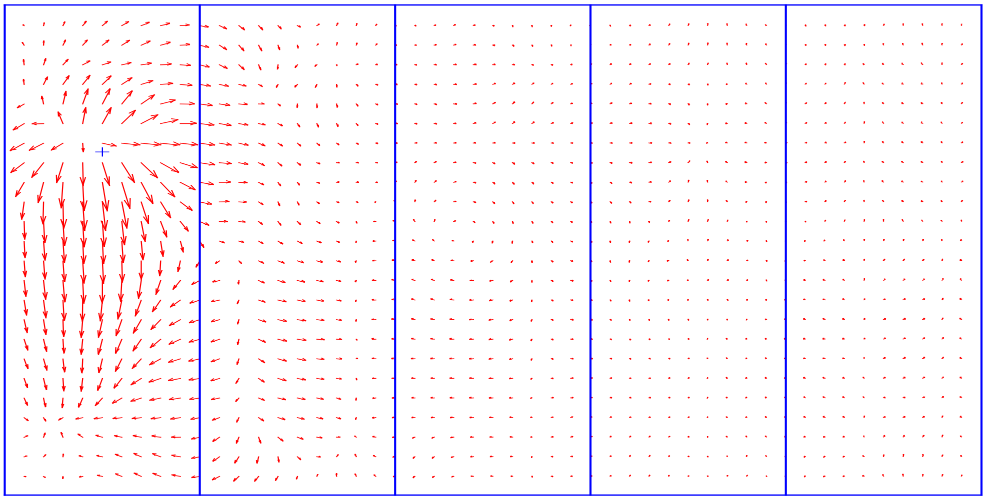

(d)

Figure 5.18 The structural intensity of a four-beam stiffened plate with elastic restrained stiffness along $y = 0$ and $y = b$ with an excitation at (0.2m, 0.7m), (a) SFSF; (b) ka^3/D_p=1000; (c) $ka^3/D_p=10^5$; (d) $ka^3/D_p=10^6$

plotted in Figs. 5.18(c) and 5.18(d).

In addition to being elastically coupled to the plate, any and all reinforcing beams can be independently supported at ends in the current model to account for some practical complications. Next example is to examine the impact on the structural power flow of the boundary conditions imposed upon the beams. Specifically, the plate is assumed to be simply supported along each edge and the beams subjected to two kinds of boundary conditions: free and clamped.

The power transmission (normalized by the input power) through the center line of the 3rd bay is plotted in Figs. 5.19a and 5.19b for two different excitation locations at (0.2 m, 0.5 m) and (0.2 m, 0.7 m). It is seen that the beam boundary conditions can significantly affect the power transmission characteristics of the periodically reinforced plate. For example, as shown in Fig. 5.19(a), the modification of beam boundary condition from free to clamped can turn a stop band, $13<\Omega<19$, (pass band, $21<\Omega<25$) into a pass (stop) band. On the other hand, it is also possible that the "extra" restraints imposed on the beams may virtually have no effect on some pass

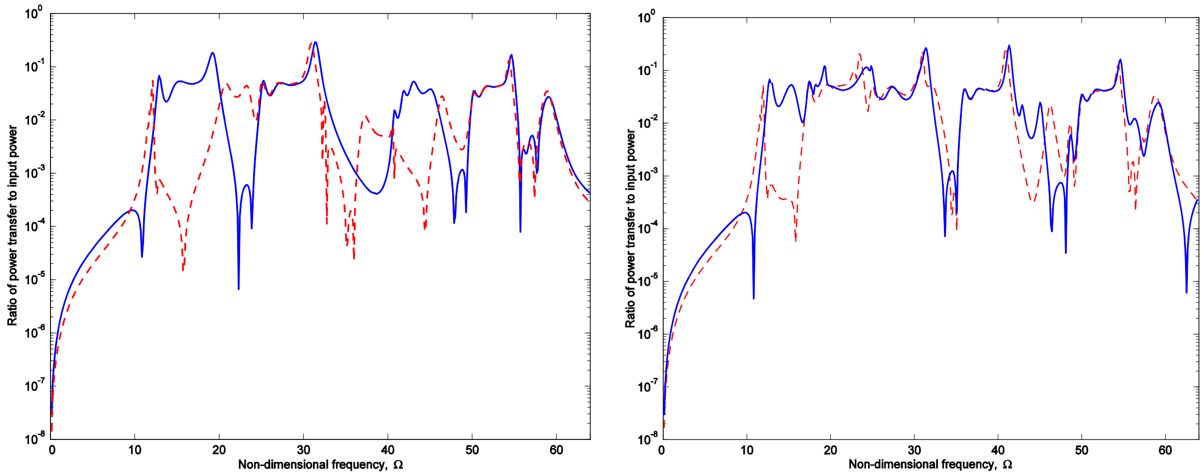

(a) (b)

Figure 5.19 The ratio of the power transferred through the 3rd bay to the input power of an SSSS plate with stiffeners having clamped and free boundary conditions at ends, — : clamped, ---: free, (a) excitation at (0.2m, 0.5m); (b) excitation at (0.2m, 0.7m)

bands, *e.g.*, $50<\Omega<56$. In comparison, the beam boundary conditions have a relatively smaller influence on the power transmission for the off-set excitation location (refer to Fig. 5.19(b)). Another important observation is that the power transmission is strongly dependent upon the location of an applied load. For instance, while the first pass band (for the plate with unrestrained beams) is located in $21<\Omega<32$ for the excitation at (0.2m, 0.5m), it expands over $17<\Omega<32$ for the excitation at (0.2m, 0.7m). Thus, stop/pass bands shall not be considered the inherent properties of a periodically reinforced plate; they are also affected by loading conditions.

The influence of beam restraints on the structural intensity is demonstrated in Fig. 5.20 for the excitation position (0.2 m, 0.7 m). It is seen that due to the removal of the restraints from the beams, the power flow pattern is noticeably modified, for example, at frequency $\Omega = 46.43$ which corresponds to the small peak at the end of the 2nd pass band on the solid curve.

In order to further understand the impact of the beam restraints, power flow ratio curves for the excitation at (0.2 m, 0.5 m) are plotted in Fig. 5.21 as a function of the stiffness of beam restraining springs. The stiffness values of restraining springs, $K_{y'}^b, K_{z'}^b, K_{x'}^b, k_{z'}^b, k_{y'}^b$, and $k_{x'}^b$, are simultaneously increased from 0 to $ka^3/D_p = 10^5$ (or $Ka/D_p = 10^5$). It is evident that the power flows are almost unaffected by the beam restraints in the frequency bands $25 < \Omega < 33$ and $50 < \Omega < 64$. The emergence of a pass band, $13 < \Omega < 19$, is clearly shown as the beam restraints become increasingly strong.

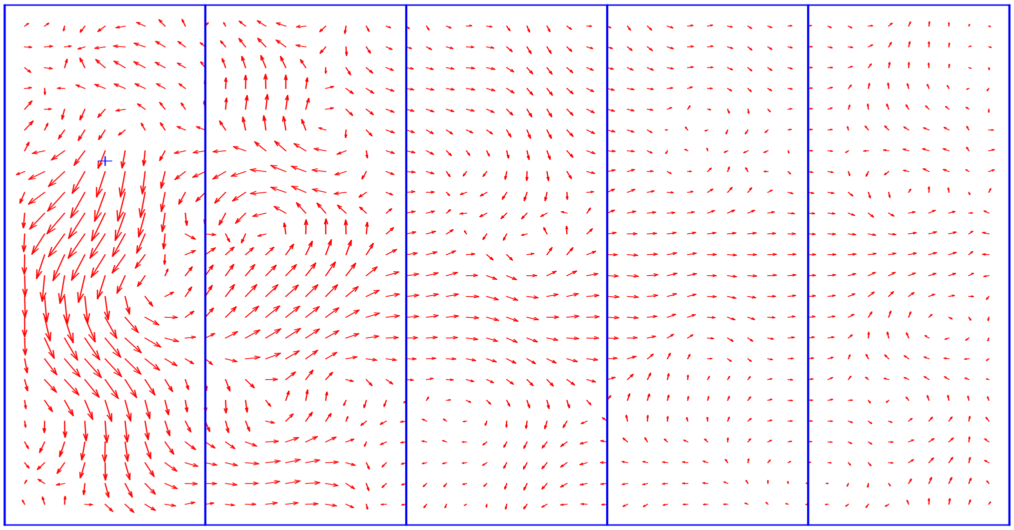

(a)

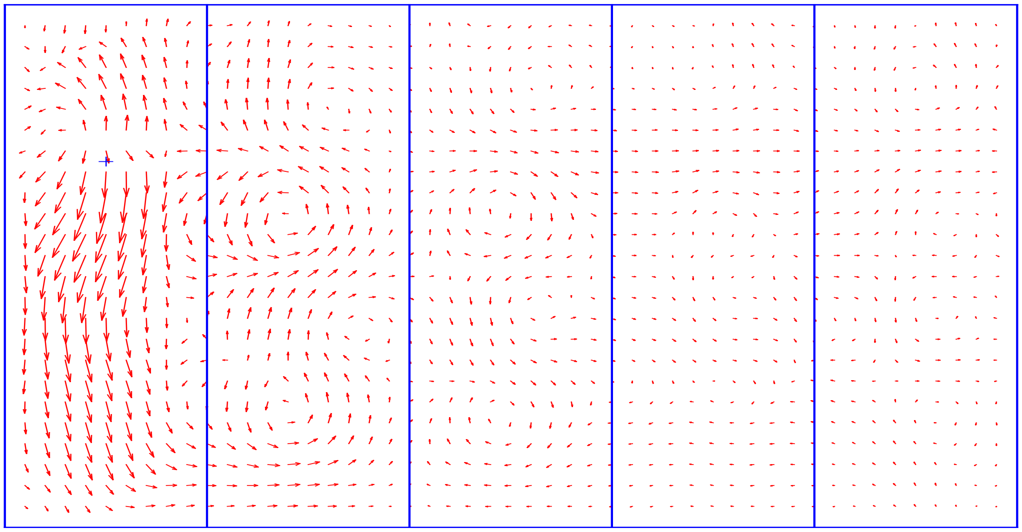

(b)

Figure 5.20 The structural intensity on an SSSS stiffened plate with an excitation at (0.2m, 0.7m), (a) Ω = 46.43, beams clamped at ends; (b) Ω = 46.43, beams being free at ends

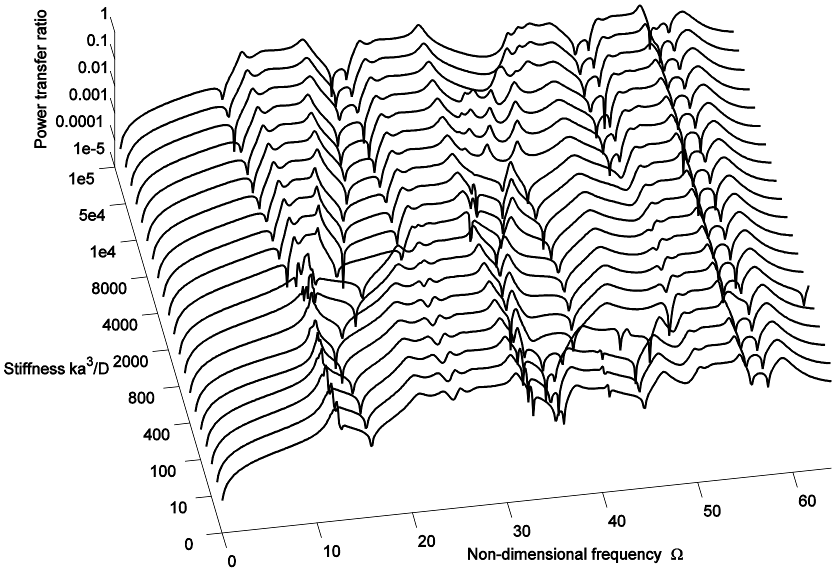

Figure 5.21 The ratio of the power transferred through the 3rd bay to the input power of an SSSS plate with elastically restrained stiffeners at both ends; the excitation at (0.2m, 0.5m)

In the current study, the plate-beam couplings are generally considered as being flexible. This treatment may be of practical importance when beams are glued or similarly bonded onto the plate. The effect of coupling strength will be examined in the following example where the plate is simply supported along each edge, and the reinforcing beams are all fixed to the ground at the ends. The ratio of beam bending to plate bending rigidities is chosen as $D_{by',i}/D_p$ = 42.2, and beam torsional to plate bending rigidities $G_{b,i}J_i/D_p$ = 3.53. To simplify the discussions, only the flexural coupling spring $k_{z'}^{pb}$ is considered flexible here and all the other springs are assumed to be infinitely rigid.

In Fig. 5.22, the ratio to the input power of the power transferred through the 3rd bay of the simply supported plate is plotted as a function of the stiffness of the coupling spring $k_{z'}^{pb}$. The unit force is applied at (0.2 m, 0.5 m), and each of beam stiffeners are clamped at both ends. For $ka^3/D_p \leq 100$, the beams have a negligible effect on the power flows. In other words, the input power can virtually flow freely down through the 3rd bay over the entire frequency range considered.

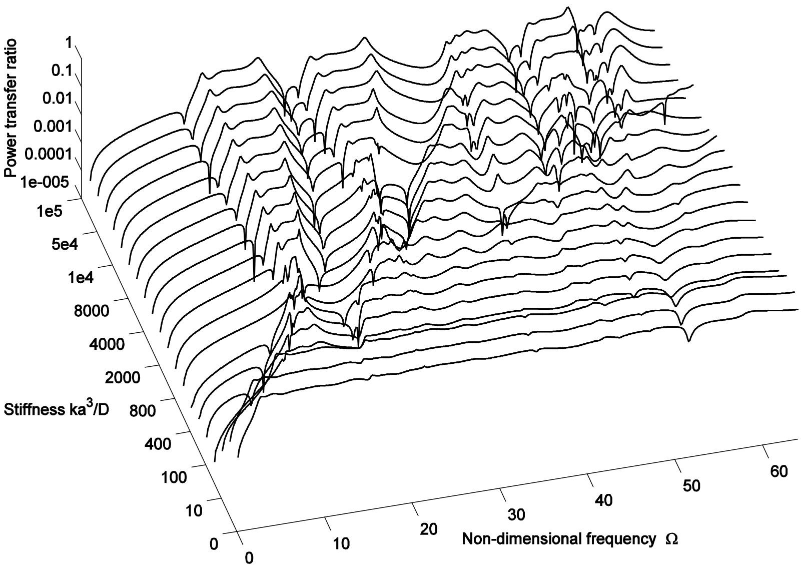

Figure 5.22 The ratio of the power transferred through the 3rd bay to the input power for an SSSS plate with elastic couplings at the beam-plate interface; the excitation is at (0.2 m, 0.5 m) and all stiffeners are clamped at both ends

It should be noted that the power flow ratio dips near $\Omega = 50$ indicating the power transmission is slightly "blocked" at this frequency. This is probably because the stiffeners elastically sitting on the plate behave like dynamic absorbers. As a consequence, the first two beams on the left of the 3rd bay will effectively consume certain portion of energies carried by the waves traveling to the right. As the coupling stiffness increases, near $\Omega = 20$ a stop band starts to form at ka^3/D_p = 400, and then evolves into a pass band at ka^3/D_p = 2000. A similar trend is also observed near $\Omega = 30$. Another interesting phenomenon is that the widths of the pass bands near $\Omega = 20$ and $\Omega = 30$ can increase with the coupling stiffness. These phenomena are of practical significance to the design of the periodically reinforced plate structures. Besides the traditional means of selecting appropriate structural parameters, engineers can also effectively design dynamic behavior, including the power transmission characteristic, of a stiffened plate structure through controlling the boundary conditions for the plate and beams, and the coupling conditions between them.

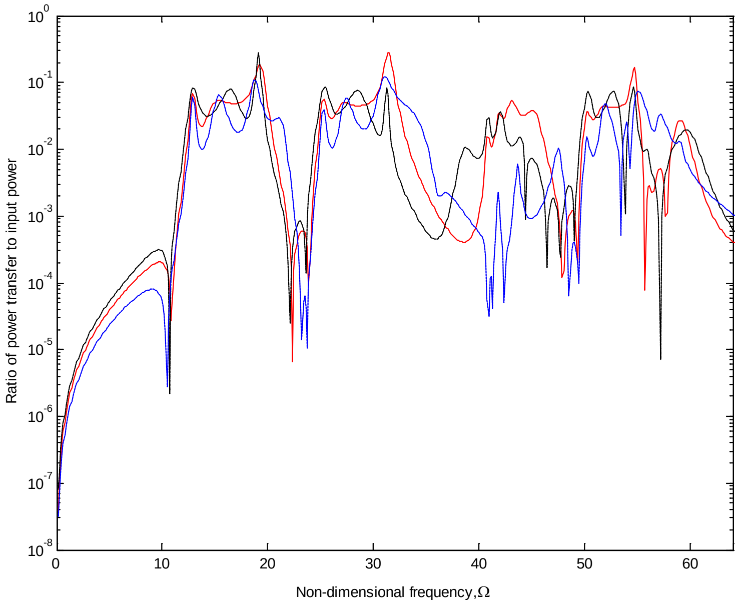

Figure 5.23 The ratio of the power transferred through the 3rd bay to input power for an SSSS plate with the first stiffener being slightly dislocated; the excitation is at (0.2m, 0.5m) and stiffeners are clamped at both ends: — : evenly spaced stiffeners, –·– : the first stiffener locates at x = 0.36m, --- : the first stiffener locates at x = 0.44m

The last example is used to demonstrate the influence of beam dislocations on the power flow of the structure. The simply supported plate with stiffeners fully restrained at ends is still used as an example here. While the dislocations may broadly represent any possible deviations of any variables from their ideal values, the current study is simply focused on the spatial dislocation due to the slight drifts of the 1st beam from its supposed position x = 0.4 m to x = 0.36 and 0.44 m to simulate installation errors or manufacturing imperfections in practice. The power transmission ratios are plotted in Fig. 5.23 for the regular and disordered positions. A common characteristic for the two disordered cases is that the moderate fluctuations occur in the pass bands. For the disordered location x = 0.36 m, the pass band, $40 < \Omega < 45$, noticeably shifts toward the lower frequency. In comparison, when the first beam is dislocated to x = 0.44 m, the third pass band has virtually disappeared, and the fourth is severely distorted to be recognizable.

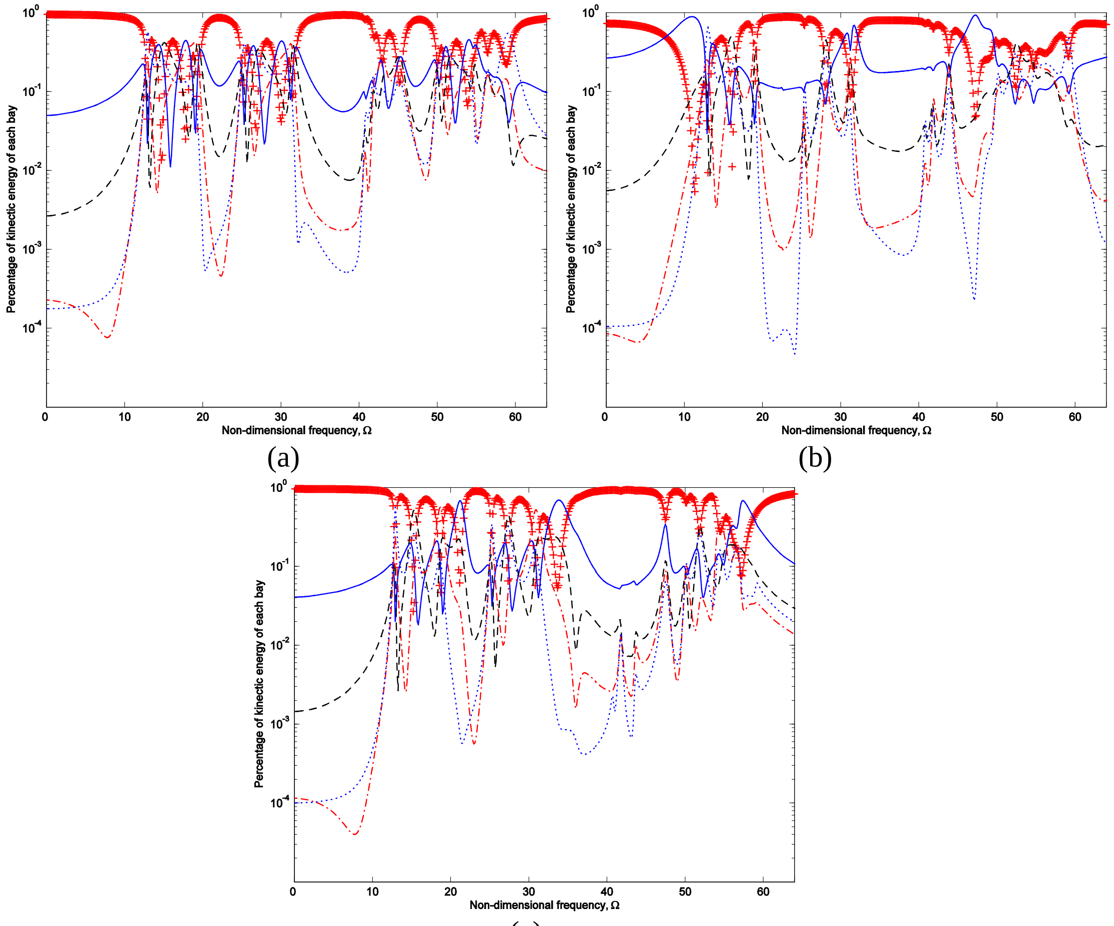

(a) (b)

(c)

Figure 5.24 The ratios of the kinetic energies on each bay to the total energy for an SSSS plate with the first stiffener being slightly dislocated; the excitation is at (0.2m, 0.5m) and stiffeners are fully clamped at both ends: + : 1st bay, — : 2nd bay, --- : 3rd bay, –·– : 4th bay, ···· : 5th bay, (a) Evenly distributed stiffeners (b) The first stiffener locates at x = 0.36m (c) The first stiffener locates at x = 0.44m

By examining the kinetic energy distributions on each section of the plate, one can also understand the effect of the stiffener dislocation on the vibrational power transmissions in both perfectly periodic and disordered cases. The above observations drawn from the power transmission ratios can be directly confirmed from the kinetic energy distributions presented in Fig. 5.24. In these plots, pass bands are identified as the frequency ranges in which the kinetic energies in each bay are of the same level. In contrast, in a stop band the kinetic energies on/near the source bay are substantially higher than those on the other bays.

5.4 Conclusions

A general analytical solution has been developed for the vibration analysis of a plate arbitrarily reinforced by beams of any lengths. All the flexural and in-plane (or axial and torsional) displacements are included in the plate and beam models to accurately take into account of the possible cross-couplings at the plate-beam interfaces. The boundary conditions for the plate and beams, and the coupling configurations between them are all generally specified in terms of elastic springs, thus allowing the creation of a unified solution method. Since each displacement component is invariably expressed as a modified Fourier series, the current method has effectively avoided many of the problems and difficulties resulting from the use of "appropriate" beam functions as typically required in other techniques. All the unknown expansion coefficients are treated equally as the generalized coordinates and determined from the Rayleigh-Ritz method. Since the constructed displacement functions are sufficiently smooth throughout the entire solution domains, secondary variables such as bending moments and shear forces (involving the second and third derivatives) can be directly calculated from the corresponding mathematical operations of the displacement functions. The accuracy and reliability of the proposed solution have been repeatedly demonstrated through numerical examples which involve various boundary conditions, coupling conditions, and reinforcement configurations.

This analytical model is also utilized to study the power flow of periodically stiffened plates. The power transmission ratio, kinetic energy distribution and structural intensity are used to study the power flow characteristics of the stiffened plates. While these three quantities are closely correlated in identifying pass/stop bands, it is preferred to use them collaboratively for a solid understanding of the local and global characteristics of the power flows in the stiffened plates.

This chapter has been specifically focused on several important, yet rarely attempted, design features which include plate boundary conditions, beam boundary conditions, excitation locations, coupling strength between the plate and beams, and the (spatial) dislocations of the reinforcements. It is demonstrated through numerical examples that each of these factors can have a direct impact on power transmission characteristics described in the forms of pass/stop bands, kinetic energies, and structural intensity fields. In particular, it is found that the increasing of the beam restraints can lead to a creation of new pass bands. Also, a stop band may be turned into a pass band as the coupling between the plate and beams becomes stronger. In the case of very weak couplings, beam stiffeners tend to have a negligible effect on the response of and power flows in the plate. However, they can behave like dynamic absorbers at a particular frequency. The effects of dislocation resulting from the misplacements of a reinforcing beam are also investigated based on numerical simulations. Not only can the dislocations cause moderate fluctuations in some pass bands, they may also severely distort and even virtually destroy a pass band. It appears that dislocations have a more remarked effect on the power transmissions than other design parameters such as beam and plate boundary restraints, coupling conditions between the plate and beams, *etc*. The observed phenomena are of practical significance to the design of the periodically reinforced plate structures, and provide additional means for controlling and designing the power transmission characteristics of stiffened plate structures.

CHAPTER VI

DYNAMIC RESPONSES OF BUILT-UP STRUCTURES WITH MODEL UNCERTAINTIES

6.1 Introduction

Traditional structural analyses are based on the assumption that the geometrical and material properties of a structure are deterministic and accurately specified. However, uncertain factors inevitably exist, to some degree, in any computational model in view of possible engineering and manufacturing errors, variance of material properties, fluctuating operating conditions, *etc*. Since the dynamic behavior of a system tends to becomes increasingly sensitive to model parameters as frequency increases, the uncertainties will have to be considered in predicting the mid- to high-frequency responses. Thus, it is necessary to take a statistic or stochastic approach in predicting the behavior and response of a dynamic system in the mid- and high-frequency regions.

Statistical Energy Analysis (SEA) is a dominant technique for the high-frequency analysis of complex structures. In SEA, the response of a dynamic system is described in terms of the frequency- and space-averaged energy levels for each subsystem, and it is assumed that the energy flow between two coupled subsystems is directly proportional to the difference in their modal energy levels (Scharton & Lyon, 1968). Central to the SEA method is the determination of coupling loss factors (CLF) which regulate energy flows between subsystems or modal (or wave) groups. The energy flow between any two subsystems is calculated as the product of the difference of their energy levels times the coupling loss factor. To a certain extent, the development of a SEA model is essentially equal to finding all the coupling loss factors between various subsystems. The coupling loss factors can be determined using one of the three major approaches: a) modal approach, b) wave approach, and c) impedance/mobility approach. In the modal approach, the coupling between two subsystems is expressed in terms of those between the individual modes of the uncoupled systems. To account for the statistical uncertainty, the effects of the modal interactions are typically processed through some averaging process against, for instance, frequency, spatial correlation, and loading condition (rain-on-the-roof). The ensemble averaging can also be accomplished through small perturbation of some model variables. For example, Newland (1968) demonstrated that the basic SEA relationship can be derived by considering the average shift of the modal natural frequency for each of the two subsystems. As a result, the SEA is considered to predict the ensemble averaged energy of the system responses. Usually, the system response is characterized as ergodic so that the ensemble-average can be realized by averaging over a frequency bandwidth. Since the modal approach is based on the modal characteristics of the uncoupled subsystems, the weak coupling condition is often assumed in advance. In the wave approach, the coupling loss factors are derived in terms of wave transmission coefficients (Mace, 1992). The wave approach is based on the observation that the impedance of a finite system behaves like that of the corresponding infinite systems when averaged over a sufficiently wide frequency range. Thus, by specifying a traveling wave impinging on a junction, the reflected and transmitted powers between the different wave components can be evaluated for various simple or complex dynamic systems. In the impedance or mobility approach, the dynamic properties of a system are determined from the transfer functions or the steady-state responses to an applied harmonic force. One or more (spatial, frequency, and/or, loading condition) averaging processes are then applied to the results to derive the quantities of statistical significance. In the wave and impedance approaches, the weak coupling condition is not necessary in deriving the coupling loss factors. In practice, coupling loss factors can be determined using, for example, the power injection method (Shankar & Keane, 1997; Bies & Hamid, 1980; Manik, 1998; Fahy, 1998), the energy level difference method (Craik, 1980), the mobility method (Cacciolati & Guyader, 1997), and the structural intensity technique (Ming, 1998). While the final system equation in the SEA is based on the powerful energy conservation principle, in the process the coupling loss factors are assumed to be unaffected by the configuration changes. In other words, it is assumed in the SEA process that the coupling loss factors calculated in isolation remain the same under the actual system environment. However, the validity of this assumption has been simply ignored in the previous literature, so it needs to be carefully studied because there is a belief that the SEA method can be readily extended to lower frequencies as long as the coupling loss factors can be somehow satisfactorily determined.

As the most popular method for investigating structural uncertainties, the Stochastic Finite Element Method (SFEM) is an extension of the classical (FEA) approach to stochastic problems by treating the model variables (mechanical, geometric and/or loading properties) and responses in a statistical manner. However, SFEM is difficult to apply to the mid- and high-frequency analyses of dynamic systems because the mesh has to be fine enough to spatially capture the essential details of the fluctuation of the random fields, which is not only computing intensive but also tends to yield a singular correlation matrix for highly correlated random variables. Since the quality of discretizing the stochastic fields can significantly affect the accuracy of the solution and the response statistics, the mesh size problems have received considerable attention in the SFEM research, and various schemes such as, the mid-point method, the nodal point method, the local average method, the interpolation method, and the weighted integral method have been proposed.

Monte Carlo Simulation (MCS), which was initially introduced to the structural dynamics by Shinozuka (1972), is widely used for determining the system response statistics through a deterministic mode. It is a quite versatile and simple tool capable of handling all types of stochastic dynamic problems. However, it is extremely expensive, or even prohibitive, when the dimension of vector random variables becomes very large. Fortunately, the efficiency of MCS can be substantially improved by the FSEM because of its extraordinary capability of reducing the size of the final system and the dimension of random variables.

In this chapter, the validity of the assumption in SEA that the coupling loss factors calculated in isolation remain the same under the actual system environment is first testified. Second, the FSEM combined with the Monte Carlo Simulation (MCS) is used for estimating the dynamic behaviors of built-up structures with uncertain model properties.

6.2 A revisit of coupling loss factors in determining power flows in structures

6.2.1 A closed form solution using the wave propagation approach

Horner and White (1991) as well as Doyle and Kamle (1987) expressed the relationship between bending and in-plane movements in terms of transmitted and reflected powers. The equations they developed are used here to find the wave transmission between different wave types.

The total power in the transversely vibrating beam can be separated into two parts associated with the shear force $EI\partial^3 W/\partial x^3$ and the bending moment $EI\partial^2 W/\partial x^2$, respectively. The instantaneous flexural power per unit length is defined as

$$P_f = \frac{1}{2}\Re e\left\{ EI\frac{\partial^3 W}{\partial x^3}\frac{\partial W^*}{\partial t} - EI\frac{\partial^2 W}{\partial x^2}\frac{\partial^2 W^*}{\partial x \partial t} \right\} \tag{6.1}$$

The far-field component of energy and power is dominant at high frequencies (Goyder & White, 1980). Therefore, by neglecting the near-field terms, the time-averaged far-field total flexural power is represented by

$$\langle P \rangle_f = EI\omega k_f^3 \left\{ \left|A_{ft}\right|^2 e^{2k_f x} - \left|A_{fr}\right|^2 e^{-2k_f x} \right\} \tag{6.2}$$

In the case of longitudinal vibration in a beam, the instantaneous and time-averaged longitudinal power flow can be respectively expressed as

$$P_l = \frac{1}{2}\Re e\left\{ -ES\frac{\partial U}{\partial x}\frac{\partial U^*}{\partial t} \right\},\ \langle P \rangle_l = \frac{1}{2}ES\omega k_l \left\{ \left|A_{lt}\right|^2 e^{2k_l x} - \left|A_{lr}\right|^2 e^{-2k_l x} \right\} \tag{6.3-4}$$

The instantaneous and time averaged far-field total flexural energy densities are, respectively,

$$E_f = \frac{1}{4}\left\{ EI\frac{\partial^2 W}{\partial x^2}\frac{\partial^2 W^*}{\partial x^2} + \rho S\frac{\partial W}{\partial t}\frac{\partial W^*}{\partial t} \right\}, \langle E \rangle_f = \frac{1}{2}\rho S\omega^2 \left\{ \left|A_{ft}\right|^2 e^{2k_f x} + \left|A_{fr}\right|^2 e^{-2k_f x} \right\} \tag{6.5-6}$$

The instantaneous and time averaged total longitudinal energy densities are, respectively,

$$E_l = \frac{1}{4}\left\{ ES\frac{\partial U}{\partial x}\frac{\partial U^*}{\partial x} + \rho S\frac{\partial U}{\partial t}\frac{\partial U^*}{\partial t} \right\},\ \langle E \rangle_l = \frac{1}{2}\rho S\omega^2 \left\{ \left|A_{lt}\right|^2 e^{2k_l x} + \left|A_{lr}\right|^2 e^{-2k_l x} \right\} \tag{6.7-8}$$

where k_f is the flexural wave number, $k_f = \sqrt{\omega}\left(\frac{\rho S}{EI}\right)^{1/4}$ (6.9)

k_l is the longitudinal wave number, $k_l = \omega\sqrt{\frac{\rho}{E}}$ (6.10)

A_{ft} , A_{fr} , A_{lt} and A_{lr} denote the amplitudes of the outgoing and incoming flexural and longitudinal waves, respectively.

First, let us consider a structure consisting of two semi-infinite beams coupled at an angle θ, as shown in Fig. 6.1. The materials are assumed to be homogeneous and isotropic, and Bernoulli's formulation is used to describe the vibrating behavior of the structure. A parametric study (Horner & White, 1991; Doyle & Kamle, 1987) showed that the structural response was relatively insensitive to the joint parameters below 10 kHz whether the joint has mass or not. For simplicity, the joint is considered massless in this study.

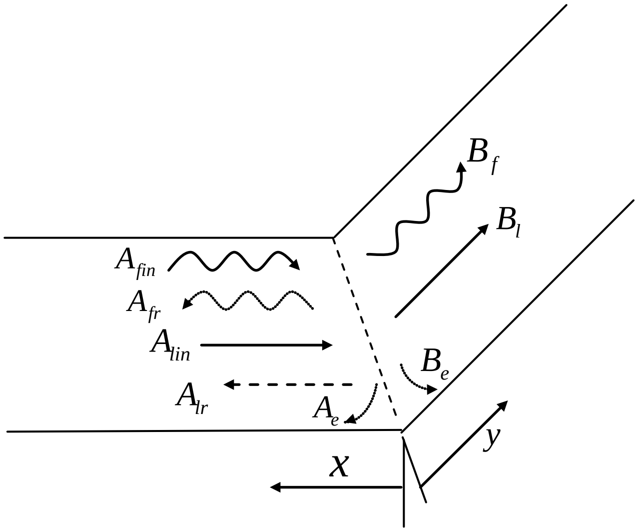

Figure 6.1 Wave motion in two coupled semi-infinite beams

Bending and longitudinal movements are respectively represented by a flexural wave $W(x,t)$ and a longitudinal wave $U(x,t)$, which can be written as

$$W_1(x,t) = \left\{A_e e^{k_{f1}x} + A_{fr} e^{ik_{f1}x} + A_{fin} e^{-ik_{f1}x}\right\} e^{-i\omega t} \tag{6.11}$$

$$U_1(x,t) = \left\{A_{lr} e^{ik_{l1}x} + A_{lin} e^{-ik_{l1}x}\right\} e^{-i\omega t} \tag{6.12}$$

$$W_2(y,t) = \left\{B_e e^{-k_{f2}y} + B_f e^{-ik_{f2}y}\right\} e^{-i\omega t} \tag{6.13}$$

$$U_2(y,t) = \left\{B_l e^{-ik_{l2}y}\right\} e^{-i\omega t} \tag{6.14}$$

where A_{fin} and B_f denote the amplitudes of the flexural wave; A_{lin} and B_l indicate the amplitudes of the longitudinal wave; A_e and B_e are near field flexural waves; A_{fin} and A_{lin} represent the flexural and longitudinal waves which may independently impinge on the joint.

By considering the conditions of continuity and equilibrium at the joint, the following equations are obtained

$$U_1 = U_2 \cos\theta - W_2 \sin\theta , \qquad W_1 = U_2 \sin\theta + W_2 \cos\theta \tag{6.15-16}$$

$$\frac{\partial W_1}{\partial x} = \frac{\partial W_2}{\partial y} , \qquad E_1 I_1 \frac{\partial^2 W_1}{\partial x^2} = E_2 I_2 \frac{\partial^2 W_2}{\partial y^2} \tag{6.17-18}$$

$$E_1 S_1 \frac{\partial U_1}{\partial x} = E_2 S_2 \frac{\partial U_2}{\partial y} \cos\theta + E_2 I_2 \frac{\partial^3 W_2}{\partial y^3} \sin\theta \tag{6.19}$$

$$- E_1 I_1 \frac{\partial^3 W_1}{\partial x^3} = E_2 S_2 \frac{\partial U_2}{\partial y} \sin\theta - E_2 I_2 \frac{\partial^3 W_2}{\partial y^3} \cos\theta \tag{6.20}$$

By substituting Eqs. (6.11-14) into Eqs. (6.15-20), six equations can be derived against an equal number of unknown amplitudes. The coefficient matrix is given in Appendix F.

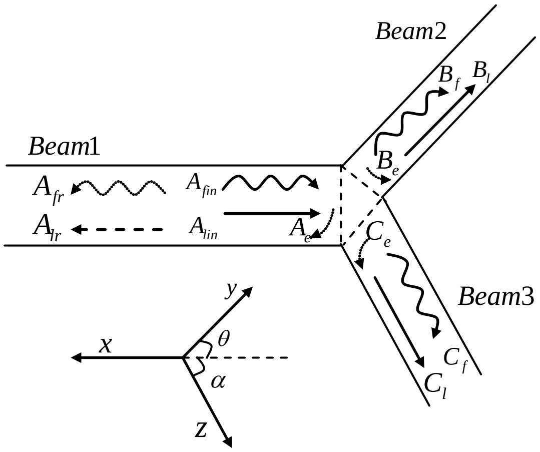

Figure 6.2 Wave motion in three coupled semi-infinite beams

For a branched joint shown in Fig. 6.2, the wave motions in each arm are given as

$$W_1(x,t) = \left\{ A_e e^{k_{f1}x} + A_{fr} e^{ik_{f1}x} + A_{fin} e^{-ik_{f1}x} \right\} e^{-i\omega t} \tag{6.21}$$

$$U_1(x,t) = \left\{ A_{lr} e^{ik_{l1}x} + A_{lin} e^{-ik_{l1}x} \right\} e^{-i\omega t} \tag{6.22}$$

$$W_2(y,t) = \left\{ B_e e^{-k_{f2}y} + B_f e^{-ik_{f2}y} \right\} e^{-i\omega t} \tag{6.23}$$

$$U_2(y,t) = \left\{ B_l e^{-ik_{l2}y} \right\} e^{-i\omega t} \tag{6.24}$$

$$W_3(z,t) = \left\{ C_e e^{-k_{f3}z} + C_f e^{-ik_{f3}z} \right\} e^{-i\omega t} \tag{6.25}$$

$$U_3(z,t) = \left\{ C_l e^{-ik_{l3}z} \right\} e^{-i\omega t} \tag{6.26}$$

In Fig. 6.2, the coupling angles between beams 1 and 2, and between beams 1 and 3 are denoted as θ and α , respectively. By considering the conditions of the continuity and equilibrium at the joint, the following equations are obtained

$$U_1 = U_2 \cos\theta - W_2 \sin\theta , \qquad U_1 = U_3 \cos\alpha - W_3 \sin\alpha \tag{6.27-28}$$

$$W_1 = U_2 \sin\theta + W_2 \cos\theta , \qquad W_1 = U_3 \sin\alpha + W_3 \cos\alpha \tag{6.29-30}$$

$$\frac{\partial W_1}{\partial x} = \frac{\partial W_2}{\partial y}, \quad \frac{\partial W_1}{\partial x} = \frac{\partial W_3}{\partial z}, \quad E_1 I_1 \frac{\partial^2 W_1}{\partial x^2} = E_2 I_2 \frac{\partial^2 W_2}{\partial y^2} + E_3 I_3 \frac{\partial^2 W_3}{\partial z^2} \tag{6.31-33}$$

$$E_1 S_1 \frac{\partial U_1}{\partial x} = E_2 S_2 \frac{\partial U_2}{\partial y} \cos\theta + E_2 I_2 \frac{\partial^3 W_2}{\partial y^3} \sin\theta + E_3 S_3 \frac{\partial U_3}{\partial z} \cos\alpha + E_3 I_3 \frac{\partial^3 W_3}{\partial z^3} \sin\alpha \tag{6.34}$$

$$-E_1 I_1 \frac{\partial^3 W_1}{\partial x^3} = E_2 S_2 \frac{\partial U_2}{\partial y} \sin\theta - E_2 I_2 \frac{\partial^3 W_2}{\partial y^3} \cos\theta + E_3 S_3 \frac{\partial U_3}{\partial z} \sin\alpha - E_3 I_3 \frac{\partial^3 W_3}{\partial z^3} \cos\alpha \tag{6.35}$$

Substituting Eqs. (21-26) into Eqs. (27-35), a set of nine simultaneous equations is obtained. The nine unknown wave amplitudes can be found directly from these equations. The matrix of the equations is given in Appendix F. Once the amplitudes of the transmitted waves are found, the wave transmission coefficients can be computed. The wave transmission coefficient τ_{ij} between any two wave components *i* and *j* is defined as the ratio of the power transmitted away from the junction by wave type *j* to the power carried towards the junction by an incident wave type *i* (Langley & Shorter, 2003). Combining Eqs. (6.2) and (6.4), the wave transmission coefficients can be written as

$$\tau_{ij} = \frac{\langle P \rangle_j}{\langle P \rangle_i} \tag{6.36}$$

By applying Eq. (6.36) to all possible beam pairs, a full set of junction transmission coefficients can be found. It should be noted that the transmission coefficient is reciprocal with $\tau_{ij} = \tau_{ji}$ (Cremer *et al.*, 1988). Analytically, CLF is defined as

$$\eta_{ij} = \frac{c_{gi}\tau_{ij}}{2\omega L_i} \tag{6.37}$$

where c_{gi} is the group velocity of the wave in beam *i*, L_i is the length of beam *i*, and τ_{ij} is the transmission coefficient across the joint relating the incident waves in subsystem *i* to the transmitted waves in subsystem *j*.

In SEA, the net power flow between two coupled subsystems *i* and *j* is written as

$$P_{coupl}^{ij} = \omega \eta_{ij} n_i \left(\frac{E_i}{n_i} - \frac{E_j}{n_j} \right) \tag{6.38}$$

where ω is the central angular frequency of the chosen constant percentage band (usually an octave or 1/3 octave), E_r is the time-averaged total energy stored in subsystem *r* (*r* = *i*, *j*), n_r is the modal density of subsystem *r*, and η_{ij} is CLF between subsystems *i* and *j*.

A T-junction involving three beams which was previously studied by Langley and Shorter (2003) is used to validate the current derivations. The T-junction is easily constructured by setting both θ and α as 90^0 (refer to Fig. 6.2). Beam properties are as follows: $E = 72\,\text{GPa}$, $\rho = 2710\,\text{kg/m}^2$, $S = 4 \times 10^{-4}\,\text{m}^2$, and $I = 3.48 \times 10^{-8}\,\text{m}^4$. Beam 1 is excited by an incident wave (flexural and longitudinal).

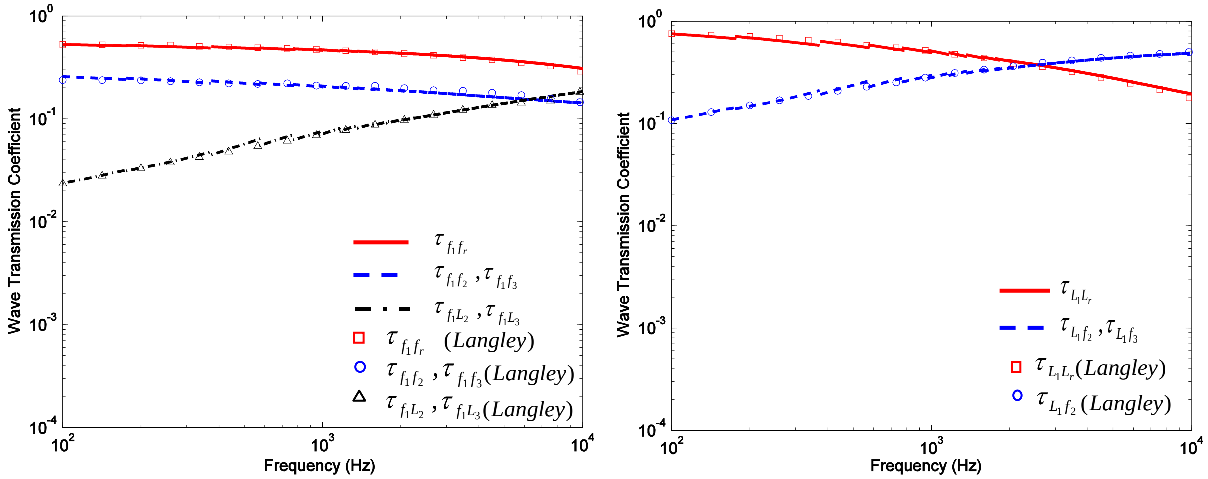

(a) (b)

Figure 6.3 Wave transmission coefficients for: (a) incident flexural wave; (b) incident longitudinal wave

Plotted in Fig. 6.3 are the calculated wave transmission coefficients as a function of frequency. The results match closely with those shown in Fig. 11 of Langley and Shorter (2003).

6.2.2 Effects on the wave transmission coefficient of adding an component to a joint

In Fig. 6.4, beams 1 and 2 are coupled at a right angle; beams 1 and 3 at 180^0 ; and beams 1, 2, and 3 in a T-shape. These three coupling types are represented as “L”, “—”, and “T” shaped beam structures. Assuming that a flexural or longitudinal wave with unit amplitude on beam 1 impinges upon the joint, transmission coefficients are calculated using Eq. (6.36) for L-, —-, and T-beams, respectively. The cross-sectional area and the moment of inertia are 10^{-5} m^2 and 10^{-10} m^4, for all beams, respectively.

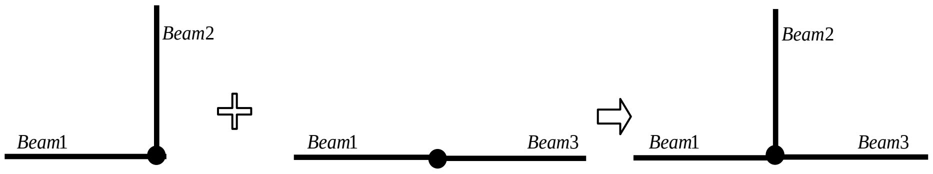

Figure 6.4 Beam assembling types for investigating wave transmission coefficients

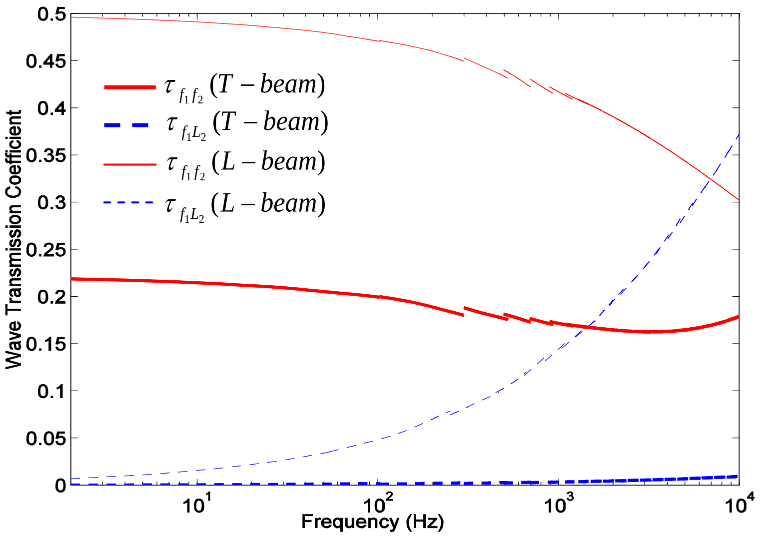

Figure 6.5 Comparison of WTCs between the L-beam and the T-beam

First, we examine the effects of the addition of beam 3 on the wave transmission coefficient between beam 1 and beam 2 by considering the L- and T- shaped beams. Beam 3 in the T-beam is viewed as an additional component added to the L-beam. Wave transmission coefficients between beam 1 and beam 2 are compared in Fig. 6.5. It can be seen that the characteristics of $\tau_{f_1f_2}$ and $\tau_{f_1L_2}$ are significantly different. For the L-beam, $\tau_{f_1f_2}$ starts from 0.5 and gradually reduces to 0.3. In comparison, $\tau_{f_1L_2}$ is relatively flat as frequency increases. At the point where $\tau_{f_1f_2}$ and $\tau_{f_1L_2}$ curves intersect, the same amount of the input power will be converted into the flexural and longitudinal power for L-shaped beam. Unlike the L-beam, both $\tau_{f_1f_2}$ and $\tau_{f_1L_2}$ vary only slightly for the T-beam. In particular, $\tau_{f_1L_2}$ is close to zero over the entire frequency range. Similar to L- and T- shaped beams, the effects of adding an additional component can also be investigated by considering the —- and T- shaped beams.

As shown in Fig. 6.4, beams 1 and 3 are coupled at 180^0 initially and form a T-beam when beam 2 joins in. Wave transmission coefficients between beam 1 and beam 3 are plotted in Fig. 6.6 for the —-, and T-shaped beams, respectively.

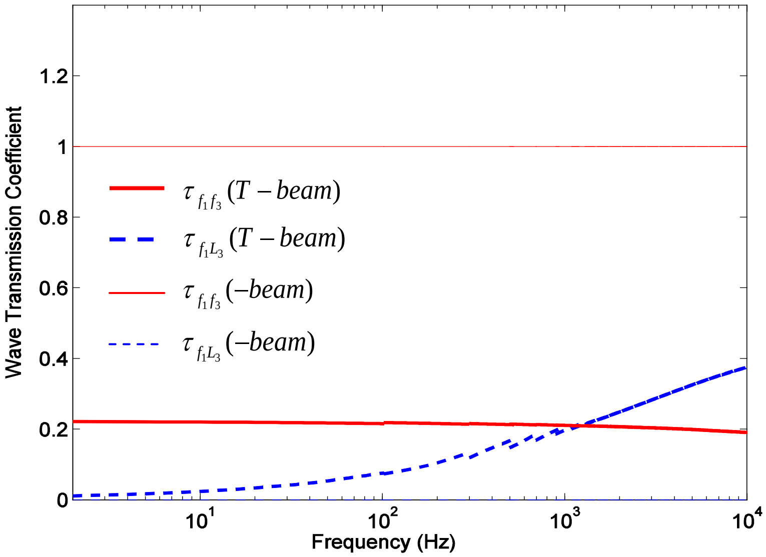

Figure 6.6 Comparison of WTCs between the —- beam and the T-beam

It can be seen that $\tau_{f_1f_3}$ equals one, and $\tau_{f_1L_3}$ equals zero over the entire frequency range indicating that all of the impinging flexural power from beam 1 is completely transmitted through the joint to beam 3 as flexural power. When beam 2 joins in, $\tau_{f_1f_3}$ drops from 1 to approximately 0.2, and $\tau_{f_1L_3}$ exhibits an increasing trend with frequency. It should be noted that in the T-beam, curves $\tau_{f_1f_3}$ and $\tau_{f_1L_3}$ intersect near 1000 Hz, which means the participation of beam 2 makes the two types of transmitted wave powers equal at this frequency.

Figs. 6.7 and 6.8 show the wave transmission coefficients when a impinging longitudinal wave is specified on beam 1. In Fig. 6.7, it can be seen that $\tau_{L_1f_2}$ in the L-beam increases much faster than that in the T-beam as frequency increases. In contrast, transmission coefficients, $\tau_{L_1L_2}$, for both the L- and T-beam are essentially negligible. Fig. 6.8 shows the wave transmission coefficients between beam 1 and beam 3 for the —- and T-shaped beams, respectively. The behaviors of $\tau_{L_1f_3}$ and $\tau_{L_1L_3}$ indicate that for two beams coupling horizontally, all the longitudinal power is completely transmitted through the joint to the longitudinal wave in beam 3, and

T-beam, $\tau_{L_1 f_3}$ and $\tau_{L_1 L_3}$ almost exhibit no variance with frequency.

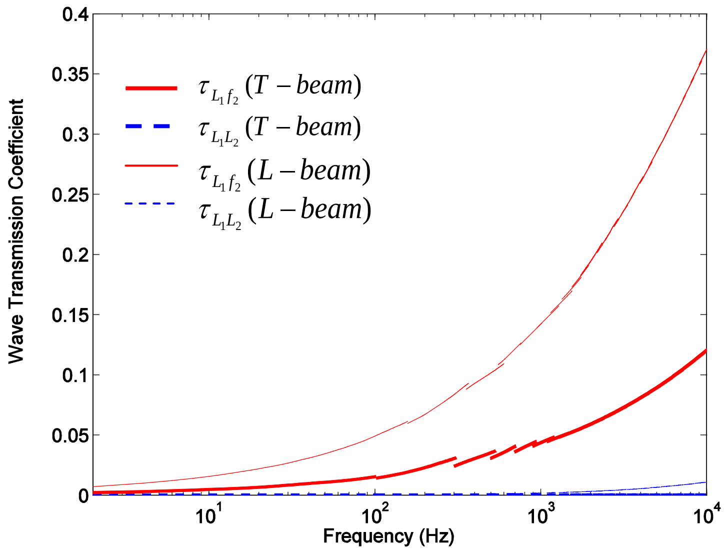

Figure 6.7 Comparison of WTCs between the L-beam and the T-beam

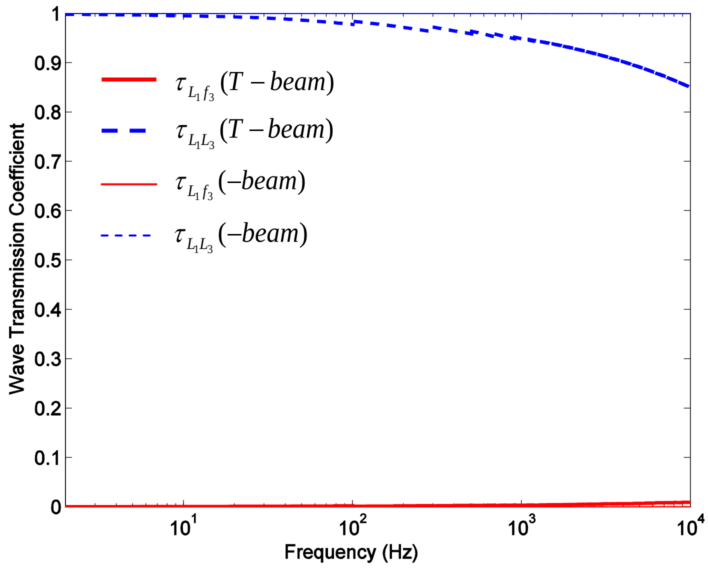

Figure 6.8 Comparison of WTCs between the —- beam and the T-beam

6.2.3 Power flow distributions in L-beam and T-beam

In this section, we will investigate the coupling loss factors from another perspective by considering the power flows. To investigate the power flows between the subsystems, let us construct an example of two and three beams assembled in different coupling fashions, as shown in Fig. 6.9.

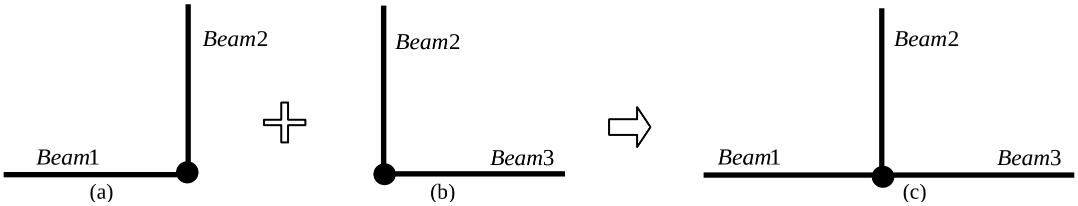

Figure 6.9 Beam assembling type for investigating power flow distributions

Table 6.1 Beam parameters and properties

Properties	Beam 1	Beam2	Beam3
$S(m^2)$	10^{-4}	10^{-5}	10^{-6}
$I(m^4)$	10^{-10}	10^{-10}	10^{-10}

Assume that a flexural wave in beam 2 impinges upon the joint. The wave transmission coefficients between beams 2 and 1 as well as between beams 2 and 3 are calculated for two pairs of L-beams, as shown in Figs. 6.9(a) and 6.9(b). For comparison, the wave transmission coefficients are also obtained for the T-beam given in Fig. 9(c). All beams are made of steel: E = 210GPa and $\rho = 7800\,\mathrm{kg/m^2}$. Other properties for the beams are listed in Table 6.1.

By comparing the results in Figs. 6.10 and 6.11, one can see that for the L-beam $\tau_{f_2 L_3}$ is much higher than $\tau_{f_2 L_1}$ over the whole frequency range, especially at the high frequency region, while $\tau_{f_2 f_1}$ and $\tau_{f_2 f_3}$ are almost the same. However, the situations are completely different for the T-beam, where $\tau_{f_2 L_3}$ drops close to zero, and $\tau_{f_2 L_1}$ becomes much higher than $\tau_{f_2 L_3}$. It is also noticed that the difference between $\tau_{f_2 f_3}$ and $\tau_{f_2 f_1}$ over the entire frequency range becomes much larger in the T-beam than for that of the L-beam cases. From those results, it is evident that the power flows in a system do not necessarily follow the rules established based on subsystem-level predictions.

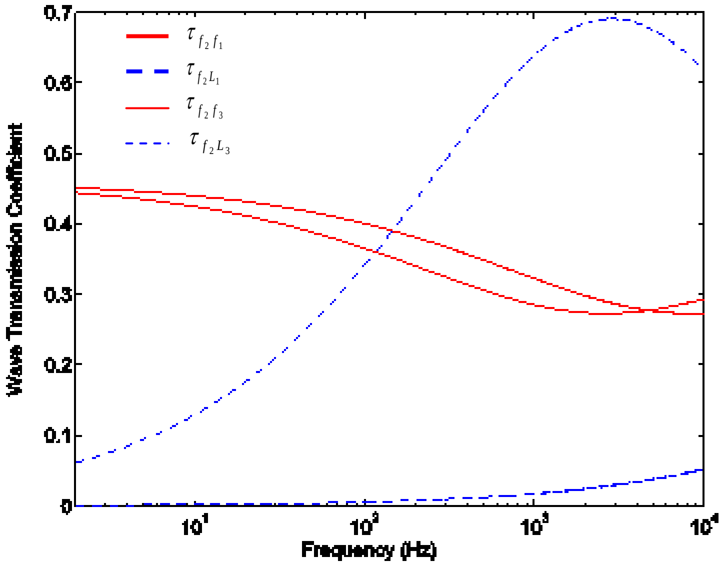

Figure 6.10 Wave transmission coefficients for L-beam

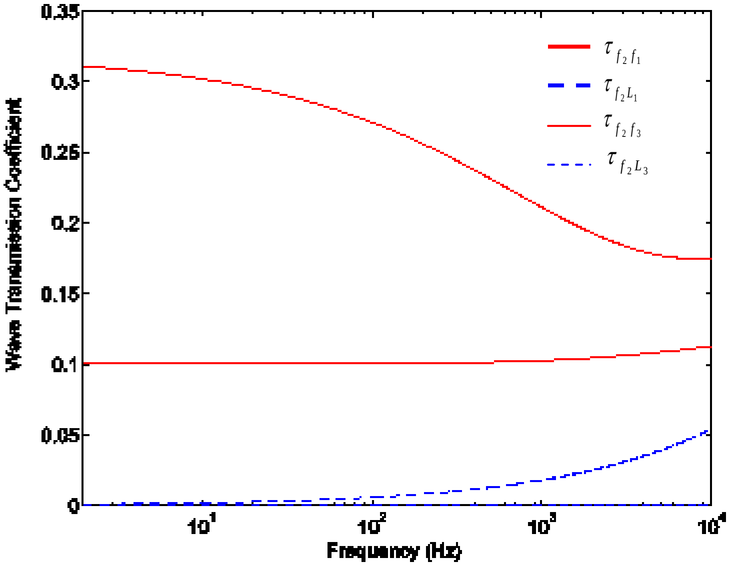

Figure 6.11 Wave transmission coefficients for T-beam

6.2.4 Discussions on the SEA assembling process of the coupling loss factor matrix

The aforementioned analysis can be summarized by revisiting the fundamental of SEA. The fundamental equation used in SEA is the power balance equation between different coupled subsystems. For a subsystem *i* connected to other subsystems *j* with *j* varying, the power balance equation can be written as

$$P_{in}^{i} = P_{diss}^{i} + \sum_{j \neq i} P_{coupl}^{ij} \tag{6.39}$$

where P_{in}^{i} is the power input to the subsystem from an external excitation, P_{diss}^{i} is the power dissipated within the subsystem *i* by the internal damping, and P_{coupl}^{ij} is the net power transmitted from subsystem *i* to subsystem *j* through dynamic coupling. The internal dissipated power is usually calculated as

$$P_{diss}^{i} = \omega \eta_i E_i \tag{6.40}$$

where η_i is the internal loss factor.

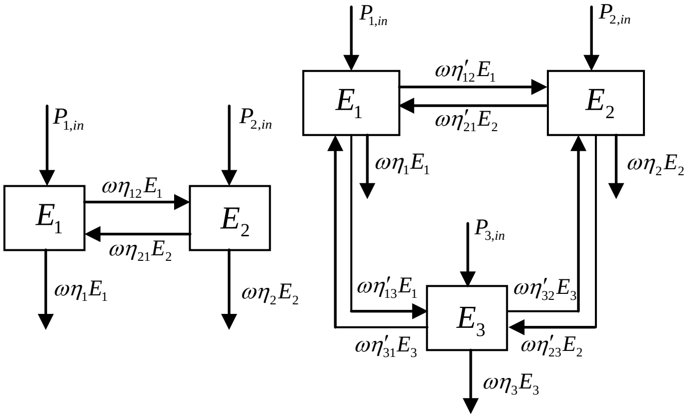

Figure 6.12 SEA modal of conservative coupled systems: (a) two coupled systems; (b) three coupled systems

In SEA, a multi-component system is divided into a number of subsystems; the coupling loss factors are first individually calculated for each pair of subsystems and then assembled to form a global matrix for predicting the system responses. The procedure is illustrated in Fig. 6.12. A system consisting of three coupled components presented in Fig. 6.12(b) can be divided into three pairs of subsystems as shown in Fig. 6.12(a). The SEA relationship for the whole system is established by using Eqs. (6.38-6.40), and a global matrix is shown in Appendix F. The coupling loss factors in the matrix are derived from each individual pair of subsystems. The aforementioned analysis indicates that the coupling loss factors predicted from each pair of subsystems are not necessarily equivalent to those estimated under the whole system situations, say, $\eta_{ij} \neq \eta'_{ij}$. As a matter of fact, only the coupling loss factors η'_{ij} that are calculated under the whole system situation can represent the actual energy flow status of the whole system. In other words, it is questionable to use coupling loss factors η_{ij} that are predicted from each pair of subsystems to form the SEA matrix.

6.3 Dynamic analysis of built-up structures in the presence of model uncertainties

6.3.1 Variability in subsystem properties

A built-up structure, as shown in Fig. 6.13, can be divided into a number of subsystems consisting of beam and plate components. The properties in each subsystem are assumed to vary randomly or in other statistical manner specified. Since the subsystems are typically manufactured by different processes, it is feasible to assume that the variations in the properties of one subsystem are independent of those of the other systems. In addition, all the primary variables in each subsystem, such as the physical and geometrical properties, are assumed to be mutually independent and uncorrelated. For instance, a mass density defined in Eq. 6.41 can be specified to vary spatially according to the Gaussian distribution.

$$\rho = \bar{\rho}(1 + \varepsilon_\rho) \tag{6.41}$$

where ρ denotes the uncertain mass density, $\bar{\rho}$ is the nominal value of the mass density, and ε_ρ represents a random field following a Gaussian distribution

$$\varepsilon_\rho \sim N(0, \sigma_\rho) \tag{6.42}$$

where σ_ρ is the standard deviation of ε_ρ.

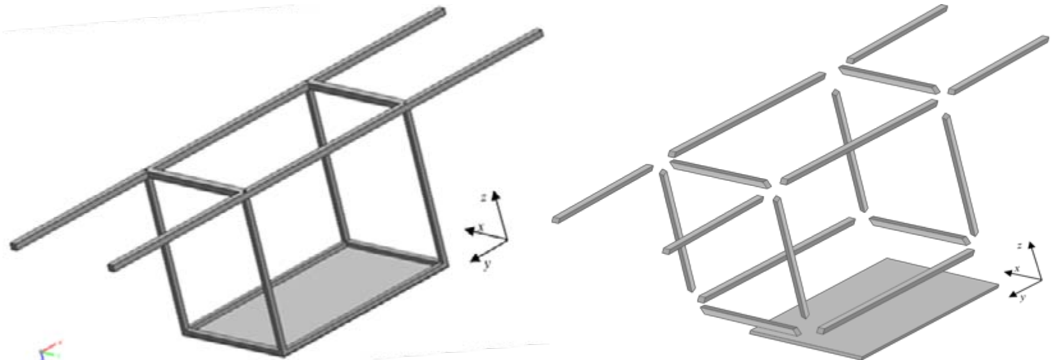

Figure 6.13 A built-up structure is naturally divided into a number of structural parts

Eventually, the ensemble statistics of the system response can be quantified in a similar way to the uncertain properties in terms of the mean values, standard deviations and so on.

6.3.2 Monte Carlo Simulation (MCS)

In this study, the Monte Carlo Simulation (MCS) is adopted to obtain the ensemble statistics of the system response by repetitively solving an eigenvalue problem for each member of the samples randomly created. In this method, N random values of $\boldsymbol{X} = \{\boldsymbol{x}_1 , \boldsymbol{x}_2 \ldots, \boldsymbol{x}_N \}$ according to its probability distribution function are generated for a specific uncertain parameters. The final equilibrium is solved for each value of $\boldsymbol{X}$ leading to a population of the response vector $\tilde{\boldsymbol{\Psi}} = \{\boldsymbol{\Psi}_1, \quad \boldsymbol{\Psi}_2, \quad \cdots \quad \boldsymbol{\Psi}_i, \quad \cdots \quad \boldsymbol{\Psi}_N\}$, where $\boldsymbol{\Psi}_i$ represents the i-th sample for a response vector consisting of displacements, shear force, strain energy etc. Based on this population, the response variability of the system is calculated using the basic relationships in statistics. For example, the unbiased estimates of the mean value and variance of the sample are the following

$$E(\boldsymbol{\Psi}_i) = \frac{1}{N}\sum_{i=1}^{N}\boldsymbol{\Psi}_i \tag{6.43}$$

$$\sigma^2(\boldsymbol{\Psi}_i) = \frac{1}{N-1}\left[\sum_{i=1}^{N}\boldsymbol{\Psi}_i^2 - N \times E^2(\boldsymbol{\Psi}_i)\right] \tag{6.44}$$

Apparently, the accuracy of the estimation is determined by the sample size, and an accurate estimation for the mean value and variance of the response can be obtained given an adequately large number of samples.

6.3.3 Uncertain analysis of a beam-plate structure

Table 6.2 The calculated natural frequencies for a built-up structure

Mode	FSEM (Hz)	FEA (Hz)	Error (%)
1	38.905	38.930	0.064
2	43.315	43.305	0.024
3	43.866	43.907	0.092
4	44.081	44.109	0.061
5	44.245	44.250	0.010
6	44.732	44.734	0.002
7	50.713	50.726	0.028
8	57.882	57.884	0.002
9	71.708	71.740	0.044
10	71.816	71.820	0.005

The first example considers a built-up structure shown in Fig. 6.13. This structure is essentially obtained by simply assembling a ladder frame together with a table frame, which have been fully discussed in chapters 3 and 5, respectively. The first ten calculated natural frequencies are given in Table 6.2 together with the FEA results. An excellent agreement is seen between the two methods. Fig. 6.14 shows several mode shapes for the structure.

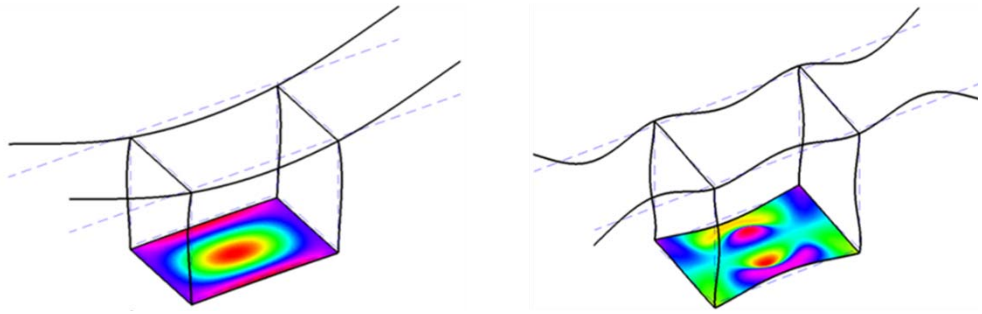

(a) (b)

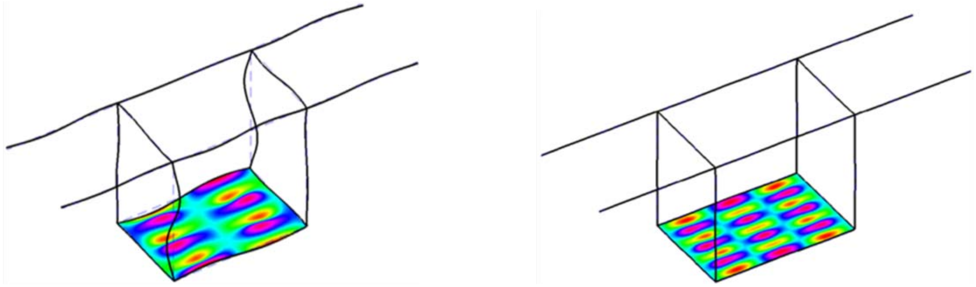
(c) (d)

Figure 6.14 Mode shapes: (a) 1st mode, 38.9 Hz; (b) 51th mode, 424.9 Hz; (c) 78th mode, 781.8 Hz; (d) 139th mode, 1551.8 Hz.

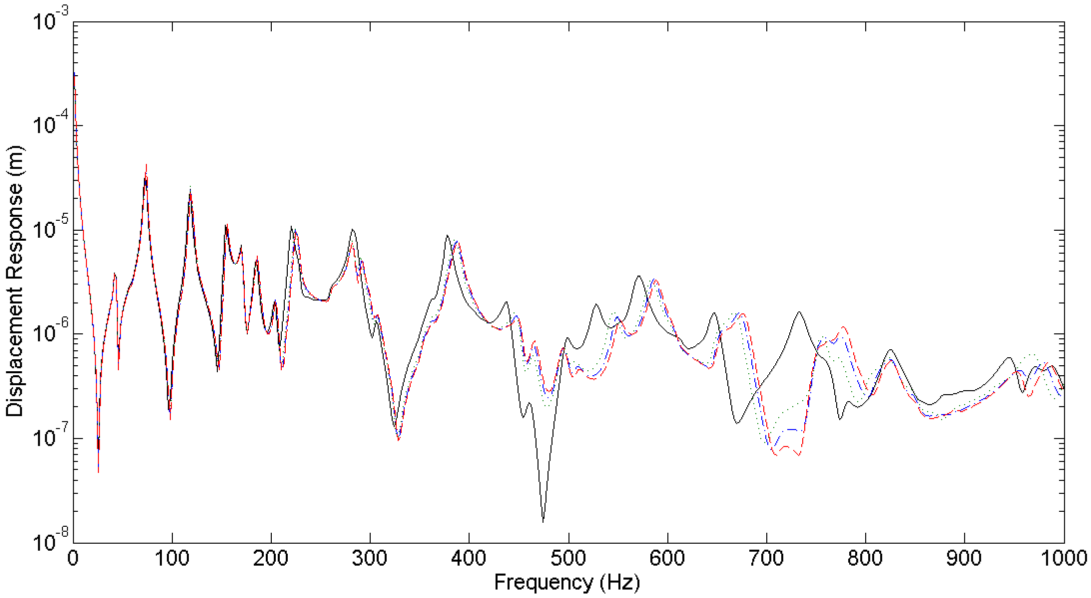

Figure 6.15 Responses of a built-up structure calculated using FEA with various mesh densities: —: 100 elements, ·····: 225 elements; −·−: 400 elements; ----: 900 elements.

Suppose a load is applied on the plate at point (0.6a, 0.4b) and a response is selected on the plate at point (0.8a, 0.2b). Fig. 6.15 plots the response calculated using FEA with various mesh densities. One notices that the discrepancies between the responses using different meshing densities become larger with increasing frequencies, which indicates that meshing becomes an uncertain factor at higher frequencies. In other words, the meshing operation in FEA tends to make the modeling process uncertain. Instead of relying on re-meshing to improve predicting accuracy in FEA, FSEM only needs to change the truncation number to improve both spatial and spectral resolutions without any model modifications.

In practice, there are numerous uncertainty types in engineering structures; for simple illustration purpose, we just pick several plate parameters as the uncertain variables, such as mass density, Young's modulus, and plate thickness for the built-up structure under consideration. All these uncertain parameters are assume to follow the Gaussian random distribution, similar to Eqs. (6.41) and (6.42), and the uncertain quantities are defined as, respectively,

$$E = \overline{E}\left(1+\varepsilon_E\right), \quad h = \overline{h}\left(1+\varepsilon_h\right) \tag{6.45-46}$$

where $E, \overline{E}, h$, and $\overline{h}$ represent the uncertain and nominal Young's modulus and plate thickness respectively; ε_E and ε_h stand for a random field following Gaussian distribution

$$\varepsilon_E \sim N(0,\sigma_E),\ \varepsilon_h \sim N(0,\sigma_h) \tag{6.47-48}$$

where σ_E and σ_h are the standard deviation of ε_E and ε_h respectively.

The first case concerns the mean square velocity response of the plate when the plate thickness is taken as the uncertain variable with an uncertain level σ_h = 0.05. Assume a unit force is applied on the plate at point (0.4a, 0.6b). Fig. 6.16 illustrates the statistical responses of the point on the plate at (0.75a, 0.6b). The several gray curves overlapping each other represent the 100 individual responses; the black curve denotes the response of the structure with nominal plate thickness; and the green and blue curves stand for the responses when the plate thickness has a plus and minus 2% variance, respectively. From a practical point of view, it is difficult to identify which curve is a truthful representation of the response of the structure due to the inherent uncertainties resulting from manufacturing errors or imperfections. Hence, the ensemble mean response denoted by the red curve is more meaningful in evaluating the dynamic behavior of the real structure in practice. When closely examining the ensemble mean response, one should notice that the response can be naturally divided into low, mid, and high frequency regions.

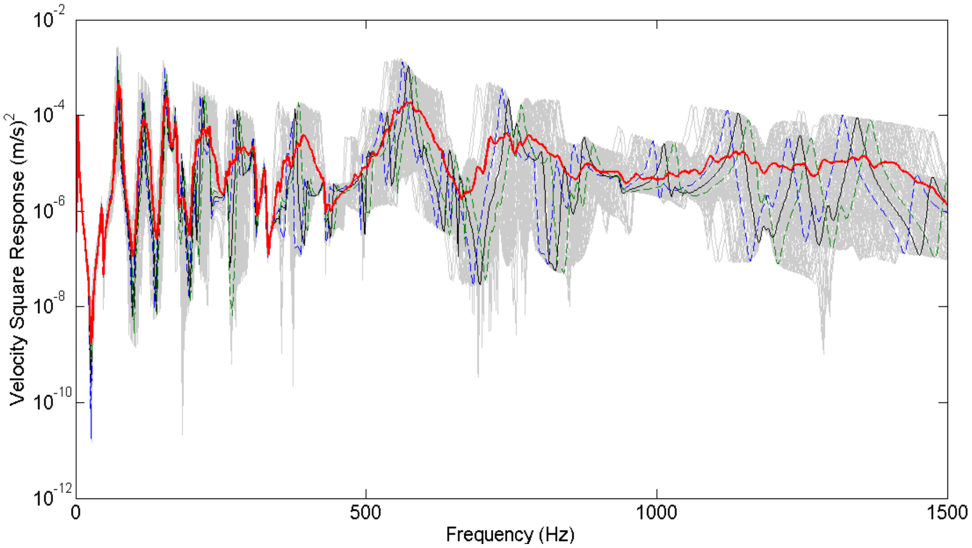

Figure 6.16 Responses of a built-up structure to a concentrated load, red thick line: mean; black line —: nominal thickness; blue line --- : thickness with a -2% tolerance, green line –·–: thickness with a 2% tolerance, grey line: 100 individual responses

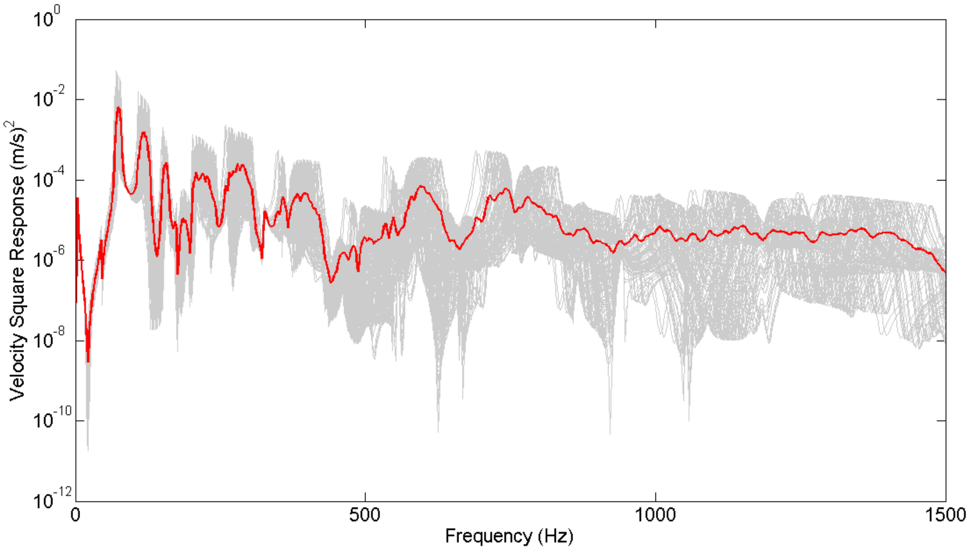

Figure 6.17 Responses of a built-up structure to a concentrated load, red line: mean, grey line: 100 individual responses

Obviously, in the low frequency range, distinct peaks can be easily differentiated indicating that the response is less sensitive to the model variance. In contrast, in the high frequency region, the ensemble mean response is generally flat without distinctive peaks, which implies that the system response is very sensitive to the input uncertainties meaning that even a tiny variance of the model parameter can significantly alter the system dynamic behavior. Between the low and high frequency regions is the mid-frequency range, which has very rich vibratory characteristics and strong resonance-like dynamic behavior. A similar trend of the ensemble mean response for the point at (0.5a, 0.3b) can be also identified in Fig. 6.17.

The second case is focused on the spatial averaged plate mean square velocity of a structure with uncertain plate thickness of two uncertain levels σ_h= 0.005 and σ_h= 0.05. It is observed in Fig. 6.18(a) that different uncertain levels for the same model parameter have different effects on the system responses. If we take a frequency average by applying the 1/3-octave band on those curves, as shown in Fig. 6.18(b), it is noticed that all the local dynamic information in the mid and high frequency ranges disappears after the spatial and frequency averages as performed in the SEA process.

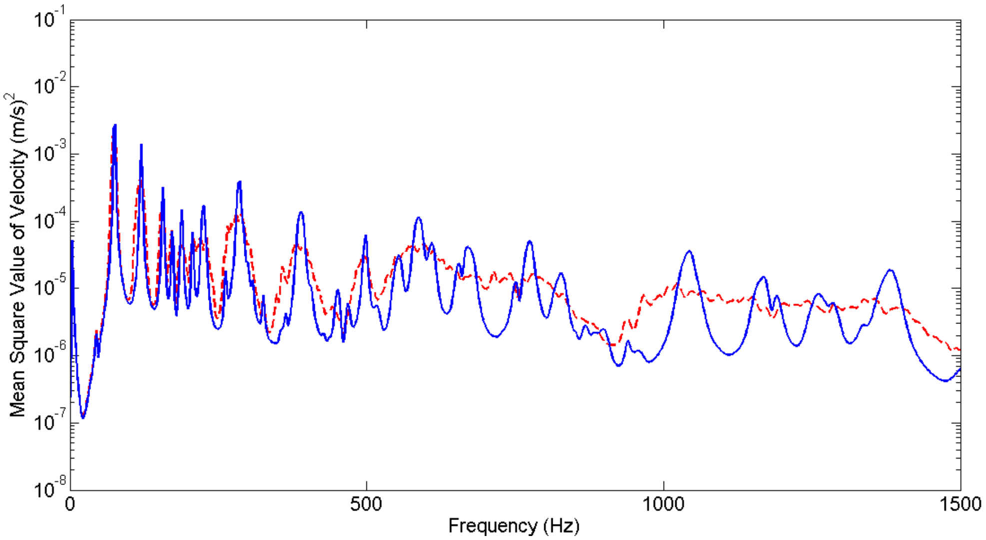

(a)

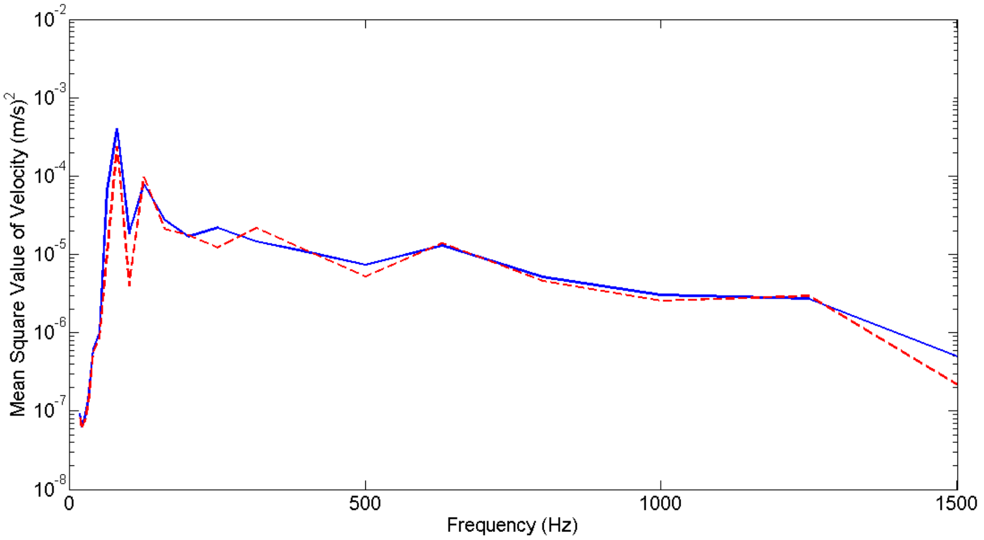

(b)

Figure 6.18 Spatial averaged mean square velocity for the plate with uncertain thickness at different uncertain levels: — σ = 0.005; --- σ = 0.05; (a) broad band; (b) 3rd octave band.

To emphasize on this point, let us consider two close frequency components, 1040 and 1050 Hz on the red curve. Fig. 6.19 shows the spatial distributions of the mean square velocity at these two particular frequencies. It is observed that even the spatial averaged mean square velocity values are almost identical at these two immediate neighboring frequencies, the actual spatial distributions of the mean square velocity are significantly different.

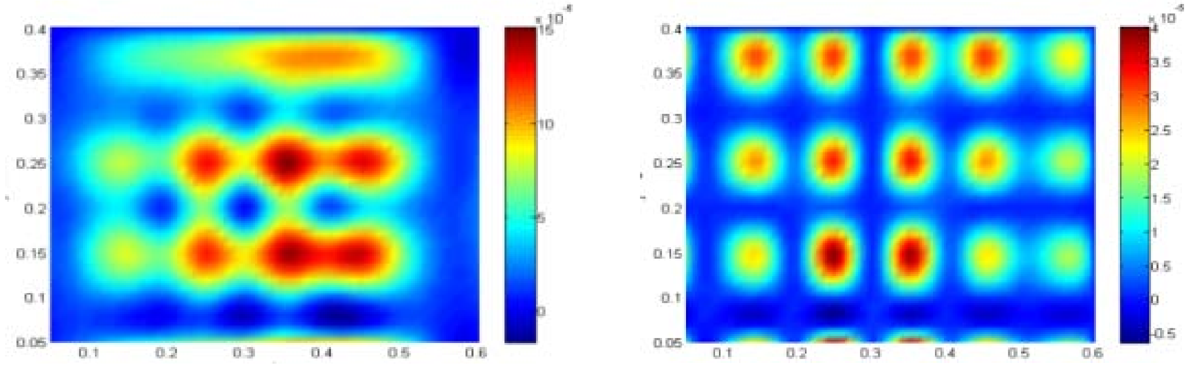

(a) (b)

Figure 6.19 Spatial distribution of mean square velocity at different frequencies for the plate with uncertain thickness (σ = 0.05); (a) 1040 Hz; (b) 1050 Hz.

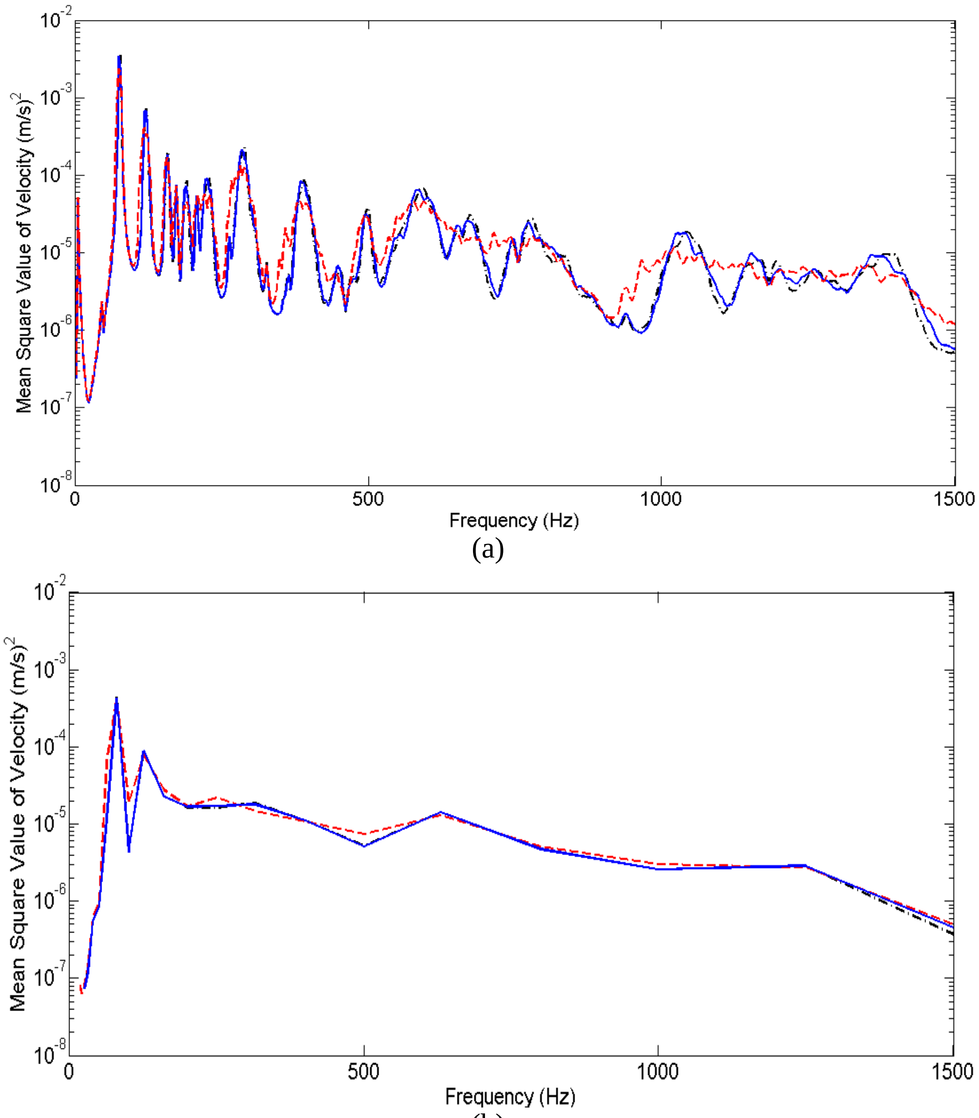

(a)

(b)

Figure 6.20 Spatial averaged mean square velocity for the plate with different uncertain parameters: — density uncertainty; --- thickness uncertainty; −·− Young's modulus uncertainty; (a) broad band; (b) 3rd octave band

In the next case, we will investigate the spatial averaged plate mean square velocity of a structure with different uncertain parameters (thickness, Young's, and mass density) at a same uncertain level $\sigma_\rho = \sigma_E = \sigma_h = 0.05$. Fig. 6.20(a) plots the broad band spatial averaged mean square velocity for the plate with different uncertain parameters. It is obvious that the same level of uncertainties with different model variables has different effects on the system dynamic behavior, which indicates that we should treat the uncertainties differently. Thus, it is difficult to differentiate between the types of uncertainties when the responses are presented in the 1/3-octave band, as shown in Fig. 6.20(b).

In FSEM, the secondary field variables such as strain/kinetic energy, can be easily derived through appropriate mathematical manipulations including differentiations. Figs. 6.21 and 6.22 show the mean kinetic energy distribution of the whole structure when a load is applied on point 6 (refer to Fig. 3.20) and on point 1 (refer to Fig. 5.8). An uncertain plate thickness with $\sigma_h = 0.05$ is assumed in this case.

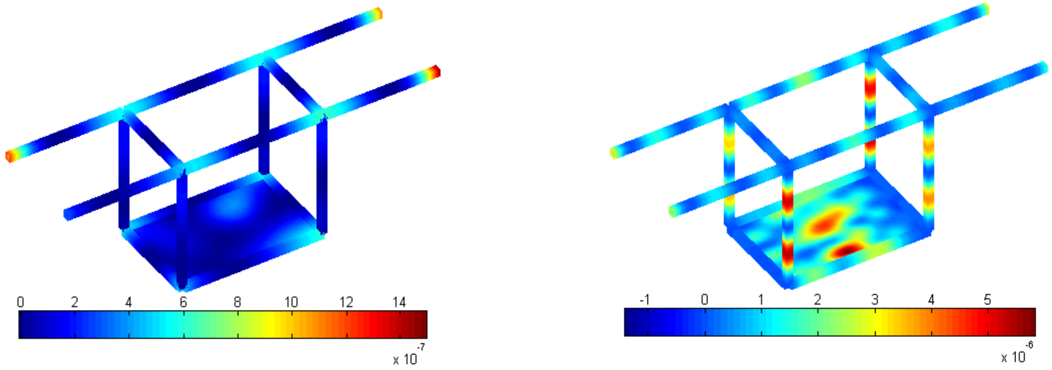

(a) (b)

Figure 6.21 Mean kinetic energy distribution of the whole structure excited by a unit force applied on beam 6 along *x* direction: (a) 54Hz; (b) 694 Hz

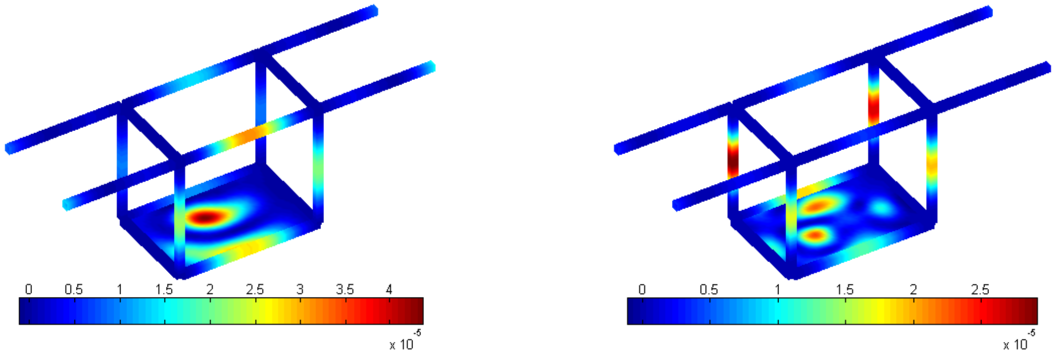

(a) (b)

Figure 6.22 Mean kinetic energy distribution of the whole structure excited by a unit force applied on the plate in *z* direction at (0.4a, 0.6b): (a) 170Hz; (b) 328 Hz.

6.3.4 Uncertain analysis of a Body-In-White structure

6.3.4.1 Description of the Body-In-White structure

In this section, let us consider a Body-In-White (BIW) structure which plays an important role in determining the vehicle dynamic performance. Fig. 6.23(a) depicts a prototype of BIW primarily consisting of beams and small panels. For convenience, here we simplify the BIW by treating it as a beam structure, as shown in Fig. 6.23(b).

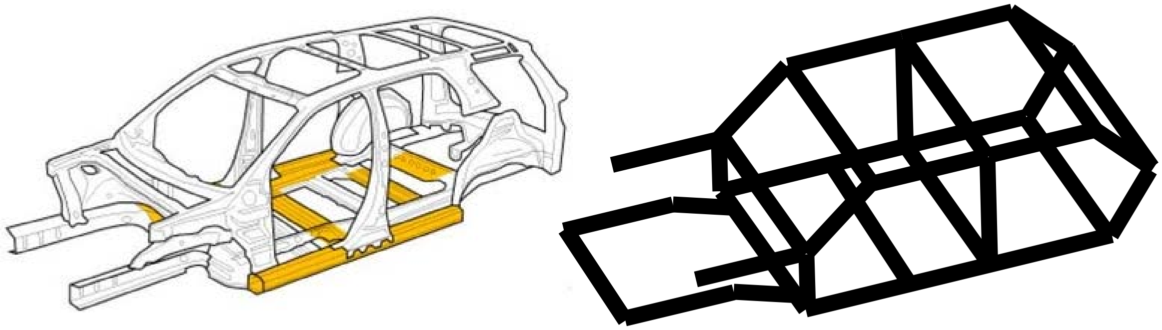

(a) (b)

Figure 6.23 A typical Body-In-White structure: (a) a BIW prototype; (b) a simplified model

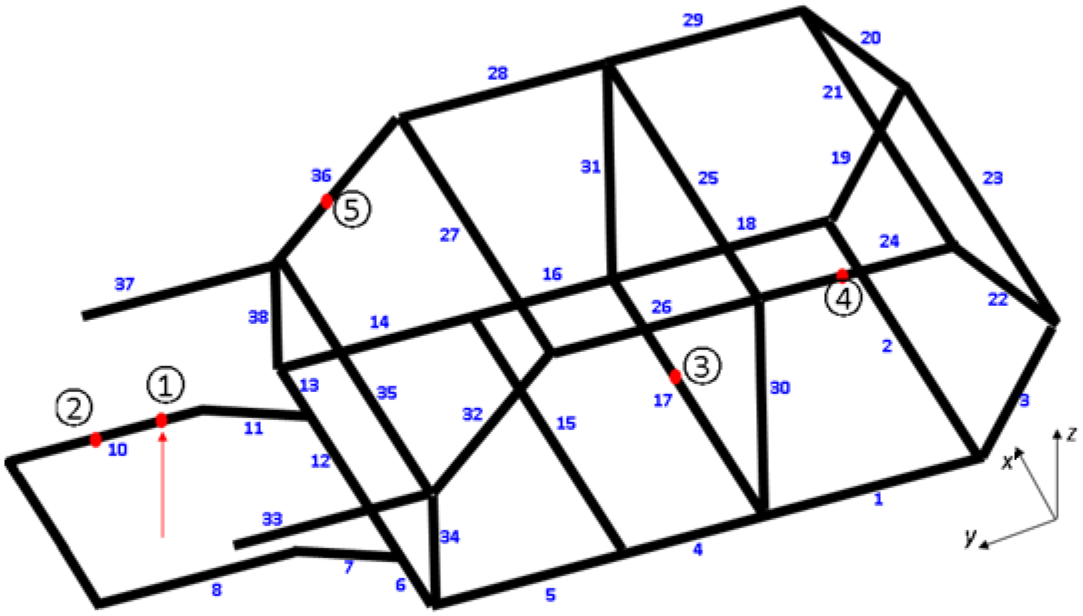

Figure 6.24 A simplified model of Body-In-White, and the excitation and response locations

Based on its physical composition, the BIW can be divided into 38 beams, as labeled in Fig. 6.24. Assume the structure is made of steel: Young's modulus $E = 2.07\times10^{11}$ N/m^2, shear modulus $G = 1.06\times10^{11}$ N/m^2, and mass density $\rho = 7800$ kg/m^3. The length for beams 6 and 13 is 0.2m; 4, 7, 11, 16, 34, and 38 is 0.4m; 3, 19, 20, and 22 is 0.46; 1, 18, 24, 26, 28, and 29 is 0.6m; 32 and 36 is 0.72m; 5, 8, 9, 10, 12, 14, 30, 31, 33, and 37 is 0.8m; and for 2, 15, 17, 21, 23, 25, 27, and 35 is 1.2m. The beam components are classified into 3 groups in terms of model parameters as tabulated in Table 6.3.

Table 6.3 Model properties of a Body-In-White structure

Properties	Group1	Group2	Group3
$S(m^2)$	0.01	0.0064	0.0025
$J(m^4)$	1.67×10^{-5}	0.68×10^{-5}	0.11×10^{-5}
$I_{yy}(m^4)$	0.83×10^{-5}	0.34×10^{-5}	0.52×10^{-6}
$I_{zz}(m^4)$	0.83×10^{-5}	0.34×10^{-5}	0.52×10^{-6}

Group1: beams 33, 34, 37, and 38;
Group2: beams 1, 2, 4, 5, 6, 7, 8, 9, 10, 11, 12, 13, 14, 15, 16, 17, 18, 30, and 31;
Group3: beam 3, 20, 21, 22, 23, 24, 25, 26, 27, 28, 29, 32, 35, and 36.

6.3.4.2 The modal-acceleration method

A primary disadvantage of MCS is its excessive computational cost for large-scale structures which often require parallel processing involve many computers. Various numerical evaluations (Shinozuka, 1987; Stefanou, 2009) of the variability response function have been developed to improve the efficiency of MCS. The modal-acceleration method, which was originally proposed by Williams in 1945, is adopted in this study to calculate the frequency response. While the direct solution requires the dynamic problem to be recalculated for each frequency step, the modal-acceleration method only needs to solve the eigenvalue problem once to eigenpairs. The modal-acceleration method is essentially a type of modal superposition method. However, it converges much faster than the traditional modal superposition method. For completeness, a brief introduction to modal-acceleration is presented as below.

In the mode-displacement solution, the frequency response vector $\mathbf{A}(\omega)$, which is the Fourier coefficient vector in this study, is given by

$$\mathbf{A}(\omega)=\sum_{r}^{M}\frac{\mathbf{\Phi}_r\mathbf{\Phi}_r^T\mathbf{F}(\omega)}{\omega_r^2(1+i\eta_r)-\omega^2} \tag{6.49}$$

where M is the modal truncation number; $\ldots_r$ is the rth eigenvector of the un-damped system; η_r and ω_r denote the rth modal damping and modal frequency, respectively; and $\mathbf{F}(\omega)$ represents the excitation force vector.

However, in the modal-acceleration solution the response vector $\mathbf{A}(\omega)$ is written as

$$\mathbf{A}(\omega)=\mathbf{K}^{-1}\mathbf{F}(\omega)-\sum_{r}^{M}\frac{\omega^2}{\omega_r^2}\left[\frac{\mathbf{\Phi}_r\mathbf{\Phi}_r^T\mathbf{F}(\omega)}{\omega_r^2(1+i\eta_r)-\omega^2}\right] \tag{6.50}$$

where $\mathbf{K}$ is the system stiffness matrix.

In Eq. (6.50), it is seen that the presence of ω_r^2 in the denominator of the last term speeds up the convergence of the mode-acceleration method as compared to the mode-displacement method. With the assistance of the modal-acceleration method, we only need to inverse the system stiffness matrix once throughout the entire response calculation. In addition, the modal-acceleration method only requires a very small subset of modes for calculating the response with sufficient accuracy.

As an example, Fig. 6.25 shows the frequency responses for the driving point 1 calculated using the direct solution and modal-acceleration method with different modal truncation numbers. The number of total modes included in this case is N_t = 2128. It can be seen that the response obtained from the modal-acceleration method gradually converge to the direct solution. In particular, a good match between these two methods is observed within 1000 Hz when the mode number truncates to $M = N_t/5$. This leads to a significant reduction for the computational load of MCS without losing accuracy. In the subsequent calculations, the Fourier series expansion term for each beam is selected as 15, and the number of modes involved in the modal-acceleration solution is $M = N_t/5 = 2888 = 577$.

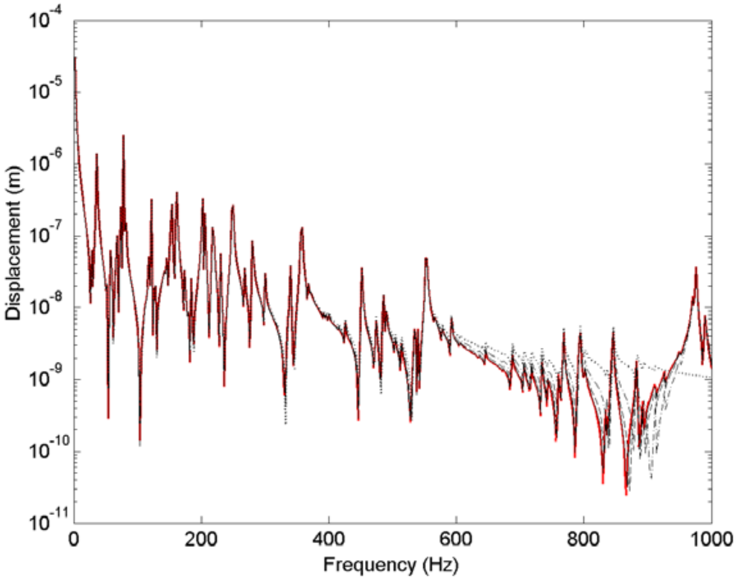

Figure 6.25 Comparison of the frequency responses between the direct solution and mode-acceleration method, red line: direct solution; —: $M = N_t/5$; ----: $M = N_t/8$; —·—: $M = N_t/10$; ·····: $M = N_t/12$

6.3.4.3 Probabilistic characteristics of uncertain dynamic behaviors

The uncertainties for physical properties (Mass density and Young's modulus) of constituent beams are assumed to follow the Gaussian distribution with standard deviations equal to 5 percent of the nominal values of physical properties. In the following calculations, the structure is assumed to have a free boundary condition and to be excited by a harmonic unit force applied at point 1 along z direction, as shown in Fig. 6.24. Four response points 2, 3, 4, and 5 are selected at the shot gun (beam 10), chassis (beam 17), roof (beam 24), and A-pillar (beam 36), respectively; and the flexural vibration in the *x*-*z* is considered.

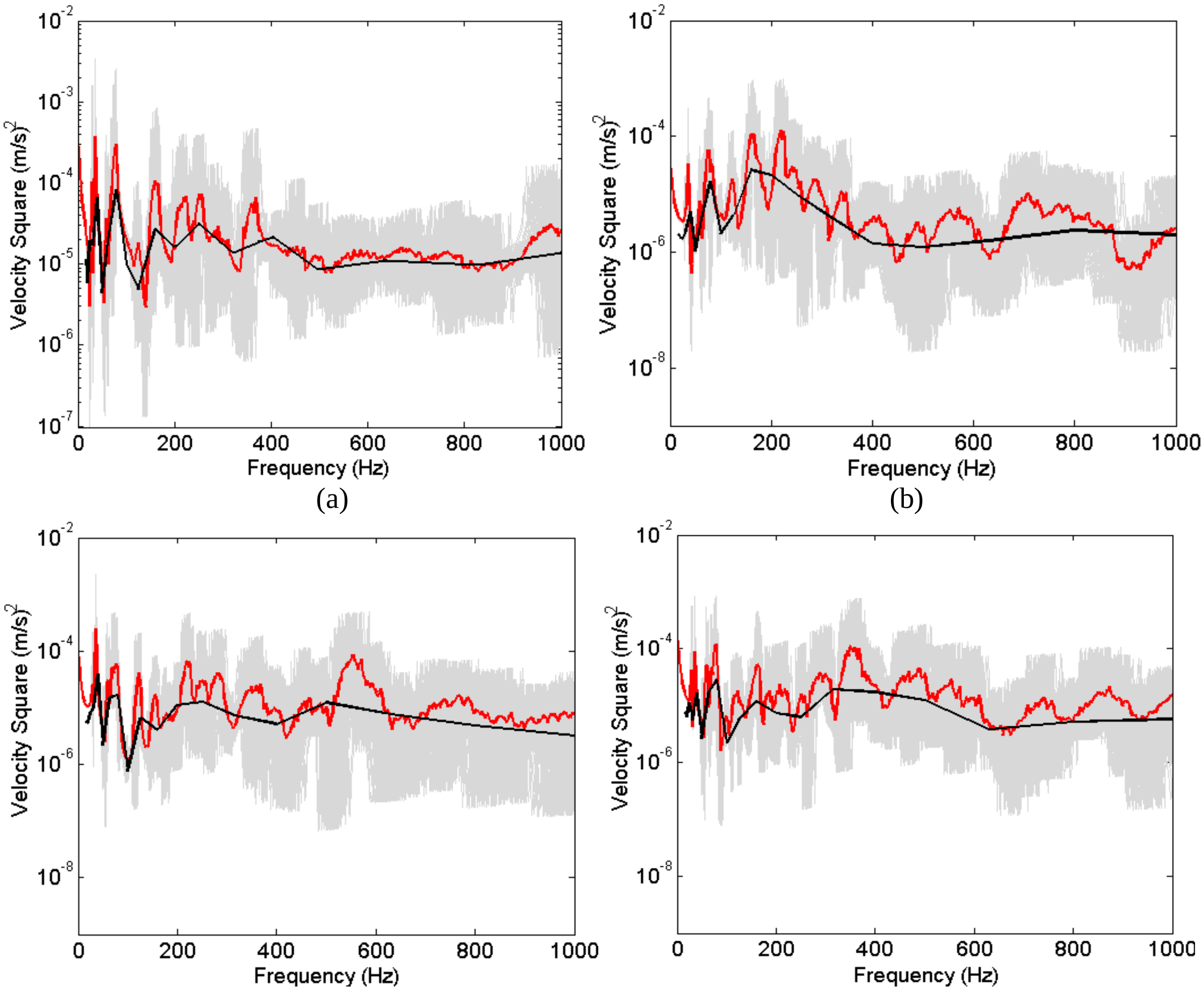

(a) (b)

(c) (d)

Figure 6.26 Responses of a Body-In-White with uncertain mass density: (a) at point 2; (b) at point 3; (c) at point 4; (d) at point 5, red line: mean; black line: 3rd octave band; grey line: 100 individual responses

Plotted in Figs. 6.26 and 6.27 are the calculated velocity responses for a BIW with uncertain mass density and Young’s modulus, respectively. It is seen that the responses exhibit quite different characteristics for different types of uncertainties. In comparing Figs. 6.26(a) and 6.26(c), one may notice that the mid-frequency region varies with different structural components. Also it is clear that the fluctuation ranges of system responses differ significantly when the structure is subjected to different uncertain inputs.

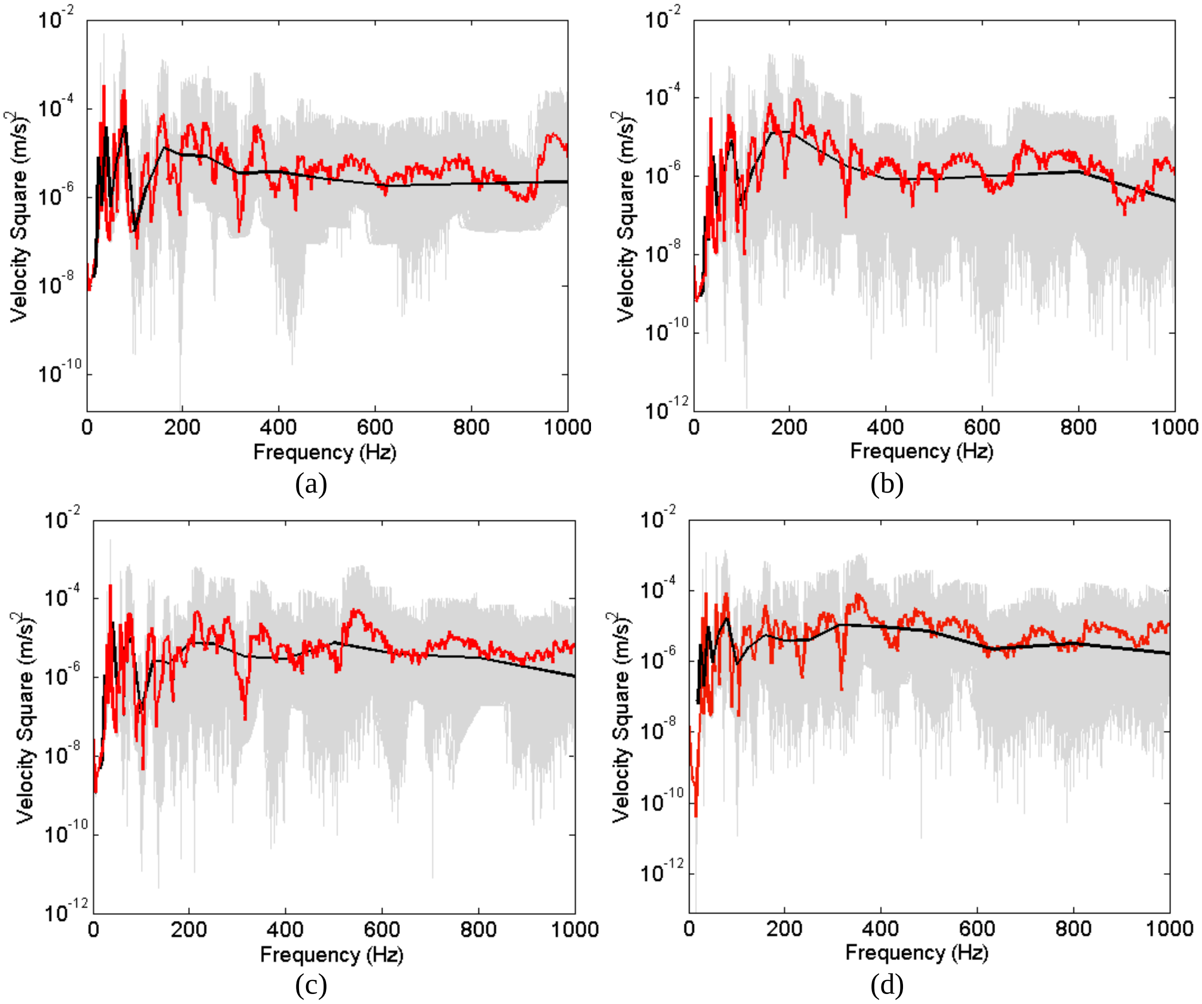

(a) (b)

(c) (d)

Figure 6.27 Responses of a Body-In-White with uncertain Young's modulus: (a) at point 1; (b) at point 2; (c) at point 3; (d) at point 4; red line: mean, black line: 3rd octave band, grey line: 100 individual responses

While the responses for the uncertain mass density varies from 10^{-8} to 10^{-2}, the responses for the uncertain Young's modulus fluctuate from 10^{-12} to 10^{-2}.

The mean kinetic energy distribution for the BIW with an uncertain mass density is illustrated in Fig. 6.28. It is seen that the mean kinetic energy exhibits a more uniform distribution in the high frequency, as shown in Fig. 6.28(d), compared to the one in the low and mid frequencies, as shown in Figs. 6.28(a-c).

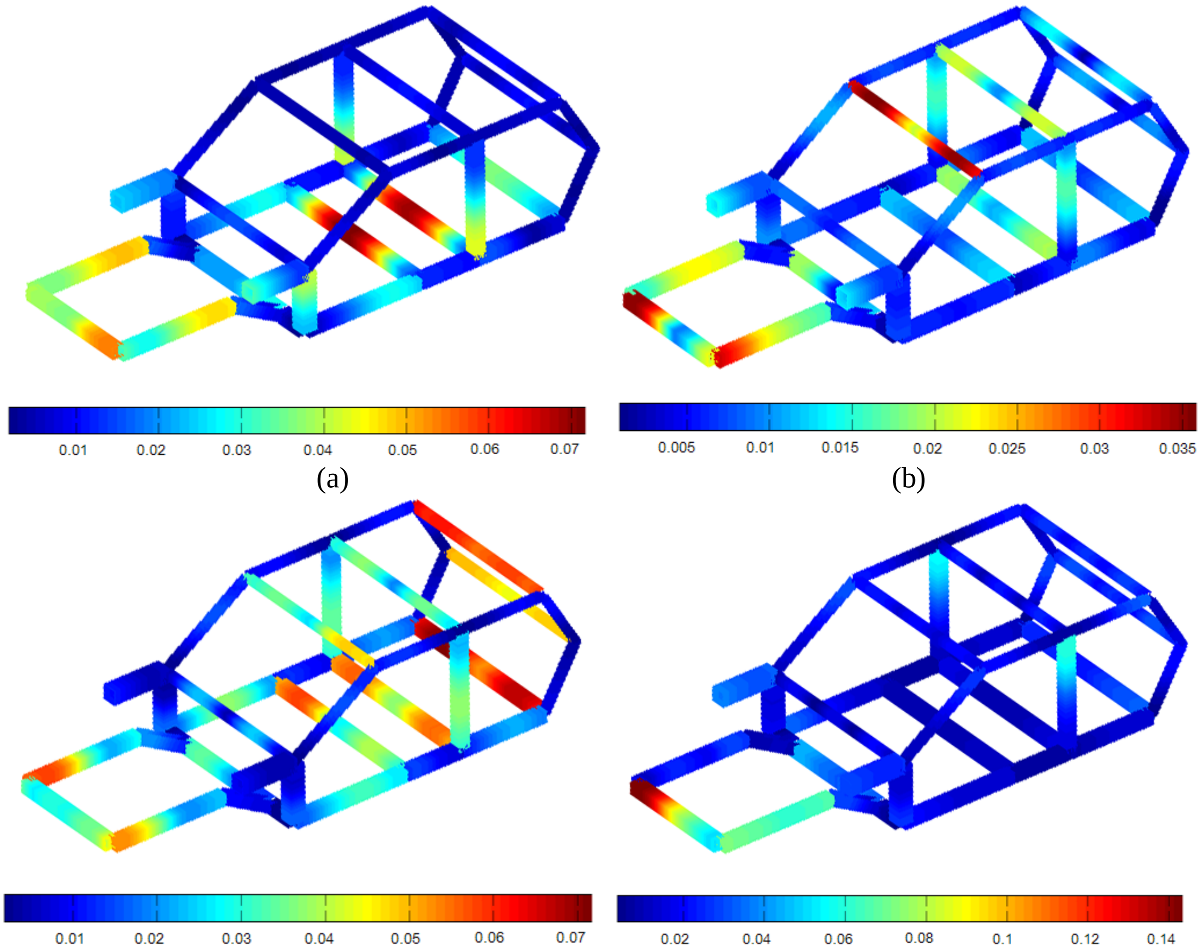

(a) (b) (c) (d)

Figure 6.28 Mean kinetic energy distribution of the BIW to a concentrated load applied along *z* direction at point 1: (a) 236Hz; (b) 396Hz; (c) 524Hz; (d) 924Hz.

6.5 Conclusions

In this chapter, the validity of a fundamental SEA assumption that the coupling loss factors are unaffected by the configuration changes is reexamined by considering a simple T-beam structure. Regarding the characteristics of the coupling loss factors in determining power flows in structures, some insightful information is obtained. First, it is shown that the power flow between any two subsystems is changed when another subsystem joins in. Second, the power flows between any two subsystems do not necessarily follow the same relationships after the subsystems are assembled into a system, which indicates that the coupling loss factors individually calculated for each pair of subsystems cannot be linearly assembled to form a global matrix for predicting the system responses.

FSEM combining with the Monte-Carlo Simulation can effectively tackle the medium frequency uncertain responses where the ensemble means exhibit strong resonance-like behavior. In contrast with SEA models, where all local details are neglected, the proposed prediction technique provides adequate inform on the statistical characteristics of the mid-frequency responses of a dynamic system by eliminating the spatial- and frequency-averaging processes. Specifically, some important findings are obtained through this preliminary study:

1. Different uncertain parameters with a same uncertain level have different effects on the system response, such as the dynamic range, the location of the "resonance-like" behavior in terms of mean values, which indicates that different uncertainties should be treated differently in practice. Unfortunately, in SEA these uncertain types are not differentiated, and their impacts are simply eliminated by the averaging process regarding space and frequency.
2. Different uncertain levels for the same uncertain parameter also exert different effects on the system responses. However, the effects of different uncertain levels can be lost in the frequency-averaging process.
3. The spatial averaged responses predicted in a narrow band do not always truthfully reflect the spatial distributions of system responses in some circumstances. For instance, even if the spatial averaged response quantities are almost identical at two immediate neighboring frequencies, a significant spatial distribution difference for the considered response quantities may exist between the these two frequencies.

CHAPTER VII

CONCLUDING REMARKS

7.1 General summary

Fourier Spectral Element Method (FSEM) was previously proposed for the dynamic analyses of simple structural components like beams and plates. In this study, FSEM was extended to the vibration and power flow analyses of complex built-up structures in a broader frequency range. In a FSEM model, a complex structure is considered as an assembly of interconnected basic structural components such as beams and plates. The key idea of this method is to express the displacement on each component as an improved Fourier series expansion consisting of a standard Fourier cosine series plus several supplementary series/functions used to ensure and accelerate the convergence of the series representation. Accordingly, series expansions of the involved displacement functions and their appropriate derivatives are guaranteed to uniformly and absolutely converge for any boundary conditions and coupling configurations. Additionally, other secondary variables of interest such as moments, shear forces, strain/kinetic energies, and power flows between substructures can be readily calculated in an analytical form.

For beam structures, the displacement over each beam element is described as a cosine series expansion supplemented by several closed-form functions. In chapter 2, the auxiliary functions are simply selected as polynomials in investigating the vibration of multi-span beam systems. Since sine functions exhibit some desired invariance with respect to certain mathematical operations such as differentiations and integrations, , in chapter 3 they are utilized as the supplementary terms to simplify the calculations .

The primary unknowns in a FSEM model are Fourier coefficients, which can be solved in an exact manner by letting the series simultaneously satisfy both the governing equation and boundary conditions (Li, 2000; Xu & Li, 2008; Du *et al.*, 2007; Li *et al.*, 2009). Although this exact solution scheme may represent the most natural choice mathematically, it will lead to the fully-populated coefficient matrices for final system equations when dealing with complicated coupling structures. As an alternative solution process which may actually be preferred in practice, all the expansion coefficients for the complementary terms are treated as independent variables, and are solved in an approximate manner by using the powerful Rayleigh-Ritz method. In this way, only the neighboring beams will be directly coupled together in the final system equations, as manifested in the highly sparse stiffness and mass matrices. Even though the solution is based on a weak (variational) sense, it is not necessarily less accurate than the exact solutions because all the selected series expansions up to the 3rd order derivatives are constructed to be continuous.

FSEM has been developed for the vibrations of multi-span beam systems, 2- and 3-D frames, plate assemblies, and beam-plate coupling systems. Its accuracy and reliability have been repeatedly demonstrated through numerical examples.

It is important to point out that FSEM can be generally applied to beams and plates structures combinations even when the other analytical methods fail to work due to, such as, the nonexistence of the closed-form expressions or the inability of satisfying the boundary or coupling conditions under the actual system condition.

FSEM allows an easy calculation of power flows between interconnected structural components in that the coupling moments and forces at the junctions can be calculated explicitly from second and third derivatives of the displacement functions. Two alternative power flow indicators were proposed for the power flow analysis: the scaled kinetic energy distribution and the structural intensity. These quantities allows a better understanding of the power flows in a complex structure.

Finally, FSEM is combined with the Monte Carlo Simulation (MCS) to study the dynamic responses of built-up structures in the presence of model uncertainties. FSEM is demonstrated to be capable of effectively predicting the statistical behavior, especially in the critical mid-frequency range where the ensemble means exhibit strong resonance-like characteristics. In contrast with the SEA analysis in which the local information is not available, the FSEM prediction includes the detailed spatial and spectral data that are of concern in the mid-frequency range.

7.2 Future work

Based on the work presented in this dissertation, some recommendations for future research are outlined as below:

In this dissertation, FSEM has been successfully applied to the structures consisting of beams and plates. In order to be able to deal with more complicated structures, FSEM should be also extended, and there seems no any intrinsic problem that will prevent from extending it, to other common structural components such as curvature beams, triangular plates, and doubly-curved shells with non-uniform and non-conforming coupling junctions.

An important advantage of FSEM over FE methods is that the resulting system in a FSEM model is significantly smaller with respect to the total number of degrees of freedom in the system. Therefore, it is more effective to use FSEM to find solutions at higher frequencies and/or over large regular domains. On the other hand, a discrete model such as FEA is more flexible in representing geometric and material details. Thus, combining the discrete (FEA) and FSEM models allows taking advantages of the best of both worlds.

In the low frequency region, the behavior of a dynamic system can be satisfactorily predicted using a deterministic method. However, a probabilistic method will have to be used in the mid- to high- frequency regions to account for model uncertainties caused by the engineering and/or manufacturing errors. The continuous stochastic fields of model variables are implicitly represented by Fourier series expansions in a FSEM model. This treatment gives rise to a more efficient and effective probabilistic modeling process because FSEM has an extraordinary capability of reducing the size of the final system and the dimension of random variable space. It is recommended that additional efforts should be directed to widening the capability of FSEM in dealing with probabilistic models for various variables.

Due to the lack of the analytical or numerical results, the validation of FSEM in predicting the dynamic responses in the mid-frequency range will have to heavily rely on experimental results. The experimental work can be conducted using the fabricated structures that are similar to those tested in this research, but involve other practical model uncertainties such as the locations and strengths of bolt joints and spot-welds.

APPENDIX A

SUB-MATRICES DEFINED IN CHAPTER 3

$$\mathbf{K}_{ii}=\begin{bmatrix}\mathbf{K}_{u_iu_i} & \mathbf{K}_{u_iw_{i,y}} & \mathbf{K}_{u_iw_{i,z}} & \mathbf{K}_{u_i\theta_i}\\ \vdots & \mathbf{K}_{w_{i,y}w_{i,y}} & \mathbf{K}_{w_{i,y}w_{i,z}} & \mathbf{K}_{w_{i,y}\theta_i}\\ \vdots & \ddots & \mathbf{K}_{w_{i,z}w_{i,z}} & \mathbf{K}_{w_{i,z}\theta_i}\\ Symmetric & \cdots & \cdots & \mathbf{K}_{\theta_i\theta_i}\end{bmatrix} \tag{A.1}$$

$$\mathbf{K}_{ij}=\begin{bmatrix}\mathbf{K}_{u_iu_j} & \mathbf{K}_{u_iw_{j,y}} & \mathbf{K}_{u_iw_{j,z}} & \mathbf{K}_{u_i\theta_j}\\ \mathbf{K}_{w_{i,y}u_j} & \mathbf{K}_{w_{i,y}w_{j,y}} & \mathbf{K}_{w_{i,y}w_{j,z}} & \mathbf{K}_{w_{i,y}\theta_j}\\ \mathbf{K}_{w_{i,z}u_j} & \mathbf{K}_{w_{i,z}w_{j,y}} & \mathbf{K}_{w_{i,z}w_{j,z}} & \mathbf{K}_{w_{i,z}\theta_j}\\ \mathbf{K}_{\theta_iu_j} & \mathbf{K}_{\theta_iw_{j,y}} & \mathbf{K}_{\theta_iw_{j,z}} & \mathbf{K}_{\theta_i\theta_j}\end{bmatrix} \tag{A.2}$$

Components of sub-matrices in Eqs. A.1 and A.2 have the common form as following

$$\begin{bmatrix}\mathbf{K}^{AA}_{\sigma_1\sigma_2} & \mathbf{K}^{AB}_{\sigma_1\sigma_2}\\ \left(\mathbf{K}^{AB}_{\sigma_1\sigma_2}\right)^T & \mathbf{K}^{BB}_{\sigma_1\sigma_2}\end{bmatrix},\ \sigma_1,\sigma_2=w_{i,z},w_{i,y},u_i,\theta_i \tag{A.3}$$

$$\left\{\mathbf{K}^{AA}_{u_iu_i}\right\}_{m,m'}=\begin{cases}m,m'=0 & k^0_{i,u}+k^L_{i,u}(-1)^{m+m'}+\left(N^0_i+N^L_i(-1)^{m+m'}\right)\mathbf{H}_{i,11}\\ m,m'\neq 0 & E_iS_i\lambda^2_m\delta_{mm'}\dfrac{L_i}{2}+k^0_{i,u}+k^L_{i,u}(-1)^{m+m'}+\left(N^0_i+N^L_i(-1)^{m+m'}\right)\mathbf{H}_{i,11}\end{cases} \tag{A.4}$$

$$\left\{\mathbf{K}^{AB}_{u_iu_i}\right\}_{m,n'}=\begin{cases}m=n' & 0\\ m\neq n' & -E_iS_i\lambda_m\lambda_{n'}mL_i\left((-1)^{m+n'}-1\right)/\pi(m^2-n'^2)\end{cases} \tag{A.5}$$

$$\left\{\mathbf{K}^{BB}_{u_iu_i}\right\}_{n,n'}=\begin{cases}n,n'=0 & L_i\\ n,n'\neq 0 & E_iS_i\lambda^2_n\delta_{nn'}\dfrac{L_i}{2}\end{cases} \tag{A.6}$$

$$\left\{\mathbf{K}^{AA}_{u_iw_{i,y}}\right\}_{m,m'}=\left(N^0_i+N^L_i(-1)^{m+m'}\right)\mathbf{H}_{i,12},\ \left\{\mathbf{K}^{AB}_{u_iw_{i,y}}\right\}_{m,n'}=\lambda_{n'}\left(N^0_i+N^L_i(-1)^{m+n'}\right)\mathbf{H}_{i,16} \tag{A.6,7}$$

$$\left\{\mathbf{K}^{AA}_{u_iw_{i,z}}\right\}_{m,m'}=\left(N^0_i+N^L_i(-1)^{m+m'}\right)\mathbf{H}_{i,13},\ \left\{\mathbf{K}^{AB}_{u_iw_{i,z}}\right\}_{m,n'}=\lambda_{n'}\left(N^0_i+N^L_i(-1)^{m+n'}\right)\mathbf{H}_{i,15} \tag{A.8,9}$$

$$\left\{\mathbf{K}^{AA}_{u_i\theta_i}\right\}_{m,m'}=\lambda_{n'}\left(N^0_i+N^L_i(-1)^{m+m'}\right)\mathbf{H}_{i,14}, \tag{A.10}$$

$$\left\{\mathbf{K}^{AA}_{w_{i,y}w_{i,y}}\right\}_{m,m'}=\begin{cases} m,m'=0 & E_i I_{i,z}\lambda_m^4\delta_{mm'}L_i+k_{i,y}^0+k_{i,y}^L(-1)^{m+m'}+\left(N_i^0+N_i^L(-1)^{m+m'}\right)\mathbf{H}_{i,22} \\ m,m'\neq 0 & E_i I_{i,z}\lambda_m^4\delta_{mm'}\dfrac{L_i}{2}+k_{i,y}^0+k_{i,y}^L(-1)^{m+m'}+\left(N_i^0+N_i^L(-1)^{m+m'}\right)\mathbf{H}_{i,22} \end{cases} \tag{A.11}$$

$$\left\{\mathbf{K}^{AB}_{w_{i,y}w_{i,y}}\right\}_{m,n'}=\begin{cases} m=n' & \lambda_{n'}\left(N_i^0+N_i^L(-1)^{m+n'}\right)\mathbf{H}_{i,26} \\ m\neq n' & E_i I_{i,z}\lambda_m^2\lambda_{n'}^2 n' L_i\left((-1)^{m+n'}-1\right)/\pi(m^2-n'^2)+\lambda_{n'}\left(N_i^0+N_i^L(-1)^{m+n'}\right)\mathbf{H}_{i,26} \end{cases} \tag{A.12}$$

$$\left\{\mathbf{K}^{BB}_{w_{i,y}w_{i,y}}\right\}_{n,n'}=\begin{cases} n,n'=0 & \lambda_n\lambda_{n'}\left[\left(K_{i,y}^0+K_{i,y}^L(-1)^{n+n'}\right)+\left(N_i^0+N_i^L(-1)^{n+n'}\right)\mathbf{H}_{i,66}\right] \\ n,n'\neq 0 & E_i I_{i,z}\lambda_n^4\delta_{nn'}\dfrac{L_i}{2}+\lambda_n\lambda_{n'}\left[\left(K_{i,y}^0+K_{i,y}^L(-1)^{n+n'}\right)+\left(N_i^0+N_i^L(-1)^{n+n'}\right)\mathbf{H}_{i,66}\right] \end{cases} \tag{A.13}$$

$$\left\{\mathbf{K}^{AA}_{w_{i,y}w_{i,z}}\right\}_{m,m'}=\left(N_i^0+N_i^L(-1)^{m+m'}\right)\mathbf{H}_{i,23},\ \left\{\mathbf{K}^{AB}_{w_{i,y}w_{i,z}}\right\}_{m,n'}=\lambda_{n'}\left(N_i^0+N_i^L(-1)^{m+n'}\right)\mathbf{H}_{i,25} \tag{A.14,15}$$

$$\left\{\mathbf{K}^{BA}_{w_{i,y}w_{i,z}}\right\}_{n,m'}=\lambda_n\left(N_i^0+N_i^L(-1)^{n+m'}\right)\mathbf{H}_{i,63},\ \left\{\mathbf{K}^{BB}_{w_{i,y}w_{i,z}}\right\}_{n,n'}=\lambda_n\lambda_{n'}\left(N_i^0+N_i^L(-1)^{m+n'}\right)\mathbf{H}_{i,65} \tag{A.16,17}$$

$$\left\{\mathbf{K}^{AA}_{w_{i,y}\theta_i}\right\}_{m,m'}=\left(N_i^0+N_i^L(-1)^{m+m'}\right)\mathbf{H}_{i,24},\ \left\{\mathbf{K}^{BA}_{w_{i,y}\theta_i}\right\}_{n,m'}=\lambda_n\left(N_i^0+N_i^L(-1)^{n+m'}\right)\mathbf{H}_{i,64} \tag{A.18,19}$$

$$\left\{\mathbf{K}^{AA}_{w_{i,z}w_{i,z}}\right\}_{m,m'}=\begin{cases} m,m'=0 & E_i I_{i,y}\lambda_m^4\delta_{mm'}L_i+k_{i,z}^0+k_{i,z}^L(-1)^{m+m'}+\left(N_i^0+N_i^L(-1)^{m+m'}\right)\mathbf{H}_{i,33} \\ m,m'\neq 0 & E_i I_{i,y}\lambda_m^4\delta_{mm'}\dfrac{L_i}{2}+k_{i,z}^0+k_{i,z}^L(-1)^{m+m'}+\left(N_i^0+N_i^L(-1)^{m+m'}\right)\mathbf{H}_{i,33} \end{cases} \tag{A.20}$$

$$\left\{\mathbf{K}^{AB}_{w_{i,z}w_{i,z}}\right\}_{m,n'}=\begin{cases} m=n' & \lambda_{n'}\left(N_i^0+N_i^L(-1)^{m+n'}\right)\mathbf{H}_{i,35} \\ m\neq n' & E_i I_{i,y}\lambda_m^2\lambda_{n'}^2 n' L_i\left((-1)^{m+n'}-1\right)/\pi(m^2-n'^2)+\lambda_{n'}\left(N_i^0+N_i^L(-1)^{m+n'}\right)\mathbf{H}_{i,35} \end{cases} \tag{A.21}$$

$$\left\{\mathbf{K}^{BB}_{w_{i,z}w_{i,z}}\right\}_{n,n'}=\begin{cases} n,n'=0 & \lambda_n\lambda_{n'}\left[\left(K_{i,z}^0+K_{i,z}^L(-1)^{n+n'}\right)+\left(N_i^0+N_i^L(-1)^{n+n'}\right)\mathbf{H}_{i,55}\right] \\ n,n'\neq 0 & E_i I_{i,y}\lambda_n^4\delta_{nn'}\dfrac{L_i}{2}+\lambda_n\lambda_{n'}\left[\left(K_{i,z}^0+K_{i,z}^L(-1)^{n+n'}\right)+\left(N_i^0+N_i^L(-1)^{n+n'}\right)\mathbf{H}_{i,55}\right] \end{cases} \tag{A.22}$$

$$\left\{\mathbf{K}^{AA}_{w_{i,y}\theta_i}\right\}_{m,m'}=\left(N_i^0+N_i^L(-1)^{m+m'}\right)\mathbf{H}_{i,34},\ \left\{\mathbf{K}^{BA}_{w_{i,y}\theta_i}\right\}_{n,m'}=\lambda_n\left(N_i^0+N_i^L(-1)^{n+m'}\right)\mathbf{H}_{i,54} \tag{A.23,24}$$

$$\left\{\mathbf{K}^{AA}_{\theta_i\theta_i}\right\}_{m,m'}=\begin{cases} m,m'=0 & K_{i,\theta}^0+K_{i,\theta}^L(-1)^{m+m'}+\left(N_i^0+N_i^L(-1)^{m+m'}\right)\mathbf{H}_{i,44} \\ m,m'\neq 0 & G_i J_i\lambda_m^2\delta_{mm'}\dfrac{L_i}{2}+K_{i,\theta}^0+K_{i,\theta}^L(-1)^{m+m'}+\left(N_i^0+N_i^L(-1)^{m+m'}\right)\mathbf{H}_{i,44} \end{cases} \tag{A.25}$$

$$\left\{\mathbf{K}^{AB}_{\theta_i\theta_i}\right\}_{m,n'}=\begin{cases} m=n' & 0 \\ m\neq n' & -G_i J_i\lambda_m\lambda_{n'} m L_i\left((-1)^{m+n'}-1\right)/\pi(m^2-n'^2) \end{cases} \tag{A.26}$$

$$\left\{\mathbf{K}^{BB}_{\theta_i\theta_i}\right\}_{n,n'} = \begin{cases} n,n'=0 & L_i \\ n,n'\neq 0 & G_i J_i \lambda_n^2 \delta_{nn'} \dfrac{L_i}{2} \end{cases} \tag{A.27}$$

$$\left\{\mathbf{K}^{AA}_{u_i u_j}\right\}_{m,m'} = (-1)^{pm+qm'}\mathbf{H}_{ij,11}, \ \left\{\mathbf{K}^{AA}_{u_i w_{j,y}}\right\}_{m,m'} = (-1)^{pm+qm'}\mathbf{H}_{ij,12} \tag{A.28-29}$$

$$\left\{\mathbf{K}^{AB}_{u_i w_{j,y}}\right\}_{m,n'} = \lambda_{n'}(-1)^{pm+qn'}\mathbf{H}_{ij,16}, \ \left\{\mathbf{K}^{AA}_{u_i w_{j,z}}\right\}_{m,m'} = (-1)^{pm+qm'}\mathbf{H}_{ij,13} \tag{A.30-31}$$

$$\left\{\mathbf{K}^{AB}_{u_i w_{j,z}}\right\}_{m,n'} = \lambda_{n'}(-1)^{pm+qn'}\mathbf{H}_{ij,15}, \ \left\{\mathbf{K}^{AA}_{u_i \theta_j}\right\}_{m,m'} = (-1)^{pm+qm'}\mathbf{H}_{ij,14} \tag{A.32-33}$$

$$\left\{\mathbf{K}^{AA}_{w_{i,y} u_j}\right\}_{m,m'} = (-1)^{pm+qm'}\mathbf{H}_{ij,21}, \left\{\mathbf{K}^{AA}_{w_{i,y} w_{j,y}}\right\}_{m,m'} = (-1)^{pm+qm'}\mathbf{H}_{ij,22} \tag{A.34-35}$$

$$\left\{\mathbf{K}^{AB}_{w_{i,y} w_{j,y}}\right\}_{m,n'} = \lambda_{n'}(-1)^{pm+qn'}\mathbf{H}_{ij,26}, \left\{\mathbf{K}^{AA}_{w_{i,y} w_{j,z}}\right\}_{m,m'} = (-1)^{pm+qm'}\mathbf{H}_{ij,23} \tag{A.36-37}$$

$$\left\{\mathbf{K}^{AB}_{w_{i,y} w_{j,z}}\right\}_{m,n'} = \lambda_{n'}(-1)^{pm+qn'}\mathbf{H}_{ij,25}, \left\{\mathbf{K}^{AA}_{w_{i,y} \theta_j}\right\}_{m,m'} = (-1)^{pm+qm'}\mathbf{H}_{ij,24} \tag{A.38-39}$$

$$\left\{\mathbf{K}^{BA}_{w_{i,y} u_j}\right\}_{n,m'} = \lambda_n(-1)^{pn+qm'}\mathbf{H}_{ij,61}, \left\{\mathbf{K}^{BA}_{w_{i,y} w_{j,y}}\right\}_{n,m'} = \lambda_n(-1)^{pn+qm'}\mathbf{H}_{ij,62} \tag{A.40,41}$$

$$\left\{\mathbf{K}^{BB}_{w_{i,y} w_{j,y}}\right\}_{n,n'} = \lambda_n\lambda_{n'}(-1)^{pn+qn'}\mathbf{H}_{ij,66}, \ \left\{\mathbf{K}^{BA}_{w_{i,y} w_{j,z}}\right\}_{n,m'} = \lambda_n(-1)^{pn+qm'}\mathbf{H}_{ij,63} \tag{A.42,43}$$

$$\left\{\mathbf{K}^{BB}_{w_{i,y} w_{j,y}}\right\}_{n,n'} = \lambda_n\lambda_{n'}(-1)^{pn+qn'}\mathbf{H}_{ij,65}, \ \left\{\mathbf{K}^{BA}_{w_{i,y} \theta_j}\right\}_{n,m'} = \lambda_n(-1)^{pn+qm'}\mathbf{H}_{ij,64} \tag{A.44,45}$$

$$\left\{\mathbf{K}^{AA}_{w_{i,z} u_j}\right\}_{m,m'} = (-1)^{pm+qm'}\mathbf{H}_{ij,31}, \left\{\mathbf{K}^{AA}_{w_{i,z} w_{j,y}}\right\}_{m,m'} = (-1)^{pm+qm'}\mathbf{H}_{ij,32} \tag{A.46,47}$$

$$\left\{\mathbf{K}^{AB}_{w_{i,z} w_{j,y}}\right\}_{m,n'} = \lambda_{n'}(-1)^{pm+qn'}\mathbf{H}_{ij,36}, \ \left\{\mathbf{K}^{AA}_{w_{i,z} w_{j,z}}\right\}_{m,m'} = (-1)^{pm+qm'}\mathbf{H}_{ij,33} \tag{A.48,49}$$

$$\left\{\mathbf{K}^{AB}_{w_{i,z} w_{j,z}}\right\}_{m,n'} = \lambda_{n'}(-1)^{pm+qn'}\mathbf{H}_{ij,35}, \ \left\{\mathbf{K}^{AA}_{w_{i,z} \theta_j}\right\}_{m,m'} = (-1)^{pm+qm'}\mathbf{H}_{ij,34} \tag{A.50,51}$$

$$\left\{\mathbf{K}^{BA}_{w_{i,z} u_j}\right\}_{n,m'} = \lambda_n(-1)^{pn+qm'}\mathbf{H}_{ij,51}, \left\{\mathbf{K}^{BA}_{w_{i,z} w_{j,y}}\right\}_{n,m'} = \lambda_n(-1)^{pn+qm'}\mathbf{H}_{ij,52} \tag{A.52,53}$$

$$\left\{\mathbf{K}^{BB}_{w_{i,z} w_{j,y}}\right\}_{n,n'} = \lambda_n\lambda_{n'}(-1)^{pn+qn'}\mathbf{H}_{ij,56}, \ \left\{\mathbf{K}^{BA}_{w_{i,z} w_{j,z}}\right\}_{n,m'} = \lambda_n(-1)^{pn+qm'}\mathbf{H}_{ij,53} \tag{A.54,55}$$

$$\left\{\mathbf{K}^{BB}_{w_{i,z} w_{j,z}}\right\}_{n,n'} = \lambda_n\lambda_{n'}(-1)^{pn+qn'}\mathbf{H}_{ij,55}, \ \left\{\mathbf{K}^{BA}_{w_{i,z} \theta_j}\right\}_{n,m'} = \lambda_n(-1)^{pn+qm'}\mathbf{H}_{ij,54} \tag{A.56,57}$$

$$\left\{\mathbf{K}^{AA}_{\theta_i \theta_j}\right\}_{m,m'} = (-1)^{pm+qm'}\mathbf{H}_{ij,41}, \ \left\{\mathbf{K}^{AA}_{\theta_i w_{j,y}}\right\}_{m,m'} = (-1)^{pm+qm'}\mathbf{H}_{ij,42} \tag{A.58-59}$$

$$\left\{\mathbf{K}^{AB}_{\theta_i w_{j,y}}\right\}_{m,n'} = \lambda_{n'}(-1)^{pm+qn'}\mathbf{H}_{ij,46} \qquad \left\{\mathbf{K}^{AA}_{\theta_i w_{j,z}}\right\}_{m,m'} = (-1)^{pm+qm'}\mathbf{H}_{ij,43} \tag{A.60-61}$$

$$\left\{\mathbf{K}^{AB}_{\theta_i w_{j,z}}\right\}_{m,n'} = \lambda_{n'}(-1)^{pm+qn'}\mathbf{H}_{ij,45}\,,\ \left\{\mathbf{K}^{AA}_{\theta_i \theta_j}\right\}_{m,m'} = (-1)^{pm+qm'}\mathbf{H}_{ij,44} \tag{A.62-63}$$

The mass matrices are defined as below

$$\mathbf{M} = diag\begin{bmatrix}\mathbf{M}_1 & \cdots & \mathbf{M}_i & \cdots\end{bmatrix},\ \mathbf{M}_i = \begin{bmatrix}\mathbf{M}^{AA}_{\sigma_1\sigma_2} & \mathbf{M}^{AB}_{\sigma_1\sigma_2} \\ \left(\mathbf{M}^{AB}_{\sigma_1\sigma_2}\right)^T & \mathbf{M}^{BB}_{\sigma_1\sigma_2}\end{bmatrix},\ \sigma_1, \sigma_2 = w_{i,z}, w_{i,y}, u_i, \theta_i \tag{A.64,65}$$

$$\left\{\mathbf{M}^{AA}_{\sigma\sigma}\right\}_{m,m'} = \frac{L_i}{2}\delta_{mm'}\left(1+\delta_{m0}\right)\rho_i S_i\,,\ \left\{\mathbf{M}^{BB}_{\sigma\sigma}\right\}_{n,n'} = \frac{L_i}{2}\delta_{nn'}\rho_i S_i \tag{A.66,67}$$

$$\left\{\mathbf{M}^{AB}_{\sigma\sigma}\right\}_{m,n'} = \begin{cases} m = n' & 0 \\ m \neq n' & \rho_i S_i n' L_i\left((-1)^{m+n'} - 1\right)/\pi(m^2 - n'^2) \end{cases},\ \left\{\mathbf{M}^{BA}_{\sigma\sigma}\right\}_{n,m'} = \left\{\mathbf{M}^{AB}_{\sigma\sigma}\right\}_{m,n'} \tag{A.68,69}$$

APPENDIX B

SUPPLEMENTARY FUNCTIONS DEFINED IN CHAPTER 4

Supplementary functions used in Eqs. (4.4-6) for the transverse and in-plane displacement expressions of the plate along the *x* direction are defined as

$$\zeta_a^1(x) = \frac{9a}{4\pi}\sin\left(\frac{\pi x}{2a}\right) - \frac{a}{12\pi}\sin\left(\frac{3\pi x}{2a}\right) \tag{B.1}$$

$$\zeta_a^2(x) = -\frac{9a}{4\pi}\cos\left(\frac{\pi x}{2a}\right) - \frac{a}{12\pi}\cos\left(\frac{3\pi x}{2a}\right) \tag{B.2}$$

$$\zeta_a^3(x) = \frac{a^3}{\pi^3}\sin\left(\frac{\pi x}{2a}\right) - \frac{a^3}{3\pi^3}\sin\left(\frac{3\pi x}{2a}\right) \tag{B.3}$$

$$\zeta_a^4(x) = -\frac{a^3}{\pi^3}\cos\left(\frac{\pi x}{2a}\right) - \frac{a^3}{3\pi^3}\cos\left(\frac{3\pi x}{2a}\right) \tag{B.4}$$

$$\xi_a^1(x) = x\left(\frac{x}{a}-1\right)^2,\ \xi_a^2(x) = \frac{x^2}{a}\left(\frac{x}{a}-1\right) \tag{B.5-6}$$

For displacements along the *y* direction, the corresponding supplementary functions can be obtained by replacing subscript *a* and variable *x* with subscript *b* and variable *y*, respectively.

APPENDIX C

SUBMATRICES DEFINED IN CHAPTER 4

Sub-matrices defined in Eq. (4.25) are given as

$$\mathbf{K}_{ii}^{c} = \begin{bmatrix} \mathbf{K}_{w_iw_i} & \mathbf{K}_{w_iu_i} & \mathbf{K}_{w_iv_i} \\ \vdots & \mathbf{K}_{u_iu_i} & \mathbf{K}_{u_iv_i} \\ Symm & \cdots & \mathbf{K}_{v_iv_i} \end{bmatrix} \tag{C.1}$$

where sub-matrices $\mathbf{K}_{w_iw_i}$ and $\mathbf{K}_{w_jw_j}$ have the same form

$$\mathbf{K}_{w_iw_i} = \begin{bmatrix} \mathbf{K}_{w_iw_i}^{11} & \mathbf{K}_{w_iw_i}^{12} & \cdots & \mathbf{K}_{w_iw_i}^{19} \\ & \mathbf{K}_{w_iw_i}^{22} & \cdots & \mathbf{K}_{w_iw_i}^{29} \\ \vdots & & \ddots & \vdots \\ Symm & \cdots & & \mathbf{K}_{w_iw_i}^{99} \end{bmatrix} \tag{C.2}$$

Components of $\mathbf{K}_{w_iw_i}$ and $\mathbf{K}_{w_jw_j}$ are defined as below

$$\left\{\mathbf{K}_{w_iw_i}^{11}\right\}_{s,t} = \Delta_{n,n'}, \quad \left\{\mathbf{K}_{w_iw_i}^{1(q+1)}\right\}_{s,m'+1} = \Xi_{n}^{f,q} \tag{C.3-4}$$

$$\left\{\mathbf{K}_{w_iw_i}^{1(q+5)}\right\}_{s,n'+1} = \left(\delta_{q1} - \delta_{q2}\frac{7a_i}{3\pi} - \delta_{q4}\frac{4a_i^3}{3\pi^3}\right)\Delta_{n,n'}, \quad \left\{\mathbf{K}_{w_iw_i}^{(p+1)(q+1)}\right\}_{m+1,m'+1} = \Gamma_{p,q}^{f} \tag{C.5-6}$$

$$\left\{\mathbf{K}_{w_iw_i}^{(p+1)(q+5)}\right\}_{m+1,n'+1} = \left(\delta_{q1} - \delta_{q2}\frac{7a_i}{3\pi} - \delta_{q4}\frac{4a_i^3}{3\pi^3}\right)\Xi_{n'}^{f,p} \tag{C.7}$$

$$\left\{\mathbf{K}_{w_iw_i}^{(p+5)(q+5)}\right\}_{n+1,n'+1} = \left[\delta_{p1}\delta_{q1} + \left(\delta_{p2}\frac{7a_i}{3\pi} + \delta_{p4}\frac{4a_i^3}{3\pi^3}\right)\left(\delta_{q2}\frac{7a_i}{3\pi} + \delta_{q4}\frac{4a_i^3}{3\pi^3}\right)\right]\Delta_{n,n'} \tag{C.8}$$

$$\left\{\mathbf{K}_{w_jw_j}^{11}\right\}_{s,t} = \left(-1\right)^{m+m'}\Delta_{n,n'}, \quad \left\{\mathbf{K}_{w_jw_j}^{1(q+1)}\right\}_{s,m'+1} = (-1)^{m+m'}\Xi_{n}^{f,q} \tag{C.9-10}$$

$$\left\{\mathbf{K}_{w_jw_j}^{1(q+5)}\right\}_{s,n'+1} = (-1)^{m}\left(\delta_{q2} + \delta_{q1}\frac{7a_j}{3\pi} + \delta_{q3}\frac{4a_j^3}{3\pi^3}\right)\Delta_{n,n'}, \quad \left\{\mathbf{K}_{w_jw_j}^{(p+1)(q+1)}\right\}_{m+1,m'+1} = (-1)^{m+m'}\Gamma_{p,q}^{f} \tag{C.11,12}$$

$$\left\{\mathbf{K}_{w_jw_j}^{(p+1)(q+5)}\right\}_{m+1,n'+1} = (-1)^m\left(\delta_{q2}+\delta_{q1}\frac{7a_j}{3\pi}+\delta_{q3}\frac{4a_j^3}{3\pi^3}\right)\Xi_{n'}^{f,p} \tag{C.13}$$

$$\left\{\mathbf{K}_{w_jw_j}^{(p+5)(q+5)}\right\}_{m+1,n'+1} = \left[\delta_{p2}\delta_{q2}+\left(\delta_{p1}\frac{7a_j}{3\pi}+\delta_{p3}\frac{4a_j^3}{3\pi^3}\right)\left(\delta_{q1}\frac{7a_j}{3\pi}+\delta_{q3}\frac{4a_j^3}{3\pi^3}\right)\right]\Delta_{n,n'} \tag{C.14}$$

where $s = m(N+1)+n+1$ and $t = m'(N+1)+n'+1$

Sub-matrices $\mathbf{K}_{u_iu_i}$, $\mathbf{K}_{v_iv_i}$ and $\mathbf{K}_{u_iv_i}$ have the same form

$$\mathbf{K}_{u_iu_i} = \begin{bmatrix} \mathbf{K}_{u_iu_i}^{11} & \mathbf{K}_{u_iu_i}^{12} & \cdots & \mathbf{K}_{u_iu_i}^{15} \\ & \mathbf{K}_{u_iu_i}^{22} & \cdots & \mathbf{K}_{u_iu_i}^{25} \\ \vdots & & \ddots & \vdots \\ Symm & \cdots & & \mathbf{K}_{u_iu_i}^{55} \end{bmatrix} \tag{C.15}$$

Components of $\mathbf{K}_{u_iu_i}$ are expressed as

$$\left\{\mathbf{K}_{u_iu_i}^{11}\right\}_{s,t} = \Delta_{n,n'}\,,\ \left\{\mathbf{K}_{u_iu_i}^{1(q+1)}\right\}_{s,m'+1} = \Xi_{n}^{in,q}\,,\ \left\{\mathbf{K}_{u_iu_i}^{(p+1)(q+1)}\right\}_{m+1,m'+1} = \Gamma_{p,q}^{in} \tag{C.16-18}$$

$$\mathbf{K}_{u_iu_i}^{1(q+3)} = \mathbf{K}_{u_iu_i}^{(p+3)(q+3)} = \mathbf{K}_{u_iu_i}^{(p+1)(q+3)} = [\mathbf{0}] \tag{C.19-21}$$

Components of $\mathbf{K}_{v_iv_i}$ and $\mathbf{K}_{u_iv_i}$ are identical to those of $\mathbf{K}_{u_ju_j}$. Components of $\mathbf{K}_{u_ju_j}$ can be obtained by multiplying Eq. (C.16-21) by $(-1)^{m+m'}$. Similarly, components of $\mathbf{K}_{v_jv_j}$ and $\mathbf{K}_{u_jv_j}$ are identical to those of $\mathbf{K}_{u_ju_j}$. The cross coupling stiffness matrix $\mathbf{K}_{ij}$ has the form

$$\mathbf{K}_{ij} = \begin{bmatrix} \mathbf{K}_{w_iw_j} & \mathbf{K}_{w_iu_j} & \mathbf{K}_{w_iv_j} \\ \mathbf{K}_{u_iw_j} & \mathbf{K}_{u_iu_j} & \mathbf{K}_{u_iv_j} \\ \mathbf{K}_{v_iw_j} & \mathbf{K}_{v_iu_j} & \mathbf{K}_{v_iv_j} \end{bmatrix} \tag{C.22}$$

where sub-matrices $\mathbf{K}_{w_iw_j}$ has the form

$$\mathbf{K}_{w_iw_j} = \begin{bmatrix} \mathbf{K}^{11}_{w_iw_j} & \mathbf{K}^{12}_{w_iw_j} & \cdots & \mathbf{K}^{19}_{w_iw_j} \\ \mathbf{K}^{21}_{w_iw_j} & \mathbf{K}^{22}_{w_iw_j} & \cdots & \mathbf{K}^{29}_{w_iw_j} \\ \vdots & \vdots & \ddots & \vdots \\ \mathbf{K}^{91}_{w_iw_j} & \mathbf{K}^{92}_{w_iw_j} & \cdots & \mathbf{K}^{99}_{w_iw_j} \end{bmatrix} \tag{C.23}$$

$$\left\{\mathbf{K}^{11}_{w_iw_j}\right\}_{s,t} = (-1)^{m'}\Delta_{n,n'}\,,\ \left\{\mathbf{K}^{1(q+1)}_{w_iw_j}\right\}_{s,m'+1} = (-1)^{m'}\Xi^{f,q}_{n} \tag{C.24-25}$$

$$\left\{\mathbf{K}^{1(q+5)}_{w_iw_j}\right\}_{s,n'+1} = \left(\delta_{q2}+\delta_{q1}\frac{7a_j}{3\pi}+\delta_{q3}\frac{4a_j^3}{3\pi^3}\right)\Delta_{n,n'}\,,\ \left\{\mathbf{K}^{(p+1)1}_{w_iw_j}\right\}_{m+1,t} = (-1)^{m'}\Xi^{f,p}_{n'} \tag{C.26-27}$$

$$\left\{\mathbf{K}^{(p+1)(q+1)}_{w_iw_j}\right\}_{m+1,m'+1} = (-1)^{m'}\Gamma^{f}_{p,q}\,,\ \left\{\mathbf{K}^{(p+1)(q+5)}_{w_iw_j}\right\}_{m+1,n'+1} = \left(\delta_{q2}+\delta_{q1}\frac{7a_j}{3\pi}+\delta_{q3}\frac{4a_j^3}{3\pi^3}\right)\Xi^{f,p}_{n'} \tag{C.28,29}$$

$$\left\{\mathbf{K}^{(p+5)1}_{w_iw_j}\right\}_{n+1,t} = (-1)^{m'}\left(\delta_{p1}-\delta_{p2}\frac{7a_i}{3\pi}-\delta_{p4}\frac{4a_i^3}{3\pi^3}\right)\Delta_{n,n'} \tag{C.30}$$

$$\left\{\mathbf{K}^{(p+5)(q+1)}_{w_iw_j}\right\}_{n+1,m'+1} = (-1)^{m'}\left(\delta_{p1}-\delta_{p2}\frac{7a_i}{3\pi}-\delta_{p4}\frac{4a_i^3}{3\pi^3}\right)\Xi^{f,q}_{n} \tag{C.31}$$

$$\left\{\mathbf{K}^{(p+5)(q+5)}_{w_iw_j}\right\}_{n+1,n'+1} = \left(\delta_{p1}-\delta_{p2}\frac{7a_i}{3\pi}+\delta_{p4}\frac{4a_i^3}{3\pi^3}\right)\left(\delta_{q2}+\delta_{q1}\frac{7a_j}{3\pi}+\delta_{q3}\frac{4a_j^3}{3\pi^3}\right)\Delta_{n,n'} \tag{C.32}$$

Sub-matrices $\mathbf{K}_{w_iu_i}$ and $\mathbf{K}_{w_ju_j}$ follow the same form

$$\mathbf{K}_{w_iu_i} = \begin{bmatrix} \mathbf{K}^{11}_{w_iu_i} & \mathbf{K}^{12}_{w_iu_i} & \cdots & \mathbf{K}^{15}_{w_iu_i} \\ \mathbf{K}^{21}_{w_iu_i} & \mathbf{K}^{22}_{w_iu_i} & \cdots & \mathbf{K}^{25}_{w_iu_i} \\ \vdots & \vdots & \ddots & \vdots \\ \mathbf{K}^{91}_{w_iu_i} & \mathbf{K}^{95}_{w_iu_i} & \cdots & \mathbf{K}^{95}_{w_iu_i} \end{bmatrix} \tag{C.33}$$

Components of $\mathbf{K}_{w_iu_i}$ are given as below

$$\left\{\mathbf{K}^{11}_{w_iu_i}\right\}_{s,t} = \Delta_{n,n'}\,,\ \left\{\mathbf{K}^{1(q+1)}_{w_iu_i}\right\}_{s,m'+1} = \Xi^{in,q}_{n}\,,\ \left\{\mathbf{K}^{(p+1)1}_{w_iu_i}\right\}_{m+1,t} = \Xi^{f,p}_{n'} \tag{C.34-36}$$

$$\left\{\mathbf{K}^{(p+1)(q+1)}_{w_iu_i}\right\}_{m+1,m'+1} = \Gamma^{f\_in}_{p,q}\,,\ \left\{\mathbf{K}^{(p+5)1}_{w_iu_i}\right\}_{n+1,t} = \left(\delta_{p1}-\delta_{p2}\frac{7a_i}{3\pi}-\delta_{p4}\frac{4a_i^3}{3\pi^3}\right)\Xi^{f,p}_{n'} \tag{C.37-38}$$

$$\left\{\mathbf{K}_{w_iu_i}^{(p+5)(q+1)}\right\}_{n+1,m'+1} = \left(\delta_{p1} - \delta_{p2}\frac{7a_i}{3\pi} - \delta_{p4}\frac{4a_i^3}{3\pi^3}\right)\Xi_n^{in,q} \tag{C.39}$$

$$\mathbf{K}_{w_iu_i}^{1(q+3)} = \mathbf{K}_{w_iu_i}^{(p+1)(q+3)} = \mathbf{K}_{w_iu_i}^{(p+5)(q+3)} = [\mathbf{0}] \tag{C.40-42}$$

Components of $\mathbf{K}_{w_ju_j}$ are given as below

$$\left\{\mathbf{K}_{w_ju_j}^{11}\right\}_{s,t} = (-1)^{m+m'}\Delta_{n,n'},\ \left\{\mathbf{K}_{w_ju_j}^{1(q+1)}\right\}_{s,m'+1} = (-1)^{m+m'}\Xi_n^{in,q},\ \left\{\mathbf{K}_{w_ju_j}^{(p+1)1}\right\}_{m+1,t} = (-1)^{m+m'}\Xi_{n'}^{f,p} \tag{C.43-45}$$

$$\left\{\mathbf{K}_{w_ju_j}^{(p+1)(q+1)}\right\}_{m+1,m'+1} = (-1)^{m+m'}\Gamma_{p,q}^{f\_in},\ \left\{\mathbf{K}_{w_ju_j}^{(p+5)1}\right\}_{n+1,t} = (-1)^{m'}\left(\delta_{p2} + \delta_{p1}\frac{7a_j}{3\pi} + \delta_{p3}\frac{4a_j^3}{3\pi^3}\right)\Xi_{n'}^{f,p} \tag{C.46-47}$$

$$\left\{\mathbf{K}_{w_ju_j}^{(p+5)(q+1)}\right\}_{n+1,m'+1} = (-1)^{m'}\left(\delta_{p2} + \delta_{p1}\frac{7a_j}{3\pi} + \delta_{p3}\frac{4a_j^3}{3\pi^3}\right)\Xi_n^{in,q} \tag{C.48}$$

$$\mathbf{K}_{w_ju_j}^{1(q+3)} = \mathbf{K}_{w_ju_j}^{(p+1)(q+3)} = \mathbf{K}_{w_ju_j}^{(p+5)(q+3)} = [\mathbf{0}] \tag{C.49}$$

Components of $\mathbf{K}_{w_iu_j}$ are given as below

$$\mathbf{K}_{w_iu_j} = \begin{bmatrix} \mathbf{K}_{w_iu_j}^{11} & \mathbf{K}_{w_iu_j}^{12} & \cdots & \mathbf{K}_{w_iu_j}^{15} \\ \mathbf{K}_{w_iu_j}^{21} & \mathbf{K}_{w_iu_j}^{22} & \cdots & \mathbf{K}_{w_iu_j}^{25} \\ \vdots & \vdots & \ddots & \vdots \\ \mathbf{K}_{w_iu_j}^{91} & \mathbf{K}_{w_iu_j}^{95} & \cdots & \mathbf{K}_{w_iu_j}^{95} \end{bmatrix} \tag{C.50}$$

$$\left\{\mathbf{K}_{w_iu_j}^{11}\right\}_{s,t} = (-1)^{m'}\Delta_{n,n'},\ \left\{\mathbf{K}_{w_iu_j}^{1(q+1)}\right\}_{s,m'+1} = (-1)^{m'}\Xi_n^{in,q},\ \left\{\mathbf{K}_{w_iu_j}^{(p+1)1}\right\}_{m+1,t} = (-1)^{m'}\Xi_{n'}^{f,p} \tag{C.51-53}$$

$$\left\{\mathbf{K}_{w_iu_j}^{(p+1)(q+1)}\right\}_{m+1,m'+1} = (-1)^{m'}\Gamma_{p,q}^{f\_in},\ \left\{\mathbf{K}_{w_iu_j}^{(p+5)1}\right\}_{n+1,t} = (-1)^{m'}\left(\delta_{p1} - \delta_{p2}\frac{7a_i}{3\pi} - \delta_{p4}\frac{4a_i^3}{3\pi^3}\right)\Xi_{n'}^{f,p} \tag{C.54,55}$$

$$\left\{\mathbf{K}_{w_iu_j}^{(p+5)(q+1)}\right\}_{n+1,m'+1} = (-1)^{m'}\left(\delta_{p1} - \delta_{p2}\frac{7a_i}{3\pi} - \delta_{p4}\frac{4a_i^3}{3\pi^3}\right)\Xi_n^{in,q} \tag{C.56}$$

$$\mathbf{K}_{w_iu_j}^{1(q+3)} = \mathbf{K}_{w_iu_j}^{(p+1)(q+3)} = \mathbf{K}_{w_iu_j}^{(p+5)(q+3)} = [\mathbf{0}] \tag{C.57-59}$$

Components of $\mathbf{K}_{u_iu_j}$ are given as below

$$\mathbf{K}_{u_i u_j} = \begin{bmatrix} \mathbf{K}_{u_i u_j}^{11} & \mathbf{K}_{u_i u_j}^{12} & \cdots & \mathbf{K}_{u_i u_j}^{15} \\ \mathbf{K}_{u_i u_j}^{21} & \mathbf{K}_{u_i u_j}^{22} & \cdots & \mathbf{K}_{u_i u_j}^{25} \\ \vdots & \vdots & \ddots & \vdots \\ \mathbf{K}_{u_i u_j}^{51} & \mathbf{K}_{u_i u_j}^{52} & \cdots & \mathbf{K}_{u_i u_j}^{55} \end{bmatrix} \tag{C.60}$$

$$\left\{\mathbf{K}_{u_i u_j}^{11}\right\}_{s,t} = (-1)^{m'} \Delta_{n,n'}, \left\{\mathbf{K}_{u_i u_j}^{1(q+1)}\right\}_{s,m'+1} = (-1)^{m'} \Xi_{n}^{in,q}, \ \left\{\mathbf{K}_{u_i u_j}^{(p+1)(q+1)}\right\}_{m+1,m'+1} = (-1)^{m'} \Gamma_{p,q}^{in} \tag{C.61-63}$$

$$\mathbf{K}_{u_i u_j}^{1(q+3)} = \mathbf{K}_{u_i u_j}^{(p+1)(q+3)} = \mathbf{K}_{u_i u_j}^{(p+3)(q+3)} = \mathbf{K}_{u_i u_j}^{(p+3)(q+1)} = 0, \ \left\{\mathbf{K}_{u_i u_j}^{(p+1)1}\right\}_{m+1,t} = (-1)^{m'} \Xi_{n'}^{in,p} \tag{C.64-68}$$

Components of $\mathbf{K}_{v_i v_j}$, $\mathbf{K}_{u_i v_j}$ and $\mathbf{K}_{v_i u_j}$ are identical to those of $\mathbf{K}_{u_i u_j}$.

.

APPENDIX D

SUBMATRICES DEFINED IN APPENDIX C

Definitions of matrices in APPENDIX C are given as

$$\zeta_1^b = \left\{ \sin\left(\frac{\pi}{2b}y\right) - \sin\left(\frac{3\pi}{2b}y\right) \right\}, \zeta_2^b = \left\{ \cos\left(\frac{\pi}{2b}y\right) - \cos\left(\frac{3\pi}{2b}y\right) \right\} \tag{D.1-2}$$

$$\tau_{b1} = \left\{ \frac{9b}{4\pi} \quad -\frac{b}{12\pi} \right\},\ \tau_{b2} = \left\{ -\frac{9b}{4\pi} \quad -\frac{b}{12\pi} \right\}, \tau_{b3} = \left\{ \frac{b^3}{\pi^3} \quad -\frac{b^3}{3\pi^3} \right\},\ \tau_{b4} = \left\{ -\frac{b^3}{\pi^3} \quad -\frac{b^3}{3\pi^3} \right\} \tag{D.3-6}$$

$$\Xi_p^{f,i} = \int_0^b \tau_{bi}^T \left[(\delta_{i1} + \delta_{i3})\zeta_1^b + (\delta_{i2} + \delta_{i4})\zeta_2^b \right] \cos\lambda_p y dy \text{, where } p = n, n' \tag{D.7}$$

$$\Gamma_{i,j}^f = \int_0^b \tau_{bi}^T \left[(\delta_{i1} + \delta_{i3})\zeta_1^b + (\delta_{i2} + \delta_{i4})\zeta_2^b \right] \times \tau_{bj}^T \left[(\delta_{j1} + \delta_{j3})\zeta_1^b + (\delta_{j2} + \delta_{j4})\zeta_2^b \right] dy \tag{D.8}$$

$$\Delta_{n,n'} = \int_0^b \cos\lambda_n y \cos\lambda_{n'} y dy = \begin{cases} n = n' = 0 & b \\ n, n' \neq 0 & \delta_{nn'} \dfrac{b}{2} \end{cases} \tag{D.9}$$

$$\kappa_{b1} = \left\{ 1 \quad -\frac{2}{b} \quad \frac{1}{b^2} \right\},\ \kappa_{b2} = \left\{ -\frac{1}{b} \quad \frac{1}{b^2} \right\}, \Xi_n^{in,i} = \int_0^a \kappa_{bi}^T \left[\delta_{i1} C_y^1 + \delta_{i2} C_y^2 \right] \cos\lambda_n dy \tag{D.10-12}$$

$$\Gamma_{i,j}^{f-in} = \int_0^b \tau_{bi}^T \left[(\delta_{i1} + \delta_{i3})\zeta_1^b + (\delta_{i2} + \delta_{i4})\zeta_2^b \right] \times \kappa_{bj}^T \left[\delta_{j1} C_y^1 + \delta_{j2} C_y^2 \right] dy \tag{D.13}$$

$$\Gamma_{i,j}^{in} = \int_0^b \kappa_{bi}^T \left[\delta_{i1} C_y^1 + \delta_{i2} C_y^2 \right] \times \kappa_{bj}^T \left[\delta_{j1} C_y^1 + \delta_{j2} C_y^2 \right] dy \tag{D.14}$$

$$C_y^0 = \{ 1 \quad y \quad y^2 \quad y^3 \quad y^4 \quad y^5 \quad y^6 \}, C_y^1 = \{ y \quad y^2 \quad y^3 \}, C_y^2 = \{ y^2 \quad y^3 \}, \tag{D.15-17}$$

$$\int_0^b C_y^0 \sin Ay dy = \left\{ \begin{array}{c} (\cos Ab - 1)/A \\ (\sin Ab + Ab\cos Ab)/A^2 \\ \left[2Ab\sin Ab + (2 - A^2b^2)\cos Ab \ -2 \right]/A^3 \\ \left[3A^2b^2 \sin Ab \ -6\sin Ab \ -Ab \ (A^2b^2 - 6)\cos Ab \ \right]/A^4 \\ \left[4b \ (A^2b^2 - 6)\sin Ab \ -(A^4b^4 - 12A^2b^2 + 24)\cos Ab \ +24 \right]/A^5 \\ \left[-Ab(A^4b^4 - 20A^2b^2 + 120)\cos Ab + 5(A^4b^4 - 12A^2b^2 + 24)\sin Ab \right]/A^6 \\ \left[6Ab(A^4b^4 - 20A^2b^2 + 120)\sin Ab - (A^6b^6 - 30A^4b^4 + 360A^2b^2 - 720)\cos Ab - 720 \right]/A^7 \end{array} \right\}^T$$

$$\int_0^b C_y^0 dy = \left\{ b \quad \frac{b^2}{2} \quad \frac{b^3}{2} \quad \frac{b^4}{2} \quad \frac{b^5}{2} \quad \frac{b^6}{2} \quad \frac{b^7}{2} \right\} dy \qquad \text{(D.18,19)}$$

where A denotes the constant coefficient

APPENDIX E

SUBMATRICES DEFNED IN CHAPTER 5

The stiffness matrix $\mathbf{K}_p$ in Eq. (5.13) is the summation of $\mathbf{K}_p^0$ and $\mathbf{K}_p^c$ reflecting the contributions due to the plate itself and the plate-beam coupling. The stiffness matrix $\mathbf{K}_p^c$ is the summation of matrices contributed by the couplings between the plate and the *i*-th beam, which is given by

$$\mathbf{K_p^c} = \sum_{\mathbf{i}=1}^{\mathbf{N}} \begin{bmatrix} \mathbf{K^i_{w_pw_p}} & 0 & 0 \\ 0 & \mathbf{K^i_{u_pu_p}} & \mathbf{K^i_{u_pv_p}} \\ 0 & \left(\mathbf{K^i_{u_pv_p}}\right)^{\mathbf{T}} & \mathbf{K^i_{v_pv_p}} \end{bmatrix} \tag{E.1}$$

where components of sub-matrices $\mathbf{K^i_{w_pw_p}}$, $\mathbf{K^i_{u_pu_p}}$, $\mathbf{K^i_{v_pv_p}}$, and $\mathbf{K^i_{u_pv_p}}$ are respectively given by

$$\begin{aligned} \left\{\mathbf{K^{11}_{w_pw_p}}\right\}_{s,t} = \int_0^L \Big\{ & k_{z'}^{pb} \cos\lambda_{am}x \cos\lambda_{bn}y \cos\lambda_{am'}x \cos\lambda_{bn'}y \\ & + K_{y'}^{pb}\left(\lambda_{am}\sin\lambda_{am}x\cos\lambda_{bn}y + \lambda_{bn}\cos\lambda_{am}x\sin\lambda_{bn}y\right)\left(\lambda_{am'}\sin\lambda_{am'}x\cos\lambda_{bn'}y + \lambda_{bn'}\cos\lambda_{am'}x\sin\lambda_{bn'}y\right) \\ & + K_{x'}^{pb}\left(\lambda_{am}\sin\lambda_{am}x\cos\lambda_{bn}y - \lambda_{bn}\cos\lambda_{am}x\sin\lambda_{bn}y\right)\left(\lambda_{am'}\sin\lambda_{am'}x\cos\lambda_{bn'}y - \lambda_{bn'}\cos\lambda_{am'}x\sin\lambda_{bn'}y\right)\Big\} dx' \end{aligned} \tag{E.2}$$

$$\begin{aligned} \left\{\mathbf{K^{1j}_{w_pw_p}}\right\}_{s,m'+1} = \int_0^L \Big\{ & k_{z'}^{pb}\zeta_{(j-1)b}(y)\cos\lambda_{am}x\cos\lambda_{bn}y\cos\lambda_{am'}x \\ & - K_{y'}^{pb}\left(\lambda_{am}\sin\lambda_{am}x\cos\lambda_{bn}y + \lambda_{bn}\cos\lambda_{am}x\sin\lambda_{bn}y\right)\left(\zeta'_{(j-1)b}(y)\cos\lambda_{am'}x - \lambda_{am'}\zeta_{(j-1)b}(y)\sin\lambda_{am'}x\right) \\ & + K_{x'}^{pb}\left(\lambda_{am}\sin\lambda_{am}x\cos\lambda_{bn}y - \lambda_{bn}\cos\lambda_{am}x\sin\lambda_{bn}y\right)\left(\zeta'_{(j-1)b}(y)\cos\lambda_{am'}x + \lambda_{am'}\zeta_{(j-1)b}(y)\sin\lambda_{am'}x\right)\Big\} dx' \end{aligned} \tag{E.3}$$

$$\begin{aligned} \left\{\mathbf{K^{1(j+4)}_{w_pw_p}}\right\}_{s,n'+1} = \int_0^L \Big\{ & k_{z'}^{pb}\zeta_{(j-1)a}(x)\cos\lambda_{am}x\cos\lambda_{bn}y\cos\lambda_{bn'}y \\ & - K_{y'}^{pb}\left(\lambda_{am}\sin\lambda_{am}x\cos\lambda_{bn}y + \lambda_{bn}\cos\lambda_{am}x\sin\lambda_{bn}y\right)\left(\zeta'_{(j-1)a}(x)\cos\lambda_{bn'}y - \lambda_{bn'}\zeta_{(j-1)a}(x)\sin\lambda_{bn'}y\right) \\ & - K_{x'}^{pb}\left(\lambda_{am}\sin\lambda_{am}x\cos\lambda_{bn}y - \lambda_{bn}\cos\lambda_{am}x\sin\lambda_{bn}y\right)\left(\zeta'_{(j-1)a}(x)\cos\lambda_{bn'}y + \lambda_{bn'}\zeta_{(j-1)a}(x)\sin\lambda_{bn'}y\right)\Big\} dx' \end{aligned}$$

$$j = 2,3,4,5 \tag{E.4}$$

$$\begin{aligned}\left\{\mathbf{K}^{11}_{\mathbf{u_p u_p}}\right\}_{s,t} &= \int_0^L \Big\{\left(k_{y'}^{pb} l_y^2 + k_{x'}^{pb} l_x^2\right)\cos\lambda_{am}x\cos\lambda_{bn}y\cos\lambda_{am'}x\cos\lambda_{bn'}y \\ &+ K_{z'}^{pb}\lambda_{bn}\lambda_{bn'}\cos\lambda_{am}x\sin\lambda_{bn}y\cos\lambda_{am'}x\sin\lambda_{bn'}y\Big\}dx'\end{aligned} \tag{E.5}$$

$$\begin{aligned}\left\{\mathbf{K}^{1\mathbf{j}}_{\mathbf{u_p u_p}}\right\}_{s,m'+1} &= \int_0^L \Big\{\left(k_{y'}^{pb} l_y^2 + k_{x'}^{pb} l_x^2\right)\zeta_{(j-1)b}(y)\cos\lambda_{am}x\cos\lambda_{bn}y\cos\lambda_{am'}x \\ &- K_{z'}^{pb}\lambda_{bn}\zeta'_{(j-1)b}(y)\cos\lambda_{am}x\sin\lambda_{bn}y\cos\lambda_{am'}x\Big\}dx'\end{aligned} \tag{E.6}$$

$$\begin{aligned}\left\{\mathbf{K}^{1(\mathbf{j}+2)}_{\mathbf{u_p u_p}}\right\}_{s,n'+1} &= \int_0^L \Big\{\left(k_{y'}^{pb} l_y^2 + k_{x'}^{pb} l_x^2\right)\zeta_{(j-1)a}(x)\cos\lambda_{am}x\cos\lambda_{bn}y\cos\lambda_{bn'}y \\ &+ K_{z'}^{pb}\lambda_{bn}\lambda_{bn'}\zeta_{(j-1)a}(x)\cos\lambda_{am}x\sin\lambda_{bn}y\sin\lambda_{bn'}y\Big\}dx'\end{aligned} \tag{E.7}$$

$$\begin{aligned}\left\{\mathbf{K}^{11}_{\mathbf{v_p v_p}}\right\}_{s,t} &= \int_0^L \Big\{\left(k_{y'}^{pb} l_x^2 + k_{x'}^{pb} l_y^2\right)\cos\lambda_{am}x\cos\lambda_{bn}y\cos\lambda_{am'}x\cos\lambda_{bn'}y \\ &+ K_{z'}^{pb}\lambda_{am}\lambda_{am'}\sin\lambda_{am}x\cos\lambda_{bn}y\sin\lambda_{am'}x\cos\lambda_{bn'}y\Big\}dx'\end{aligned} \tag{E.8}$$

$$\begin{aligned}\left\{\mathbf{K}^{1\mathbf{j}}_{\mathbf{v_p v_p}}\right\}_{s,m'+1} &= \int_0^L \Big\{\left(k_{y'}^{pb} l_x^2 + k_{x'}^{pb} l_y^2\right)\zeta_{(j-1)b}(y)\cos\lambda_{am}x\cos\lambda_{bn}y\cos\lambda_{am'}x \\ &+ K_{z'}^{pb}\lambda_{am}\lambda_{am'}\zeta_{(j-1)b}(y)\sin\lambda_{am}x\cos\lambda_{bn}y\sin\lambda_{am'}x\Big\}dx'\end{aligned} \tag{E.9}$$

$$\begin{aligned}\left\{\mathbf{K}^{1(\mathbf{j}+2)}_{\mathbf{v_p v_p}}\right\}_{s,n'+1} &= \int_0^L \Big\{\left(k_{y'}^{pb} l_x^2 + k_{x'}^{pb} l_y^2\right)\zeta_{(j-1)a}(x)\cos\lambda_{am}x\cos\lambda_{bn}y\cos\lambda_{bn'}y \\ &- K_{z'}^{pb}\lambda_{am}\zeta'_{(j-1)a}(x)\sin\lambda_{am}x\cos\lambda_{bn}y\cos\lambda_{bn'}y\Big\}dx'\end{aligned} \tag{E.10}$$

$$\begin{aligned}\left\{\mathbf{K}^{11}_{\mathbf{u_p v_p}}\right\}_{s,t} &= \int_0^L \Big\{\left(-k_{y'}^{pb} l_x l_y + k_{x'}^{pb} l_x l_y\right)\cos\lambda_{am}x\cos\lambda_{bn}y\cos\lambda_{am'}x\cos\lambda_{bn'}y \\ &- K_{z'}^{pb}\lambda_{bn}\lambda_{am'}\cos\lambda_{am}x\sin\lambda_{bn}y\sin\lambda_{am'}x\cos\lambda_{bn'}y\Big\}dx'\end{aligned} \tag{E.11}$$

$$\begin{aligned}\left\{\mathbf{K}^{1\mathbf{j}}_{\mathbf{u_p v_p}}\right\}_{s,m'+1} &= \int_0^L \Big\{l_x l_y\left(k_{x'}^{pb} - k_{y'}^{pb}\right)\zeta_{(j-1)b}(y)\cos\lambda_{am}x\cos\lambda_{bn}y\cos\lambda_{am'}x \\ &- K_{z'}^{pb}\lambda_{bn}\lambda_{am'}\zeta_{(j-1)b}(y)\cos\lambda_{am}x\sin\lambda_{bn}y\sin\lambda_{am'}x\Big\}dx'\end{aligned} \tag{E.12}$$

$$\left\{\mathbf{K}^{1(\mathbf{j}+2)}_{\mathbf{u_p v_p}}\right\}_{s,n'+1} = \int_0^L \Big\{l_x l_y\left(k_{x'}^{pb} - k_{y'}^{pb}\right)\zeta_{(j-1)a}(x)\cos\lambda_{am}x\cos\lambda_{bn}y\cos\lambda_{bn'}y$$

$$+K_{z'}^{pb}\lambda_{bn}\zeta'_{(j-1)a}(x)\cos\lambda_{am}x\sin\lambda_{bn}y\cos\lambda_{bn'}y\big\}dx' \quad j=2,3 \tag{E.13}$$

It should be noted that components of the sub-matrix are only partially given by the equations above for conciseness. The expressions for other components of the sub-matrices can be obtained following the similar manipulations.

The plate-beam coupling stiffness matrix is express as

$$\mathbf{K_{pb}} = \begin{bmatrix}\mathbf{K_{pb}^{1}} & \mathbf{K_{pb}^{2}} & \dots & \mathbf{K_{pb}^{N}}\end{bmatrix} \tag{E.14}$$

$$\text{where } \mathbf{K_{pb}^{i}} = \begin{bmatrix} \mathbf{K^{i}_{w_p w_{bz'}}} & 0 & 0 & \mathbf{K^{i}_{w_p\theta}} \\ 0 & \mathbf{K^{i}_{u_p w_{by'}}} & 0 & 0 \\ 0 & \mathbf{K^{i}_{v_p w_{by'}}} & \mathbf{K^{i}_{v_p u_b}} & 0 \end{bmatrix} \tag{E.15}$$

Components of sub-matrices $\mathbf{K^{i}_{w_p w_{bz'}}}$ are partially given by

$$\big\{\mathbf{K}^{11}_{\mathbf{w_p w_{bz'}}}\big\}_{s,m'+1} = -\int_0^L \big\{k_{z'}^{pb}\cos\lambda_{am}x\cos\lambda_{bn}y\cos\lambda_{m'}x' +$$

$$K_{y'}^{pb}\big(l_x\lambda_{am}\sin\lambda_{am}x\cos\lambda_{bn}y + l_y\lambda_{bn}\cos\lambda_{am}x\sin\lambda_{bn}y\big)\lambda_{m'}\sin\lambda_{m'}x'\big\}dx' \tag{E.16}$$

$$\big\{\mathbf{K^{12}_{w_p w_{bz'}}}\big\}_{s,n'+1} = -\int_0^L \big\{k_{z'}^{pb}\cos\lambda_{am}x\cos\lambda_{bn}y\sin\lambda_{n'}x' +$$

$$K_{y'}^{pb}\big(l_x\lambda_{am}\sin\lambda_{am}x\cos\lambda_{bn}y + l_y\lambda_{bn}\cos\lambda_{am}x\sin\lambda_{bn}y\big)\lambda_{n'}\cos\lambda_{n'}x'\big\}dx' \tag{E.17}$$

$$\big\{\mathbf{K^{i1}_{w_p w_{bz'}}}\big\}_{m+1,m'+1} = -\int_0^L \big\{k_{z'}^{pb}\zeta_{(i-1)b}(y)\cos\lambda_{am}x\cos\lambda_{m'}x' +$$

$$K_{y'}^{pb}\big(l_y\zeta'_{(i-1)b}(y)\cos\lambda_{am}x - l_x\lambda_{am}\zeta_{(i-1)b}(y)\sin\lambda_{am}x\big)\lambda_{m'}\sin\lambda_{m'}x'\big\}dx' \tag{E.18}$$

$$\big\{\mathbf{K^{i2}_{w_p w_{bz'}}}\big\}_{m+1,n'+1} = -\int_0^L \big\{k_{z'}^{pb}\zeta_{(i-1)b}(y)\cos\lambda_{am}x\sin\lambda_{n'}x' +$$

$$K_{y'}^{pb}\big(l_y\zeta'_{(i-1)b}(y)\cos\lambda_{am}x - l_x\lambda_{am}\zeta_{(i-1)b}(y)\sin\lambda_{am}x\big)\lambda_{n'}\cos\lambda_{n'}x'\big\}dx' \tag{E.19}$$

$$\big\{\mathbf{K^{(i+4)1}_{w_p w_{bz'}}}\big\}_{n+1,m'+1} = -\int_0^L \big\{k_{z'}^{pb}\zeta_{(i-1)a}(x)\cos\lambda_{bn}y\cos\lambda_{m'}x' +$$

$$K_{y'}^{pb}\left(l_x\zeta'_{(i-1)a}(x)\cos\lambda_{bn}y - l_y\zeta_{(i-1)a}(x)\lambda_{bn}\sin\lambda_{bn}y\right)\lambda_{m'}\sin\lambda_{m'}x'\Big\}dx' \tag{E.20}$$

$$\left\{\mathbf{K}_{\mathbf{w_p w_{bz'}}}^{\mathbf{(i+4)2}}\right\}_{n+1,n'+1} = -\int_0^L\Big\{k_{z'}^{pb}\zeta_{(i-1)a}(x)\cos\lambda_{bn}y\sin\lambda_{n'}x' +$$

$$K_{y'}^{pb}\left(l_x\zeta'_{(i-1)a}(x)\cos\lambda_{bn}y - l_y\zeta_{(i-1)a}(x)\lambda_{bn}\sin\lambda_{bn}y\right)\lambda_{n'}\cos\lambda_{n'}x'\Big\}dx' \tag{E.21}$$

$$\left\{\mathbf{K}_{\mathbf{w_p\theta}}^{11}\right\}_{s,m'+1} = -\int_0^L K_{x'}^{pb}l_y\lambda_{am}\sin\lambda_{am}x\left(\cos\lambda_{bn}y\cos\lambda_{m'}x'\right)dx' \tag{E.22}$$

$$\left\{\mathbf{K}_{\mathbf{w_p\theta}}^{12}\right\}_{s,n'+1} = -\int_0^L K_{x'}^{pb}l_y\lambda_{am}\sin\lambda_{am}x\left(\cos\lambda_{bn}y\sin\lambda_{n'}x'\right)dx' \tag{E.23}$$

$$\left\{\mathbf{K}_{\mathbf{w_p\theta}}^{\mathbf{i}1}\right\}_{m+1,m'+1} = -\int_0^L K_{x'}^{pb}l_y\lambda_{am}\sin\lambda_{am}x\left(\zeta_{(i-1)b}(y)\cos\lambda_{m'}x'\right)dx' \tag{E.24}$$

$$\left\{\mathbf{K}_{\mathbf{w_p\theta}}^{\mathbf{i}2}\right\}_{m+1,n'+1} = -\int_0^L K_{x'}^{pb}l_y\lambda_{am}\sin\lambda_{am}x\left(\zeta_{(i-1)b}(y)\sin\lambda_{n'}x'\right)dx' \tag{E.25}$$

$$\left\{\mathbf{K}_{\mathbf{w_p}\theta}^{\mathbf{(i+4)1}}\right\}_{n+1,m'+1} = \int_0^L K_{x'}^{pb}\zeta'_{(i-1)a}(x)l_y\left(\cos\lambda_{bn}y\cos\lambda_{m'}x'\right)dx' \tag{E.26}$$

$$\left\{\mathbf{K}_{\mathbf{w_p}\theta}^{\mathbf{(i+4)2}}\right\}_{n+1,n'+1} = \int_0^L\left\{K_{x'}^{pb}\zeta'_{(i-1)a}(x)l_y\left(\cos\lambda_{bn}y\sin\lambda_{n'}x'\right)\right\}dx',\ i = 2,3,4,5 \tag{E.27}$$

Other components $\mathbf{K}_{\mathbf{w_p}\theta}^{\mathbf{i}}$, $\mathbf{K}_{\mathbf{u_p w_{by'}}}^{\mathbf{i}}$, $\mathbf{K}_{\mathbf{v_p w_{by'}}}^{\mathbf{i}}$, and $\mathbf{K}_{\mathbf{v_p u_p}}^{\mathbf{i}}$ are not given here for simplification.

The stiffness matrix $\mathbf{K_b}$ is given by

$$\mathbf{K_b} = \begin{bmatrix} \mathbf{K_b^1} & \mathbf{0} & \mathbf{0} & \mathbf{0} \\ & \mathbf{K_b^2} & \mathbf{0} & \mathbf{0} \\ \vdots & & \ddots & \mathbf{0} \\ \mathbf{S} & \cdots & & \mathbf{K_b^N} \end{bmatrix} \tag{E.28}$$

where the stiffness matrix of the *i*-th beam $\mathbf{K_b^i}$ is the summation of $\mathbf{K_b^{i,0}}$ and $\mathbf{K_b^{i,c}}$ reflecting the contributions due to the beam itself and the plate-beam coupling.

$$\mathbf{K_b^i} = \mathbf{K_b^{i,0}} + \mathbf{K_b^{i,c}} \tag{E.29}$$

with

$$\mathbf{K}_{\mathbf{b}}^{\mathbf{i,0}} = \begin{bmatrix} \mathbf{K}^{\mathbf{0}}_{\mathbf{w_{bz'}w_{bz'}}} & \mathbf{0} & \mathbf{0} & \mathbf{0} \\ \vdots & \mathbf{K}^{\mathbf{0}}_{\mathbf{w_{by'}w_{by'}}} & \mathbf{0} & \mathbf{0} \\ \vdots & \vdots & \mathbf{K}^{\mathbf{0}}_{\mathbf{u_b u_b}} & \mathbf{0} \\ \mathbf{S} & \cdots & \cdots & \mathbf{K}^{\mathbf{0}}_{\theta\theta} \end{bmatrix}, \quad \mathbf{K}_{\mathbf{b}}^{\mathbf{i,c}} = \begin{bmatrix} \mathbf{K}^{\mathbf{c}}_{\mathbf{w_{bz'}w_{bz'}}} & \mathbf{0} & \mathbf{0} & \mathbf{0} \\ \vdots & \mathbf{K}^{\mathbf{c}}_{\mathbf{w_{by'}w_{by'}}} & \mathbf{0} & \mathbf{0} \\ \vdots & \vdots & \mathbf{K}^{\mathbf{c}}_{\mathbf{u_b u_b}} & \mathbf{0} \\ \mathbf{S} & \cdots & \cdots & \mathbf{K}^{\mathbf{c}}_{\theta\theta} \end{bmatrix} \quad \text{(E.30,31)}$$

Components of sub-matrices $\mathbf{K}_{\mathbf{b}}^{\mathbf{i,0}}$ and $\mathbf{K}_{\mathbf{b}}^{\mathbf{i,c}}$ are partially given by

$$\mathbf{K}^{\mathbf{0}}_{\mathbf{w_{bz'}w_{bz'}}} = \begin{bmatrix} \mathbf{K}^{\mathbf{0,AA}}_{\mathbf{w_{bz'}w_{bz'}}} & \mathbf{K}^{\mathbf{0,AB}}_{\mathbf{w_{bz'}w_{bz'}}} \\ \left(\mathbf{K}^{\mathbf{0,AB}}_{\mathbf{w_{bz'}w_{bz'}}}\right)^{\mathbf{T}} & \mathbf{K}^{\mathbf{0,BB}}_{\mathbf{w_{bz'}w_{bz'}}} \end{bmatrix}, \quad \mathbf{K}^{\mathbf{c}}_{\mathbf{w_{bz'}w_{bz'}}} = \begin{bmatrix} \mathbf{K}^{\mathbf{c,AA}}_{\mathbf{w_{bz'}w_{bz'}}} & \mathbf{K}^{\mathbf{c,AB}}_{\mathbf{w_{bz'}w_{bz'}}} \\ \left(\mathbf{K}^{\mathbf{c,AB}}_{\mathbf{w_{bz'}w_{bz'}}}\right)^{\mathbf{T}} & \mathbf{K}^{\mathbf{c,BB}}_{\mathbf{w_{bz'}w_{bz'}}} \end{bmatrix} \quad \text{(E.32,33)}$$

where

$$\left\{\mathbf{K}^{0,\mathbf{AA}}_{\mathbf{w_{bz'}w_{bz'}}}\right\}_{m,m'} = D_{by'} \times \int_0^L \lambda_m^2 \lambda_{m'}^2 \cos\lambda_m x' \cos\lambda_{m'} x' dx' + k^b_{z',0} + k^b_{z',L}(-1)^{m+m'} \quad \text{(E.34)}$$

$$\left\{\mathbf{K}^{0,\mathbf{AB}}_{\mathbf{w_{bz'}w_{bz'}}}\right\}_{m,n'} = D_{by'} \times \int_0^L \lambda_m^2 \lambda_{n'}^2 \cos\lambda_m x' \sin\lambda_{n'} x' dx' \quad \text{(E.35)}$$

$$\left\{\mathbf{K}^{0,\mathbf{BB}}_{\mathbf{w_{bz'}w_{bz'}}}\right\}_{n,n'} = D_{by'} \times \int_0^L \lambda_n^2 \lambda_{n'}^2 \sin\lambda_n x' \sin\lambda_{n'} x' dx' + \lambda_n \lambda_{n'}\left(K^b_{z',0} + K^b_{z',L}(-1)^{n+n'}\right)$$

$$\text{(E.36)}$$

$$\left\{\mathbf{K}^{0,\mathbf{AA}}_{\mathbf{w_{by'}w_{by'}}}\right\}_{m,m'} = D_{bz'} \times \int_0^L \lambda_m^2 \lambda_{m'}^2 \cos\lambda_m x' \cos\lambda_{m'} x' dx' + k^b_{y',0} + k^b_{y',L}(-1)^{m+m'} \quad \text{(E.37)}$$

$$\left\{\mathbf{K}^{0,\mathbf{AB}}_{\mathbf{w_{by'}w_{by'}}}\right\}_{m,n'} = D_{bz'} \times \int_0^L \lambda_m^2 \lambda_{n'}^2 \cos\lambda_m x' \sin\lambda_{n'} x' dx' \quad \text{(E.38)}$$

$$\left\{\mathbf{K}^{0,\mathbf{BB}}_{\mathbf{w_{by'}w_{by'}}}\right\}_{n,n'} = D_{bz'} \times \int_0^L \lambda_n^2 \lambda_{n'}^2 \sin\lambda_n x' \sin\lambda_{n'} x' dx' + \lambda_n \lambda_{n'}\left(K^b_{y',0} + K^b_{y',L}(-1)^{n+n'}\right) \quad \text{(E.39)}$$

$$\left\{\mathbf{K}^{0,\mathbf{AA}}_{\mathbf{u_b u_b}}\right\}_{m,m'} = E_b S \times \int_0^L \lambda_m \lambda_{m'} \sin\lambda_m x' \sin\lambda_{m'} x' dx' + k^b_{u,0} + k^b_{u,L}(-1)^{m+m'} \quad \text{(E.40)}$$

$$\left\{\mathbf{K}^{0,\mathbf{AB}}_{\mathbf{u_b u_b}}\right\}_{m,n'} = -E_b S \times \int_0^L \lambda_m \lambda_{n'} \sin\lambda_m x' \cos\lambda_{n'} x' dx' \quad \text{(E.41)}$$

$$\left\{\mathbf{K}^{0,\mathbf{BB}}_{\mathbf{u_b u_b}}\right\}_{n,n'} = E_b S \times \int_0^L \lambda_n \lambda_{n'} \cos\lambda_n x' \cos\lambda_{n'} x' dx' \quad \text{(E.42)}$$

$$\left\{\mathbf{K}^{0,\mathbf{AA}}_{\theta\theta}\right\}_{m,m'} = G_b J \times \int_0^L \lambda_m \lambda_{m'} \sin\lambda_m x' \sin\lambda_{m'} x' dx' + K^b_{\theta,0} + K^b_{\theta,0}(-1)^{m+m'} \quad \text{(E.43)}$$

$$\left\{\mathbf{K}_{\theta\theta}^{0,\mathbf{AB}}\right\}_{m,n'} = -G_b J \times \int_0^L \lambda_m \lambda_{n'} \sin\lambda_m x' \cos\lambda_{n'} x' dx' \tag{E.44}$$

$$\left\{\mathbf{K}_{\theta\theta}^{0,\mathbf{BB}}\right\}_{n,n'} = G_b J \times \int_0^L \lambda_n \lambda_{n'} \cos\lambda_n x' \cos\lambda_{n'} x' dx' \tag{E.45}$$

$$\left\{\mathbf{K}_{\mathbf{w}_{\mathbf{bz}'}\mathbf{w}_{\mathbf{bz}'}}^{\mathbf{c},\mathbf{AA}}\right\}_{m,m'} = k_{z'}^{b} \times \int_0^L \cos\lambda_m x' \cos\lambda_{m'} x' dx' + K_{y'}^{b} \times \int_0^L \lambda_m \lambda_{m'} \sin\lambda_m x' \sin\lambda_{m'} x' dx' \tag{E.46}$$

$$\left\{\mathbf{K}_{\mathbf{w}_{\mathbf{bz}'}\mathbf{w}_{\mathbf{bz}'}}^{\mathbf{c},\mathbf{AB}}\right\}_{m,n'} = k_{z'}^{pb} \times \int_0^L \cos\lambda_m x' \sin\lambda_{n'} x' dx' - K_{y'}^{pb} \times \int_0^L \lambda_m \lambda_{n'} \sin\lambda_{m'} x' \cos\lambda_{n'} x' dx' \tag{E.47}$$

$$\left\{\mathbf{K}_{\mathbf{w}_{\mathbf{bz}'}\mathbf{w}_{\mathbf{bz}'}}^{\mathbf{c},\mathbf{BB}}\right\}_{n,n'} = k_{z'}^{pb} \times \int_0^L \sin\lambda_n x' \sin\lambda_{n'} x' dx' + K_{y'}^{pb} \times \int_0^L \lambda_n \lambda_{n'} \cos\lambda_n x' \cos\lambda_{n'} x' dx' \tag{E.48}$$

$$\left\{\mathbf{K}_{\mathbf{w}_{\mathbf{by}'}\mathbf{w}_{\mathbf{by}'}}^{\mathbf{c},\mathbf{AA}}\right\}_{m,m'} = k_{y'}^{pb} \times \int_0^L \cos\lambda_m x' \cos\lambda_{m'} x' dx' + K_{z'}^{pb} \times \int_0^L \lambda_m \lambda_{m'} \sin\lambda_m x' \sin\lambda_{m'} x' dx' \tag{E.49}$$

$$\left\{\mathbf{K}_{\mathbf{w}_{\mathbf{by}'}\mathbf{w}_{\mathbf{by}'}}^{\mathbf{c},\mathbf{AB}}\right\}_{m,n'} = k_{y'}^{pb} \times \int_0^L \cos\lambda_m x' \sin\lambda_{n'} x' dx' - K_{z'}^{pb} \times \int_0^L \lambda_m \lambda_{n'} \sin\lambda_{m'} x' \cos\lambda_{n'} x' dx' \tag{E.50}$$

$$\left\{\mathbf{K}_{\mathbf{w}_{\mathbf{by}'}\mathbf{w}_{\mathbf{by}'}}^{\mathbf{c},\mathbf{BB}}\right\}_{n,n'} = k_{y'}^{pb} \times \int_0^L \sin\lambda_n x' \sin\lambda_{n'} x' dx' + K_{z'}^{pb} \times \int_0^L \lambda_n \lambda_{n'} \cos\lambda_n x' \cos\lambda_{n'} x' dx' \tag{E.51}$$

$$\left\{\mathbf{K}_{\mathbf{u_b u_b}}^{\mathbf{c},\mathbf{AA}}\right\}_{m,m'} = k_{x'}^{pb} \times \int_0^L \cos\lambda_m x' \cos\lambda_{m'} x' dx', \quad \left\{\mathbf{K}_{\mathbf{u_b u_b}}^{\mathbf{c},\mathbf{AB}}\right\}_{m,n'} = k_{x'}^{pb} \times \int_0^L \cos\lambda_m x' \sin\lambda_{n'} x' dx' \tag{E.52,53}$$

$$\left\{\mathbf{K}_{\mathbf{u_b u_b}}^{\mathbf{c},\mathbf{BB}}\right\}_{n,n'} = k_{x'}^{pb} \times \int_0^L \sin\lambda_n x' \sin\lambda_{n'} x' dx', \quad \left\{\mathbf{K}_{\theta\theta}^{\mathbf{c},\mathbf{AA}}\right\}_{m,m'} = K_{x'}^{pb} \times \int_0^L \cos\lambda_m x' \cos\lambda_{m'} x' dx' \tag{E.54,55}$$

$$\left\{\mathbf{K}_{\theta\theta}^{\mathbf{c},\mathbf{AB}}\right\}_{m,n'} = K_{x'}^{pb} \times \int_0^L \cos\lambda_m x' \sin\lambda_{n'} x' dx', \quad \left\{\mathbf{K}_{\theta\theta}^{\mathbf{c},\mathbf{BB}}\right\}_{n,n'} = K_{x'}^{pb} \times \int_0^L \sin\lambda_n x' \sin\lambda_{n'} x' dx' \tag{E.56,57}$$

The mass matrices are given by

$$\mathbf{M_b} = \begin{bmatrix} \mathbf{M_b^1} & \mathbf{0} & \mathbf{0} & \mathbf{0} \\ & \mathbf{M_b^2} & \mathbf{0} & \mathbf{0} \\ \vdots & & \ddots & \mathbf{0} \\ \mathbf{S} & \cdots & & \mathbf{M_b^N} \end{bmatrix}, \text{ where } \mathbf{M_b^i} = \begin{bmatrix} \mathbf{M}_{\mathbf{w}_{\mathbf{bz}'}\mathbf{w}_{\mathbf{bz}'}} & \mathbf{0} & \mathbf{0} & \mathbf{0} \\ \vdots & \mathbf{M}_{\mathbf{w}_{\mathbf{by}'}\mathbf{w}_{\mathbf{by}'}} & \mathbf{0} & \mathbf{0} \\ \vdots & \vdots & \mathbf{M}_{\mathbf{u_b u_b}} & \mathbf{0} \\ \mathbf{S} & \cdots & \cdots & \mathbf{M}_{\theta\theta} \end{bmatrix} \tag{E.58,59}$$

The components are given by

$$\mathbf{M}_{\mathbf{w}_{\mathbf{bz}'}\mathbf{w}_{\mathbf{bz}'}} = \begin{bmatrix} \mathbf{M}_{\mathbf{w}_{\mathbf{bz}'}\mathbf{w}_{\mathbf{bz}'}}^{\mathbf{AA}} & \mathbf{M}_{\mathbf{w}_{\mathbf{bz}'}\mathbf{w}_{\mathbf{bz}'}}^{\mathbf{AB}} \\ \left(\mathbf{M}_{\mathbf{w}_{\mathbf{bz}'}\mathbf{w}_{\mathbf{bz}'}}^{\mathbf{AB}}\right)^{\mathbf{T}} & \mathbf{M}_{\mathbf{w}_{\mathbf{bz}'}\mathbf{w}_{\mathbf{bz}'}}^{\mathbf{BB}} \end{bmatrix} \tag{E.60}$$

$$\left\{\mathbf{M}^{\mathbf{AA}}_{\mathbf{w_{bz'}w_{bz'}}}\right\}_{m,m'} = \rho_b S_b \times \int_0^L \cos\lambda_m x' \cos\lambda_{m'} x' dx' \tag{E.61}$$

$$\left\{\mathbf{M}^{\mathbf{AB}}_{\mathbf{w_{bz'}w_{bz'}}}\right\}_{m,n'} = \rho_b S_b \times \int_0^L \cos\lambda_m x' \sin\lambda_{n'} x' dx' \tag{E.62}$$

$$\left\{\mathbf{M}^{\mathbf{BB}}_{\mathbf{w_{bz'}w_{bz'}}}\right\}_{n,n'} = \rho_b S_b \times \int_0^L \sin\lambda_n x' \sin\lambda_{n'} x' dx' \tag{E.63}$$

$$\left\{\mathbf{M}^{\mathbf{AA}}_{\mathbf{w_{by'}w_{by'}}}\right\}_{m,m'} = \rho_b S_b \times \int_0^L \cos\lambda_m x' \cos\lambda_{m'} x' dx' \tag{E.64}$$

$$\left\{\mathbf{M}^{\mathbf{AB}}_{\mathbf{w_{by'}w_{by'}}}\right\}_{m,n'} = \rho_b S_b \times \int_0^L \cos\lambda_m x' \sin\lambda_{n'} x' dx' \tag{E.65}$$

$$\left\{\mathbf{M}^{\mathbf{BB}}_{\mathbf{w_{by'}w_{by'}}}\right\}_{n,n'} = \rho_b S_b \times \int_0^L \sin\lambda_n x' \sin\lambda_{n'} x' dx' \tag{E.66}$$

$$\left\{\mathbf{M}^{\mathbf{AA}}_{\mathbf{u_b u_b}}\right\}_{m,m'} = \rho_b S_b \times \int_0^L \cos\lambda_m x' \cos\lambda_{m'} x' dx' \tag{E.67}$$

$$\left\{\mathbf{M}^{\mathbf{AB}}_{\mathbf{u_b u_b}}\right\}_{m,n'} = \rho_b S_b \times \int_0^L \cos\lambda_m x' \sin\lambda_{n'} x' dx' \tag{E.68}$$

$$\left\{\mathbf{M}^{\mathbf{BB}}_{\mathbf{u_b u_b}}\right\}_{n,n'} = \rho_b S_b \times \int_0^L \sin\lambda_n x' \sin\lambda_{n'} x' dx' \tag{E.69}$$

APPENDIX F

SUBMATRICES DEFINED IN CAHPTER 6

The coefficient matrix for two beams coupling at an angle is given as

$$[X]=\begin{bmatrix} 0 & \sin\theta & 0 & \sin\theta & -\cos\theta & 1 \\ 1 & -\cos\theta & 1 & -\cos\theta & -\sin\theta & 0 \\ k_{f_1} & k_{f_2} & ik_{f_1} & ik_{f_2} & 0 & 0 \\ E_1I_1k_{f_1}^2 & -E_2I_2k_{f_2}^2 & -E_1I_1k_{f_1}^2 & E_2I_2k_{f_2}^2 & 0 & 0 \\ 0 & E_2I_2k_{f_2}^3\sin\theta & 0 & -iE_2I_2k_{f_2}^3\sin\theta & iE_2S_2k_{l_2}\cos\theta & iE_1S_1k_{l_1} \\ -E_1I_1k_{f_1}^3 & -E_2I_2k_{f_2}^3\cos\theta & iE_1I_1k_{f_1}^3 & iE_2I_2k_{f_2}^3\cos\theta & iE_2S_2k_{l_2}\sin\theta & 0 \end{bmatrix}$$

(F.1)

$$[X]\{Y\}=\{Z\},\ \{Y\}=\{A_e \quad B_e \quad A_{fr} \quad B_f \quad B_l \quad A_{lr}\}^T \tag{F.2-3}$$

$$\{Z\}=\{-A_{lin} \quad -A_{fin} \quad -ik_{f_1}A_{fin} \quad A_{fin}E_1I_1k_{f_1}^2 \quad -A_{lin}iE_1S_1k_{l_1} \quad -A_{fin}iE_1I_1k_{f_1}^3\}^T \tag{F.4}$$

$$[X]=\begin{bmatrix} 0 & \sin\theta & 0 & \sin\theta & 0 & 0 & 0 & -\cos\theta & 1 \\ 0 & 0 & 0 & 0 & \sin\alpha & \sin\alpha & -\cos\alpha & 0 & 1 \\ 1 & -\cos\theta & 1 & -\cos\theta & 0 & 0 & 0 & -\sin\theta & 0 \\ 1 & 0 & 1 & 0 & -\cos\alpha & -\cos\alpha & -\sin\alpha & 0 & 0 \\ k_{f_1} & k_{f_2} & ik_{f_1} & ik_{f_2} & 0 & 0 & 0 & 0 & 0 \\ k_{f_1} & 0 & ik_{f_1} & 0 & k_{f_3} & ik_{f_3} & 0 & 0 & 0 \\ E_1I_1k_{f_1}^2 & -E_2I_2k_{f_2}^2 & -E_1I_1k_{f_1}^2 & E_2I_2k_{f_2}^2 & -E_3I_3k_{f_3}^2 & E_3I_3k_{f_3}^2 & 0 & 0 & 0 \\ 0 & E_2I_2k_{f_2}^3\sin\theta & 0 & -iE_2I_2k_{f_2}^3\sin\theta & E_3I_3k_{f_3}^3\sin\alpha & -iE_3I_3k_{f_3}^3\sin\alpha & iE_3S_3k_{l_3}\cos\alpha & iE_2S_2k_{l_2}\cos\theta & iE_1S_1k_{l_1} \\ -E_1I_1k_{f_1}^3 & -E_2I_2k_{f_2}^3\cos\theta & -iE_1I_1k_{f_1}^3 & iE_2I_2k_{f_2}^3\cos\theta & -E_3I_3k_{f_3}^3\cos\alpha & iE_3I_3k_{f_3}^3\cos\alpha & iE_3S_3k_{l_3}\sin\alpha & iE_2S_2k_{l_2}\sin\theta & 0 \end{bmatrix} \tag{F.5}$$

$$\{Y\}=\{A_e \quad B_e \quad A_{fr} \quad B_f \quad C_e \quad C_f \quad C_l \quad B_l \quad A_{lr}\}^T \tag{F.6}$$

$$\{Z\}=\{-A_{lin} \quad -A_{lin} \quad -A_{fin} \quad -A_{fin} \quad -ik_{f_1}A_{fin} \quad -ik_{f_1}A_{fin} \quad A_{fin}E_1I_1k_{f_1}^2 \quad -A_{lin}iE_1S_1k_{l_1} \quad -A_{fin}iE_1I_1k_{f_1}^3\}^T$$

(F.7)

The SEA assembling process is defined by

$$\{\mathbf{P}_{in}\}=[L]\{E\} \tag{F.8}$$

where $[L]$ is a matrix of damping and coupling loss factors given by

$$[L] = \omega diag(\eta_i) + \omega[X] \tag{F.9}$$

$$[X] = \begin{bmatrix} \sum_{i\neq 1}\left(\eta_{f_1 f_i, l_i}\right) + \eta_{f_1 l_r} & -\eta_{l_1 f_r} & -\eta_{f_2 f_1} & -\eta_{l_2 f_1} & -\eta_{f_3 f_1} & -\eta_{l_3 f_1} \\ -\eta_{f_1 l_r} & . & -\eta_{f_2 l_1} & -\eta_{l_2 l_1} & -\eta_{f_3 l_1} & -\eta_{l_3 l_1} \\ -\eta_{f_1 f_2} & -\eta_{l_1 f_2} & . & -\eta_{l_2 f_r} & -\eta_{f_3 f_2} & -\eta_{l_3 f_2} \\ -\eta_{f_1 l_2} & -\eta_{l_1 l_2} & -\eta_{f_2 l_r} & . & -\eta_{f_3 l_2} & -\eta_{l_3 l_2} \\ -\eta_{f_1 f_3} & -\eta_{l_1 f_3} & -\eta_{f_2 f_3} & -\eta_{l_2 f_3} & . & -\eta_{f_3 l_r} \\ -\eta_{f_1 l_3} & -\eta_{l_1 l_3} & -\eta_{f_2 l_3} & -\eta_{l_2 l_3} & -\eta_{l_3 f_r} & \sum_{i\neq 1}\left(\eta_{l_3 f_i, l_i}\right) + \eta_{f_3 l_r} \end{bmatrix} \tag{F.10}$$

$$\{E\} = \{E_{f_1} \quad E_{l_1} \quad E_{f_2} \quad E_{l_2} \quad E_{f_3} \quad E_{l_3}\}^T \tag{F.11}$$

$$\{P_{in}\} = \{P_{in,f_1} \quad P_{in,l_1} \quad P_{in,f_2} \quad P_{in,l_2} \quad P_{in,f_3} \quad P_{in,l_3}\}^T \tag{F.12}$$

REFERENCES

Abu-Hilal, M., Forced vibration of Euler-Bernoulli beams by means of dynamic Green functions. Journal of Sound and Vibration 267 (2002) 191-207.

Adhikari, S., Manohar C. S., Dynamic analysis of framed structures with statistical uncertainties. International Journal for numerical Methods in Engineering 44 (1999) 1157-1178.

Adhikari, S., Manohar C. S., Transient dynamics of stochastically parametered beams. ASCE Journal of Engineering Mechanics 126 (11) (1998) 1131-1140.

Ahmida, K. M., Arruda, J. R. F., Spectral element-based prediction of active power flow in Timoshenko beams. International Journal of Solids and Structures 38 (2001) 1669-1679.

Arruda, J. R. F., Gautier, F. and Donadon, L. V., Computing refection and transmission coefficients for plate reinforcement beams. Journal of Sound and Vibration 307 (2007) 564-577.

Asku, G. and Ali, R., Free vibration analysis of stiffened plates using finite difference method. Journal of Sound and Vibration 48 (1976) 15-25.

Azimi, S., Hamilton, J. F. and Soedel, W., The receptance method applied to the free vibration of continuous rectangular plates. Journal of Sound and Vibration 93 (1984) 9-29.

Barik, M., Mukhopadhyay, M., Free flexural vibration analysis of arbitrary plates with arbitrary stiffeners. Journal of Vibration and Control 5 (5) (1999) 667-683.

Bercin, A. N., Eigenfrequencies of rectangular plate assemblies. Computers and Structures 65 (5) (1997) 703-711.

Bercin, A. N., Langley, R. S., Application of the dynamic stiffness technique to the inplane vibrations of plate structures. Computers and Structures 59 (1996) 869–875.

Bercin, A. N., Langley, R. S., Application of the dynamics stiffness technique to the in-plane vibration of plate structure. Computers and Structures 59 (5) (1996) 869-875.

Beshara, M., Keane, A. J., Vibrational energy flows between plates with compliant and dissipative couplings. Journal of Sound and Vibration 213 (3) (1998) 511-535.

Beshara, M., Keane, A. J., Vibrational power flows in beam networks with compliant and dissipative joints. Journal of Sound and Vibration 203 (1997) 321-339.

Bhat, R. B., Vibrations of panels with non-uniformly spaced stiffeners. Journal of Sound and Vibration 84 (3) (1982) 449-452.

Bies, D. A., Hamid, S., In situ determination of loss and coupling loss factors by the power injection method. Journal of Sound and Vibration 70 (1980) 187-204.

Bouthier, O. M., Bernhard, R. J., Models of space-averaged energetics of plate. American Institute of Aeronautics and Astronautics Journal 30 (1992) 616-623.

Cacciolati, C., Guyader, J. L., Measurement of SEA coupling loss factors using point mobilities. Statistical Energy Analysis, edited by A. J. Keane and W. G. Price (Cambridge U.P., Cambridge, England, 1997) 35-45.

Carcaterra, A., Sestieri, A., Energy density equations and power flow in structures. Journal of Sound and Vibration 188 (2) (1995) 269-282.

Cavdar, O., Bayraktar, A., Cavdar, A. and Adanur, S., Perturbation based stochastic finite element analysis of the structural systems with composite sections under earthquake forces. Steel and Composite Structures (8) 2, (2008) 129-144.

Cha, P. D., A general approach to formulating the frequency equations for a beam carrying miscellaneous attachments. Journal of Sound and Vibration 286 (2005) 921-939.

Cha, P.D., A general approach to formulating the frequency equations for a beam carrying miscellaneous attachments. Journal of Sound and Vibration 286 (2005) 921-939.

Chang, T.P., Chang, F.I. and Liu, M.F., On the eigenvalues of a viscously damped simple beam carrying point masses and springs. Journal of Sound and Vibration 240 (2001) 769-778.

Cheung, Y. K., Jin, W. G. and Zienkiewicz, O. C., Trefftz method for Kirchhoff plate bending problems. International Journal of Numerical Methods in Engineering 36 (1993) 765-781.

Chiba, M., Yoshida, I., Free vibration of a rectangular plate-beam coupled system. Journal of Sound and Vibration 194 (1) (1996) 49-65.

Cho, P. E., Bernhard, R. J., Energy flow analysis of coupled beams. Journal of Sound and Vibration 211 (1998) 593-605.

Cox, H. L., Bernfield, W. A., Vibration of uniform square plates bounded by flexible beams. Journal of Acoustical Society of America 31 (1959) 963-966.

Craik, R. J. M., A study of sound transmission through buildings using statistical energy analysis. Ph.D thesis, Heriot-Watt University, U.K. (1980).

Craik, R. J. M., Steel, J. A. and Evans, D. I., Statistical energy analysis of structure-borne sound transmission at low frequencies. Journal of Sound and Vibration 144 (1991) 95–107.

Cremer, L., Heckl, M. and Ungar, E. E., Structure-Borne Sound, Springer, Berlin, 2nd edition (1988).

Cuschieri, J. M., Structural power-flow analysis using a mobility approach of an L-shaped plate. Journal of Acoustical Society of America 87 (3) (1990) 1159-1165.

Cuschieri, J. M., Vibration transmission through periodic structures using a mobility power flow approach. Journal of Sound and Vibration 143 (1) (1990) 65-74.

Deodatis, G., Bounds on response variability of stochastic finite element systems. ASCE Journal of Engineering Mechanics 116 (1990) 565-585.

Deodatis, G., Weighted integral method. I: stochastic stiffness matrix. ASCE Journal of Engineering Mechanics 117 (8) (1991) 1851-1864.

Desmet, W., Mid-frequency vibro-acoustic modeling: challenges and potential solutions. Proceeding of ISMA Volume II (2002) 835-862.

Dickinson, S. M., Warburton, G. B., Vibration of box-type structures. Journal of Mechanical Engineering Science 9 (4) (1967) 325-335.

Dowell, E.H., On some general properties of combined dynamical systems. Journal of Applied Mechanics 46 (1979) 206-209.

Doyle, J. F., Kamle, S., An experimental study of the reflection and transmission of flexural waves at an arbitrary T-Joint. Transactions of the ASME 54 (1987) 136-140.

Doyle, J. F., Wave Propagation in Structures, Springer, Berlin, 1989.

Doze, L., Ricciardi, M., Free vibration analysis of ribbed plates by a combined analytical-numerical method. Journal of Sound and Vibration 319 (2009) 681-697.

Du, J. T., Li, W. L., Jin, G. Y., Yang, T. J. and Liu, Z. G., An analytical method for the in-plane vibration analysis of rectangular plates with elastically restrained edges. Journal of Sound and Vibration 306 (2007) 908-927.

Du, J. T., Li, W. L., Liu, Z. G., Jin, G. Y. and Yang, T. J., Vibration analysis of plate structures under general boundary and coupling conditions. revised and resubmitted to Journal of Sound and Vibration.

Dugush, Y. A., Eisenberger, M., Vibrations of non-uniform continuous beams under moving loads. Journal of Sound and Vibration 254 (2002) 911-926.

Fahy, F. J., An alternative to the SEA coupling loss factor: rationale and method for determination. Journal of Sound and Vibration 214 (2) (1998) 261-267.

Fahy, F. J., Mohamed, A. D., A study of uncertainty in application of SEA to coupled beam and plate systems, Part I: computational experiments. Journal of Sound and Vibration 158 (1992) 45–67.

Fahy, F. J., Statistical Energy Analysis - a critical review. Shock and Vibration Digest 6 (1974) 14-33.

Fahy, F. J., Statistical Energy Analysis in Noise and Vibration. 1987 Chichester. John Wiley.

Fahy, F. J., Statistical energy analysis: an overview, in: A. J. Keane, W. G. Price (Eds.), Statistical Energy Analysis: A Critical Overview, with Applications in Structural Dynamics, Cambridge University Press, Cambridge, 1–18, 1997.

Farag, N. H., Pan, J., Dynamic response and power flow in three-dimensional coupled beam structures. I. Analytical modeling. Journal of the Acoustical Society of America 102 (1997) 315-325.

Farag, N. H., Pan, J., On the free and forced vibration of single and coupled rectangular plates. Journal of Acoustical Society of America 104 (1) (1998) 204-216.

Fischer, P., Belyaev, A. K., and Pradlwarter, H., Combined integral and FE analysis of broadband random vibration in structural members. Probabilistic Engineering Mechanics 10 (1995) 241-251.

Foda, M. A., Abduljabbar, Z., A dynamic Green function formulation for the response of a beam structure to a moving mass. Journal of Sound and Vibration 210 (1998) 295-306.

Fulford, R. A., Peterson, B. A. T., Estimation of vibration power in built-up systems involving box-like structures, Part 1: uniform force distribution. Journal of Sound and Vibration 232 (5) (2000) 877-895.

Gavric, L., Pavic, G., A finite element method for computation of structural intensity by the normal mode approach. Journal of Sound and Vibration 164 (1) (1993) 29-43.

Goyder, H. G. D., White, R. G., Vibration power flow from machines into built-up structures, Part I: Introduction and approximate analyses of beam and plate-like foundations. Journal of Sound and Vibration 68 (1) (1980) 59-75.

Goyder, H. G. D., White, R. G., Vibrational power flow from machines into built-up structures, part II: Wave propagation and power flow in beam-stiffened plates. Journal of Sound and Vibration 68 (1) (1980) 77-96.

Graham, L.L. and Deodatis, G., Response and eigenvalue analysis of stochastic finite element systems with multiple correlated material and geometric properties. Probabilistic Engineering Mechanics 16 (2001) 11-29.

Grice, R. M., Pinnington, R. J., A method for the vibration analysis of built-up structures, part II: analysis of the plate-stiffened beam using a combination of finite element analysis and analytical impedances. Journal of Sound and Vibration 230 (4) (2000) 851-875.

Grice, R. M., Pinnington, R. J., Analysis of the flexural vibration of a thin-plate box using a combination of finite element analysis and analytical impedances. Journal of Sound and Vibration 249 (3) (2002) 499-527.

Grice, R. M., Pinnington, R. J., Vibration analysis of a thin-plate box using a finite element model which accommodates only in-plane motion. Journal of Sound and Vibration, 232 (2) (2000) 449-471.

Guyader, J. L., Boisson, C. and Lesueur, C., Energy transmission in finite coupled plates, part 1: theory. Journal of Sound and Vibration 81 (1) (1982) 81-92.

Halling, M. W., Muhammad, I. and Womack, K. C., Dynamic field testing for condition assessment of bridge bents. Journal Structural Engineering 127 (2001) 161-167.

Hamada, R., Dynamic analysis of a beam under a moving force: a double Laplace transform solution. Journal of Sound and Vibration 74 (1981) 221-233.

Hambric, S. A., Power flow and mechanical intensity calculations in structural finite element analysis. Journal of Vibration and Acoustics 112 (1990) 542-549.

Han, F., Bernhard, R. J. and Mongeau, L. G., Energy flow analysis of vibrating beams and plates for discrete random excitations. Journal of Sound and Vibration 208 (5) (1997) 841-859.

Heckl, M., Wave propagation on beam-plate systems. Journal of Acoustical Society of America 33 (5) (1961) 640-651.

Henchi, K., Fafard, M., Dynamic behavior of multi-span beams under moving loads. Journal of Sound and Vibration 199 (1997) 33-50.

Hino, J., Yoshimura, T. and Ananthanarayana, N., A finite element method prediction of the vibration of a bridge subjected to a moving vehicle load. Journal of Sound and Vibration 96 (1984) 45-53.

Hochard, Ch., Proslier, L., A simplified analysis of plate structures using Trefftz functions. International Journal of Numerical Methods in Engineering 34 (1992) 179-195.

Hodges, C. H., Woodhouse, J., Theories of noise and vibration transmission in complex structures. Rep. Prog, Phys. 49 (1986) 107-170.

Hodges, C. H., Woodhouse, J., Vibration isolation from irregularity in a nearly periodic structure: theory and measurements. Journal of Acoustical Society of America 74 (3)

(1983) 894-905.

Hodges, C. H., Woodhouse, J., Vibration isolation from uniformity in a nearly periodic structure: Theory and measurements. Journal of the Acoustical Society of America 74 (1983) 94-905.

Hong, S. B., Wang, A. M. and Vlahopoulos, N., A hybrid finite element formulation for a beam-plate system. Journal of Sound and Vibration 298 (2006) 233-256.

Horner, J. L., White, R. G., Prediction of vibrational power transmission through bends and joints in beam-like structures. Journal of Sound and Vibration 147 (1) (1991) 87-103.

Hugin, C. T., Power transmission between two finite beams at low modal overlap. Journal of Sound and Vibration 212 (5) (1998) 829-854.

Ichikawa, M., Miyakawa, Y., Vibration analysis of the continuous beam subjected to a moving mass. Journal of Sound and Vibration 230 (2000) 493-506.

Igawa, H., Komatru, K., Yamaguchi, I. and Kasai, T., Wave propagation analysis of frame structures using the spectral element method. Journal of Sound and Vibration 277 (2004) 1071-1081.

Jin, W. G., Cheung, Y. K., and Zienkiewicz, O. C., Application of the Trefftz method in plane elasticity problems. International Journal of Numerical Methods in Engineering 30 (1990) 1147-1161.

Keane, A. J., Energy flows between arbitrary configurations of conservatively coupled multi-modal elastic subsystems. Proceedings of the Royal Society of London A 436 (1992) 537-568.

Keane, A. J., Price, W. G., A note on the power flowing between two conservatively coupled multi-modal sub-system. Journal of Sound and Vibration 144 (1991) 185-196.

Khumbah, F. M., Langley, R. S., Efficient dynamic modeling of aerospace box-type structures. The 27th international congress on noise control engineering (Internoise); Vol. 3, November 1998.

Kim, C. S., Dickinson, S. M., The flexural vibration of line supported rectangular plate systems. Journal of Sound and Vibration 114 (1) (1987) 129-142.

Kim, H. S., Kang, H. J. and Kim, J. S., Transmission of bending waves in inter-connected rectangular plates. Journal of the Acoustical Society of America 96 (1994) 1557-1562

Kita, E, Kamiya, N., Trefftz method: an overview. Advances in Engineering Software 24 (1995) 3-12.

Klos, J., Modeling point excited plates using an energy finite element method. Proceedings of NOISE-CON 2004, 355-366, Baltimore, Maryland.

Kobayashi, N., Sugiyama, H., Dynamics of flexible beam using a component mode synthesis based formulation. Proc. of ASME Design Engineering Technical Conferences, Pittsburgh, Pennsylvania, DETC2001/VIB-21351 (2001).

Langley, R. S., A variational principle for periodic structures. Journal of Sound and Vibration 135 (1) (1989) 135-142.

Langley, R. S., An elastic wave technique for the free vibration analysis of plate assemblies. Journal of Sound and Vibration 145 (2) (1991) 261-277.

Langley, R. S., Analysis of power flow in beams and frameworks using the direct-dynamic stiffness method. Journal of Sound and Vibration 136 (1990) 439-452.

Langley, R. S., Application of the dynamic stiffness method to the free and forced vibrations of aircraft panels. Journal of Sound and Vibration 135 (2) (1989) 319-331.

Langley, R. S., Cotoni, V., Response variance prediction in the statistical energy analysis of built-up systems. Journal of Acoustical Society of America 115 (2) (2004) 706-718.

Langley, R. S., Heron, K. H., Elastic wave transmission through plate/beam junctions. Journal of Sound and Vibration 143 (2) (1990) 241-253.

Langley, R. S., On the modal density and energy flow characteristics of periodic structures. Journal of Sound and Vibration 172 (4) (1994) 491-511.

Langley, R. S., Shorter, P. J., The wave transmission coefficients and coupling loss factors of point connected structures. Journal of the Acoustical Society of America 113 (1) (2003) 1947-1964.

Langley, R., Bremner, P., A hybrid-method for the vibration analysis of complex structural acoustic systems. Journal of the Acoustical Society of America, 105 (1999) 1657-1671.

Langley, R.S., A derivation of the coupling loss factors used in statistical energy analysis. Journal of Sound and Vibration 141 (1990) 207-219.

Laura, P. A. A., Gutierrez, R. H., A note on transverse vibrations of stiffened rectangular plates with edges elastically restrained against rotation. Journal of Sound and Vibration 78 (1976) 139-144.

Lee, H. P., Dynamic response of a beam with intermediate point constraints subject to a moving load. Journal of Sound and Vibration171 (1994) 361-368.

Lee, H. P., Dynamic response of a beam on multiple supports with a moving mass. Journal of Structural Engineering and Mechanics 4 (1996) 303-312.

Leung, A. Y. T., Zeng, S. P., Analytical formulation of dynamic stiffness. Journal of Sound and Vibration 177 (1994) 555-564.

Li, W. L. and Xu, H. A., An exact Fourier series method for the vibration analysis of multi-span beam systems. ASME Journal of Computational and Nonlinear Dynamics 4 (2) (2009) 1-9.

Li, W. L., Bonilha, M. W. and Xiao, J., Vibrations and power flow in a coupled beam system. ASME Journal of Vibration and Acoustics 129 (2007) 616-622.

Li, W. L., Bonilha, M.W. and Xiao, J., Prediction of the vibrations and power flows between two beams connected at an arbitrarily angle. Proc. of SAE Noise and Vibration Conference, Traverse City, Michigan, 05NVC-222 (2005).

Li, W. L., Comparison of Fourier sine and cosine series expansions for beams with arbitrary boundary conditions. Journal of Sound and Vibration 255 (2002) 185-194.

Li, W. L., Free vibration of beams with general boundary conditions. Journal of Sound and Vibration 237 (2000) 709-725.

Li, W. L., Lavrich, P., Use of SEA in modeling power flows in mixed modal density systems for an air conditioner, in Proc. NOISE-CON 96, (ed., J.D. Chalupnik, S.E. Marshall and R.C. Klein), (1996) 785- 790.

Li, W. L., Xu, H. A., Fourier-space element method for the vibration and power flow analyses of frame structures. 7th European Conference on Structural Dynamics 2008, July 7-9, 2008, Southampton, UK.

Li, W. L., Xu, H. A., Vibration and power flow analyses of built-up structures in a broad frequency range, IMAC XXVII, Orlando, Florida, USA, 2009.

Li, W. L., Xu, H. A., A new method for low- to mid-frequency vibration and power flow analyses, NoiseCon2008-ASME NCAD, Dearborn, Michigan, USA, 2008.

Li, W. L., Xu, H. A., Fourier-space element method for the vibration and power flow analyses of frame structures, Proceedings of 7th European Conference on Structural Dynamics, Southampton, U.K., 2008.

Li, W. L., Xu, H. A., A Fourier method for the vibration analysis of colinearly coupled beams systems, NOISE-CON 2007, Reno, Nevada, USA, 2007.

Li, W. L., Xu, H. A., Modeling the Vibrations and Energy Flows in Complex Dynamic Systems, NSF Grantee Conference on International Research and Education in Engineering, West Lafayette, Indiana, USA, 2007.

Li, W. L., Zhang, X. F., Du, J. T. and Liu, Z. G., An exact series solution for the transverse vibration of rectangular plates with general elastic boundary supports. Journal of Sound and Vibration 321 (2009) 254-269.

Liew, K. M., Xiang, Y., and Kitipornchai, S., Research on thick plate vibration: A literature survey. Journal of Sound and Vibration 180 (1) (1995) 163-176.

Liew, K. M., Xiang, Y., Kitipornchai, S. and Lim, M. K., Vibration of rectangular Mindlin plates with intermediate stiffeners. Journal of Vibration and Acoustics 116 (1994) 529-535.

Lin, T. R, A study of modal characteristics and the control mechanism of finite periodic and irregular ribbed plates. Journal of Acoustical Society of America 123 (2) (2008) 729-737.

Lyon, R.H., Statistical Energy Analysis of Dynamical Systems. Cambridge. Massachusetts 1975.

Mace, B. R., Power flow between two continuous one-dimensional subsystems: A wave solution. Journal of Sound and Vibration 154 (2) (1992) 289-319.

Mace, B. R., Rosenberg, J., The SEA of two coupled plates: an investigation into the effects of system irregularity. Journal of Sound and Vibration 212 (1999) 395–415.

Mace, B. R., Shorter, P., Energy flow models from finite element analysis. Journal of Sound and Vibration 233 (2000) 369–389.

Mace, B. R., Statistical energy analysis, energy distribution models and system modes. Journal of Sound and Vibration 264 (2003) 391-409.

Maidanik, G., Response of ribbed panels to reverberant acoustic fields. Journal of Acoustical Society of America 34 (1962) 809-826.

Manik, D. N., A New method for determining coupling loss factors for SEA. Journal of Sound and Vibration 211 (3) (1998) 521-526.

Manohar, C. S., Adhikari, S., Dynamic stiffness of randomly parametered beams. Probabilistic Engineering Mechanics 13 (1) (1998) 39-51.

Manohar, C. S., Adhikari, S., Statistics of vibration energy flow in randomly parametered trusses. Journal of Sound and Vibration 217 (1) (1998) 43-74.

Marcelin, J. L., Genetic optimization of vibrating stiffened plates. Structural Engineering and Mechanics 24 (5) (2006) 529-541.

McDaniel, T. J., Henderson, J. P., Review of transfer matrix vibration analysis of Skin-Stringer structures. The shock and vibration digest 6 (1974) 13-19.

Mead, D. J., A new method of analyzing wave propagation in periodic structures: applications to periodic timoshenko beams and stiffened plates. Journal of Sound and Vibration 104 (1) (1986) 9-27.

Mead, D. J., Wave propagation in continuous periodic structures: research contributions from Southampton, 1964-1995. Journal of Sound and Vibration 190 (3) (1996) 495-524.

Ming, R., The measurement of coupling loss factors using the structural intensity technique. Journal of the Acoustical Society of America 103 (1) (1998) 401-407.

Mukherjee, A., Mukhopadhyay, M., A review of dynamic behavior of stiffened plates. The shock and vibration digest 18 (6) (1986) 3-8.

Mukhopadhyay, M., Mukherjee, A., Recent advances on the dynamic behavior of stiffened plates. The shock and vibration digest 21 (1989) 6-9.

Nair, P. S., Rao, M. S., On vibration of plates with varying stiffener length. Journal of Sound and Vibration 95 (1984) 19-29.

Nefske, D. J., Sung, S. H., Power flow finite element analysis of dynamic systems: basic theory and application to beams. Journal of Vibration and Acoustics 111 (1989) 94-100.

Newland, D. E., Power flow between a class of coupled oscillators. Journal of the Acoustical Society of America 43 (3) (1968) 553-558.

Ojeda, R., Prusty, B. G., Lawrence, N. and Thomas, G. A., A new approach for the large deflection finite element analysis of isotropic and composite plates with arbitrary orientated stiffeners. Finite Elements in Analysis and Design 43 (13) (2007) 989-1002.

Olsson, M., Finite element, modal co-ordinate analysis of structures subjected to moving loads. Journal of Sound and Vibration 99 (1985) 1-12.

Ouisse, M., Guyader, J. L., Vibration sensitive behavior of a connecting angle: Case of coupled beams and plates. Journal of Sound and Vibration 267 (4) 2003 809-850.

Park, D. H., Hong, S. Y., Power flow models and analysis of in-plane waves in finite coupled thin plates. Journal of Sound and Vibration 244 (4) (2001) 651-668.

Park, Y. H., Hong, S. Y., Hybrid power flow analysis using coupling loss factor of SEA for low-damping system – Part I: Formulation of 1-D and 2-D cases. Journal of Sound and Vibration 299 (2007) 484-503.

Peng, L. X., Liew, K. M. and Kitipornchai, S., Buckling and free vibration analysis of stiffened plates using the FSDT mesh-free method. Journal of Sound and Vibration 289 (2006) 421-449.

Popplewell, N., The response of box-like structures to weak explosions. Journal of Sound and Vibration 42 (1) (1975) 65-84.

Popplewell, N., The vibration of box-like structure I: Natural frequencies and normal modes. Journal of Sound and Vibration 13 (4) (1971) 357-365.

Pratellesi, A, Viktorovitch, M, Baldanzini and N, Pierini, M., A hybrid formulation for mid-frequency analysis of assembled structures. Journal of Vibration and Acoustics 309 (2009) 545-568.

Rabbiolo, G., Bernhard, R. J. and Milner, F. A., Definition of a high-frequency threshold for plates and acoustical spaces. Journal of Sound and Vibration 277 (2004) 647-667.

Rebillard, E., Guyader, J. L., Vibration behavior of a population of coupled plates: Hypersensitivity to the connexion angle. Journal of Sound and Vibration 188 (3) (1995) 435-454.

Rook, T. E., Singh, R., Modal truncation issues in synthesis procedures for vibratory power flow and dissipation. Journal of Acoustical Society of America 99 (4) (1996) 2158-2166.

Rook, T. E., Singh, R., Structural intensity calculations for compliant plate-beam structures connected by bearings. Journal of Sound and Vibration 211 (3) (1998) 365-387.

Roy, A. K., Plunkett, R., Wave attenuation in periodic structures. Journal of Sound and Vibration 104 (3) (1986) 395-410.

Scharton, T. D., Lyon, R. H., Power flow and energy sharing in random vibration. Journal of the Acoustical Society of America 43 (6) (1968) 1332-1343.

Seo, S. H., Hong, S. Y., Power flow analysis of reinforced beam-plate coupled structures. Journal of Sound and Vibration 259 (5) (2003), 1109-1129.

Shankar, K., Keane, A. J., Power flow predictions in a structure of rigidly joined beams using receptance theory. Journal of Sound and Vibration 180 (1995) 867-890.

Shankar, K., Keane, A. J., Vibrational energy flow analysis using a substructure approach: the application of receptance theory to FEA and SEA. Journal of Sound and Vibration 201 (1997) 491-513.

Shastry, P., Venkateswara, R. G., Vibration of thin rectangular plates with arbitrarily oriented stiffeners. Computer Structure 7 (1977) 627-629.

Sheikh, A. H., Mukhopadhyay, M., Free vibration analysis of stiffened plates with arbitrary platform by the general spline finite strip method. Journal of Sound and Vibration 162 (1) (1993) 147-164.

Shinozuka, M., Deodatis, G., Response variability of stochastic finite element systems. ASCE Journal of Engineering Mechanics 114 (1988) 499-519.

Shinozuka, M., Structure response variability. ASCE Journal of Engineering Mechanics 113 (1987) 825-842.

Shorter P.J., Langley, R., Vibroacoustic analysis of complex systems, Journal of Sound and Vibration 117 (2005) 85-95.

Soize, C., A model and numerical method in the medium frequency range for vibroacoustic predictions using the theory of structural fuzzy. Journal of the Acoustical Society of America 94 (1993) 849-865.

Soize, C., Estimation of fuzzy substructure model parameters using the mean power flow equation of the fuzzy structure. Journal of Vibration and Acoustics 210 (1998) 279-286.

Soize, C., Vibration damping in low-frequency range due to structural complexity: a model based on the theory of fuzzy structures and model parameters estimation. Computers and Structures 58 (1995) 901-915.

Stefanou, G., Papadrakakis, M., The stochastic finite element method: Past, present and future. Computer Methods in Applied Mechanics and Engineering 198 (2009) 1031-1051.

Stefanou, G., The stochastic finite element method: Past, present and future. Computer Methods in Applied Mechanics and Engineering 193 (2004) 139-160.

Sun, J. C., Wang, C. and Sun, Z. H., Power flow between three series coupled oscillators. Journal of Sound and Vibration 189 (2) (1996) 215-229.

Takada, T., Weighted integral method in stochastic finite element analysis. Probabilistic Engineering Mechanics 5 (1990) 146-156.

Tan, Y. C., Efficient modeling of low- to mid-frequency vibration and power flow in complex structures. Ph.D. dissertation, University of Michigan (2001).

Tolstov, G. P. (1965). Fourier Series. Englewood Cliffs NJ: Prentice-Hall.

Tso, Y. K., Hansen, C. H., The transmission of vibration through a coupled periodic structure. Journal of Sound and Vibration 215 (1) (1998) 63-79.

Ungar, E. E., Steady state response of one-dimensional periodic flexural systems. Journal of the Acoustical Society of America 39 (1966) 887-894.

Wang, Z. H., Xing, J. T. and Price, W. G., An investigation of power flow characteristics of L-shaped plates adopting a substructure approach. Journal of Sound and Vibration 254 (4) (2002) 627-648.

Wester, E. C. N., Mace, B. R., Statistical energy analysis of two edge-coupled rectangular plates: ensemble averages. Journal of Sound and Vibration 193 (1996) 793–822.

Williams, D., Dynamic loads in aeroplanes under given impulsive loads with particular reference to landing and gust loads on a large flying boat. RAE Reports SMU 3309 and 3316 (1945).

Williams, D., Dynamic loads in aeroplanes under given impulsive loads with particular reference to landing and gust loads on a large flying boat. RAE Reports SMU 1945, 3309-3316.

Wohlever, J. C., Bernhard, R. J., Mechanical energy flow models of rods and beams. Journal of Sound and Vibration 153 (1992) 1-19.

Woodhouse, J., An approach to the theoretical background of statistical energy analysis applied to structural vibration. Journal of the Acoustical Society of America 69 (1981) 1695-1709

Wu, C. J., White, R. G., Vibrational power transmission in a finite multi-supported beam. Journal of Sound and Vibration 181 (1) (1995) 99-114.

Wu, J. R., Liu, W. H., Vibration of rectangular plates with edge restraints and intermediate stiffeners. Journal of Sound and Vibration 123 (1) (1988) 103-113.

Wu, T. X., Thompson, D. J., Application of a multiple-beam model for lateral vibration analysis of a discretely supported rail at high frequencies. Journal of the Acoustical Society of America 108 (2000) 1341-1344.

Xie, W. C., Buckling mode localization in rib-stiffened plates with randomly misplaced stiffeners. Computers & Structures 67 (1998) 175-189.

Xu, H. A., Li, W. L., Dynamic behavior of multi-span bridges under moving loads with focusing on the effect of the coupling conditions between spans. Journal of Sound and Vibration 312 (4-5) (2008) 736-753.

Xu, H. A., Du, J. T. and Li, W. L., Vibrations of rectangular plates reinforced by any number of beams of arbitrary lengths and placement angles, Journal of Sound and Vibration 329

(18) (2010) 3759-3779.

Xu, H. A., Li, W. L., Vibration and power flow analysis of periodically reinforced plates with arbitrary boundary conditions, 3rd International Conference on Dynamics, Vibration and Control, Hangzhou, China, 2010.

Xu, H. A., Du, J. T. and Li, W. L., Predicting the dynamic responses of and energy flows in complex systems in the presence of model uncertainty, 158th Meeting Acoustical Society of America, Antonio, Texas, USA, 2009.

Xu, H. A., Li, W. L., Dynamic modeling of complex structures in a broad frequency range, 157th Meeting Acoustical Society of America, Portland, Oregon, USA, 2009.

Xu, H. A., Li, W. L., A revisit of the coupling loss factors in determining power flows in structures, Proceedings of NCAD2008, NoiseCon2008-ASME NCAD, Dearborn, Michigan, USA, 2008.

Xu, H. A., Li, W. L., Vibrations of multi-span bridges under moving loads, 14th International congress on Sound and Vibration, Cairns, Australia, 2007.

Xu, X. D., Lee, H. P. and Lu, C., Power flow paths in stiffened plates. Journal of Sound and Vibration 282 (3-5) (2005) 1264-1272.

Xu, X. D., Lee, H. P., Wang, Y. Y. and Lu, C., The energy flow analysis in stiffened plates of marine structures. Thin-Walled Structures 42 (2004) 979-994.

Yamazaki, F., Shinozuka, M. and Dasgupta, G, Neumann expansion for stochastic finite element analysis. Journal of Engineering Mechanics 114 (1988) 1335-1354.

Yap, F. F., Woodhouse, J., Investigation of damping effects on statistical energy analysis of coupled structures. Journal of Sound and Vibration 197 (1996) 351–371.

Yuan, J., Dickinson, S. M. The flexural vibration of rectangular plate systems approached by using artificial springs in the Rayleigh-Ritz method. Journal of Sound and Vibration 159 (1) (1992) 39-55.

Yuan, J., Dickinson, S. M., On the continuity conditions enforced when using artificial springs in the Rayleigh-Ritz method. Journal of Sound and Vibration 161 (3) (1993) 538-544.

Zalizniak, V., Tso, Y., and Wood, L. A., Waves transmission through plate and beam junctions. International Journal of Mechanical Sciences 41 (1991) 831-843.

Zeng, H. C., Bert, W., A differential quadrature analysis of vibration for rectangular stiffened plates. Journal of Sound and Vibration 241 (2) (2001) 247-252.

Zhang, X. F., Li, W. L., Vibrations of rectangular plates with arbitrary non-uniform elastic edge restraints. Journal of Sound and Vibration 326 (2009) 221-234.

Zhao, X., Vlahopoulos, N., A basic hybrid finite element formulation for mid-frequency analysis of beams connected at an arbitrary angle, Journal of Sound and Vibration 269 (2004) 135-164.

Zheng, D. Y., Cheung, Y. K., Au, F. T. K. and Cheng, Y. S., Vibration of multi-span non-uniform beams under moving loads by using modified beam vibration functions. Journal of Sound and Vibration 212 (1998) 455-467.

Zheng, D. Y., Cheung, Y. K., Au, F. T. K. and Cheng, Y. S., Vibration of multi-span non-uniform beams under moving loads by using modified beam vibration functions. Journal of Sound and Vibration 212 (1998), 455-467.

Zhu, X. Q., Law, S. S., Moving forces identification on a multi-span continuous bridge. Journal of Sound and Vibration 228 (1999) 377-396.

ABSTRACT

THE FOURIER SPECTRAL ELEMENT METHOD FOR VIBRATION AND POWER FLOW ANALYSIS OF COMPLEX DYNAMIC SYSTEMS

by

HONGAN XU

May 2011

Advisor: Dr. Wen Li

Major: Mechanical Engineering

Degree: Doctor of Philosophy

A general numerical method, the so-called Fourier-Space Element Method (FSEM), is proposed for the vibration and power flow analyses of complex built-up structures. In a FSEM model, a complex structure is considered as a number of interconnected basic structural elements such as beams and plates. The essence of this method is to invariably express each of displacement functions as an improved Fourier series which consists of a standard Fourier cosine series plus several supplementary series/functions used to ensure and improve the uniform convergence of the series representation. Thus, the series expansions of the displacement functions and their relevant derivatives are guaranteed to uniformly and absolutely converge for any boundary conditions and coupling configurations. Additionally, and the secondary variables of interest such as interaction forces, bending moments, shear forces, strain/kinetic energies, and power flows between substructures can be calculated analytically.

Unlike most existing techniques, FSEM essentially represents a powerful mathematical means for solving general boundary value problems and offers a unified solution to the vibration problems and power flow analyses for 2- and 3-D frames, plate assemblies, and beam-plate

coupling systems, regardless of their boundary conditions and coupling configurations. The accuracy and reliability of FSEM are repeatedly demonstrated through benchmarking against other numerical techniques and experimental results.

FSEM, because of its exceptional computational efficacy, can be efficiently combined with the Monte Carlo Simulation (MCS) to predict the statistical characteristics of the dynamic responses of built-up structures in the presence of model uncertainties. Several examples are presented to demonstrate the mean behaviors of complex built-up structures in the critical mid-frequency range in which the responses of the systems are typically very sensitive to the variances of model variables.

AUTOBIOGRAPHICAL STATEMENT

Hongan Xu was born on August 22, 1976 in Hebei, CHINA. He earned his B.S degree in Mechanical Manufacturing & Automation at Beijing Institute of Machinery, Beijing, China. He completed his B.S in July, 1998 and began working on his M.S. in Electromechanical Engineering at Beijing Institute of Machinery, Beijing, China the following semester. His M.S. thesis was titled, "Non-stationary Condition Health Monitoring of Large Rotary Equipment". His M.S. was awarded in May of 2001. Following that, he joined Beijing University of Technology working as a research associate. There, his research focused on a multi-sensor fusion monitoring system for the NC machining process. In Fall 2005, he began pursuing his Ph.D. under the guidance of Prof. Wen Li in Mechanical Engineering, which he has continued pursuing to present.